UNIVERSIDADE FEDERAL DE SÃO CARLOS
CENTRO DE CIÊNCIAS EXATAS E DE TECNOLOGIA
PROGRAMA DE PÓS-GRADUAÇÃO EM ENGENHARIA CIVIL

UNIVERSITY OF CALGARY
FACULTY OF GRADUATE STUDIES
GRADUATE PROGRAM IN CIVIL ENGINEERING

Klaus André de Sousa Medeiros

MASONRY SHEAR WALLS GROUTED AND REINFORCED AT THEIR ENDS: BEHAVIOR, CAPACITY, SEISMIC PERFORMANCE, AND SIMPLIFIED DESIGN MODELS

SÃO CARLOS - SP
2023

Klaus André de Sousa Medeiros

MASONRY SHEAR WALLS GROUTED AND REINFORCED AT THEIR ENDS: BEHAVIOR, CAPACITY, SEISMIC PERFORMANCE, AND SIMPLIFIED DESIGN MODELS

Tese apresentada ao Programa de Pós-Graduação em Engenharia Civil da Universidade Federal de São Carlos como parte dos requisitos para a obtenção do título de Doutor em Engenharia Civil.

A thesis submitted to the Faculty of Graduate Studies in partial fulfilment of the requirements for the degree of Doctor of Philosophy in Civil Engineering.

Concentration Area: Structures and Geotechnics

Advisor: Prof. Dr. Guilherme Aris Parsekian

Co-Advisor: Prof. Dr. Nigel Graham Shrive

SÃO CARLOS - SP

2023

UNIVERSIDADE FEDERAL DE SÃO CARLOS

Centro de Ciências Exatas e de Tecnologia
Programa de Pós-Graduação em Engenharia Civil

Folha de Aprovação

Defesa de Tese de Doutorado do candidato Klaus André de Sousa Medeiros, realizada em 09/03/2023.

Comissão Julgadora:

Prof. Dr. Guilherme Aris Parsekian (UFSCar)

Prof. Dr. Nigel Graham Shrive (UofC)

Prof. Dr. Sergio Hampshire de Carvalho Santos (UFRJ)

Prof. Dr. Jason Maxwell Ingham (UoA)

Prof. Dr. Rafael Aguilar-Velez (PUC-Perú)

Prof. Dr. Ron Chik-Kwong Wong (UofC)

O Relatório de Defesa assinado pelos membros da Comissão Julgadora encontra-se arquivado junto ao Programa de Pós-Graduação em Engenharia Civil.

ACKNOWLEDGEMENTS

I would like to thank

God,
for making me continue with every discouragement, giving me the determination to never give up in the face of the innumerous difficulties that life imposes on us.

All professors,
for sharing your knowledge with me. In particular, I express my immense gratitude to my supervisors, Dr. Guilherme Parsekian, Dr. Nigel Shrive, and Dr. Fernando Fonseca, who guided me with patience, motivation, and valuable advice through this long journey. I also thank professor Joel Araújo, who always believed in my potential and motivated me to follow the academic carrier.

My family,
Cleomax, Neto, Kátia, Elba, Batista, Junior, Thomas, Lara, and Lays, who are always present in my life. Special gratitude to my mother, who helps me immensely.

My friends,
Wallisson, Bruno, and Samira, for their support, company, and welcome in São Carlos; Gilvan, for his valuable tips, advice, and friendship; Cleber and Andre, who accompanied me on several classes and works; Rodolfo Palhares, for his essential collaboration in this work; Renata, for your love and companionship.

the UFERSA,
for granting me the work license that permitted me to be dedicated exclusively to this research. Special thanks to my coworker Luis for your comprehension and generosity in giving me priority on the license list.

ABSTRACT

Medeiros, Klaus André de Sousa. Masonry shear walls grouted and reinforced at their ends: behavior, capacity, seismic performance, and simplified design models. 253p. Ph.D. Thesis. Civil Engineering – Federal University of São Carlos, São Carlos - SP, Brazil, 2023.

Partially grouted masonry structures are widely used worldwide, preferably in regions with low and mid-intensity wind and seismic loads. Thus, this thesis focuses on partially grouted masonry walls (PGMW), especially those with grout and reinforcement placed at their ends. The objectives were to evaluate the in-plane behavior, capacity, and seismic performance of multi-story coupled masonry walls, and to assess simplified design models. The thesis is divided into four parts.

In the first part, finite element (FE) models were developed to assess the influence of several parameters on the load capacity, deflection, and initial stiffness of multi-story PGMW with openings. The base model was validated with experimental data from three walls tested previously by the research group. The analyses indicated that the load capacity of masonry walls was sensitive to the ungrouted and grouted masonry strengths, mortar shear strength, vertical reinforcement ratio, aspect ratio, and axial stress; and almost insensitive to the opening size, reinforcement spacing, and horizontal reinforcement ratio. The deflection of the walls had well-defined correlations with the masonry strength, vertical reinforcement, axial stress, and aspect ratio. The initial stiffness was especially sensitive to the axial stress and the aspect ratio, but weakly correlated with the opening size, and the spacing and size of the reinforcement.

In the second part, relevant existing shear equations, including the equations of the TMS 402/602 (2016) and the CSA S304 (2014), were evaluated, and a new equation was proposed. Also, different approaches were examined to determine the most consistent method of predicting the shear load capacity (SLC) of single and multi-story PGMW with openings. The database used in this study comprises ninety-six masonry walls created using the previously developed FE model, which was adjusted and recalibrated, and fifty-nine experimental masonry walls reported in the literature. The statistical analysis showed that the new proposed equation performed more precisely than the other shear equations and highlighted the need of updating the expressions in TMS 402/602 (2016) and the CSA S304 (2014) since those equations made the most inaccurate predictions of those assessed. The results confirm that is unsafe to calculate the SLC of a wall ignoring the openings. The most accurate predictions for the perforated walls were obtained using the proposed equation considering the strength of the wall as the sum of the strength of the wall piers with dimensions defined by the openings of the same story.

The third part focused on evaluating the in-plane behavior and seismic performance of multi-story perforated PGMW with grout and reinforcement placed at the ends. The FE model was further validated against more specific data from the previous experimental tests. Besides two traditional bilinear idealizations for the actual wall response, a trilinear approach was presented with deduced equations for the seismic performance factors (SPFs). Results demonstrated that the reinforced masonry beam over the openings effectively coupled the wall piers yielding a frame-type behavior. Also, the results suggest that the walls behaved as a continuous frame, with the grouted parts acting like columns and the ungrouted parts acting like confined masonry. The loss of ductility evidenced in the backbone curves and the decrease of the SPFs confirmed that a high vertical pre-compression led the walls to a brittle response while also increasing the lateral load capacity. Concentrating the grouting and reinforcement at the wall pier ends showed a similar detailing design efficiency compared to distributing them along the wall piers. The

stiffness degradation was more intense when the walls were subjected to a lower pre-compression level. Furthermore, the stiffness degradation curves were best fitted with power and logarithmic functions for walls with the lower and higher axial load, respectively.

In the fourth part, linear and non-linear frame models were assessed in simulating the in-plane load-displacement response of multi-story, perforated PGMW. Different configurations of linear frame models were assessed for replicating the initial lateral stiffness of the walls: additional involvement of SPFs and ultimate top drift limits enabled assessment of prediction of an idealized load-displacement response. Also, a new non-linear frame model approach was evaluated to simulate the actual load-displacement response of the walls. Results indicated that including rigid offsets on the horizontal and vertical elements of the portal frame model resulted in an initial lateral stiffness close to that of experimental walls. It was possible to reproduce the idealized lateral response of the walls using the initial lateral stiffness of the linear models associated with adequate SPFs and ultimate top drifts. The idealized curves better matched the actual response when the lateral stiffness of the linear models was closer to that of the reference walls. An imposed ultimate drift higher than the actual amplified the estimation of the lateral load capacity and vice-versa, using all the approaches assessed. Values of 0.4% and 0.2% for the ultimate top drifts proved to be reasonable options for the cases in which the walls were submitted to a pre-compression of $0.04f'_m$ and $0.2f'_m$, respectively. Furthermore, the proposed non-linear braced frame model could predict the envelope curves of the experimental walls up to the peak load but did not present the expected strength degradation in the post-peak stage.

Keywords: structural masonry, shear walls, load capacity, simplified models, seismic performance.

RESUMO

Medeiros, Klaus André de Sousa. Paredes de contraventamento de alvenaria grauteadas e armadas nas extremidades: comportamento, capacidade, desempenho sísmico e modelos simplificados de projeto. 253p. Tese de doutorado em Engenharia Civil – Universidade Federal de São Carlos, São Carlos - SP, Brasil, 2023.

Estruturas de alvenaria parcialmente grauteadas são amplamente utilizadas em todo o mundo, preferencialmente em regiões com ventos e sismos de baixa e média intensidade. Assim, esta tese acerta sobre paredes de alvenaria parcialmente grauteadas (PAPG), especialmente aquelas com graute e armadura concentrados em suas extremidades. Os objetivos foram avaliar o comportamento no plano, capacidade, desempenho sísmico e modelos simplificados de projeto de paredes de alvenaria acopladas de vários andares. A tese está dividida em quatro partes.

Na primeira parte, modelos de elementos finitos (EF) foram desenvolvidos para avaliar a influência de vários parâmetros na capacidade de carga, deslocamento lateral e rigidez inicial de PAPG de vários andares e com aberturas. O modelo base foi validado com dados experimentais de três paredes testadas previamente pelo grupo de pesquisa. As análises indicaram que a capacidade de carga das paredes foi sensível às resistências da alvenaria não grauteada e grauteada, resistência ao cisalhamento da argamassa, taxa de armadura vertical, relação de aspecto e tensão axial; e quase insensível ao tamanho da abertura, espaçamento das armaduras e taxa da armadura horizontal. O deslocamento lateral das paredes teve correlações bem definidas com a resistência da alvenaria, armadura vertical, tensão axial e relação de aspecto. A rigidez inicial foi especialmente sensível à tensão axial e à relação de aspecto, mas fracamente correlacionada com o tamanho da abertura, espaçamento e taxa da armadura.

Na segunda parte, relevantes equações de cisalhamento existentes, incluindo as equações da TMS 402/602 (2016) e da CSA S304 (2014), foram avaliadas e uma nova equação foi proposta. Ademais, diferentes abordagens foram examinadas para determinar o método mais consistente de prever a capacidade de carga de cisalhamento (CCC) de PAPG de um e vários andares com aberturas. A base de dados utilizada neste estudo é composta por noventa e seis paredes de alvenaria criadas com o modelo EF previamente desenvolvido, que foi ajustado e recalibrado, e cinquenta e nove paredes de alvenaria experimentais relatadas na literatura. A análise estatística mostrou que a nova equação proposta teve um desempenho mais preciso do que as outras equações de cisalhamento e destacou a necessidade de atualizar as expressões na TMS 402/602 (2016) e na CSA S304 (2014), uma vez que essas equações fizeram as previsões mais imprecisas dentre todas avaliadas. Os resultados confirmam que não é seguro calcular a CCC de uma parede ignorando as aberturas. As previsões mais precisas para as paredes com aberturas foram obtidas usando a equação proposta considerando a resistência da parede como a soma da resistência dos nembos da parede com dimensões definidas pelas aberturas do mesmo andar.

A terceira parte concentrou-se na avaliação do comportamento no plano e do desempenho sísmico de PAPG com aberturas, vários andares e com graute e armadura concentrados nas extremidades. O modelo EF foi suplementarmente validado contra dados mais específicos dos testes experimentais prévios. Além de duas idealizações bilineares tradicionais para a resposta real da parede, uma abordagem trilinear foi apresentada com equações deduzidas para os coeficientes de desempenho sísmico (CDS). Os resultados demonstraram que a viga de alvenaria armada sobre as aberturas acoplou efetivamente os nembos da parede, gerando um comportamento do tipo pórtico. Outrossim, os resultados sugerem que as paredes se comportaram como um pórtico contínuo, com as partes grauteadas atuando como pilares e as

partes não grauteadas atuando como alvenaria confinada. A perda de ductilidade evidenciada nas envoltórias e a diminuição dos CDS confirmaram que uma elevada pré-compressão vertical induziu as paredes a uma resposta frágil ao mesmo tempo que aumentou a capacidade de carga lateral. Concentrar o graute e a armadura nas extremidades dos nembos da parede gerou uma eficiência de detalhamento de projeto semelhante com a distribuição ao longo dos nembos da parede. A degradação da rigidez foi mais intensa quando as paredes foram submetidas a um menor nível de pré-compressão. Além disso, as curvas de degradação de rigidez foram melhor ajustadas com as funções de potência e logarítmica para paredes com carga axial menor e maior, respectivamente.

Na quarta parte, modelos lineares e não lineares de pórtico foram estudados na simulação da resposta força-deslocamento no plano de PAPG com aberturas e de vários andares. Diferentes configurações de modelos de pórticos lineares foram avaliadas para replicar a rigidez lateral inicial das paredes; envolvimento adicional destes com CDS e com *drifts* limites de topo permitiram a uma previsão de uma resposta força-deslocamento idealizada. Além disso, uma nova abordagem de modelo não linear de pórtico foi analisada para simular a resposta real força-deslocamento das paredes. Os resultados indicaram que a inclusão de trechos rígidos nos elementos horizontais e verticais do modelo de pórtico simples resultou em uma rigidez lateral inicial próxima à das paredes experimentais. Foi possível reproduzir a resposta lateral idealizada das paredes usando a rigidez lateral inicial dos modelos lineares associados a CDS adequados e *drifts* limites de topo. As curvas idealizadas corresponderam melhor à resposta real quando a rigidez lateral dos modelos lineares estava mais próxima daquela das paredes de referência. Um *drift* imposto maior que o real ampliou a estimativa da capacidade de carga lateral e vice-versa, usando todas as abordagens avaliadas. Valores de 0,4% e 0,2% para os *drifts* de topo mostraram-se opções razoáveis para os casos em que as paredes foram submetidas a uma pré-compressão de $0{,}04f'_m$ e $0{,}2f'_m$, respectivamente. Ademais, o modelo de pórtico não linear proposto conseguiu prever as curvas de envoltória das paredes experimentais até o pico de carga, mas não apresentou a degradação de resistência esperada no estágio pós-pico.

Palavras-chave: alvenaria estrutural, paredes de contraventamento, capacidade de carga, desempenho sísmico, modelos simplificados.

LIST OF FIGURES

LIST OF TABLES

LIST OF ABBREVIATIONS

ABNT	Associação Brasileira de Normas Técnicas
ACI	American Concrete Institute
AS	Australia Standards
ASCE	American Society of Civil Engineers
ASTM	American Society for Testing and Materials
ATC	Applied Technology Council
BBC	British Broadcasting Corporation
BF	Braced Frame
BL	Bilinear
BS	British Standards
BYU	Brigham Young University
CMDC	Canada Masonry Design Centre
CMR	Collapse Margin Ratio
CoV	Coefficient of Variation
CSA	Canadian Standards Association
CSI	Computer and Structures Inc.
DSFM	Disturbed Stress Field Model
EF	Equivalent Frame
EN	Euro Norm
FAPESP	Fundação de Amparo à Pesquisa do Estado de São Paulo
FE	Finite Element
FEM	Finite Element Method
FEMA	Federal Emergency Management Agency
FG	Fully Grouted
H	High
JSSR	Joint Shear Strength Ratio
L	Low
LVDT	Linear Variable Differential Transformer
MCE	Maximum Considered Earthquake
MCFT	Modified Compression Field Theory
ME	Mean Error

MPM	Multi-Pier-Macro
MSJC	Masonry Standards Joint Committee
NBCC	National Building Code of Canada
NBR	Norma Brasileira
NCh	Norma Chilena
NEHRP	National Earthquake Hazards Reduction Program
NIST	National Institute of Standards and Technology
NZS	New Zealand Standard
PCTL	Percentile
PF	Portal Frame
PG	Partially Grouted
PGA	Peak Ground Acceleration
PGD	Peak Ground Displacement
PGMW	Partially Grouted Masonry Walls
PGV	Peak Ground Velocity
PUCP	Pontificia Universidad Católica del Perú
RMSE	Root Mean Squared Error
SA	Shear Approach
SAP	Structural Analysis Program
SFRS	Seismic Force-Resisting System
SG	Strain-Gauges
SLC	Shear Load Capacity
SP	String-Potentiometers
SPF	Seismic Performance Factor
STDV	Standard Deviation
TL	Trilinear
TMS	The Masonry Society
UBC	Uniform Building Code
UFRJ	Universidade Federal do Rio de Janeiro
UFSCar	Universidade Federal de São Carlos
UoA	University of Auckland
UofC	University of Calgary
USA	United States of America

LIST OF SYMBOLS

a	Stiffness degradation parameter
A_d	Cross-sectional area of diagonal elements
A_{eh}	Total effective horizontal cross-sectional area of masonry
$A_{eh,ug}$	Effective horizontal cross-sectional area of ungrouted masonry
$A_{eh,g}$	Effective horizontal cross-sectional area of grouted masonry
A_{ev}	Effective vertical cross-sectional area of masonry
A_g	Gross cross-sectional area of masonry
A_h	Total cross-sectional area of horizontal reinforcement
A_{hb}	Cross-sectional area of horizontal reinforcement bar
A_{infill}	Area of a single infilled masonry panel
A_v	Total cross-sectional area of vertical reinforcement
A_{vf}	Total cross-sectional area of exterior vertical reinforcement
A_{vi}	Total cross-sectional area of interior vertical reinforcement
A_{vib}	Cross-sectional area of interior vertical reinforcement bar
b	Stiffness degradation parameter
b_w	Width of wall
c	Distance from the extreme compression fiber to the neutral axis
C	Factor concerning the kind of masonry
C_d	Displacement amplification factor
d	Distance from the extreme compression fiber to the vertical reinforcement bar
d'	Distance from the edge of the wall to the nearest vertical reinforcement bar
d_e	Reduced effective depth of wall section
d_v	Effective depth of wall
d_y	Yield displacement
d_u	Ultimate displacement
E_s	Elastic modulus of steel
E_m	Elastic modulus of masonry
f_b	Compressive strength of block
f_{ci}	Principal compressive stress
f_j	Joint shear strength

f_{mt}	Compressive strength of mortar
f'_m	Compressive strength of masonry
$f'_{m,g}$	Compressive strength of the grouted masonry parts
$f'_{m,ug}$	Compressive strength of the ungrouted masonry parts
F_n	Nominal flexural load capacity
f_p	Peak compressive stress
f_t	Tensile strength
f_v	Stress of vertical reinforcement bar
f_{yh}	Yield strength of horizontal reinforcement
f_{yv}	Yield strength of vertical reinforcement
G_c	Shear modulus of concrete
G_h	Horizontal grouting
G_m	Shear modulus of masonry
G_v	Vertical grouting
h_e	Effective height of wall
h_w	Height of wall
H_{op}	Height of opening adjacent to the pier
k	Degradation ductility coefficient
k_c	Correction factor concerning the prism height-to-thickness ratio
k_{gh}	Factor concerning the horizontal grouting
k_{gv}	Factor concerning the vertical grouting
k_1	Ductility factor for shear load capacity provided by masonry and axial compression load
k_2	Ductility factor for shear load capacity provided by horizontal reinforcement
k_u	Factor concerning the kind of masonry and grouting
k_p	Factor concerning the flexural reinforcement
K_{el}	Initial elastic stiffness
K_0	Initial tangent stiffness
$K_{p_{ug}}$	Shear stiffness of the ungrouted region into the related wall pier
l_b	Actual length of blocks
l_{dw}	Anchorage length of the reinforcement
l_w	Length of wall

L_d	Length of diagonal elements
M_p	Plastic moment of the frame
M_n	Nominal moment capacity
M	Moment at the section under consideration
n_{ugph}	Number of the horizontal ungrouted panels formed along the wall height
n_{ugpv}	Number of the vertical ungrouted panels formed along the wall length
P	Axial compressive load on the section under consideration
r	Prism height-to-thickness ratio
R	Response modification factor
R_d	Ductility-related seismic force modification factor
R^2	Correlation factor
s_{gh}	Spacing between the horizontal grouting
s_{gv}	Spacing between the vertical grouting
s_h	Spacing between horizontal reinforcement
s_v	Spacing between vertical reinforcement
t_{eff}	Effective wall thickness
t_{fs}	Face shell thickness of blocks
T_n	Natural period of vibration
U_t	Total energy
V	Shear force at the section under consideration
V_{bm}	Basic contribution of the masonry
V_{el}	Elastic load level
V_{frame}	Shear contribution of each frame formed by the grouted cells
V_{infill}	Shear contribution of each infill ungrouted masonry panel
V_m	Factored shear load capacity provided by masonry
V_{max}	Maximum lateral load
$V_{max,avg}$	Average maximum lateral load
V_n	Nominal shear load capacity
$V_{n,pred}$	Predicted value for the nominal shear load capacity
V_p	Factored shear load capacity provided by axial compression load
V_r	Factored shear load capacity provided by reinforcement
V_{rh}	Factored shear load capacity provided by horizontal reinforcement

V_{rv}	Factored shear load capacity provided by vertical reinforcement
V_y	Yield load level
V_u	Ultimate lateral load
W	Total effective seismic weight of the structure
Y	Allowable stress factor
α	Factor concerning the action to confined grout
β	Depth factor of the equivalent rectangular stress diagram
β_r	Factor concerning the shear span ratio
γ	Stress level factor of the equivalent rectangular stress diagram
γ_g	Factor concerning the partial grouting
δ	Factor concerning the loading method
ε_{ci}	Compressive principal strain
ε_p	Strain concerning the peak stress
ε_u	Maximum compressive strain of masonry
θ	Angle formed between the wall axis and the strut
μ_d	Displacement ductility factor
ν	Poisson's ratio
ρ_h	Total horizontal reinforcement ratio
ρ_v	Total vertical reinforcement ratio
ρ_{vf}	Vertical reinforcement ratio of edge tension bars
σ	Axial compressive stress
σ_0	Axial compressive stress in gross area
τ	Shear strength
τ_a	Shear strength without axial stress
φ	Friction angle
$Ø$	Diameter
$\emptyset_m$	Masonry strength reduction factor
$\emptyset_s$	Steel strength reduction factor
Ω	Overstrength factor

TABLE OF CONTENTS

1. INTRODUCTION

Structural masonry is consolidated as an advantageous construction system in Brazil and other countries, especially because it allows rationalization to the construction process. The structure is primarily formed by walls of blocks laid with mortar joints and concrete slabs. Hollow clay or concrete blocks are mostly used.

The blocks' cells may be filled with grout and reinforced to improve the behavior of masonry members. The member is considered fully grouted (FG) when all blocks' cells are grouted and partially grouted (PG) if just some of the blocks' cells are filled. The Brazilian design code ABNT NBR 16868-1 (2020) (Structural Masonry - Part 1: Design) classifies masonry members as reinforced or unreinforced when passive reinforcement is designed or not. The code also defines prestressed masonry members in which active reinforcement is used.

The reinforcement is included to resist tensile forces and ensure greater ductility to the masonry members in the vertical grouting cells (walls) and in the horizontal grouting cells (lintels, beams, and bond beams). The main situations where tensile forces arise in residential buildings occur when the building is submitted to lateral actions due to wind or seismic events. To resist these actions, masonry building in-plane strength capacity is provided by the so-called shear walls.

Shear walls can be experimentally evaluated through monotonic or cyclic static tests or dynamic tests. Among these, the dynamic test better represents a real earthquake, but the need to use a shake table often makes it unfeasible; therefore, quasi-static tests are the most used. An intrinsic difficulty in all test methods is the construction of specimens with the actual dimensions of the walls, being often necessary to produce samples in reduced scale, which must comply with the similarity laws.

Due to the costs involved in carrying out the tests and their complexity, computational modeling is used as an alternative to simulate and study the behavior of shear walls widely. Nevertheless, it is necessary to calibrate and validate the models with experimental data so that the numerical results are reliable. Once calibrated, the models can be used inexpensively for extensive analyses.

There are many methods to numerically simulate masonry walls using devices that allow simplified and super-refined models. Some options to represent masonry walls are the strut-

and-tie model, the cantilever model with equivalent stiffness, the coupled frame model, the micro or macro truss models, the model with plane finite elements (2D), and the model with volumetric finite elements (3D). Models with 2D and 3D finite elements can also have micro or macro modeling approaches, i.e., individual discretization of all components or these discretized as a composite. Using these models is essential in the most careful analysis of design cases in which simple calculation methods may be limited.

With different potentials of experimental and numerical analyses, it is possible to distinguish how the characteristics of the shear walls affect their behavior. Furthermore, equations can also be formulated using mathematical and/or statistical models to predict the compressive, shear, and flexural load capacity of walls .

Studies on masonry shear walls have contributed to growing the understanding of the system's behavior when submitted to lateral actions. However, the seismic performance of structures is still often neglected when designing buildings in Brazil. It is noted that more systematic seismological analyses are carried out only for more critical installations, such as nuclear plants and hydroelectric and tailings dams. Some factors why most designers ignore these analyzes are listed (Dantas, 2013):

- Propagation of common sense that seismic events do not occur in Brazil;
- It is believed in the hypothesis that even if seismic events occur, they will not cause significant damage to the buildings, and;
- Technical lack of knowledge on how to consider seismic parameters and coefficients in the building design.

The lack of concern about the seismic behavior of the structures is based on the information that the Brazilian territory is located in the central region of the South American Plate and not close to its edges, where earthquakes are more prone to occur. However, it is known that earthquakes can occur even in passive zones, in this case, due to geological faults.

The development of ABNT NBR 15421 (2006) (Design of seismic resistant structures – Procedure) makes mandatory the necessity to verify the safety of the regular civil construction structures to seismic actions. The code presents criteria for quantifying these actions, the resistances to be considered in building structures, and design coefficients for various systems. However, no mention is made in the code for structural masonry as a seismic force-resisting system (SFRS), which demonstrates the wide lack of knowledge regarding the seismic effects on masonry structures built in Brazil.

1.1 OBJECTIVES

The research aims to expand the knowledge about the behavior of structural masonry walls submitted to in-plane lateral actions, especially for partially grouted walls with grout and reinforcement at their ends. More specifically, the objectives of this study are:

- Analyze the influence of material properties, geometric aspects, reinforcement detailing, and loading conditions on the behavior of multi-story perforated partially grouted shear walls;
- Investigate analytical formulations and propose a new one to predict the shear load capacity of unperforated and perforated partially grouted shear walls;
- Evaluate the seismic behavior, parameters and performance of multi-story perforated shear walls with grout and reinforcement concentrated at their pier ends;
- Assess simplified models considering the coupling effects to simulate the behavior of perforated shear walls with grout and reinforcement concentrated at their pier ends.

Therefore, the purpose is to contribute to a better understanding of the topic and support design, verification, and detailing of shear walls in structural masonry buildings.

1.2 SIGNIFICANCE OF RESEARCH

The behavior of masonry shear walls has been extensively studied in recent decades. However, there are no studies focused on walls that are simultaneously multi-story, with openings, and typically grouted and reinforced at their pier ends.

Therefore, an extensive analysis of the parameters that influence the behavior of those typical walls is necessary, as well as an evaluation of the accuracy of existing equations to predict their shear load capacity. It is noteworthy that equations from international design codes, such as the American TMS 402/602 (2016) and the Canadian CSA S304 (2014), are based on empirical research results with one-story walls and without openings.

Neglecting lateral seismic loads in designing buildings in Brazil is still common since there is a false idea that these actions are neglectable in all regions of the country. Since the publication of the ABNT NBR 15421 seismic code, there are notable advances in the national literature on studies of seismic-resistant systems in steel and reinforced concrete structures ABNT NBR 15421 (2006). However, even after this code's development, little is known about the seismic performance of structural masonry shear walls considering local detailing standards.

The potential strength and stiffness gains in walls with openings conferred by the coupling of the piers by the reinforced beams are not considered in the simple design models, such as isolated bars (cantilevers) with equivalent stiffness. These models can be very conservative and uneconomical in the design of buildings subject to intense lateral actions. More refined forms of computational modeling, such as models with two- and three-dimensional finite elements, require more knowledge and longer processing time. Thus, developing simplified models that consider the coupling of masonry piers is of great value.

In this context, the research is motivated by the need for a study reproducing typical detailing of multi-story coupled structural masonry walls submitted to lateral actions to provide engineers with coherent parameters, equations, and design models.

1.3 THESIS SCOPE AND ORGANIZATION

This work is part of the studies developed by the research group formed through a partnership between the Universidade Federal de São Carlos (UFSCar) – Brazil, the University of Calgary (UofC) – Canada, and the Brigham Young University (BYU) – United States of America. Previous studies of the group support the investigations performed in this thesis.

Although the general theme is common to all the specific objectives, they are not intrinsically dependent on each other. Therefore, this thesis does not have exclusive chapters for literature review and methodology to simplify the organization and understanding. Each chapter contains the theoretical background, methodology, results, discussion, and concluding remarks on the specific topic. The final chapter comprises all the conclusions. The thesis consists of six chapters, which are briefly described here in order to elucidate the sequence of the work. For a better interpretation, the organization of the thesis is illustrated in Figure 1.

This Chapter 1 brings an introduction contextualizing the research themes and their relevance, as well as the objectives to be achieved, the motivation, and an overall view of how the thesis is organized.

Chapter 2 describes experimental tests conducted in a previous study of the research group, which serves as the main experimental data background for this thesis. Then, preliminary numerical analyses also performed in a previous investigation are remade, observing numerical perturbations and model limitations to avoid inconsistent results. The parametric analysis investigates the influence of the constituent material properties, geometric aspects, and loading conditions on the behavior of multi-story perforated partially grouted masonry shear walls.

In Chapter 3, the numerical model is improved and used in conjunction with experimental results from the literature to examine the applicability and accuracy of existing equations and a new equation is proposed to predict the lateral load capacity of non-perforated and perforated partially grouted shear walls failing by diagonal shear.

In Chapter 4, the improved numerical model is further validated to ensure a suitable model for a more specific analysis. Then, the experimental tests and the numerical model are used to analyze the responses qualitatively and quantify the seismic performance of multi-story perforated shear walls with grout and reinforcement concentrated at their pier ends.

Chapter 5 assesses linear and non-linear simplified frame models considering the coupling effects to simulate the load-displacement response of perforated shear walls with grout and reinforcement concentrated at their pier ends.

Chapter 6 includes all conclusions about the results and analyses made in the previous chapters. References and appendices are presented after this chapter.

Figure 1: Thesis organization chart.

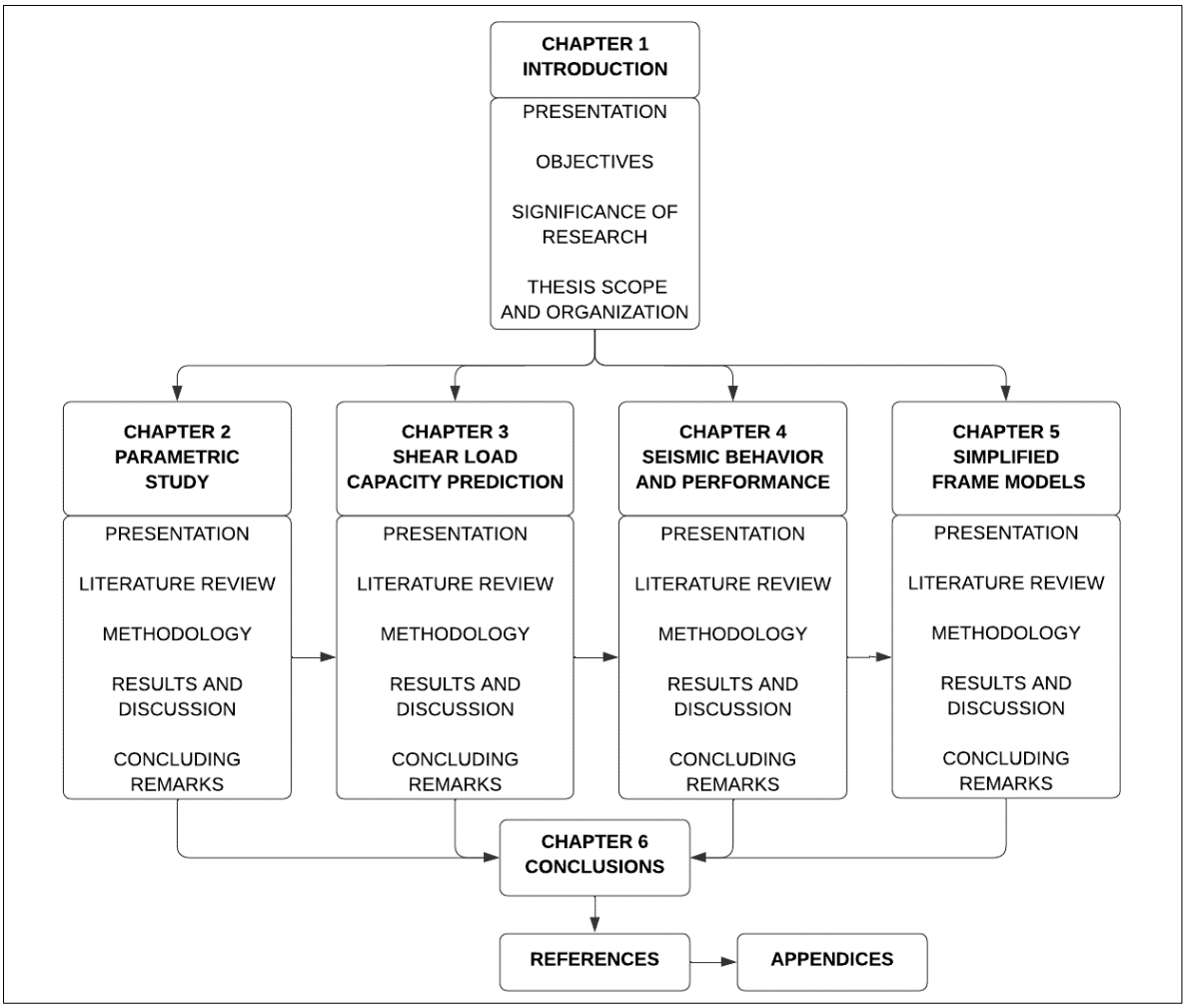

Source: Author.

2. PARAMETRIC STUDY

The influence of several parameters on the behavior of multi-story perforated partially grouted masonry shear walls is studied in this chapter through a systematic numerical analysis. Characteristics related to the properties of the constituent materials and components, the geometric aspect, and the loading conditions of the walls are evaluated.

The study presented in this chapter led to the following publication:

- Medeiros, K. A. S., Chavez, K. H., Fonseca, F. S., Parsekian, G. A., Shrive, N. G., 2020, Parametric study of multi-story, perforated, partially grouted masonry walls subjected to in-plane cyclic actions. Canadian Journal of Civil Engineering. 48(8): 1046-1055. https://doi.org/10.1139/cjce-2020-0128.

2.1 LITERATURE REVIEW

There is general agreement that the performance of shear walls is conditioned by parameters as the aspect ratio (height/length) of the wall, grouting, amount and spacing of reinforcement, openings, the strength of each component, boundary conditions, and axial load (Priestley and Elder, 1982; Matsumura, 1986; Shing et al., 1988, 1989, 1990; Ghanem et al., 1992; Voon and Ingham, 2006, 2008; Shedid et al., 2008; Oan and Shrive, 2009, 2010; Haach et al., 2011; Calderón et al., 2017, 2019, 2020). The different possible combinations of these parameters and the masonry heterogeneity make the wall behavior even more complex. Several experimental and numerical research are assessed here, emphasizing the characteristics of the walls tested and the influence of each parameter evaluated on their behavior.

a) Priestley and Elder (1982)

Priestley and Elder (1982) tested masonry walls that were multi-story, grouted and reinforced, constructed with concrete blocks on a reduced scale of 1:0.737, and submitted to in-plane cyclic displacements applied at the top of the walls. The general characteristics of the walls are illustrated in Figure 2.

The results showed that slender walls (large aspect ratio) presented more significant ductility problems than squat walls (small aspect ratio). It was also identified that confined walls exhibited better behavior than non-confined walls, which suffered strength degradation at low levels of ductility, especially for the wall with the highest applied axial load. Also, the

overlap length of the flexural reinforcement (vertical rebars) has been shown to affect the behavior of the walls significantly, and therefore, it should be avoided at the base of the walls and other areas where plastic hinges are probable to form.

Figure 2: Arrangement of a wall tested by Priestley and Elder (1982).

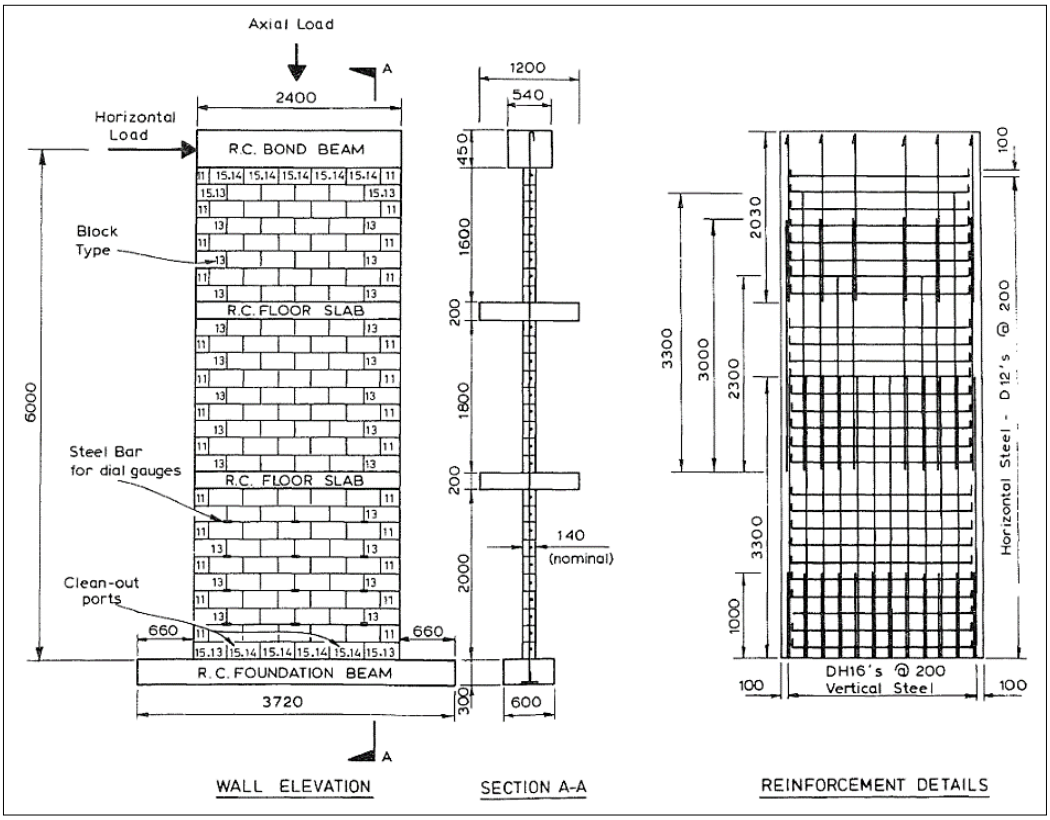

Source: Priestley and Elder (1982).

b) Matsumura (1986, 1988)

Matsumura (1986, 1988) studied the in-plane behavior of masonry walls made of clay and concrete blocks. As shown in Figure 3, the walls were one-story, unperforated, grouted and reinforced. The main variables evaluated were the masonry strength, horizontal reinforcement ratio, axial stress, aspect ratio, and full or partial grouting. Besides the test method with lateral loading on top of the walls, Figure 3(a), additional tests were performed with the walls laid horizontally as if they were deep beams and the loading applied vertically, Figure 3(b).

The author observed that the lateral strength of the walls was inversely proportional to the aspect ratio and directly proportional to the masonry compressive strength, axial load, and horizontal shear reinforcement. Considering the same geometry, partially grouted walls showed lower strength than fully grouted walls. The lateral load capacity of the walls for the formation level of the first cracks was strongly affected by the axial stress and the aspect ratio, while the other parameters demonstrated little influence.

Figure 3: Test arrangement of walls evaluated by Matsumura (1986, 1988).

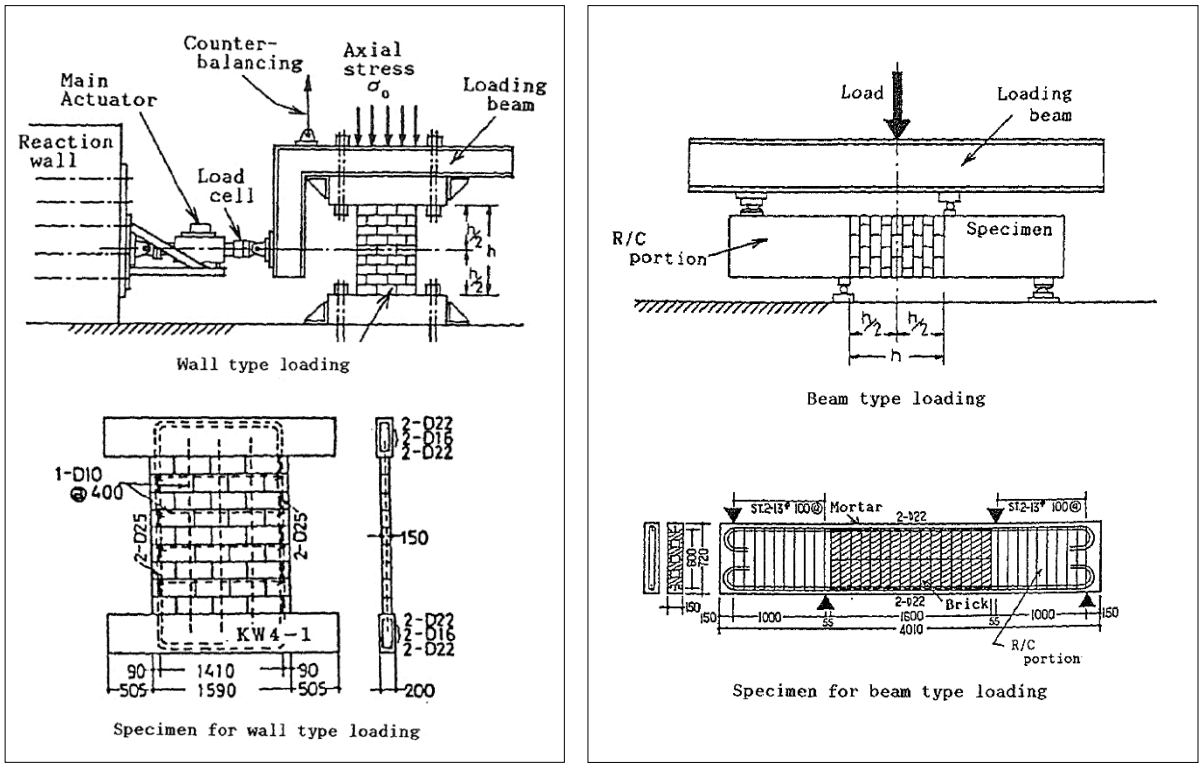

(a) Wall type loading (b) Beam type loading

Source: Matsumura (1986, 1988).

c) Shing et al. (1988, 1989, 1990)

Shing et al. (1988, 1989, 1990) conducted an experimental and numerical study with full-scale grouted masonry shear walls with reinforcement distributed uniformly, as illustrated in Figure 4.

Figure 4: General arrangement of walls tested by Shing et al. (1988, 1989, 1990).

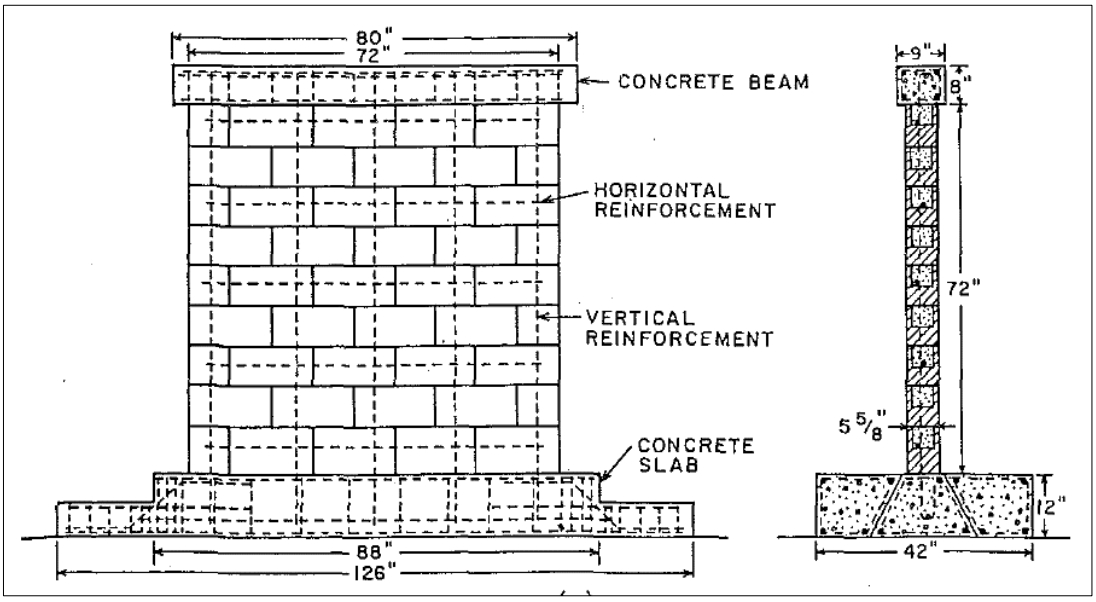

Source: Shing et al. (1988, 1989, 1990).

The results revealed a correlation between the increase of the horizontal reinforcement and the increase in the strength and ductility of the walls, concluding that using an adequate amount of horizontal reinforcement will avoid the brittle rupture of the wall by shear. The authors also concluded that the flexural and shear failure modes are sensitive to the axial stress and that the wall behavior is extremely complex after diagonal cracking has taken place. Once the diagonal cracks appear, the residual masonry strength is contributed by the dowel forces of the vertical flexural reinforcement, the horizontal reinforcement, and the aggregate-interlock forces. The latter depends on axial loading, which in turn limits crack opening.

Furthermore, the authors commented that diagonal tension cracks propagate through the blocks rather than along the mortar joints in the fully grouted shear walls; therefore, mortar joints have little influence on the shear strength of these walls. However, researchers such as Shing and Cao (1997) and Drysdale et al. (1999) indicate that the mortar joints are the inherent planes of weakness in partially grouted shear walls.

d) Ghanem et al. (1992)

Ghanem et al. (1992) evaluated the influence of vertical and horizontal reinforcement distribution on the behavior of partially grouted and reinforced shear walls. The walls were built with concrete blocks on a reduced scale, single-story, without openings, and submitted to monotonic or cyclic lateral loading. The arrangement of the walls is illustrated in Figure 5.

Figure 5: Arrangement of the walls studied by Ghanem et al. (1992).

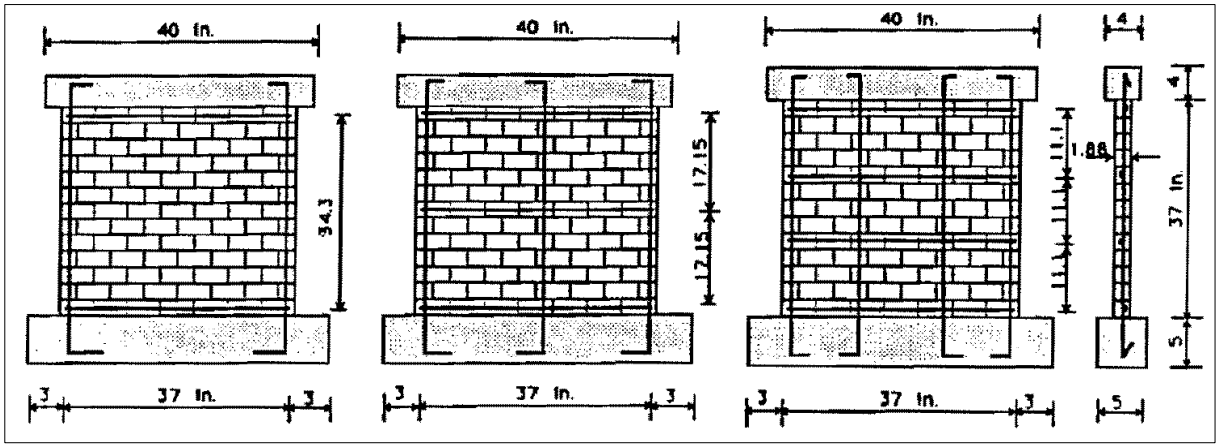

Source: Ghanem et al. (1992).

The results showed that the distribution of vertical and horizontal reinforcements significantly impacted the behavior of the walls, specifically in the failure mode, strength, and aspect of the load-displacement curve. A more spaced distribution of both reinforcements increased the shear strength of the walls but decreased the flexural strength. However, the

concentration of vertical reinforcement at the ends of the walls improved their flexural strength and conferred a slight increase in their shear strength.

According to the authors, it is necessary to distribute the horizontal reinforcement and concentrate the vertical reinforcement at the ends of the walls to ensure better flexural strength and avoid brittle failure.

e) Klingner and Leiva (1992)

The experimental program of Klingner and Leiva (1992) investigated several full-scale masonry shear walls. The walls were made of concrete blocks, two stories, perforated, and fully grouted and reinforced, as can be seen in Figure 6.

Figure 6: Arrangement of the walls tested by Klingner and Leiva (1992).

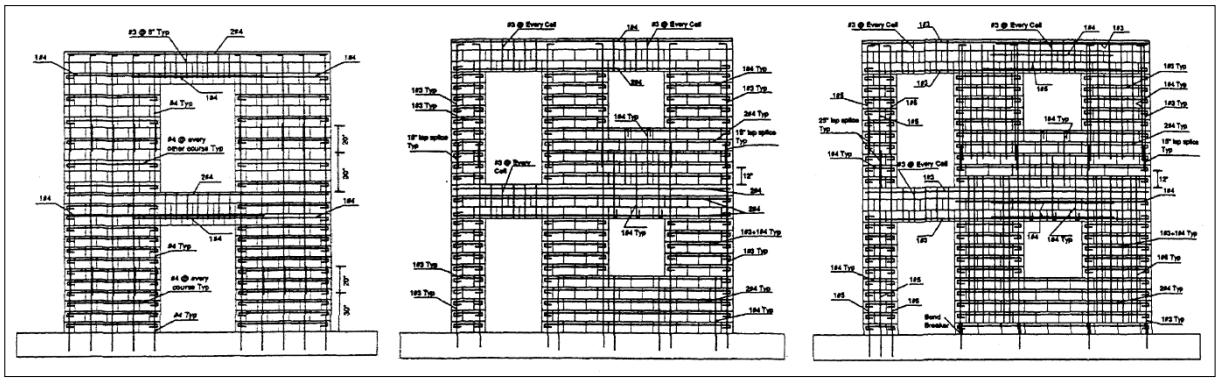

Source: Klingner and Leiva (1992).

The authors demonstrated that it was possible to induce the formation of plastic hinges in specific regions of interest in the wall by altering the reinforcement detailing. Thus, the design can be conducted to avoid brittle failure and ensure a greater wall ductility capacity.

f) Shing and Cao (1997)

Shing and Cao (1997) explored the ability of numerical models to simulate the behavior of masonry walls submitted to in-plane cyclic lateral loads. The experimental results of the walls tested by Schultz (1994) were used to calibrate and validate the models. As shown in Figure 7, the walls were partially grouted, single-story, and without openings.

Different elements were used for the joints and blocks in the models to capture the heterogeneity and anisotropy introduced to the walls by the mortar joints. An interface element with plastic behavior was adopted to represent the shear and tension in the joints, while elements with associated cracks were adopted for the masonry units.

Figure 7: General arrangement of walls studied by Shing and Cao (1997).

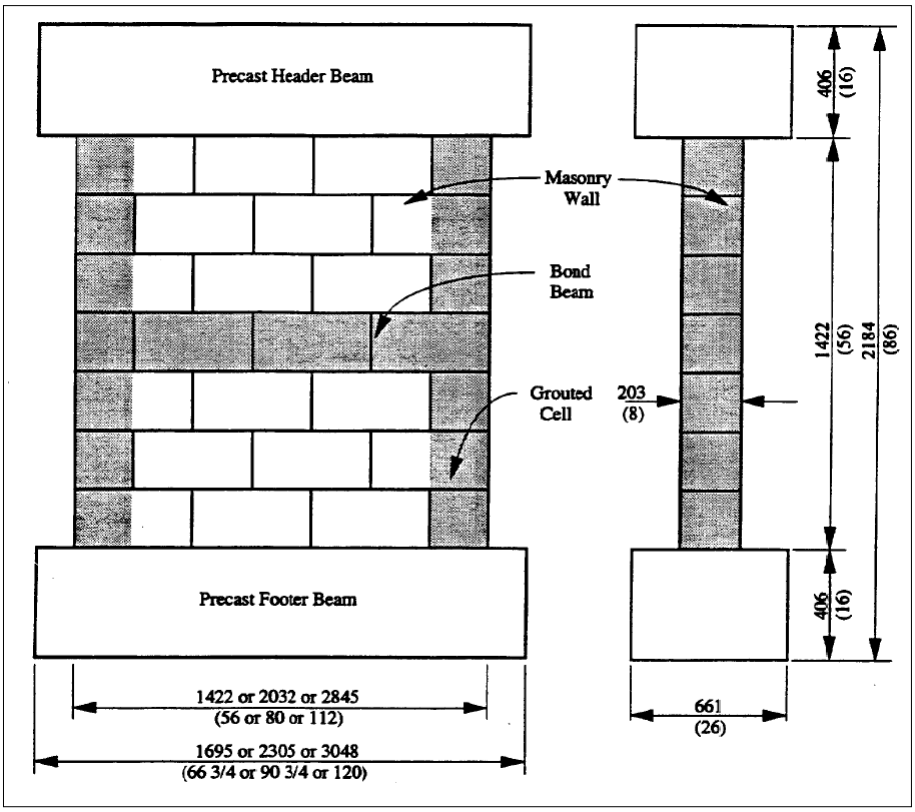

Source: Schultz (1994), apud Shing and Cao (1997).

According to the authors, one of the challenges of the study was the lack of available information on the tensile and shear behavior of mortar joints. It was emphasized the difficulty of accurately simulating the complex behavior of the shear walls in the numerical models.

Given the numerical results, the authors concluded that the amount of horizontal reinforcement in the intermediate bond beam had little influence on the behavior of the walls. It was also possible to observe that walls with a low aspect ratio tended to exhibit shear failure by sliding the horizontal joints at half the height of the wall. In contrast, walls with a high aspect ratio showed more expressive cracks in the vertical joints of the panels.

g) Voon and Ingham (2006, 2008)

Voon and Ingham (2006) studied fully and partially grouted single-story masonry shear walls made of concrete blocks. It was varied the ratio and spacing of the vertical and horizontal reinforcement, axial compression load, and aspect ratio. The general arrangement of the walls and the instrumentation used in the tests can be seen in Figure 8.

The results indicated that by increasing the horizontal shear reinforcement ratio, the strength and ductility of the walls also increased. The ductility, especially after crack formation,

was higher for the case where the same horizontal reinforcement ratio was distributed along the height of the wall using more bars with smaller diameters. The axial stress directly influenced the lateral strength and inversely the ductility of the walls, while the aspect ratio and spacing between the vertical grout points were inversely related to the load capacity of the walls.

Figure 8: Arrangement and instrumentation of walls tested by Voon and Ingham (2006).

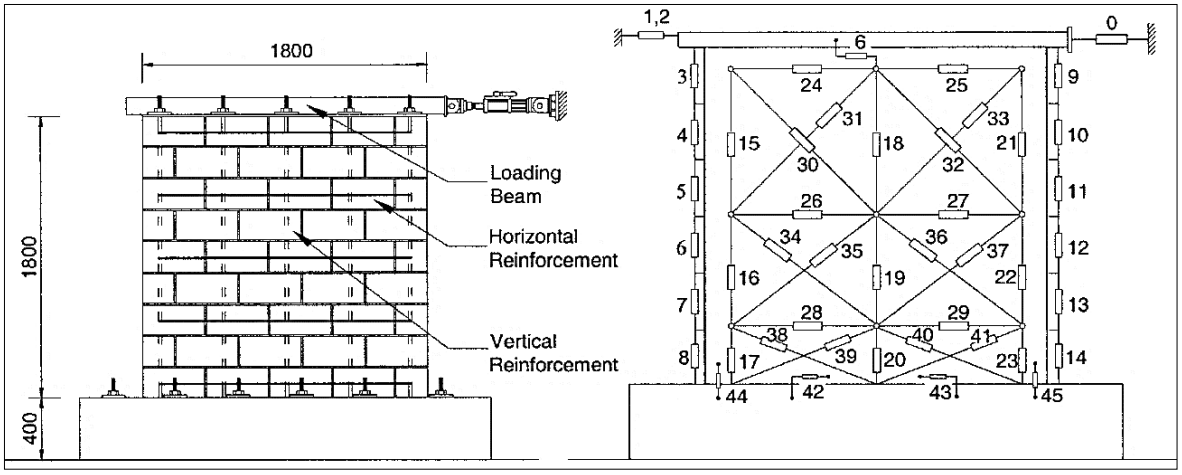

Source: Voon and Ingham (2006).

Additional research by Voon and Ingham (2008) evaluated the effect of openings in partially grouted shear walls, illustrated in Figure 9. The authors observed that increasing the opening height caused a decrease in the lateral strength of the walls and that increasing the horizontal shear reinforcement improved the strength and ductility of the walls. Furthermore, the authors noted that the available effective shear area of the piers directly affected the load distribution and capacity of the walls.

Figure 9: Arrangement of walls tested by Voon and Ingham (2008).

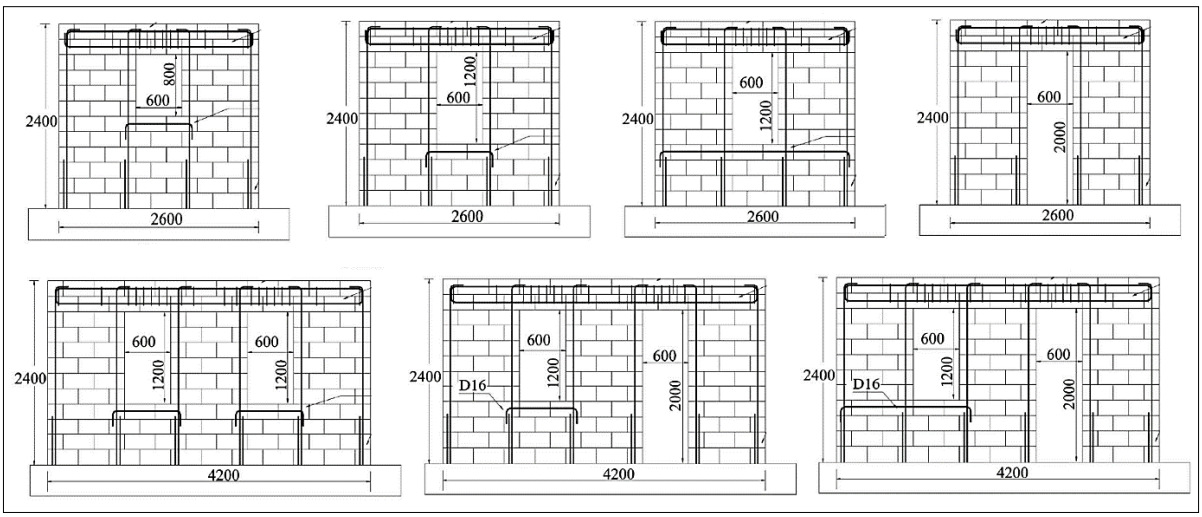

Source: Voon and Ingham (2008).

h) Shedid et al. (2008)

Shedid et al. (2008) evaluated the ductility of grouted and reinforced concrete masonry shear walls. The walls were submitted to in-plane cyclic lateral loads and induced to fail by flexure conditioned by an aspect ratio greater than 2.0. Different levels of axial stress and variations in the amount and spacing of the vertical reinforcement had their influence verified in the flexural behavior of the walls. The dimensions of the blocks and walls and the whole apparatus used in the tests are illustrated in Figure 10.

Figure 10: Wall test setup used by Shedid et al. (2008).

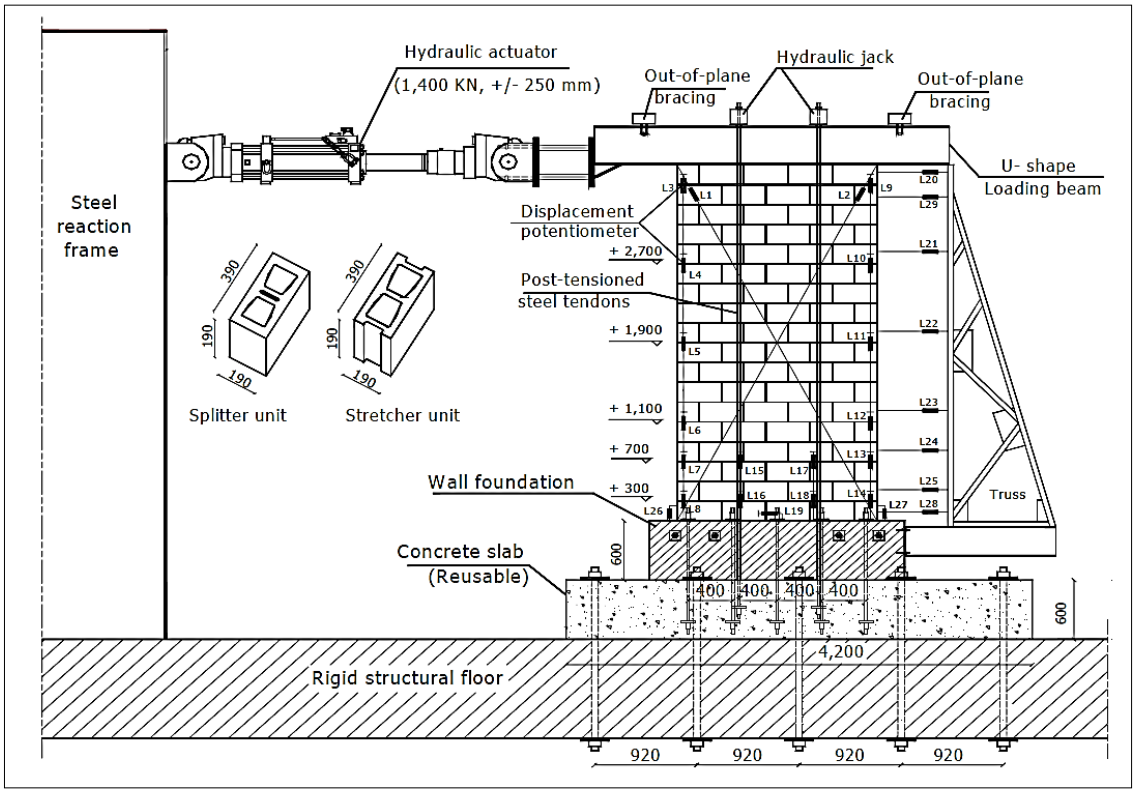

Source: Shedid et al. (2008).

The results indicated that the top drift (horizontal displacement at the top of the walls), relative to the beginning of vertical reinforcement yield, strongly depended on the reinforcement ratio, but it was minimally affected by the applied axial load. However, when the maximum lateral load was reached, the displacement was less sensitive to axial stress and vertical reinforcement ratio. It was also observed that high ductility levels were generally accompanied by low strength degradation.

i) Minaie and Moon (2009)

Minaie and Moon (2009) conducted experimental and numerical research on the behavior of fully and partially grouted masonry shear walls. The walls studied were built with

full-scale concrete and clay blocks, as shown in Figure 11. The main parameters evaluated were the level of axial stress, aspect ratio, and variations in the formulation of the laying mortar.

Figure 11: Test setup of walls evaluated by Minaie and Moon (2009).

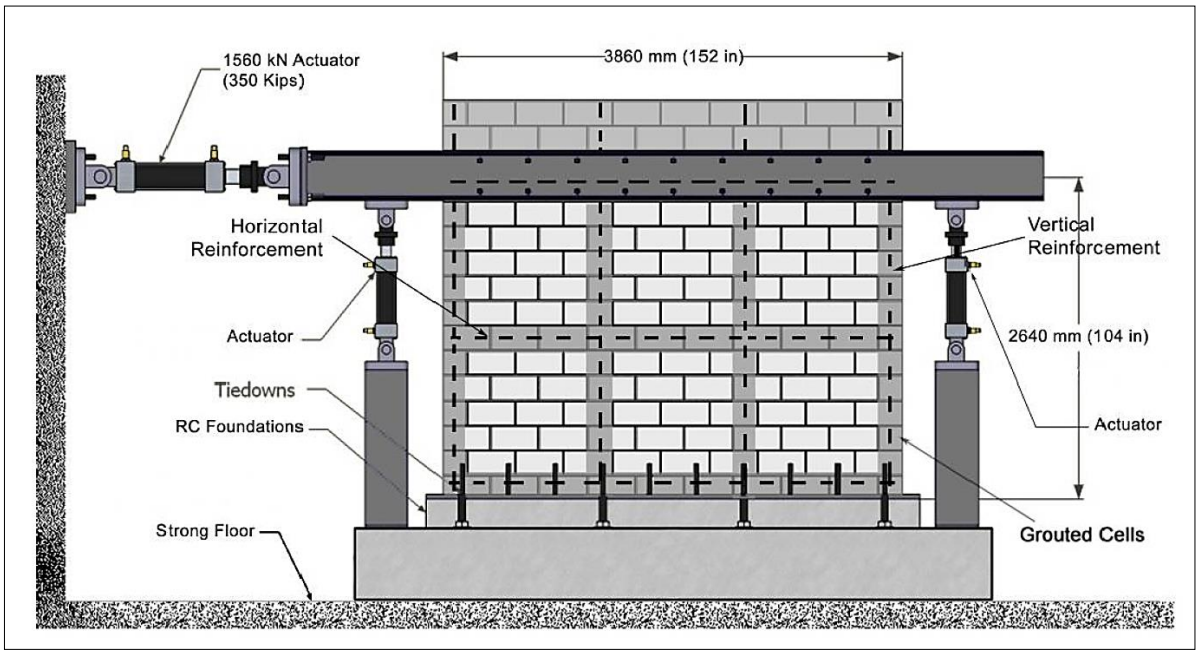

Source: Minaie and Moon (2009).

The authors concluded that partially grouted walls behave similarly to in-filled frames. The reinforced parts deform like a frame, while the unreinforced masonry panels act like an infill. It is highlighted that this behavior is completely different from how grouted walls behave.

The variations in the mortar properties did not cause significant effects on the strength and behavior of the grouted walls. However, the author commented that the effects were indeterminate for partially grouted walls, as the results diverged.

j) Oan and Shrive (2009, 2010)

Oan and Shrive (2009, 2010) tested several squat partially grouted concrete masonry walls submitted to monotonic in-plane action, as illustrated in Figure 12. The authors noted that the axial load influences the wall strength due to the increment in friction forces in the slip planes and that the horizontal shear reinforcement at the joints only acts after the masonry fails. The authors concluded, therefore, that the adoption of horizontal shear reinforcement in the joints does not increase the lateral load capacity but rather contributes to the increase in the ductility of the walls after failure. Schultz et al. (1998) and Fódi and Bódi (2010) also indicated that the lateral strength of the walls is not significantly affected by the horizontal shear reinforcement.

Figure 12: Default arrangement of tests performed by Oan and Shrive (2009, 2010).

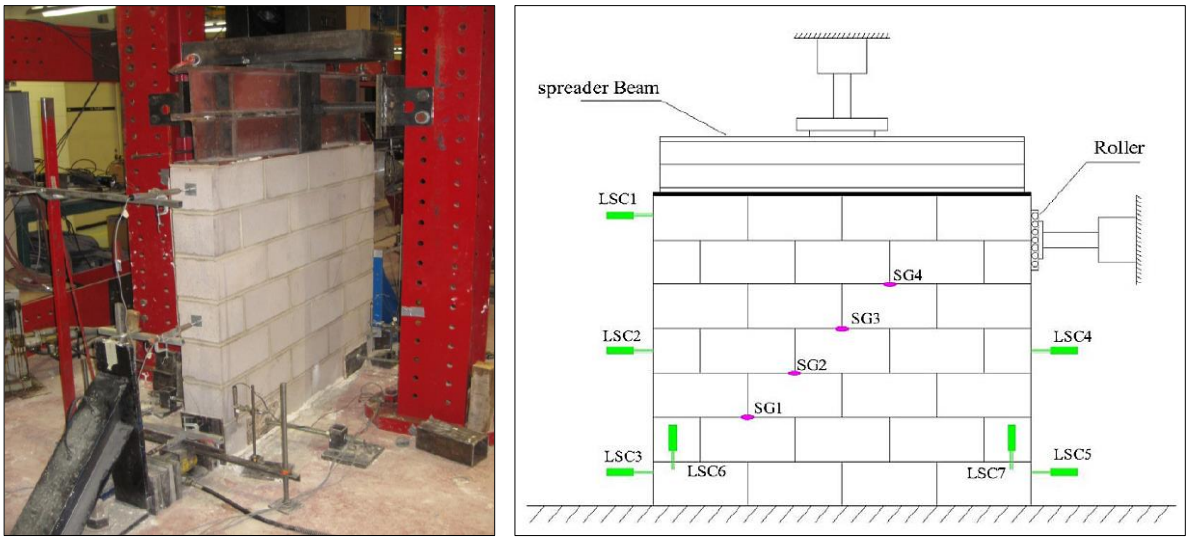

Source: Oan and Shrive (2009, 2010).

k) Elmapruk and ElGawady (2010), and Nolph and ElGawady (2010)

Elmapruk and ElGawady (2010), and Nolph and ElGawady (2010) developed similar studies with partially grouted masonry shear walls at Washington State University. The walls were made of concrete blocks, with a single story and without openings, as shown in Figure 13. The analyzed parameters were the vertical reinforcement spacing and the horizontal reinforcement ratio. Elmapruk and ElGawady (2010) evaluated walls with an aspect ratio of approximately 0.6, while Nolph and ElGawady (2010) analyzed walls with an aspect ratio of approximately 0.9.

Figure 13: Arrangement of walls tested by Elmapruk and ElGawady (2010).

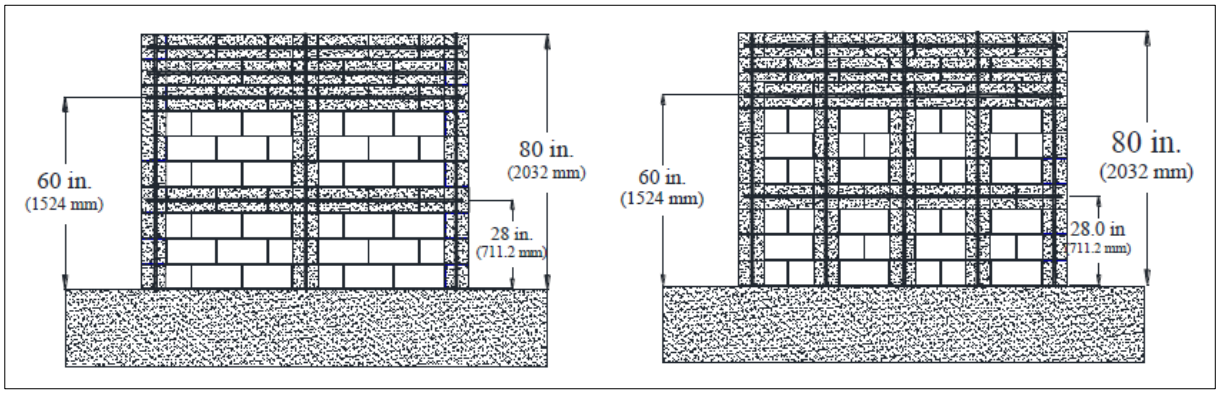

Source: Elmapruk and ElGawady (2010).

The authors observed that the lateral strength increases by decreasing the vertical reinforcement spacing and that there is a horizontal reinforcement ratio that any increase beyond does not cause more significant gains in the lateral load capacity of the walls.

l) Haach et al. (2011)

Haach et al. (2011) modeled masonry shear walls using micro-modeling techniques, as represented in Figure 14. The models were validated with differences of less than 10% against the experimental data regarding the strength capacity of the walls.

Figure 14: Representation of wall and mesh adopted by Haach et al. (2011).

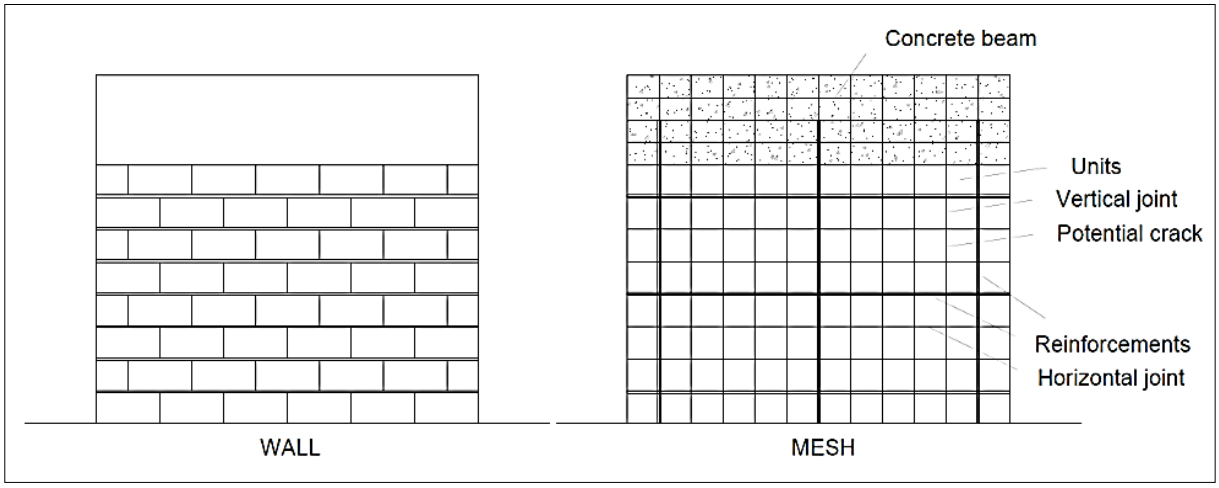

Source: Haach et al. (2011).

The authors concluded that the walls with a low aspect ratio predominantly exhibited shear failure modes, whereas the walls with a high aspect ratio mainly developed flexural failure modes. In addition, walls fixed only at the base typically failed by flexure, whereas walls fixed at both ends typically failed by shear. The authors also observed that the lateral strength of the walls increased with the adoption of vertical reinforcement when flexure was the failure mode, but negligible effects occurred when the failure mode was by shear with diagonal cracking. Like Oan and Shrive (2009, 2010), the authors stated that the horizontal shear reinforcement starts to act after the diagonal cracks occur and, thus, the redistribution of stresses from the masonry to the reinforcement has occurred.

m) Ramírez et al. (2016)

Ramírez et al. (2016) conducted an experimental study with single-story unperforated partially grouted concrete masonry shear walls submitted to in-plane cyclic lateral actions, as shown in Figure 15.

The authors observed that the horizontal reinforcement ratio and the axial pre-compression did not significantly influence the loss of stiffness of the walls, while the aspect ratio was the parameter that predominantly influenced the stiffness degradation; low walls had more significant stiffness losses than high walls. The results indicated that the lateral strength

of the wall is inversely correlated with the aspect ratio and directly with the horizontal reinforcement ratio and axial stress. The effects of varying the horizontal reinforcement ratio and axial pre-compression stress on the wall strength were more pronounced, respectively, for high and low walls. A well-defined effect of the parameters evaluated on the ductility of the wall was observed.

Figure 15: Arrangement of the walls tested by Ramírez et al. (2016).

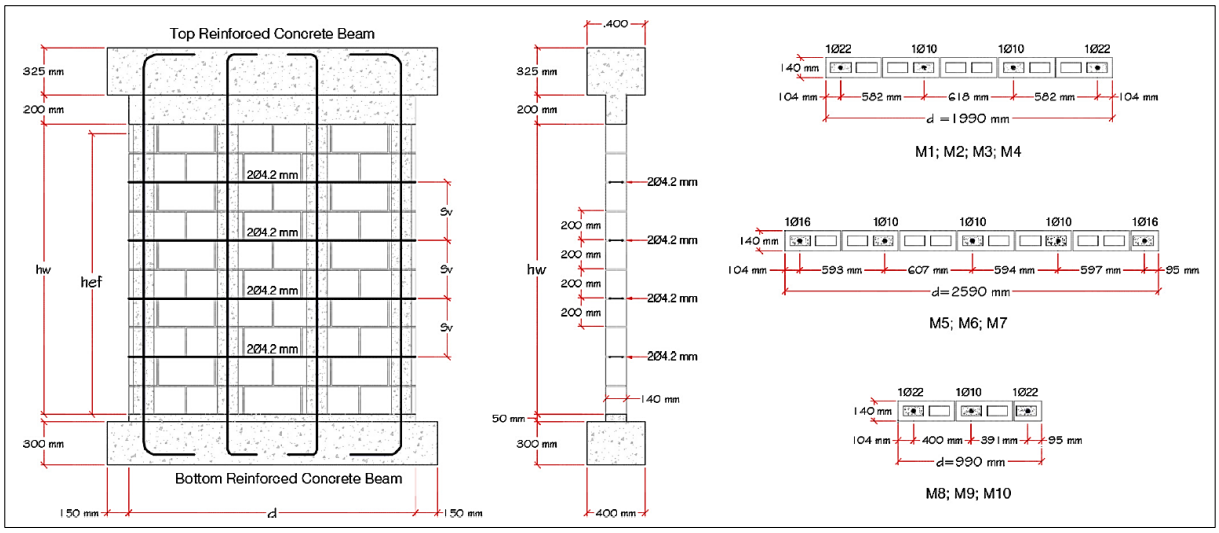

Source: Ramírez et al. (2016).

n) Dhanasekar et al. (2017)

Dhanasekar et al. (2017) examined, experimentally and numerically, if increasing the strength of mortar joints improves the in-plane shear strength of the walls. Small-scale concrete blocks joined by thin joints with high bond strength polymeric cement mortar were used. As illustrated in Figure 16, the walls were unreinforced, single-story, without openings, and submitted to monotonic lateral loading.

Contrary to the authors' expectations, the tested shear walls showed low capacity and failed due to sliding of the course at the wall base. The numerical model indicated that when the pre-compression stress was 15% greater than the masonry compressive strength, the shear capacity of the wall increased, and the failure mode changed from sliding to diagonal cracking. Therefore, increasing joint strength without the proper pre-compression level may not be efficient on unreinforced masonry shear walls with high bond strength joints.

Figure 16: Arrangement of the walls tested by Dhanasekar et al. (2017).

Source: Dhanasekar et al. (2017).

o) Hung et al. (2018)

Hung et al. (2018) performed an analysis of the results available in literature of several partially grouted shear walls using artificial neural networks. According to the authors, this analysis technique has great potential to study highly complex problems with nonlinear relationships, determining the weighted effect of each parameter. As illustrated in Figure 17, the study identified several trends, such as:

- Smaller walls (low aspect ratio) resist lateral loading more effectively than larger walls (high aspect ratio);
- As the grout ratio increases, the wall strength also increases;
- Masonry compressive strength does not have a direct and positive correlation with wall capacity; thus, masonry tensile strength may be more relevant in cases of rupture by diagonal shear cracks;
- The addition of vertical and horizontal reinforcement increases the strength of the wall, but the vertical reinforcement exerts less influence compared to the other parameters, and the horizontal reinforcement has less effect as it increases;
- Ultimate shear wall capacity increases for greater axial loads.

Figure 17: Sensitive analysis of the parameters evaluated by Hung et al. (2018).

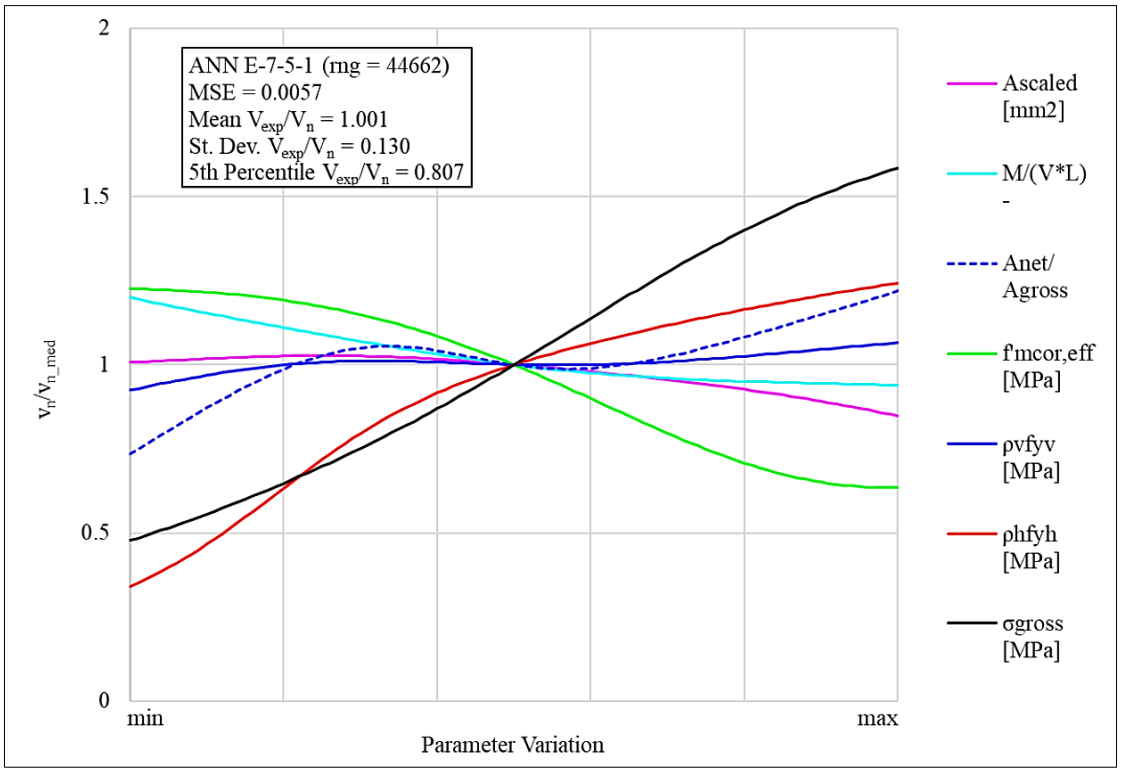

Source: Hung et al. (2018).

An important conclusion is also given about the interaction of some variables; so that as the aspect ratio decreases, the axial load and the horizontal reinforcement ratio have, respectively, greater and smaller influence on the shear wall capacity.

p) Calderón et al. (2017, 2019, 2021b)

Calderón et al. (2017, 2019) studied experimentally and numerically the response of masonry walls made of clay blocks and submitted to cyclic lateral loading. The walls were full-scale, single-story, partially grouted and reinforced, and with or without a central window opening, as shown in Figure 18.

The authors observed that a high vertical reinforcement ratio could induce a shear failure mode. Test results indicated that the presence of a central opening reduced the lateral strength and ductility and increased the degradation rate of the wall lateral stiffness. It was also found experimentally that the walls studied with openings of different heights, keeping the same length, did not have significantly different resistance capacities. On the other hand, the numerical models showed that the increase in the opening dimensions resulted in a decrease in lateral resistance and an increase in the displacement of the walls. The authors indicated that detailed micro-modeling is a laborious practice due to the need for an appropriate selection of constitutive models of materials and their corresponding input parameters.

Figure 18: Arrangement of the walls studied by Calderón et al. (2017, 2019).

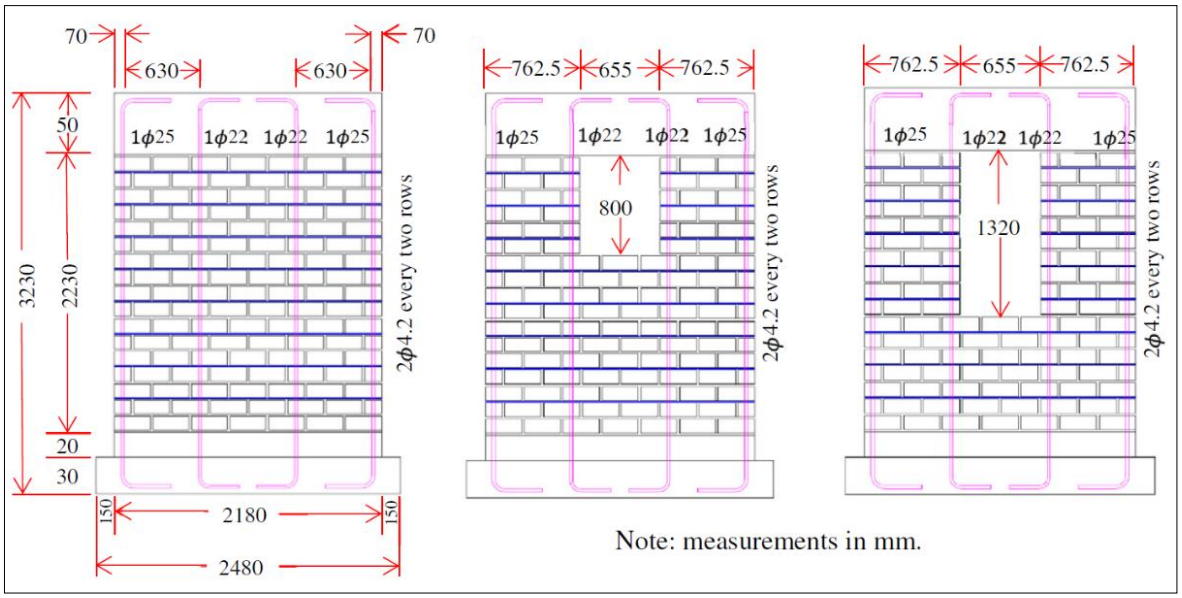

Source: Calderón et al. (2017, 2019).

In recent research, Calderón et al. (2021b) evaluated the influence of the type of horizontal reinforcement scheme adopted in masonry shear walls. The authors explained that, depending on local construction practices, the horizontal reinforcement is embedded in the bed-joints, Figure 19(a), or placed inside the grout of the horizontal courses, forming the so-called bond-beams, Figure 19(b).

Figure 19: Types of horizontal reinforcement scheme.

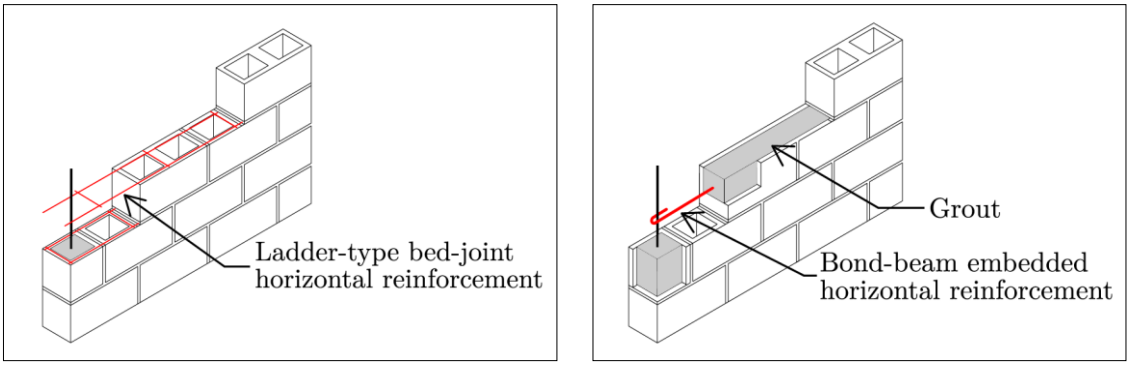

(a) Bed-joint horizontal reinforcement (b) Bond-beam horizontal reinforcement

Source: Calderón et al. (2021b).

In this context, three types of walls were tested experimentally, as illustrated in Figure 20, varying the horizontal reinforcement layout: in the first, reinforcement was adopted only at the bed joints; in the second, the reinforcement was adopted as bond beams; and on the third type, a combination was made with bed joint and bond beam reinforcements. Despite the variation in the type of reinforcement, practically the same horizontal reinforcement ratio was maintained, and the vertical reinforcement ratio and the applied axial load were also kept

constant. The walls were made of concrete blocks with an aspect ratio of approximately 0.86. It is noteworthy that the walls were detailed with a high vertical reinforcement ratio to induce shear failure mode; thus, the importance of horizontal reinforcement detailing was evaluated.

Figure 20: Arrangement of the walls tested by Calderón et al. (2021b).

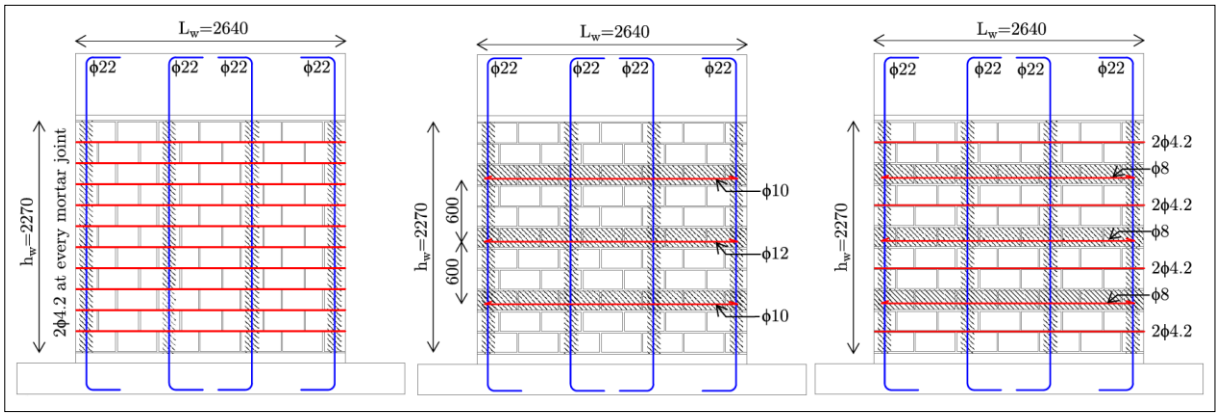

Source: Calderón et al. (2021b) .

The results showed that the lateral capacity of the walls was unaffected by the use of the different horizontal reinforcement layouts when the same horizontal reinforcement ratio and material were employed. In controlling crack widths, it was found that the distributed bed-joint reinforcement arrangement performed better than the bond-beam reinforcement layout. Based on hysteretic behavior, energy dissipation capacity, and ductility, the combination of bond-beams and bed-joint reinforcement appeared to be the most appropriate reinforcing strategy.

2.2 PREVIOUS EXPERIMENTAL PROGRAM

The experimental program was conceived and carried out by the research group formed by the partnership between the Universidade Federal de São Carlos (UFSCar), the University of Calgary (UofC), and the Brigham Young University (BYU), with support from the São Paulo Research Foundation (FAPESP) and the Canada Masonry Design Centre (CMDC).

Fortes and Parsekian (2017) conducted and reported tests of nine multi-story perforated partially grouted and reinforced masonry shear walls. The walls had door or window openings, being the piers coupled with reinforced masonry or concrete beams, as shown in Figure 21. Among all the walls tested, this research focused on those coupled with masonry beams.

The experimental walls were built in running bond with half-scale 185 × 90 × 90 mm (length, thickness, height) hollow concrete blocks (void percentage of approximately 49.5%), Figure 22, and face shell bedding with joints of 5 mm. According to Long et al. (2005), half-

scale scale shear walls can be used as a direct model concerning full-scale walls. Authors such as Long (2006), Shedid et al. (2010), and Banting and El-Dakhakhni (2014) used the same type of block in their research.

Figure 21: Arrangement of the walls tested by Fortes and Parsekian (2017).

Source: Fortes and Parsekian (2017).

Figure 22: Half-scale hollow concrete block used in the tests; dimensions in mm.

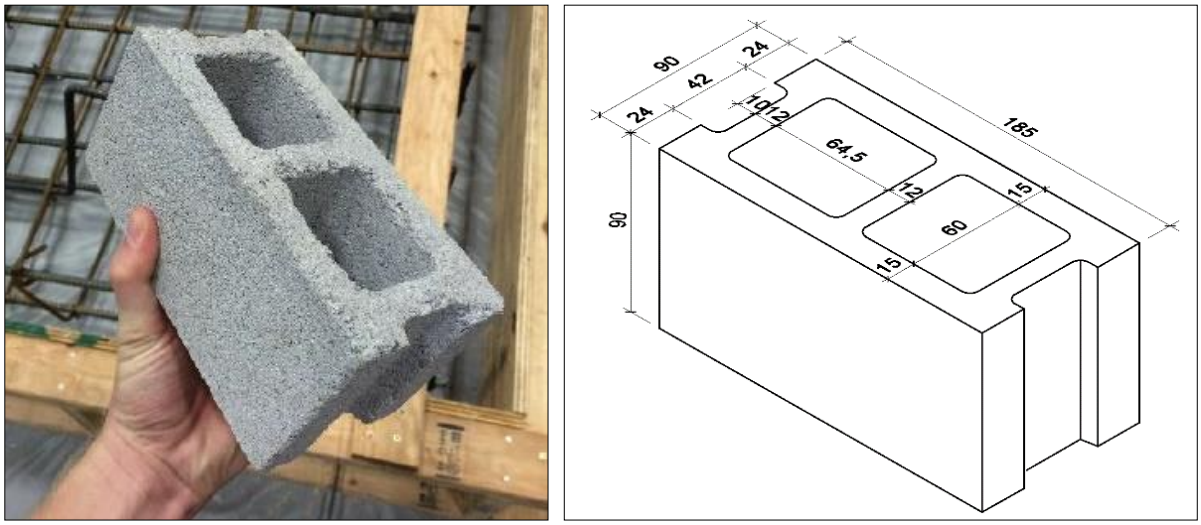

Source: Adapted from Fortes and Parsekian (2017).

The walls were fixed only at the base and composed of three stories with 14 courses each, totaling dimensions of approximately 4,490 mm in height, 3,605 mm in length, and 90 mm in thickness. The stories were separated by solid reinforced concrete beams simulating slabs, and on the last story, there was a reinforced concrete beam to receive the vertical and lateral loads and distribute them along the wall.

Six samples of walls coupled with masonry beams, illustrated in Figure 23 to Figure 26, were tested with arrangements that differed by the opening type and the horizontal reinforcement in the fifth course of each story. The openings in walls W1, W2, and W3 were window type (575 × 575 mm), while in walls D1, D2, and D3, they were door type (575 × 1,050 mm). Walls W3, D1, and D2 contained grout and reinforcement along the entire length of the fifth course, while in walls W1 and W2, there was grout and reinforcement only below the window plus three additional cells on each side of the opening. Wall D3 did not have grout and reinforcement in the fifth course.

According to the typical reinforcement detailing used in Brazil, a vertical rebar with a diameter of 9.5 mm (#3 American rebar) was placed in each of the first three cells of the blocks adjacent to the openings and at the wall ends on all stories. The idea is to concentrate material and reinforcement at the ends of the wall piers to improve flexural stiffness. Only the blocks with reinforcement were vertically grouted, taking place in two stages: the first in the 5th course and the second in the 14th course. String-Potentiometers (SPs) and Linear Variable Differential Transformers (LVDTs) were attached at various locations for data acquisition. Strain-Gauges (SGs) were also installed on several reinforcing bars prior to construction of the wall.

Figure 23: Experimental arrangement of walls W1 and W2; dimensions in mm.

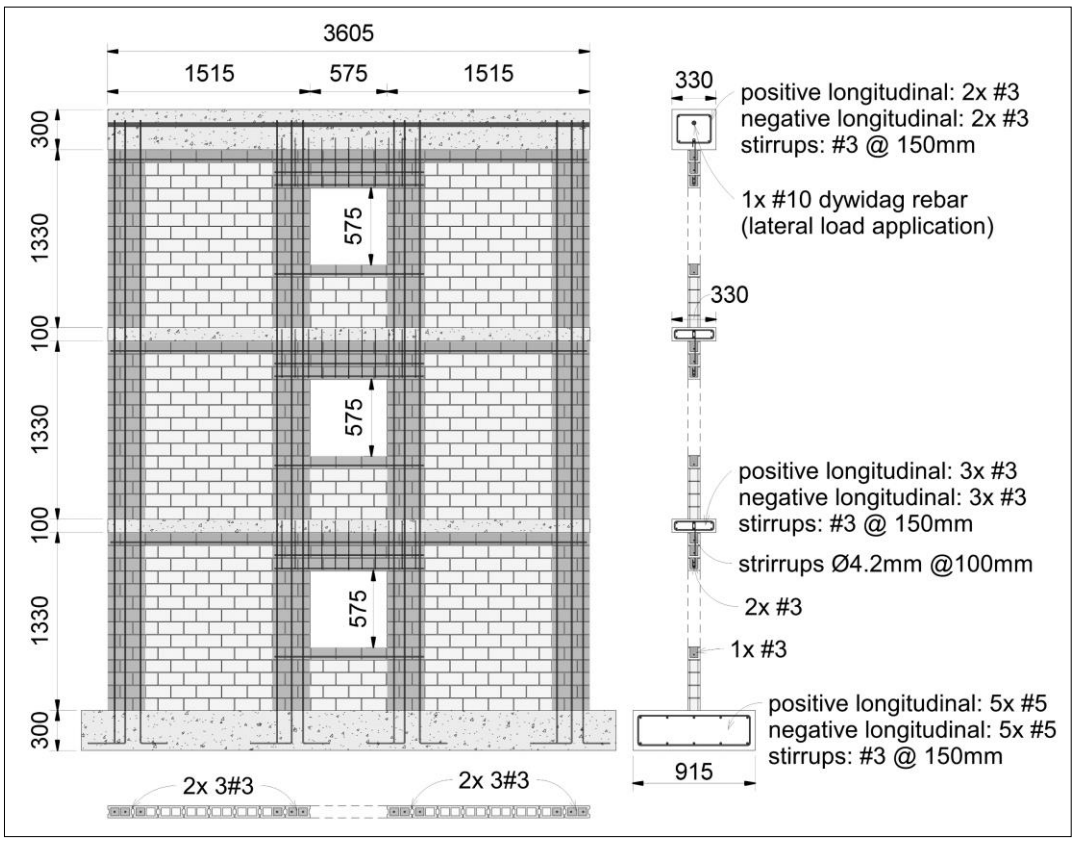

Source: Author.

Figure 24: Experimental arrangement of wall W3; dimensions in mm.

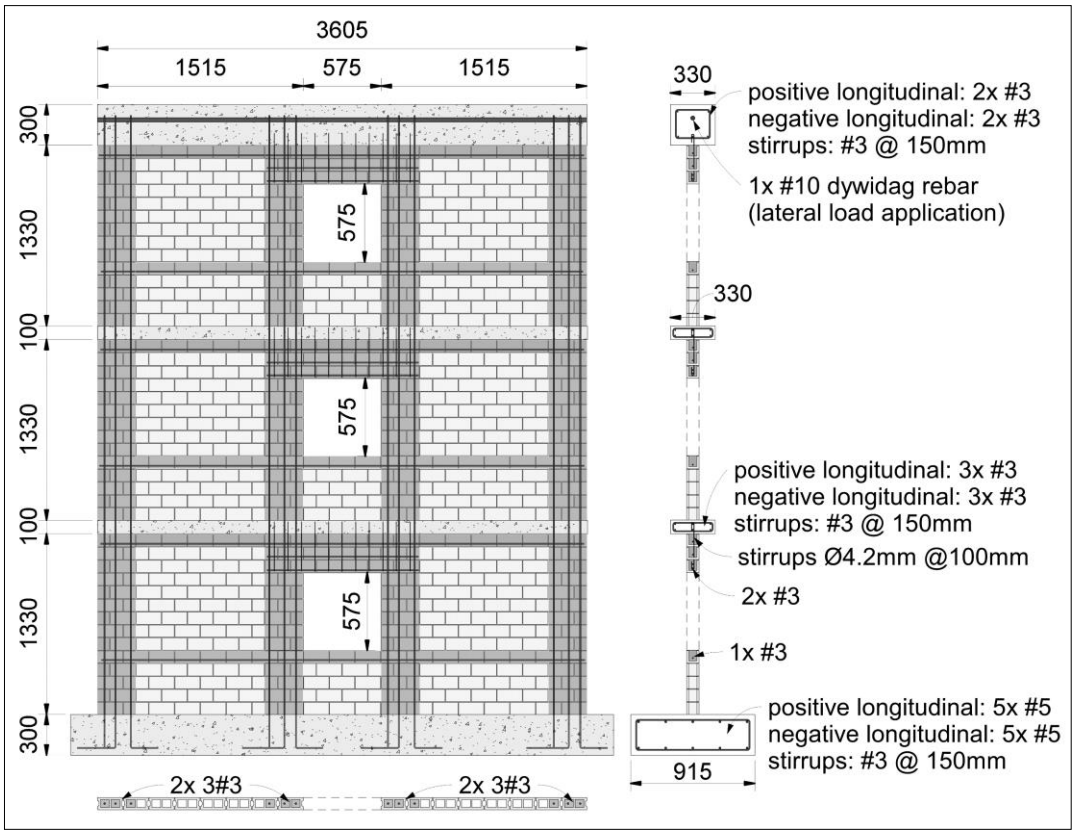

Source: Author.

Figure 25: Experimental arrangement of walls D1 and D2; dimensions in mm.

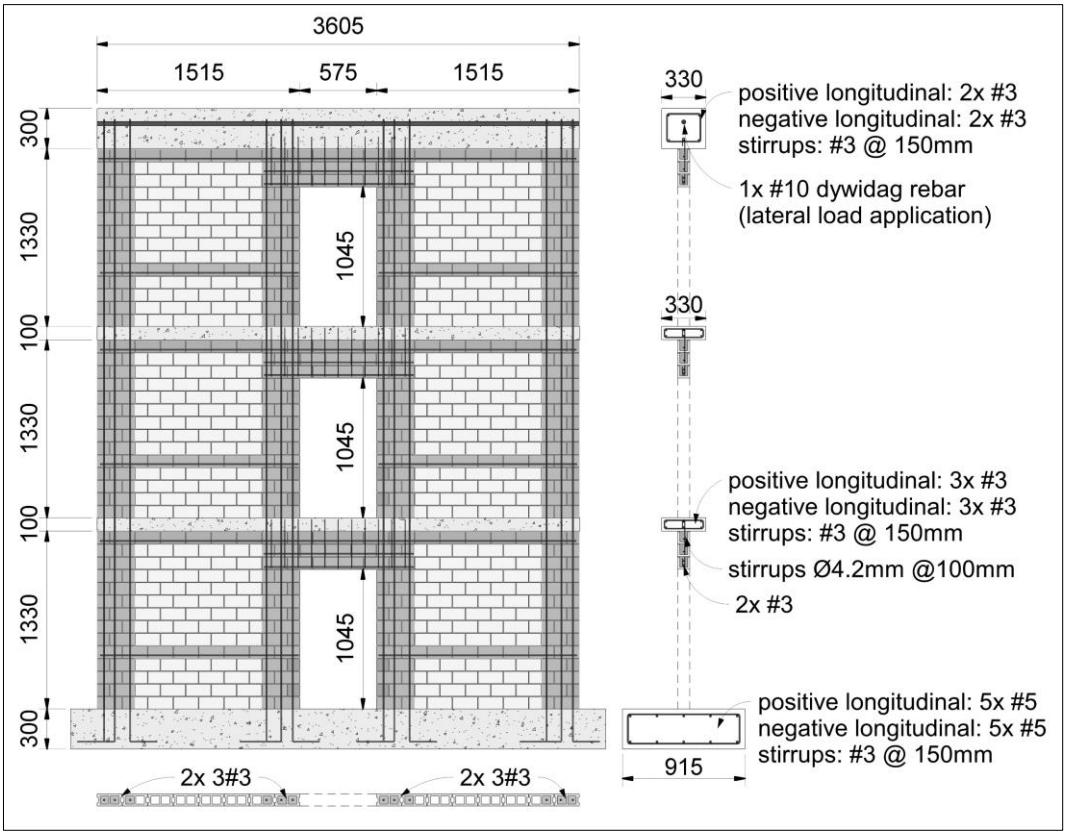

Source: Author.

Figure 26: Experimental arrangement of wall D3; dimensions in mm.

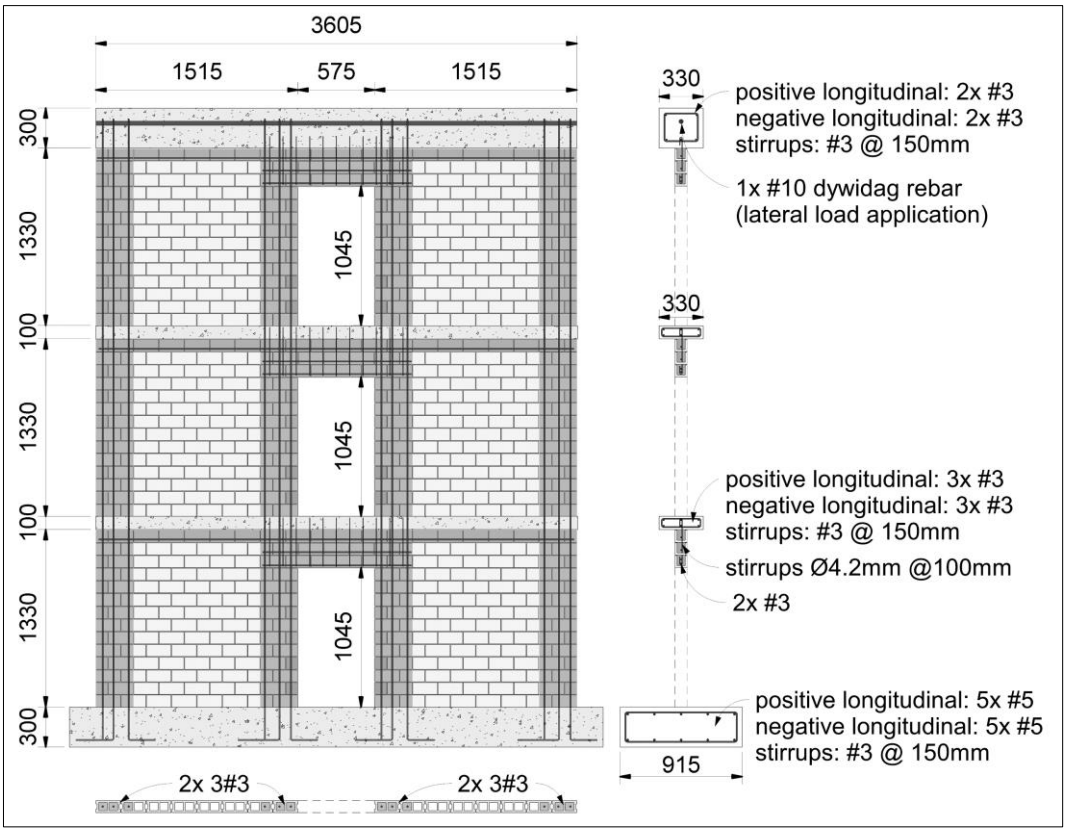

Source: Author.

All walls had the top course of each story completely grouted and reinforced with a horizontal bar of 9.5 mm in diameter. The two courses above the openings were grouted and reinforced in three additional cells beyond either side of the openings. Two horizontal rebars of 9.5 mm in diameter were used in the course immediately above the opening, and one rebar of the same type was in the subsequent course. Vertical stirrups with a diameter of 4.2 mm (Brazilian standard steel) were placed one in each cell of the blocks, interlacing these courses above the openings with the concrete slab, thus forming the masonry beam. All reinforcing bars were ribbed except the stirrups in the masonry beams, which were plain.

Reinforced concrete footings with dimensions of 3,962 × 1,219 × 300 mm (length, thickness, height) supported the walls and served to connect the walls to the structural floor. The footing reinforcement consisted of two mats of 16 mm diameter longitudinal bars tied to 9.5 mm diameter closed loop transverse bars. To connect the footing to the wall, dowel bars were positioned at each of the first three vertical cells at the ends of the wall and adjacent to the openings. These bars were extended to the top of the wall, with the splice occurring in the middle of the story. Details of the wall foundation can be seen in Figure 27.

Figure 27: Foundation of the walls.

Source: Fortes and Parsekian (2017).

The materials and constituent components used in the construction of the walls had their mechanical properties determined by tests standardized by the American Society for Testing and Materials (ASTM). The longitudinal reinforcements (vertical and horizontal) and the stirrups were tested in tension (ASTM A615, 2009) and presented the properties listed in Table 1 and the stress-strain curves shown in Figure 28. The average results for the other tests and the relevant reference for each one of them are presented in Table 2. It is essential to mention that the net area was considered in calculating the strength of the blocks and prisms.

Table 1: Mechanical properties of reinforcements.

REINFORCEMENT	YIELD STRENGTH (C.V)	ULTIMATE STRENGTH (C.V)	ELASTIC MODULUS (C.V)
Longitudinal (Ø9,5 mm)	540 MPa (4.6%)	742 MPa (0.8%)	203,512 MPa (5.4%)
Stirrups (Ø4,2 mm)	743 MPa (0.4%)	812 MPa (0.3%)	222,799 MPa (1.9%)

Source: Author.

Figure 28: Stress-strain curve of the reinforcing bars used in the experimental walls.

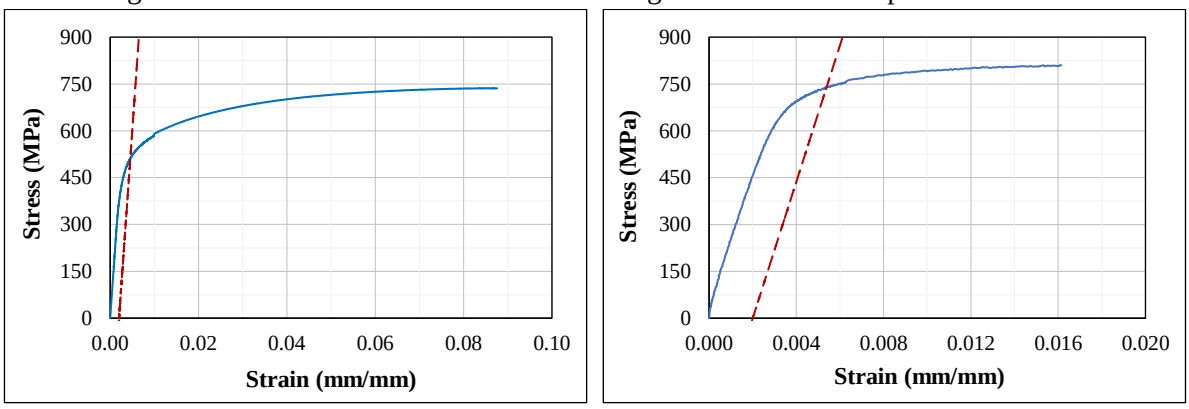

(a) Longitudinal (Ø9,5 mm) (b) Stirrups (Ø4,2 mm)

Source: Author.

Table 2: Test results of the materials and constituent components of the walls.

MATERIAL / COMPONENT	STRENGTH (C.V)	REFERENCE
Type S mortar	25.9 MPa (12.0%)	Cube strength (ASTM C780, 2009)
Hollow concrete block	21.3 MPa (5.1%)	Block strength (ASTM C140, 2010)
Fine grout	28.1 MPa (7.4%)	Cylinder strength (ASTM C476, 2010)
Concrete of the intermediate slabs	36.1 MPa (10.7%)	Cylinder strength (ASTM C39, 2010)
Concrete of the top beam	31.5 MPa (7.6%)	Cylinder strength (ASTM C39, 2010)
Concrete of the foundation	47.9 MPa (2.8%)	Cylinder strength (ASTM C39, 2010)
Hollow masonry prism - 3 courses	11.8 MPa (0.1%)	Prism strength (ASTM C1314, 2010)
Grouted masonry prism - 3 courses	12.2 MPa (5.1%)	Prism strength (ASTM C1314, 2010)

Source: Adapted from Fortes and Parsekian (2017).

A reaction frame, shown in Figure 29, was built with steel sections. Three diagonal supports, Figure 29(a), were added to minimize undesirable movements and to increase the in-plane stiffness of the frame. Out-of-plane supports were also used at the story levels to minimize only out-of-plane movement, as shown in Figure 29(b). Both the reaction frame and the supports were fixed to the structural floor with tensioned dywidag rods. The actuator was bolted to the main vertical reaction column and was supported by other steel columns.

Figure 29: Reaction frame.

(a) The actuator and in-plane supports (b) Out-of-plane supports

Source: Fortes and Parsekian (2017).

An axial load of 50 kN, which corresponds to approximately 14 kN/m, representing a typical service load for a 3-floor residential building, was uniformly distributed on the top of the walls. The load was applied using a steel section positioned over the walls. A neoprene pad was placed between the steel section and walls to minimize points of stress concentrations.

The horizontal load was applied to the top of the walls in the form of quasi-static, displacement-controlled cyclic loads with two complete repetitions of pushing and pulling per cycle. As shown in Figure 30, a total of 37 displacement cycles were planned in four phases: 7 initial cycles with an increment of 0.8 mm, 11 cycles with an increment of 2.0 mm, 13 cycles with an increment of 3.2 mm, and 6 cycles with an increment of 4.8 mm. The tests were stopped when the lateral force dropped to approximately 60% below the maximum measured force.

Figure 30: Actuator load protocol.

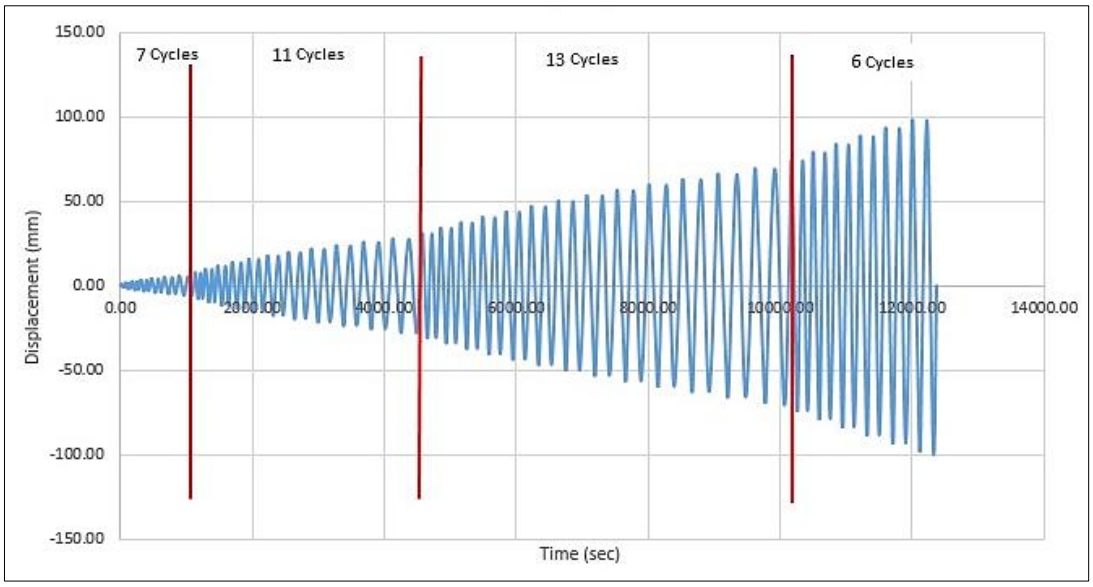

Source: Chavez and Fonseca (2018).

2.3 DESCRIPTION OF THE NUMERICAL MODEL

The numerical model was initially developed by Chavez and Fonseca (2018) as part of the research group's studies. The model was assembled with the nonlinear finite element analysis program VecTor2 (Wong et al., 2013; VecTor2, V4.4, 2019), which is based on the Modified Compression Field Theory (MCFT) (Vecchio and Collins, 1986) and Disturbed Stress Field Model (DSFM) (Vecchio, 2000). The program was originally conceived for modeling reinforced concrete structures but has been expanded to be able to model other materials, including masonry.

2.3.1 Conceptualization

Plane membrane elements were employed with dimensions of 95 × 95 mm to represent each cell of the blocks, an approached that has been used by others (Lotfi and Shing, 1991; Haach et al., 2011; Facconi et al., 2014; Elmeligy et al., 2021). The thickness was adopted equal to 90 mm for the grouted elements and 30 mm for the ungrouted elements, which is equivalent to the sum of the thickness of face shells. Blocks, concrete, and reinforcement in masonry were modeled as discrete elements whereas grout, mortar and reinforcement in concrete were considered smeared with the blocks and beam elements. The elements were connected directly node by node, and as such, the displacements of the elements were compatible. The mesh and model configuration of walls W1 and W2 are illustrated in Figure 31.

Figure 31: Numerical arrangement of walls W1 and W2.

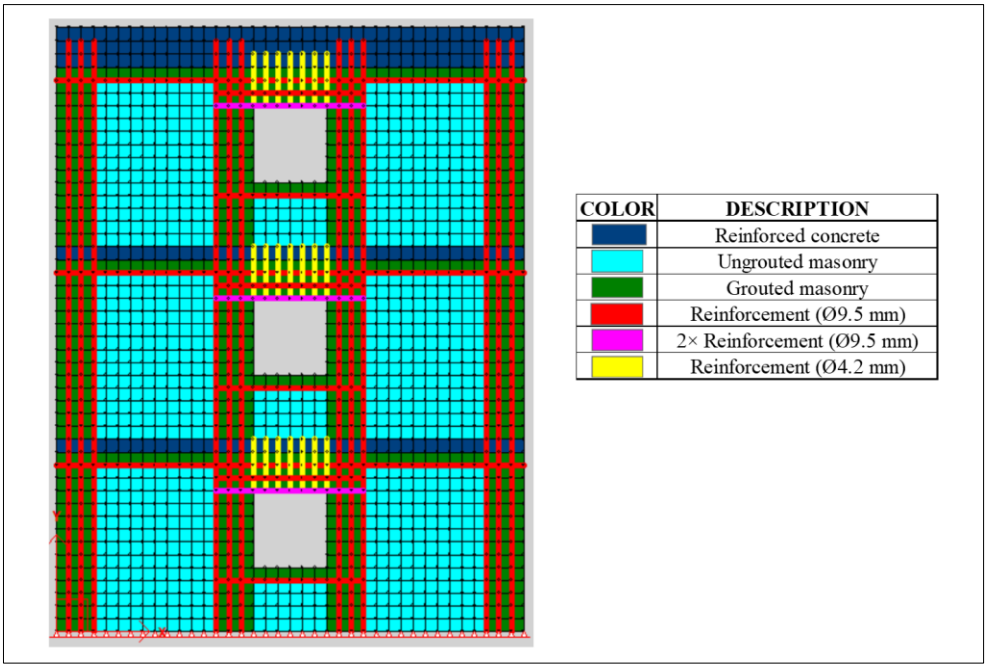

Source: Author.

Since the tensile strength of the masonry was not determined experimentally by Fortes and Parsekian (2017) and it is generally low, it was assumed to be zero, which is conservative. The ungrouted and grouted compressive masonry strengths were set equal to 11.8 and 12.2 MPa, according to Table 2. The initial tangent elastic modulus of the ungrouted and grouted masonry were not measured experimentally; rather, they were calculated using Equation 1 (Wong et al., 2013; VecTor2, V4.4, 2019), resulting in 18,305 and 18,496 MPa.

$$E_m = 3320\sqrt{f'_m} + 6900\ MPa \qquad \text{Eq. 1}$$

The mortar shear strength was also not obtained experimentally but was estimated as 265 kPa using Equation 2 (TMS 402/602, 2016). PGMW typically fail through the ungrouted

masonry joints (Shing and Cao, 1997; Drysdale et al., 1999); thus, Equation 2 was used with the compressive strength of ungrouted masonry as a substitute for mortar shear strength. In the software, the mortar shear strength is considered indirectly through the parameter joint shear strength ratio (JSSR), which is the ratio between the mortar shear strength and the masonry compressive strength. A weighted average of the grouted and ungrouted masonry compressive strengths was considered to estimate the joint shear strength ratio, resulting in a value of 0.0189.

$$V_n = 0.083\gamma_g \left[4.0 - 1.75\left(\frac{M}{Vd_v}\right)\right] A_{eh}\sqrt{f'_m} \quad \text{Eq. 2}$$

The masonry is treated in the software as an orthotropic continuum material with joint failures smeared across the finite element and controlled by the smeared crack approach. Even when this continuum is uncracked, it may slip at the head and bed joints in a single finite element since the DSFM was adjusted for masonry materials (Wong et al., 2013; VecTor2, V4.4, 2019). The mesh is thus conditioned to the block size. The user should specify the spacing between head and bed joints, which in this case were 190 and 95 mm in the x and y directions in agreement with the physical walls. As suggested by Vecchio and Lai (2004), the Walraven stress model (Walraven, 1981; Walraven and Reinhardt, 1981), which is based on an analysis of the crack structure and contact area of crack faces, was adopted to crack slip calculations.

The yield and ultimate strengths, and the elastic modulus of the reinforcement, used both in masonry and in concrete beams, were adopted in the models according to the test results shown in Table 1. The reinforcement was categorized as ductile steel with a trilinear stress-strain response: an initial linear-elastic response, a yield plateau, and a linear strain-hardening phase until rupture. The hysteretic response, dowel action, and buckling effects were also incorporated in the models (Wong et al., 2013; VecTor2, V4.4, 2019).

The axial load was applied as 1.34 kN at the nodes along the wall top, for a total of 50.7 kN. The self-weight was also considered using 2,400 kg/m^3 and 2,250 kg/m^3 as the mass density for the concrete and masonry. The lateral displacement was applied using a cyclic incremental factor of 2.65 mm divided into 0.2 mm steps, which was calculated using a weighted average of the number of cycles and displacements.

The model of Hognestad (Hognestad, 1951) and the Base Curve model (Palermo and Vecchio, 2001) were adopted for pre-peak and post-peak compression responses, respectively. The stress-strain curve of the Hognestad model is a parabola described by Equation 3 with a symmetric relationship at peak stress corresponding to ε_p strain, decreasing to zero stress at

zero and $2\varepsilon_p$ strain points. This model is suitable for concrete with a compressive strength of less than 40 MPa, and as the masonry had a compressive strength not beyond this value, the model was considered a proper choice. The Base Curve model for the post-peak compression phase is a coherent choice if the Hognestad model is used for the pre-peak compression phase. With this model, the post-peak compressive stresses are computed using the equations of the descending part of the adopted stress-strain curve (Wong et al., 2013; VecTor2, V4.4, 2019).

$$f_{ci} = -f_p \left[2\left(\frac{\varepsilon_{ci}}{\varepsilon_p}\right) - \left(\frac{\varepsilon_{ci}}{\varepsilon_p}\right)^2 \right] < 0 \quad for \quad \varepsilon_{ci} < 0 \qquad \text{Eq. 3}$$

The model proposed by Vecchio (Vecchio, 1999) was adopted to define the hysteretic response accounting for internal damage with plastic offsets and nonlinear loading/unloading (Wong et al., 2013; VecTor2, V4.4, 2019; Elmeligy et al., 2021). The model uses the failure criterion for masonry established by Ganz (Ganz, 1985) in terms of the principal stresses and the Mohr-Coulomb Stress as the cracking criterion with a cohesion considering the friction angle φ as 37° (Wong et al., 2013; Angelillo et al., 2014; Abdulla et al., 2017; VecTor2, V4.4, 2019; Elmeligy et al., 2021). The analysis involved static-nonlinear load steps with the convergence criterion being the weighted average of the displacements with a convergence limit equal to 1.00001 or 50 iterations. At each load step, the stiffness of the structure was recalculated using the mathematical constitutive models based on stresses and strains. More specific information about the constitutive models can be found in Appendix A.

2.3.2 Model validation

The numerical model was compared with the experimental results of the walls that contained a window opening (walls W1, W2, and W3). The hysteresis and backbone curves of the experimental walls and FE models are shown in Figure 32.

As seen in the graphs of Figure 32, especially in the backbones, the numerical models showed a large increase in displacements at the peak load region that does not exist in the experimental curves. This difference was possibly caused by an unsuitable choice for the post-peak constitutive relationship since the model could not adequately capture the strength and stiffness degradation at this stage. Thus, the value of the displacement immediately before the peak load, i.e., the displacement value at 97% of the peak load, was adopted for comparison to avoid an incorrect interpretation of the displacement capacity of the walls.

Figure 32: Experimental and numerical response of walls W1, W2 and W3.

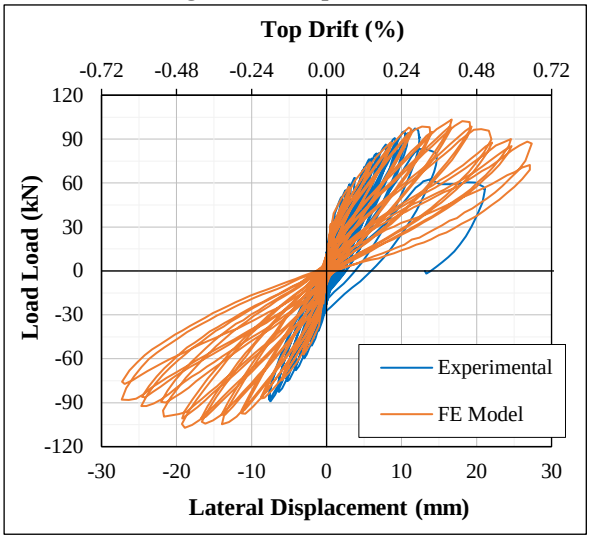

(a) Hysteresis curves of wall W1

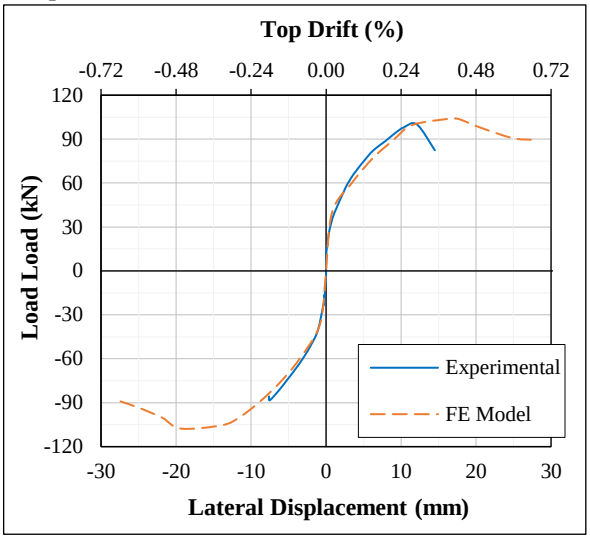

(b) Backbone curves of wall W1

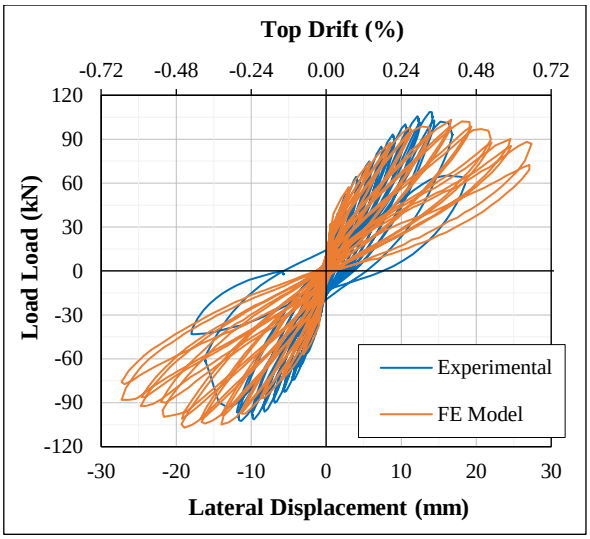

(c) Hysteresis curves of wall W2

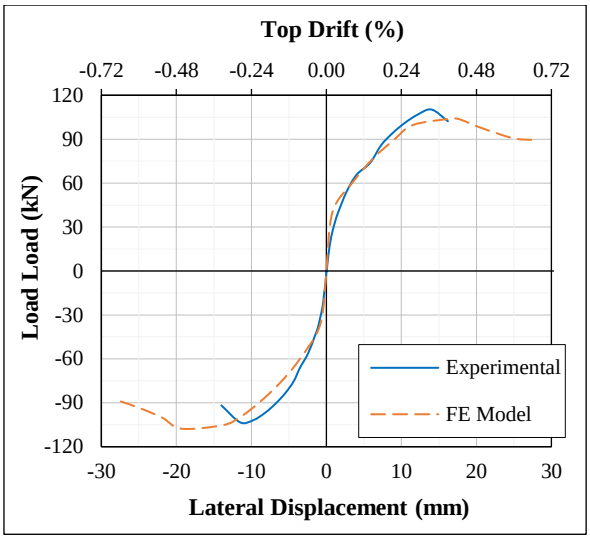

(d) Backbone curves of wall W2

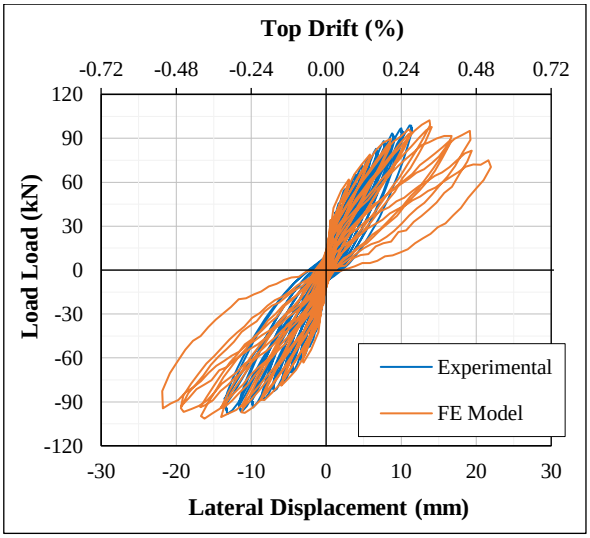

(e) Hysteresis curves of wall W3

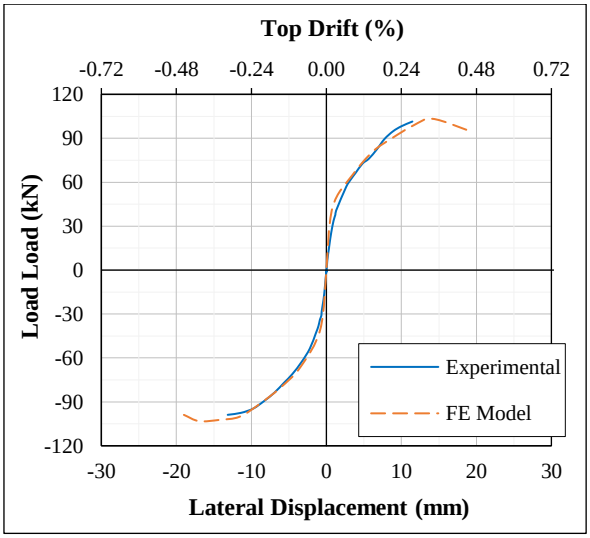

(f) Backbone curves of wall W3

Source: Author.

The experimental walls W1 and W2 had a lateral load capacity of 100 and 110 kN, and a displacement of 10 and 12 mm, respectively. The FE model predicted the maximum lateral load value for these two walls at 107.7 kN, only 7.7% and 2.1% higher and lower, respectively, than the values obtained experimentally. The displacement presented in the model for walls W1-2 was approximately 13.5 mm, which is 35% and 12.5% higher than the experimental values. Wall W3 presented a lateral load capacity of 101.5 kN and a displacement of 10 mm; the numerical model had a peak load of 103 kN and a displacement of 11.5 mm. Thus, for wall W3, the numerical model predicted the load capacity 1.5% higher and the displacement 15% higher than the experimental values.

In addition to the numerical validation of the load-displacement curves, the crack patterns obtained from the finite element model were compared to the cracks observed during the testing of the walls. These crack patterns are shown for wall W3 in Figure 33 and Figure 34 for the push and pull regimes. The darker red lines show where the stresses exceed the capacity and indicate the general crack direction.

The general crack direction and pattern, as indicated by the principal stresses from the numerical model, are very similar to that observed during testing for both the pull and push regimes. The diagonal cracking and sliding indicate failure due to shear.

Figure 33: Cracks noted in the push regime of the experimental and numerical wall W3.

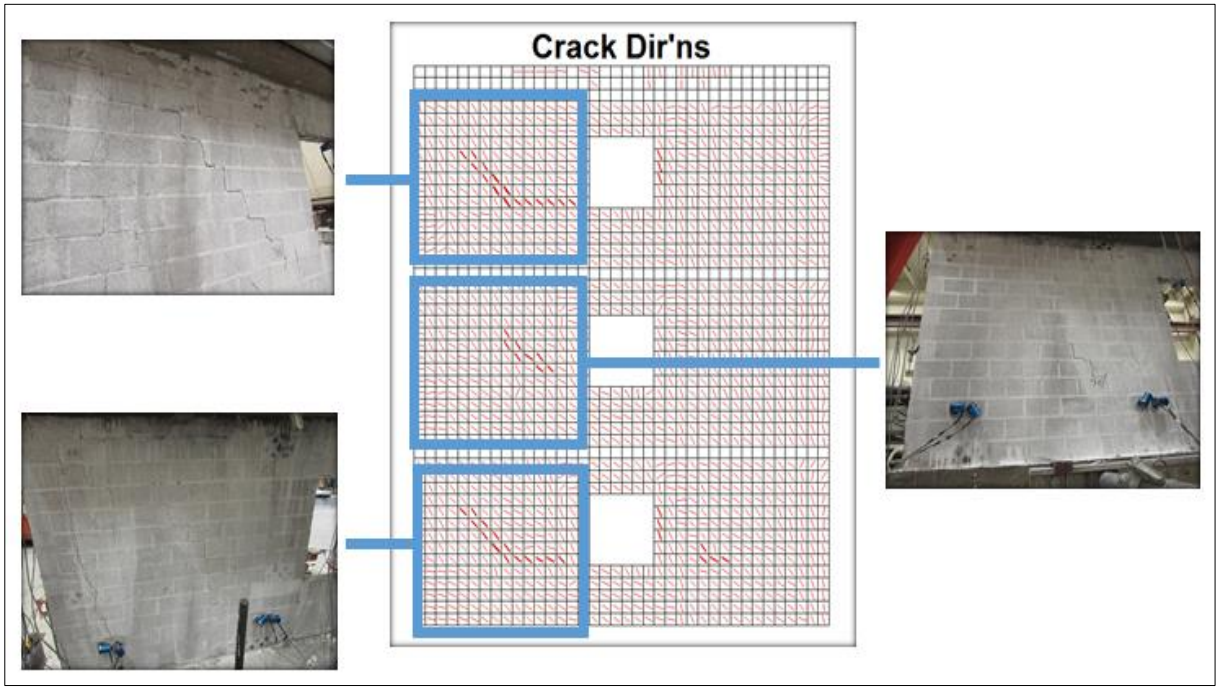

Source: Adapted from Chavez and Fonseca (2018).

Figure 34: Cracks noted in the pull regime of the experimental and numerical wall W3.

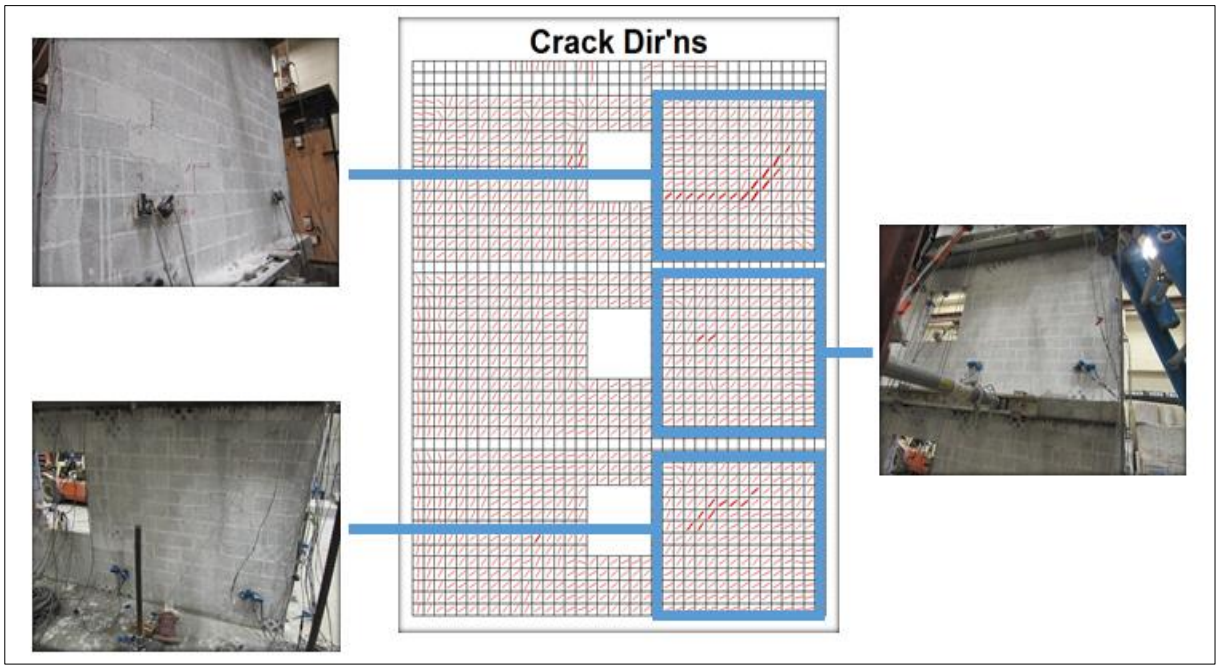

Source: Adapted from Chavez and Fonseca (2018).

Overall, the finite element model was able to capture the response of the wall up to the peak load reasonably well. The model also captured the general cracking pattern observed during testing. Even though not able to capture the post-peak behavior of the wall as well as desired, the FE model can be considered able to represent the walls' responses satisfactorily for the purpose of this study.

2.4 PARAMETRIC EVALUATION

After validation, the finite element model was used to study the influence of the compressive strength of ungrouted and grouted masonry, mortar shear strength, amount and spacing of reinforcement, applied axial stress, aspect ratio, and opening size on the response of the wall. Each parameter was studied separately by varying the value of that parameter in the model while maintaining the value of other parameters unchanged. The base model for comparison was that of the tested walls W1-2.

2.4.1 Evaluated parameters

a) Compressive strength of ungrouted and grouted masonry

The values adopted for the strength of ungrouted masonry in the models are presented in Table 3. The same values were used for the strength of grouted masonry, except for that of the base model, which was 12.2 MPa.

Table 3: Models varying the compressive strength of ungrouted masonry.

Model	Strength (MPa)
Base Model	11.8
Model 1	17.2
Model 2	20.7
Model 3	24.1

Source: Author.

b) Mortar shear strength

The chosen values for evaluating the mortar influence in the masonry panels are listed together with the corresponding JSSR in Table 4. The mortar shear strength values varied from 140.2 kPa (model 1) to 630.9 kPa (model 8) with an increment of 70.1 kPa. The corresponding JSSR varied from 0.010 to 0.045 with an increment of 0.005.

Table 4: Models varying the mortar shear strength.

Model	Mortar Strength (kPa)	JSSR
Base Model	265.0	0.0189
Model 1	140.2	0.0100
Model 2	210.3	0.0150
Model 3	280.4	0.0200
Model 4	350.5	0.0250
Model 5	420.6	0.0300
Model 6	490.7	0.0350
Model 7	560.8	0.0400
Model 8	630.9	0.0450

Source: Author.

c) Reinforcement

Various arrangements of vertical and horizontal reinforcements were supposed to assess their influence on the wall behavior. First, as seen in Table 5, the size of the bars was varied for each type of reinforcement, keeping the same distribution (spacing) made in the experimental wall; then, the spacing between bars was varied for each type of reinforcement, keeping the reinforcement ratio constant, as shown in Table 6. In this study, the spacing does not refer to that among bars within the same block cell but rather to the spacing between the grouted cells.

Table 5: Models varying the reinforcement size.

Model	Vertical Bars (mm)	Vert. Reinf. Ratio (ρ_v)	Horizontal Bars (mm)	Hor. Reinf. Ratio (ρ_h)
Base Model	Ø9.5	0.0025	Ø9.5	0.00105
Model 1	Ø6.3	0.0011	Ø9.5	0.00105
Model 2	Ø12.7	0.0045	Ø9.5	0.00105
Model 3	Ø9.5	0.0025	Ø6.3	0.00048
Model 4	Ø9.5	0.0025	Ø12.7	0.00191
Model 5	Ø6.3	0.0011	Ø6.3	0.00048
Model 6	Ø12.7	0.0045	Ø12.7	0.00191

Source: Author.

Table 6: Models varying the reinforcement spacing.

Model	Vert. Reinf. Ratio (ρ_v)	Hor. Reinf. Ratio (ρ_h)	Horizontal Spacing (mm)	Vertical Spacing (mm)
Base Model	0.0025	0.00105	1118	914
Model 1	0.0025	0.00105	406	914
Model 2	0.0025	0.00105	610	914
Model 3	0.0025	0.00105	1118	508
Model 4	0.0025	0.00105	1118	610
Model 5	0.0025	0.00105	1118	1118

Source: Author.

d) Axial stress

The axial loads adopted and the corresponding stress for each model are presented in Table 7. Loads from 0 to 111 kN, with increments of 22 kN, were used and compared to the base model, which had a load of 50 kN.

Table 7: Models varying the axial stress.

Model	Axial Load (kN)	Axial Stress (kPa)
Base Model	50	148
Model 1	0	0
Model 2	22	65
Model 3	67	194
Model 4	89	259
Model 5	111	324

Source: Author.

e) Aspect Ratio

In contrast to most existing research in which walls with aspect ratios of 1.0 have been analyzed, the base model of this study, i.e., the walls tested, had an aspect ratio of 1.24, considering the total length of the coupled walls and three stories. The other models studied were idealized to correspond to walls of 1, 2, and 4 stories, as shown in Table 8.

Table 8: Models varying the aspect ratio.

Model	Aspect Ratio	Nº of Stories
Base Model	1.24	3
Model 1	0.45	1
Model 2	0.84	2
Model 3	1.63	4

Source: Author.

f) Opening Size

To evaluate the influence of the dimensions of the openings, models were created with variations in both height and length of the openings. As summarized in Table 10, in Models 1 to 3, the width was kept constant and the height was varied, while in Models 4 and 5, the height was kept constant and the width was varied. The height variation consisted of adding or

removing one course of blocks at a time from the vertical dimension of the opening. The length variation occurred by adding or removing half a block at a time on each side of the opening.

Table 9: Models varying the size of the openings.

Model	Height (mm)	Opening Height / Story Height	Width (mm)	Opening Width / Story Width
Base Model	570	0.40	570	0.158
Model 1	475	0.33	570	0.158
Model 2	665	0.47	570	0.158
Model 3	755	0.53	570	0.158
Model 4	570	0.40	760	0.210
Model 5	570	0.40	950	0.263

Source: Author.

2.4.2 Sensitivity analysis

For the sensitivity analysis of the wall behavior to each parameter, the walls' response data were tabulated and backbone curves, up to the peak loads and corresponding displacements, were generated. Sensitivity curves were then created to indicate trends for the load capacity (i.e., maximum absolute load), displacement and the initial lateral stiffness as a function of the evaluated parameter. The sensitivity is reported as the ratio of the obtained value from each model to that from the base model. Like during the model validation, the corresponding displacement at 97% of the peak load was adopted in the analysis. The values and discussion presented herein are not absolutes but general trends and observations. The complete hysteresis curves of each wall model can be seen in Appendix B.

a) Compressive strength of ungrouted masonry

The numerical results of the influence of the compressive strength of ungrouted masonry on the behavior of the walls are presented in Table 10 and illustrated by the backbone curves shown in Figure 35(a) and by the sensitivity curves shown in Figure 35(b).

Table 10: Numerical results for the influence of the compressive strength of ungrouted masonry.

Model	Load Capacity		Displacement*		Initial Stiffness	
	V_{max} (kN)	ΔV_{max} (%)	δ (mm)	Δδ (%)	K (kN/mm)	ΔK (%)
Base Model (11.8 MPa)	107.7	0.0	13.5	0.0	47.2	0.0
Model 1 (17.2 MPa)	121.5	12.8	14.5	7.4	53.8	14.0
Model 2 (20.7 MPa)	141.7	31.6	18.6	37.8	56.0	18.6
Model 3 (24.1 MPa)	142.8	32.6	19.3	43.0	58.5	23.9

* Corresponding displacement at 97% of the peak load.

Source: Author.

The load capacity of the wall increased with increasing ungrouted masonry strength. The increase in load capacity is almost linear by 32% when the ungrouted masonry strength

increased by 66%; thereafter, the load capacity of the wall remained almost constant with increasing in masonry strength, which indicates that the masonry has contributed all it could to the capacity of the wall. Similarly, the deflection increased by 38% when the ungrouted masonry strength increased by 66%, and then the increase in displacement was only 4% for further increases in the ungrouted masonry strength.

Figure 35: Wall behavior as a function of the compressive strength of ungrouted masonry.

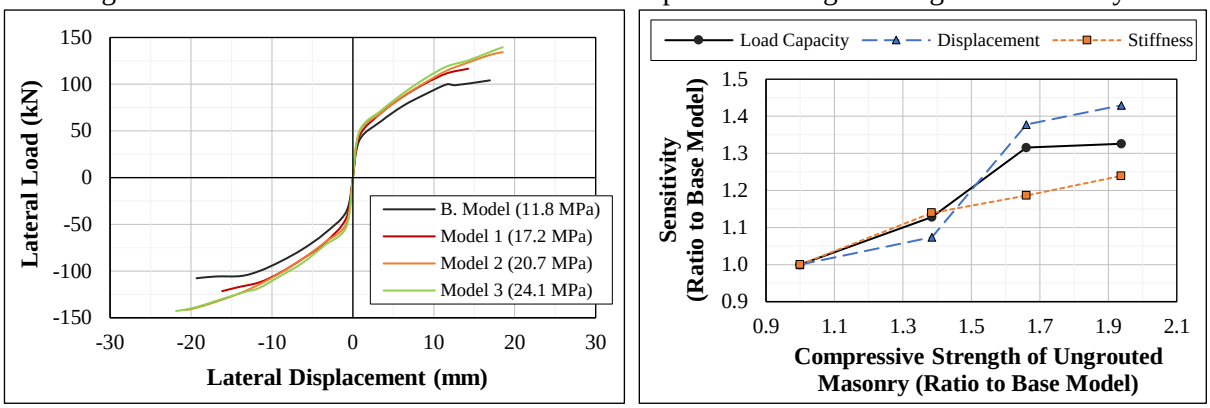

(a) Backbone curves (b) Sensitivity curves

Source: Author.

The initial stiffness increased almost linearly up to approximately 24% with up to 100% increase in the compressive strength of ungrouted masonry. Such an increase in wall stiffness is consistent since the masonry governed the wall behavior during the initial stages of loading, i.e., the wall had not yet experienced significant cracking.

b) Compressive strength of grouted masonry

The numerical results for the models when the grouted masonry compressive strength was varied are summarized in Table 11. The backbone and sensitivity curves are presented in Figure 36(a) and (b), respectively.

Table 11: Numerical results for the influence of the compressive strength of grouted masonry.

Model	Load Capacity		Displacement*		Initial Stiffness	
	V_{max} (kN)	ΔV_{max} (%)	δ (mm)	Δδ (%)	K (kN/mm)	ΔK (%)
Base Model (12.2 MPa)	107.7	0.0	13.5	0.0	47.2	0.0
Model 1 (17.2 MPa)	117.4	9.0	16.3	20.7	52.1	10.4
Model 2 (20.7 MPa)	123.1	14.3	17.0	25.9	55.5	17.6
Model 3 (24.1 MPa)	122.2	13.5	15.0	11.1	53.4	13.1

* Corresponding displacement at 97% of the peak load.

Source: Author.

Qualitatively, the results were similar to those observed when the ungrouted masonry strength increased. However, the gains were smaller since the wall is mostly ungrouted

masonry. As shown in Figure 36(b), the wall load capacity, displacement, and initial stiffness increased by 14%, 26%, and 18%, respectively, when the grouted masonry strength increased by 40%. Nevertheless, for further increases in the grouted masonry strength, the gain in load capacity was negligible, while the deflection and initial stiffness decreased.

Figure 36: Wall behavior as a function of the compressive strength of grouted masonry.

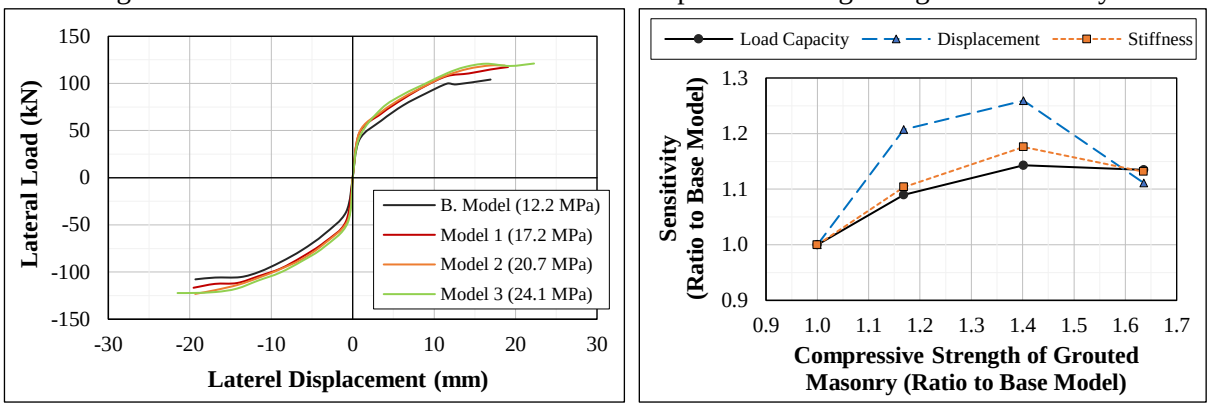

(a) Backbone curves (b) Sensitivity curves

Source: Author.

c) Mortar shear strength

The numerical results for the models varying the mortar shear strengths are presented in Table 12. The backbone and sensitivity curves are shown in Figure 37.

Table 12: Numerical results for the influence of the mortar shear strength.

Model	Load Capacity		Displacement*		Initial Stiffness	
	V_{max} (kN)	ΔV_{max} (%)	δ (mm)	Δδ (%)	K (kN/mm)	ΔK (%)
Model 1 (140.2 kPa)	86.0	-20.1	13.9	3.0	39.5	-16.3
Model 2 (210.3 kPa)	97.8	-9.2	13.5	0.0	43.5	-7.8
Base Model (265.0 kPa)	107.7	0.0	13.5	0.0	47.2	0.0
Model 3 (280.4 kPa)	111.5	3.5	13.7	1.5	46.7	-1.1
Model 4 (350.5 kPa)	119.0	10.5	13.3	-1.5	49.4	4.7
Model 5 (420.6 kPa)	127.3	18.2	13.4	-0.7	51.2	8.5
Model 6 (490.7 kPa)	136.0	26.3	14.0	3.7	52.2	10.6
Model 7 (560.8 kPa)	145.2	34.8	14.5	7.4	55.1	16.7
Model 8 (630.9 kPa)	148.7	38.1	13.9	3.0	56.3	19.3

* Corresponding displacement at 97% of the peak load.

Source: Author.

The load capacity of the wall increased almost linearly with increasing mortar shear strength, clearly indicating that the wall load capacity is sensitive to the mortar shear strength: for instance, the load capacity increased by 10%, 20%, and 30% when the mortar shear strength increased by 30%, 60%, and 85%, respectively. The initial wall stiffness also increased almost linearly with increasing mortar shear strength. These outcomes are coherent since cracks in PGMW tend to develop along the mortar planes (Shing and Cao, 1997; Drysdale et al., 1999).

Therefore, if mortar planes are strengthened, the wall load capacity and initial stiffness would be expected to increase. In general, the displacement showed indifference with increasing the mortar shear strength, indicating, most likely, that the masonry units and the reinforcement are controlling the displacement capacity of the wall.

Figure 37: Wall behavior as a function of the mortar shear strength.

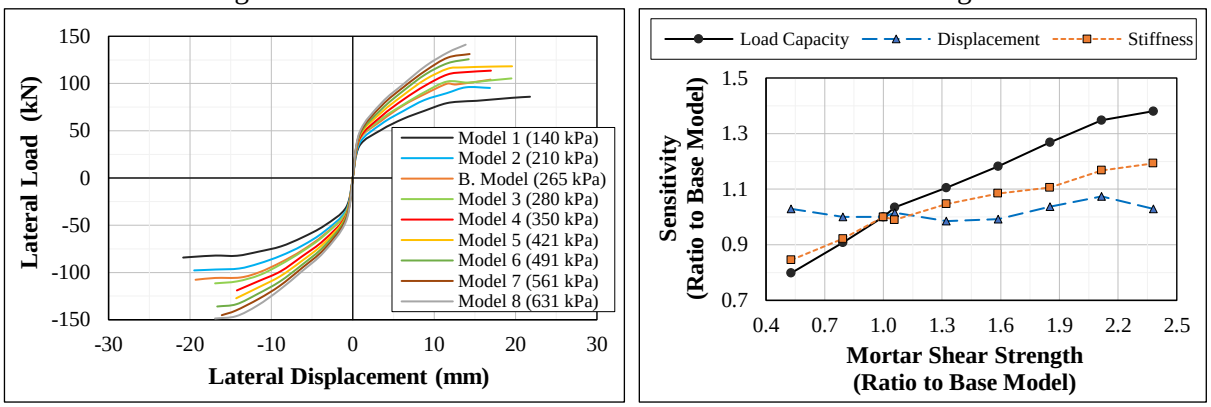

(a) Backbone curves (b) Sensitivity curves

Source: Author.

d) Reinforcement

The numerical results for the models with various reinforcement ratios are presented in Table 13. The backbone and sensitivity curves referring to the variation of the vertical and horizontal reinforcement ratios are illustrated, respectively, in Figure 38 and Figure 39. In turn, the numerical results for the influence of the spacing between the vertical and horizontal reinforcement, keeping the reinforcement ratios constant, are shown, respectively, in Table 14 and Table 15. The backbone and sensitivity curves are presented in Figure 40 and Figure 41, respectively, for the vertical and horizontal reinforcement spacing variation.

Table 13: Numerical results for the influence of the reinforcement ratios.

Model	Load Capacity		Displacement*		Initial Stiffness	
	V_{max} (kN)	ΔV_{max} (%)	δ (mm)	Δδ (%)	K (kN/mm)	ΔK (%)
Model 1 (0.0011V - 0.00105H)	87.5	-18.8	15.4	14.1	44.0	-6.8
Model 5 (0.0011V - 0.00048H)	90.1	-16.3	15.1	11.9	45.1	-4.4
Model 3 (0.0025V - 0.00048H)	108.3	0.6	13.5	0.0	46.4	-1.7
Base Model (0.0025V - 0.00105H)	107.7	0.0	13.5	0.0	47.2	0.0
Model 4 (0.0025V - 0.00191H)	106.7	-0.9	13.4	-0.7	45.5	-3.6
Model 6 (0.0045V - 0.00191H)	123.3	14.5	12.5	-7.4	47.0	-0.4
Model 2 (0.0045V - 0.00105H)	121.6	12.9	11.7	-13.3	46.9	-0.6

* Corresponding displacement at 97% of the peak load.

Source: Author.

The data demonstrated that the performance of the wall was more sensitive to the vertical reinforcement than to the horizontal reinforcement ratio. The lateral wall load capacity

decreased 19% when the vertical reinforcement ratio decreased from 0.0025 (base model) to 0.0011 (model 1) and increased 13% when the vertical reinforcement ratio increased from 0.0025 (base model) to 0.0045 (model 2). Conversely, the displacement increased and decreased 14% and 13% when the vertical reinforcement ratio changed from 0.0025 to 0.0011 and from 0.0025 to 0.0045. The initial stiffness decreased when the vertical reinforcement ratio decreased from 0.0025 to 0.0011 but remained unchanged when the vertical reinforcement increased from 0.0025 to 0.0045.

The response of the wall appears almost independent of the horizontal reinforcement ratio since the changes in load, displacement, and initial stiffness are very small when the horizontal reinforcement ratio changed from 0.00105 (base model) to 0.00048 (model 3) and from 0.00105 (base model) to 0.00191 (model 4). Similar results were discussed by Shing and Cao (1997), Schultz et al. (1998), and Fódi and Bódi (2010). It is noteworthy to mention that the horizontal rebars were embedded in the grout of the blocks and not positioned in the mortar joints, which could possibly change the behavior of the wall.

Figure 38: Wall behavior as a function of the vertical reinforcement ratio.

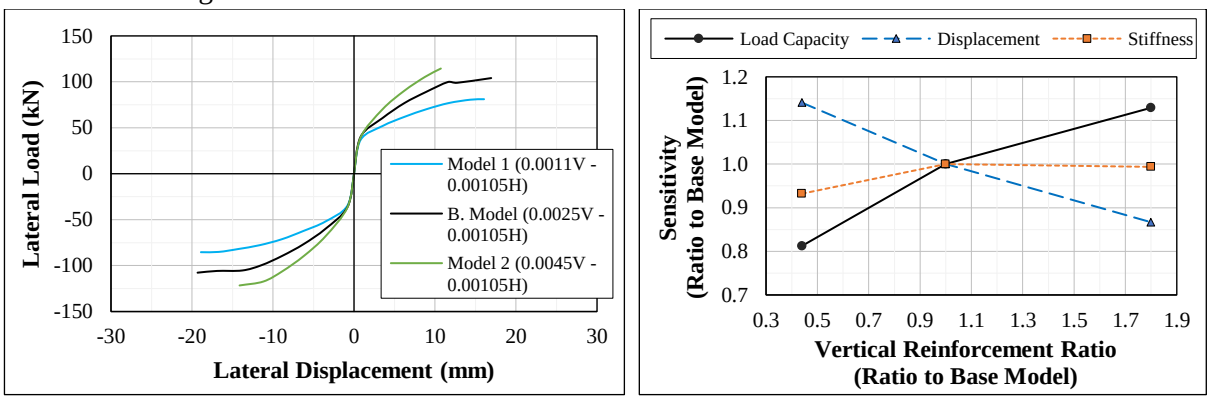

(a) Backbone curves (b) Sensitivity curves

Source: Author.

Figure 39: Wall behavior as a function of the horizontal reinforcement ratio.

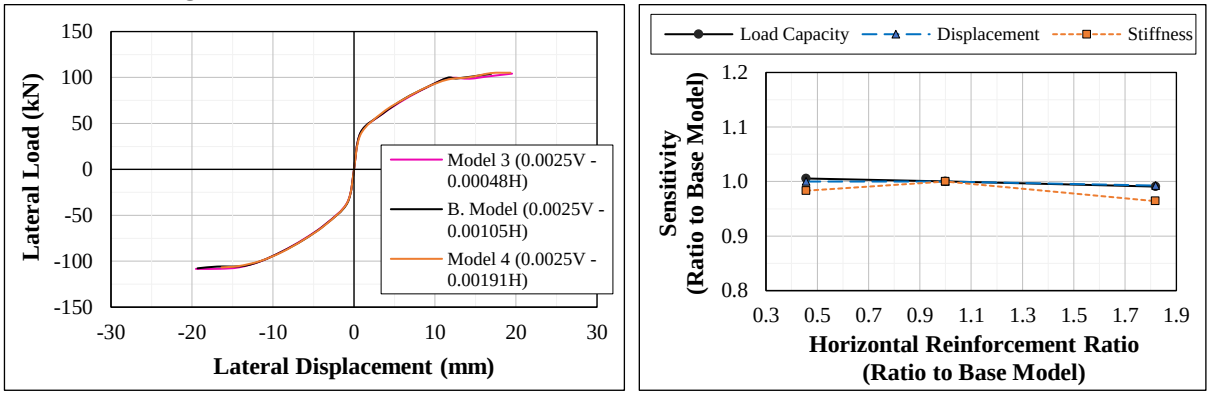

(a) Backbone curves (b) Sensitivity curves

Source: Author.

Table 14: Numerical results for the influence of the spacing between the vertical reinforcement.

Model	Load Capacity		Displacement*		Initial Stiffness	
	V_{max} (kN)	ΔV_{max} (%)	δ (mm)	Δδ (%)	K (kN/mm)	ΔK (%)
Model 1 (406 mm)	105.3	-2.2	13.5	0.0	44.0	-6.8
Model 2 (610 mm)	106.0	-1.6	13.6	0.7	43.4	-8.1
Base Model (1118 mm)	107.7	0.0	13.5	0.0	47.2	0.0

* Corresponding displacement at 97% of the peak load.

Source: Author.

Figure 40: Wall behavior as a function of the spacing between the vertical reinforcement.

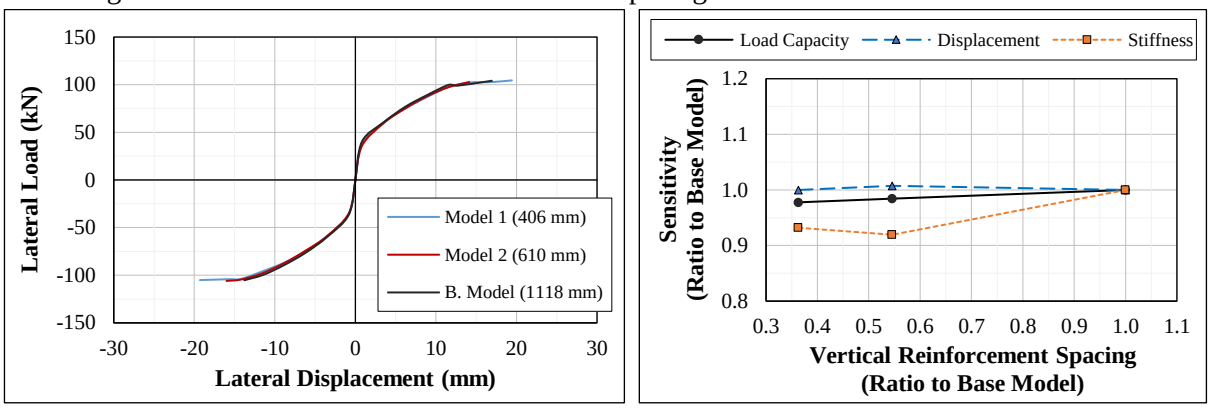

(a) Backbone curves (b) Sensitivity curves

Source: Author.

Table 15: Numerical results for the influence of the spacing between the horizontal reinforcement.

Model	Load Capacity		Displacement*		Initial Stiffness	
	V_{max} (kN)	ΔV_{max} (%)	δ (mm)	Δδ (%)	K (kN/mm)	ΔK (%)
Model 1 (508 mm)	110.6	2.7	13.0	-3.7	51.4	8.9
Model 2 (610 mm)	110.6	2.7	13.0	-3.7	52.2	10.6
Base Model (914 mm)	107.7	0.0	13.5	0.0	47.2	0.0
Model 3 (1118 mm)	108.9	1.1	14.0	3.7	51.4	8.9

* Corresponding displacement at 97% of the peak load.

Source: Author.

Figure 41: Wall behavior as a function of the spacing between the horizontal reinforcement.

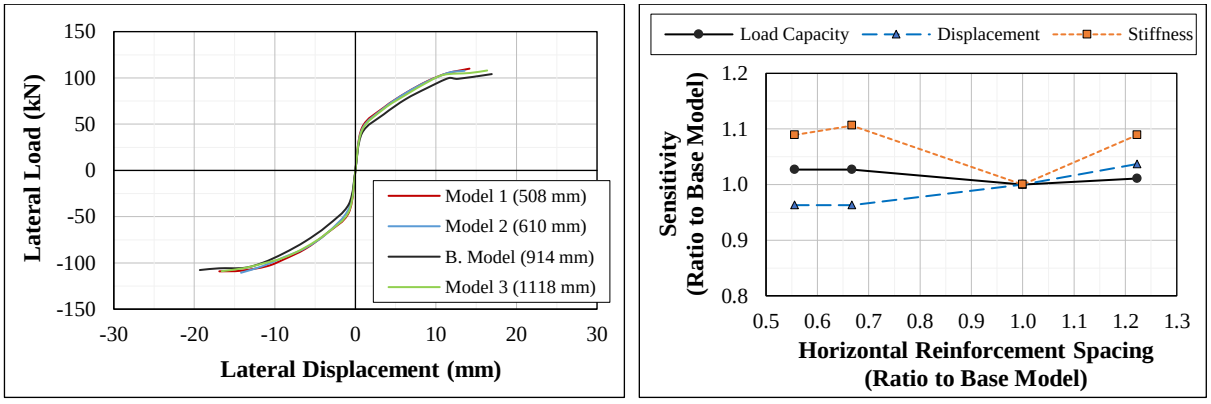

(a) Backbone curves (b) Sensitivity curves

Source: Author.

Regarding the spacing between the vertical and horizontal reinforcements, it can be seen that the envelopes almost overlap entirely in the two situations. Also, the values demonstrate that the load capacity and displacement were impacted by less than 4%. The initial stiffness varied distinctly in models by up to approximately 11%.

e) Axial stress

The numerical results for this parameter are presented in Table 16 and are illustrated by the backbone curves in Figure 42(a). The sensitivity curves are presented in Figure 42(b).

Table 16: Numerical results for the influence of the axial stress.

Model	Load Capacity		Displacement*		Initial Stiffness	
	V_{max} (kN)	ΔV_{max} (%)	δ (mm)	Δδ (%)	K (kN/mm)	ΔK (%)
Model 1 (0 kN - 0 kPa)	99.2	-7.9	17.4	28.9	29.7	-37.1
Model 2 (22 kN - 65 kPa)	102.8	-4.5	14.5	7.4	37.1	-21.4
Base Model (50 kN - 148 kPa)	107.7	0.0	13.5	0.0	47.2	0.0
Model 3 (67 kN - 194 kPa)	111.4	3.4	13.3	-1.5	48.5	2.8
Model 4 (89 kN - 259 kPa)	112.3	4.3	13.0	-3.7	54.0	14.4
Model 5 (111 kN - 324 kPa)	116.5	8.2	12.5	-7.4	59.1	25.2

* Corresponding displacement at 97% of the peak load.

Source: Author.

Figure 42: Wall behavior as a function of the axial stress.

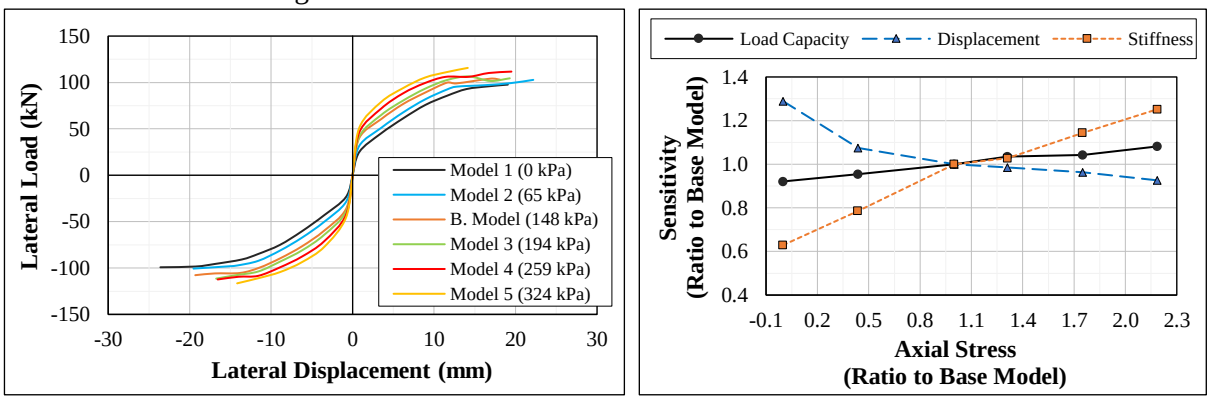

(a) Backbone curves (b) Sensitivity curves

Source: Author.

The results show that the higher the applied axial load, the higher the capacity of the shear wall but the smaller the ductility. For example, for a stress of 65 kPa (model 2), the displacement was 14.5 mm and the load capacity was 102.8 kN; for a stress of 324 kPa (model 5), the displacement was 12.5 mm and the load capacity was 116.5 kN. For these two models, the initial stiffness changed from 37.1 kN/mm to 59.1 kN/mm. It appears that as the axial stress increased, the failure mode became less flexural, i.e., less governed by the reinforcement, and more shear dominated, i.e., more governed by the masonry.

As shown in Figure 42(b), the sensitivity of the measured parameters varies almost linearly relative to the axial stress. It was, however, necessary to increase the axial stress 120% to increase the load capacity and initial lateral stiffness by 10% and 25%; the corresponding displacement decreased by 7%.

f) Aspect ratio

The numerical results for the models with different aspect ratios are summarized in Table 17, while the backbone curves and the parameter sensitivity are shown, respectively, in Figure 43(a) and (b).

Table 17: Numerical results for the influence of the aspect ratio.

Model	Load Capacity		Displacement*		Initial Stiffness	
	V_{max} (kN)	ΔV_{max} (%)	δ (mm)	Δδ (%)	K (kN/mm)	ΔK (%)
Model 1 (0.45 – 1 Story)	123.1	14.3	4.3	-68.1	100.6	113.1
Model 2 (0.84 – 2 Stories)	115.9	7.6	8.4	-37.8	65.5	38.8
Base Model (1.24 – 3 Stories)	107.7	0.0	13.5	0.0	47.2	0.0
Model 3 (1.63 – 4 Stories)	101.8	-5.5	23.7	75.6	32.4	-31.3

* Corresponding displacement at 97% of the peak load.

Source: Author.

Figure 43: Wall behavior as a function of the aspect ratio.

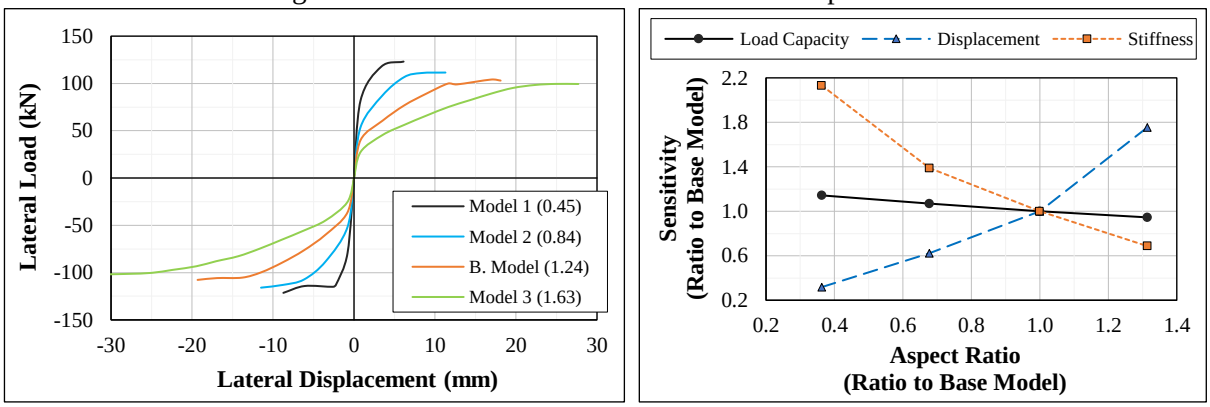

(a) Backbone curves (b) Sensitivity curves

Source: Author.

The results indicate that the load capacity and initial stiffness of the wall are inversely proportional to the aspect ratio and that the deflections are directly proportional to the aspect ratio. For example, when the aspect ratio increased from 0.45 (1 story) to 0,84 (2 stories), the load capacity decreased from 123.1 to 115.1 kN, the displacement increased from 4.3 to 8.4 mm and the initial stiffness decreased from 100.6 to 65.5 kN/mm. These changes represent, respectively, a decrease in load capacity of 6.5%, an increase in displacement of 95%, and a decrease in stiffness of 35%. It appears that the increase in aspect ratio changes the failure mode of the wall from shear dominated to flexure dominated.

g) Opening Size

The numerical results for variations in the height and width of the openings are shown, respectively, in Table 18 and Table 19. The backbone and sensitivity curves are illustrated in Figure 44 and Figure 45 for changes in the height and width of the openings, respectively.

Table 18: Numerical results for the influence of the opening height.

Model	Load Capacity		Displacement*		Initial Stiffness	
	V_{max} (kN)	ΔV_{max} (%)	δ (mm)	Δδ (%)	K (kN/mm)	ΔK (%)
Model 1 (475 mm)	111.0	3.1	15.6	15.6	46.5	-1.5
Base Model (570 mm)	107.7	0.0	13.5	0.0	47.2	0.0
Model 2 (665 mm)	105.7	-1.9	13.0	-3.7	45.1	-4.4
Model 3 (755 mm)	104.9	-2.6	13.4	-0.7	42.9	-9.1

* Corresponding displacement at 97% of the peak load.

Source: Author.

Figure 44: Wall behavior as a function of the opening height.

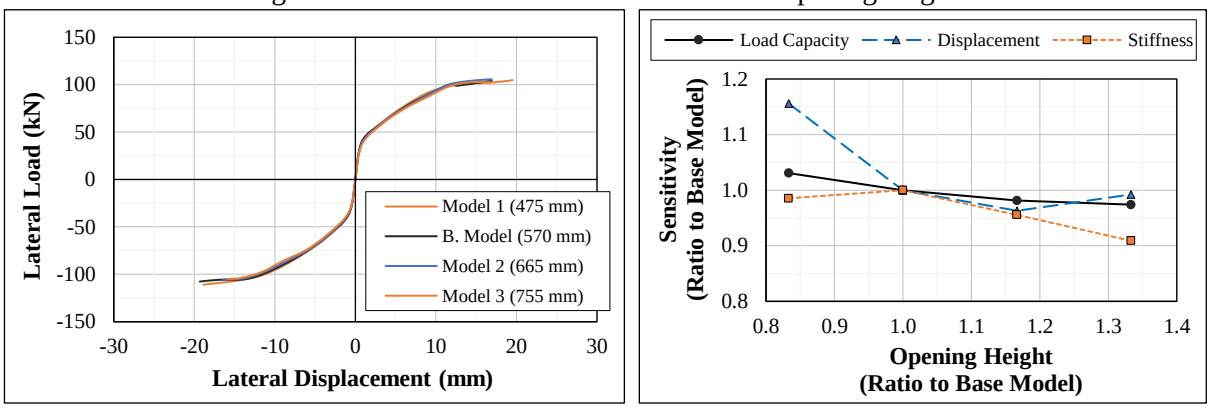

(a) Backbone curves (b) Sensitivity curves

Source: Author.

Table 19: Numerical results for the influence of the opening width.

Model	Load Capacity		Displacement*		Initial Stiffness	
	V_{max} (kN)	ΔV_{max} (%)	δ (mm)	Δδ (%)	K (kN/mm)	ΔK (%)
Base Model (570 mm)	107.7	0.0	13.5	0.0	47.2	0.0
Model 4 (760 mm)	106.3	-1.3	14.0	3.7	44.2	-6.4
Model 5 (950 mm)	103.8	-3.6	14.6	8.1	41.7	-11.7

* Corresponding displacement at 97% of the peak load.

Source: Author.

It is observed that the backbone curves overlap almost entirely in both situations. In addition, the results indicated that the wall load capacity did not vary by more than 4% as the height or width of the openings changed concerning the existing openings in the base model. The displacement and initial lateral stiffness varied, respectively, by up to approximately 16% and 12% with changes in opening dimensions. It should be noted that the height of the openings was changed keeping the width constant and vice-versa. Furthermore, it is important to mention

that the predominant failure mode of the wall was by shear and that the increase in the dimensions of the openings analyzed here caused a reduction in the available cross-sectional area of only 12.5%.

Figure 45: Wall behavior as a function of the opening width.

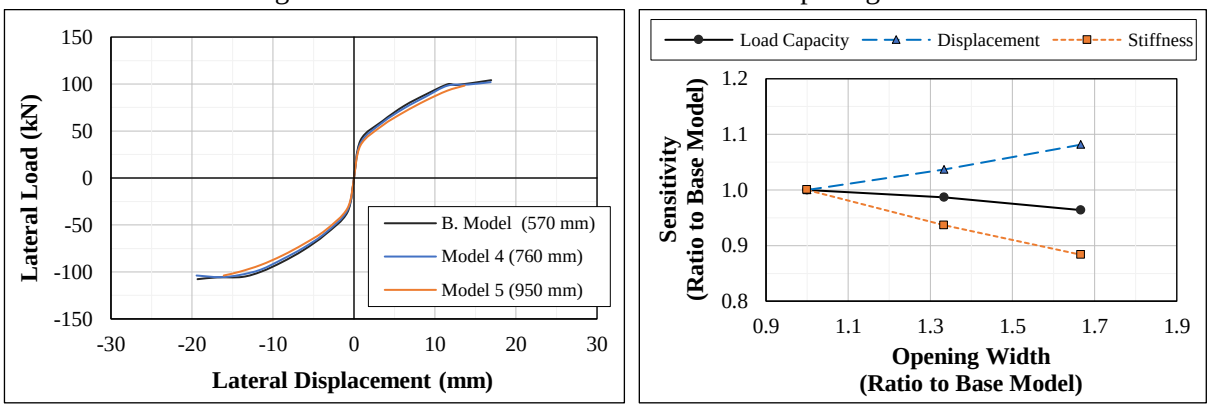

(a) Backbone curves (b) Sensitivity curves

Source: Author.

The increase in opening height causes the height of the pier adjacent to the opening to increase. As the pier height increases, the model becomes less stiff and the peak load is reached at a smaller overall wall displacement. It appears that as the opening height increases, the coupling beams above and below the opening will dictate if the wall will behave as a wall or as two independent piers.

2.5 CONCLUDING REMARKS

The study presented in this chapter aimed at studying, through finite element modeling, the influence of several parameters on the response of partially grouted multi-story masonry walls with openings subjected to in-plane cyclic actions.

The numerical model proposed by Chavez and Fonseca (2018) was adequately validated with the experimental data of Fortes and Parsekian (2017) and considered able to simulate the behavior of the walls up to the peak load satisfactorily. Therefore, the model was used to analyze the different variations of the walls as a function of the load capacity, displacement preceding the maximum load, and initial lateral stiffness. The correlations between the parameters evaluated and the behavior of the walls are summarized in Table 20.

According to results, the wall load capacity experienced significant changes when the strengths of the ungrouted and grouted masonry, the mortar shear strength, the vertical reinforcement ratio, and the aspect ratio were varied. A variation of approximately 120% in the

axial stress caused only approximately 10% of change on the wall load capacity. All these parameters, except the aspect ratio, were positively correlated with the load capacity of the wall. The opening size, the spacing between reinforcements, and the horizontal reinforcement ratio did not affect the wall capacity by more than 4%.

Table 20: Summary of the general influence of each parameter on the wall behavior.

Parameter	Correlation		
	Load Capacity	**Displacement**	**Initial Stiffness**
Ungrouted masonry strength	Positive	Positive	Positive
Grouted masonry strength	Positive	Positive	Positive
Mortar Shear Strength	Positive	Indifferent	Positive
Vertical reinforcement ratio	Positive	Negative	Indifferent
Horizontal reinforcement ratio	Indifferent	Indifferent	Indifferent
Vertical reinforcement spacing	Indifferent	Indifferent	Inconclusive
Horizontal reinforcement spacing	Indifferent	Indifferent	Inconclusive
Axial stress	Positive	Negative	Positive
Aspect ratio	Negative	Positive	Negative
Opening height	Negative	Inconclusive	Inconclusive
Opening width	Negative	Positive	Negative

Source: Author.

The deflection of the walls related positively with the strengths of the ungrouted and grouted masonry, the aspect ratio and the opening width, and negatively with the vertical reinforcement ratio and the axial stress. The displacements were not significantly impacted for changes in the mortar shear strength, the horizontal reinforcement ratio and the spacing between reinforcements. Clear relationship between the deflection of the walls could not be observed with the opening height.

The initial stiffness of the walls was sensitive to variations in the strengths of the ungrouted and grouted masonry, in the joint mortar shear strength, and especially in the axial stress and aspect ratio. The initial stiffness was less affected by the changes in the opening size and in the spacing and size of the reinforcement. Similar to the load capacity, the initial stiffness of the walls was negatively correlated only with the aspect ratio and the opening width.

The conclusions regarding the changes in the opening dimensions should not be considered absolute, as the changes imposed on them in this study represented a reduction of, at most, 12.5% in the effective cross-sectional area and with a failure mode dominated by shear. More investigations are needed to verify the impact of greater variations in opening dimensions.

There appear to be a limit in which an increase in the strengths of the ungrouted and grouted masonry no longer affected the wall capacity and deflection, which herein was approximately 65% and 40% of the strength of the base model, respectively. Such finding may be a direct consequence of the heterogeneity of masonry walls, which may experience different

failure modes, i.e., once the capacity of a failing component increases, failure will occur because of another weaker component. Grouted and reinforced cells were located mainly in the ends of the walls, but even the grouted cells cracked due to the shear stresses causing diagonal stepping cracks through the mortar joints between the ungrouted cells. The sliding and cracks caused by shear propagated because of the low capacity of the mortar planes to resist tension. Therefore, the wall capacity was sensitive to the mortar shear strength.

The response of the walls was sensitive to the variation of the vertical reinforcement size, but it was indifferent to variation of the horizontal reinforcement and spacing. The load capacity and initial stiffness were positively correlated to the axial stress while the displacement was negatively correlated with it; the aspect ratio had the inverse effect. Both parameters caused the failure mode to change: the increase in the axial stress caused the failure mode to become shear dominated while the increase in aspect ratio shifted the failure to be flexural dominated.

3. SHEAR LOAD CAPACITY PREDICTION

Many experimental and numerical investigations have been conducted with the purpose of predicting the in-plane behavior of masonry walls. In particular, the purpose has been to predict the lateral load capacity of walls so that safety can be guaranteed in the design of such walls in buildings. While there is an agreement in the literature on how to determine the flexural load capacity of a masonry shear wall, there are several propositions on how to predict the shear load capacity (SLC).

Since there is still no consensus on how to predict the SLC of unperforated PGMW, the study presented herein aims to suggest a new shear equation and to examine the accuracy of some relevant existing shear expressions. Approaches to predict the SLC of single and multi-story perforated PGMW are also investigated.

The study presented in this chapter led to the following publication:

- Medeiros, K. A. S., Parsekian, G. A., Shrive, N. G., Fonseca, F. S., 2022, Shear load capacity prediction of unperforated and perforated partially grouted masonry walls. Engineering Structures, 256, 113927. https://doi.org/10.1016/j.engstruct.2022.113927

3.1 LITERATURE REVIEW

Masonry shear walls fail in a flexural, shear, sliding or mixed failure mode. When the wall is dominated by flexure, failure is controlled by deformations resulting from the vertical reinforcement yielding and the formation of plastic hinges in certain zones of the wall. Modes dominated by shear are characterized by diagonal tensile cracks, sliding of the horizontal mortar joints, or a combination thereof, implying a rapid degradation in strength after reaching the peak load. Consequently, these modes involve a relatively more brittle failure, which must be avoided (Shedid et al., 2008).

Several factors influence from the initial performance to the failure mode of a masonry shear wall, among which the impact of the aspect ratio, the axial load, and the ratio of vertical and horizontal reinforcement stand out. As illustrated in Figure 46, the behavior of the wall becomes more dominated by shear and, consequently, less by flexure when the aspect ratio is reduced and when the axial load and the vertical reinforcement ratio are increased. The inverse

effect is also expected, and the combination of these factors can also change the behavior of the wall (Kingsley et al., 2014).

Figure 46: Wall behavior trend as a function of the aspect ratio, axial load, and ratio of vertical and horizontal reinforcement.

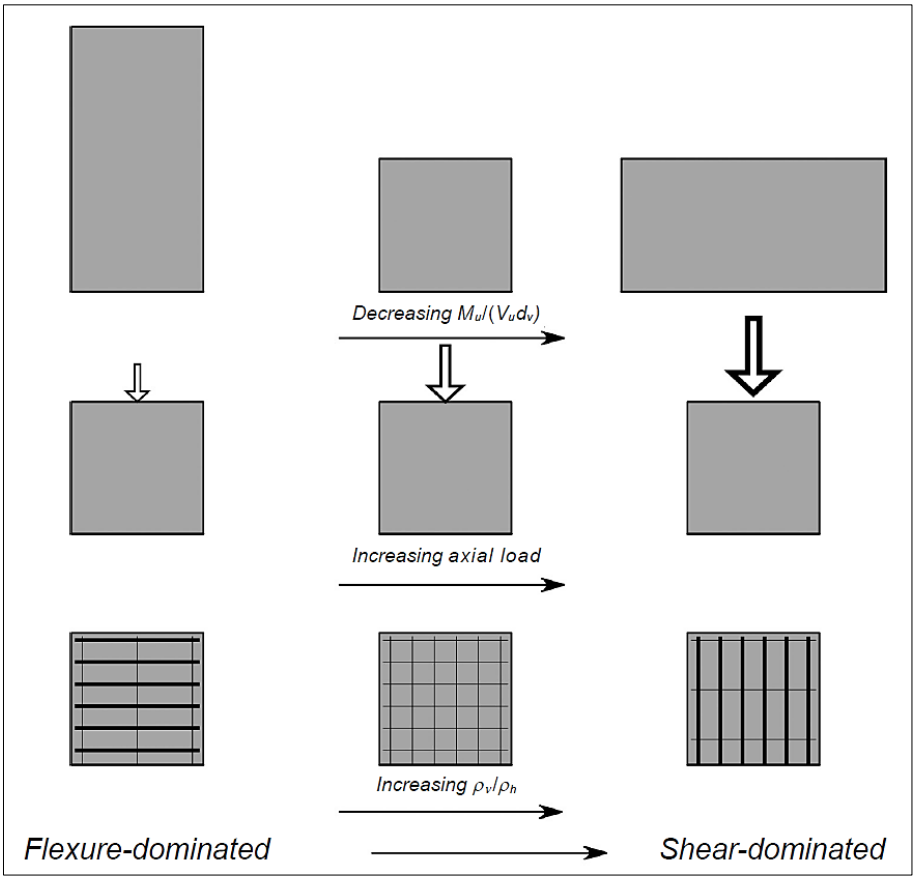

Source: Kingsley et al. (2014).

The capacity and type of response of a masonry shear wall can be predicted by comparing its flexural and shear load capacities, with the smaller of the two indicating the most likely governing failure mode.

3.1.1 Determination of flexural load capacity

The behavior of reinforced masonry shear walls failing predominantly in flexure is well defined and can be modeled following classical beam theory based on the hypothesis that plane sections remain plane after deformation (Priestley, 1986; Shing et al., 1990; Voon and Ingham, 2002; Seif ElDin et al., 2019a). The flexural load capacity of a wall with distributed reinforcement can be calculated following the development shown in Equations 4 to 9. As illustrated in Figure 47, it is assumed that the section remains plane even after deforming, and the flexural strength of the masonry is approximated to an equivalent rectangular stress diagram

with height (stress level) equal to $\gamma f'_m$ and depth $a = \beta c$, where f'_m is the masonry compressive strength, and c is the distance between the neutral axis and the furthest compressed fiber. The coefficients γ e β, which define the equivalent rectangular diagram, and the maximum strain of the most compressed outer fiber (ε_u) can assume different values according to each design codes, as seen in Table 21.

Given the balance of forces in the section, the axial force is:

$$P = \gamma f'_m \beta c b_w - \sum_i^n A_{v_i} f_{v_i} \quad \text{Eq. 4}$$

where P is the axial load including the self-weight of the wall, b_w is the thickness of the wall, A_{v_i} and f_{v_i} are, respectively, the cross-sectional area and the acting stress on the i-th member, and n is the number of rebars.

Isolating the depth of the compression zone in Equation 4, brings to:

$$c = \frac{P + \sum_i^n A_{v_i} f_{v_i}}{\gamma f'_m \beta b_w} \quad \text{Eq. 5}$$

By the similarity of triangles in the strain diagram, the elongation of each bar (ε_i) is obtained as a function of the maximum shortening of the most compressed fiber (ε_u):

$$\frac{\varepsilon_u}{\varepsilon_i} = \frac{c}{d_i - c} \quad \therefore \quad \varepsilon_i = \varepsilon_u \frac{d_i - c}{c} \quad \text{Eq. 6}$$

where d_i is the distance from the i-th rebar to the compressed edge.

Given the deformation of each rebar, the stress acting on these rebars is known by:

$$f_{v_i} = E_{v_i} \varepsilon_i \quad \therefore \quad f_{v_i} = E_{v_i} \varepsilon_u \frac{d_i - c}{c} \leq f_{y_i} \quad \text{Eq. 7}$$

where f_{y_i} is the yield strength of the steel of the i-th rebar.

The moment capacity is determined by the balance of moments in the section:

$$M_n = \gamma f'_m \beta c b_w \left(\frac{l_w}{2} - \frac{\beta c}{2}\right) + \sum_i^n A_{v_i} f_{v_i} \left(d_i - \frac{l_w}{2}\right) \quad \text{Eq. 8}$$

The flexural load capacity is then determined by dividing the moment capacity (M_n) by the effective height of the wall (h_e):

$$F_n = \frac{M_n}{h_e} \quad \text{Eq. 9}$$

Figure 47: Idealization of flexural behavior.

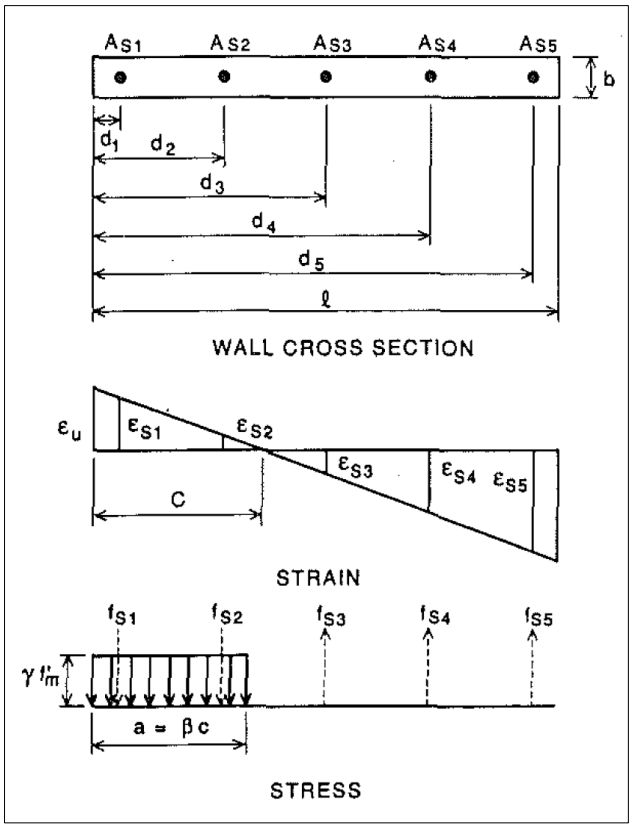

Source: Shing et al. (1990).

Table 21: Values of γ, β e ε_u in relevant design codes.

Design Code	γ	β	ε_u	
			Concrete	Clay
ABNT NBR 16868-1 (2020)	0.70	0.80	0.0030	0.0030
TMS 402/602 (2016)	0.80	0.80	0.0025	0.0035
CSA S304 (2014)	0.85	0.80	0.0030	0.0030
NZS 4230 (2004)	0.85	0.85	0.0030	0.0030

Source: Author.

The design codes recommend, conservatively, ignoring the contribution of reinforcement under compression, except for cases in which it is ensured that they are properly tied. Shedid et al. (2008) evaluated this issue using experimental results from six walls, which were previously designed to fail by flexure as they had an aspect ratio of 2.0. The authors estimated the flexural load capacity of the walls by applying the coefficients indicated by the CSA S304.1 (2004) and MSJC (2005) codes, with and without considering the compressed reinforcement. The results showed that, by ignoring the contribution of the compressed reinforcement, the two codes presented values close to each other and adequately conservative in estimating the maximum load for the walls. When considering the compressed reinforcement, the predictions were relatively better, especially for walls subjected to high axial stress; however, the values were slightly overestimated in general. The authors commented that

the research results corroborate the studies carried out by Priestley (1986), Shing et al. (1989), and Zhang and Wang (2000).

3.1.2 Equations for shear load capacity

In the elaboration of formulations to predict the shear load capacity of shear walls, the number of parameters included in it and how the interaction between them is considered delineates the calibration coefficients and, consequently, the final result. Most equations consider the contribution of at least three parameters: the masonry's resistance, the axial compressive load's influence on that resistance, and the effect of reinforcement.

a) Matsumura (1988)

Matsumura (1988) presented Equation 10 to predict the shear load capacity of fully and partially grouted shear walls. Regression analysis was applied using test results with approximately 60 concrete masonry walls and 30 clay brick masonry walls. The parameters considered in the proposed expression were the masonry strength, axial stress, reinforcement ratios, wall aspect ratio, and partial or total grouting.

The relationship between the shear strength of the walls (τ) and the compressive strength of the masonry (f'_m) was determined as $\tau \propto \sqrt{f'_m}$, while the contribution of the axial stress (σ_0) was determined as $\tau \propto \tau_a + 0.2\sigma_0$, where τ_a is the shear strength of the wall without axial stress. The relationship between the shear strength of the walls and the horizontal reinforcement ratio (ρ_h) was defined as proportional to $0.18\alpha\delta\sqrt{\rho_h f_{yh} f'_m}$, where α is the factor relative to the action of the confined grout, δ is the factor related to the loading method, and f_{yh} is the yield strength of the horizontal reinforcement. Matsumura (1988) used f'_m relative to the gross cross-sectional area.

The influence of vertical reinforcement was considered by the factor $k_\rho = 1.16{\rho_{vf}}^{0.3}$, where ρ_{vf} is the reinforcement ratio corresponding to the tensioned bars at the ends of the wall. The expression $\frac{0.76}{h_w/d_v + 0.7} + 0.012$ considers the influence of the aspect ratio (h_w/d_v; height/length). The k_u factor is responsible for considering the type of masonry and the grouting mode. The thickness and effective length of the wall are, respectively, represented by b_w and d_v; the effective length is included in the factor j such that $j = (7/8)d_v$.

$$V_u = \left[k_u k_\rho \left(\frac{0.76}{h_w/d_v + 0.7} + 0.012\right)\sqrt{f'_m} + 0.18\alpha\delta\sqrt{\rho_h f_{yh} f'_m} + 0.2\sigma_0\right] b_w j \qquad \text{Eq. 10}$$

Values for the factors k_u, α, and δ are adopted as following:

- $k_u = 1.0$ for fully grouted masonry, $k_u = 0.8$ for partially grouted clay brick masonry, and $k_u = 0.64$ for partially grouted concrete masonry;
- $\alpha = 1.0$ for hoop type reinforcement closing grout within it, $\gamma = 0.8$ for single reinforcement bar with semi-circular hooks at the ends, e $\gamma = 0.6$ for the same reinforcement in partially grouted concrete masonry;
- $\delta = 1.0$ for loading that causes an inflection point at half the height of the wall, and $\delta = 0.6$ for loading that causes a single curvature in a cantilever wall.

b) Shing et al. (1990)

Shing et al. (1990) studied the flexural and shear strengths of fully grouted masonry shear walls. Sixteen concrete masonry walls and six clay masonry walls were tested, all with a uniform vertical and horizontal reinforcement distribution.

The authors evaluated the accuracy of the shear load capacity equation presented by the Uniform Building Code (UBC, 1988) and suggested a new equation. The nominal shear load capacity (V_n) admitted by UBC (1988) is given by $V_n = V_m + V_{rh}$, where V_m is the contribution of the masonry, estimated as $1.2A_{eh}\sqrt{f'_m}$, and V_{rh} the contribution of the horizontal reinforcement, considered equal to $A_{eh}\rho_h f_{yh}$; where A is the net cross-sectional area, f'_m is the compressive strength of the masonry, ρ_h is the horizontal reinforcement ratio, and f_{yh} is the yield strength of steel. The authors evaluated the UBC (1988) definitions to be simplistic in describing the complexity of the mechanism of residual wall resistance after diagonal cracks have occurred; therefore, they proposed new relationships.

The axial stress (σ) was not considered separately, but like the vertical reinforcement, it was included in the masonry contribution term. The influence of the horizontal reinforcement was estimated without including the bars at the bottom and top, as they did not have sufficient anchorage length to develop tensile strength when diagonal cracks occurred. Thus, it was proposed $V_m = \left[0.0018\left(\rho_v f_{yv} + \sigma\right) + 2\right]A_{eh}\sqrt{f'_m}$ and $V_r = \left(\frac{l-2d'}{s_h} - 1\right)A_{hb}f_{yh}$, where ρ_v is vertical reinforcement ratio, l_w is the horizontal length of the wall, d' is the distance from the wall edge to the nearest vertical bar, s_h the spacing between horizontal reinforcement, and A_{hb} is the area of a horizontal rebar. The final formulation adapted to the international system of units is the one described by Equation 11.

$$V_n = \left[0.0217\left(\rho_v f_{yv} + \sigma\right) + 0.166\right] A_{eh}\sqrt{f'_m} + \left(\frac{l-2d'}{s_h} - 1\right) A_{hb} f_{yh} \quad \text{Eq. 11}$$

c) Anderson and Priestley (1992)

Anderson and Priestley (1992) analyzed the equations of Matsumura (1988) and Shing et al. (1990) and then proposed Equation 12, which was calibrated with the results of the tests by Sveinsson et al. (1985), Matsumura (1986), and Shing et al. (1990).

$$V_n = CkA_g\sqrt{f'_m} + 0.25P + 0.5A_{hb} f_{yh}\frac{d_v}{s_h} \quad \text{Eq. 12}$$

The expression was pointed out as more simplified by considering the contribution given by the masonry ($V_m = CkA_g\sqrt{f'_m}$), by the axial load ($V_p = 0.25P$), and by the horizontal reinforcement ($V_{rh} = 0.5A_{hb} f_{yh}\frac{d_v}{s_h}$) independently. However, the influence of the aspect ratio, vertical reinforcement, and partial grouting was neglected. It was argued that the contribution of the horizontal reinforcement was reduced due to the masonry losing capacity soon for small cracks and, consequently, the reinforcement does not reach yield.

The authors differentiated the type of masonry to be used through the C factor and included the degradation of the masonry strength that occurs in the plastic phase under cyclic lateral loads through the ductility coefficient $k = 1 - \frac{(\mu_d - 2)}{2}$. The C factor must be equal to 0.24 and 0.12 for concrete and clay masonry, respectively. It has been suggested that the coefficient k is equal to 1.0 when the ductility (μ_d) is less than 2.0, and linearly decreasing from 1.0 to 0 when the ductility factor is from 2.0 to 4.0.

d) New Zealand Standard (NZS 4230, 2004)

NZS 4230 (2004) presented Equation 13 for calculating the nominal shear load capacity of masonry walls. Individual contributions to the masonry (V_m), axial pre-compression (V_p), and horizontal reinforcement (V_{rh}) were considered.

$$V_n = \left(k_\rho + \beta_r\right) k V_{bm} b_w d_v + 0.9P\tan\alpha + C_3 A_{hb} f_{yh}\frac{d_v}{s_h} \leq 0.45 b_w d_v\sqrt{f'_m} \quad \text{Eq. 13}$$

The parameters k_ρ, β_r, and k, associated with the masonry contribution given by $V_m = (k_\rho + C_2)kV_{bm}b_w d_v$ are related to the influence of vertical reinforcement, aspect ratio, and ductility (μ_d), respectively. $k_\rho = 33\rho_v\frac{f_{yv}}{300}$ is calculated with the vertical reinforcement ratio (ρ_v) being greater than 0.07%, while β_r is estimated according to the conditions shown in

Equation 14. The degradation imposed on the masonry strength by the levels of displacements is estimated by the factor $k = \left(1 - \frac{\mu_d - 1.25}{2.75}\right)$, which was assumed to have no effect when $\mu_d \leq 1.25$ and maximum effect, nullifying the masonry contribution, when $\mu_d \geq 4.0$. According to the standard, for general cases, the basic contribution of the masonry to the shear (V_{bm}) is admitted equal to $0.2\sqrt{f'_m}$. It should be noted that there is no specific factor to consider for partial grouting, but it is recommended to use the thickness equivalent to the sum of the thickness of face shells.

$$\beta_r = \begin{cases} 1.5 & \Rightarrow \quad \left(\frac{M}{Vl_w}\right) < 0.25 \\ 0.42\left(4 - 1.75\frac{M}{Vl_w}\right) & \Rightarrow \quad 0.25 \leq \left(\frac{M}{Vl_w}\right) \leq 1.0 \\ 1.0 & \Rightarrow \quad \left(\frac{M}{Vl_w}\right) > 1.0 \end{cases} \qquad \text{Eq. 14}$$

The contribution of the axial pre-compression to the wall capacity is estimated by $V_p = 0.9\mathrm{P}\tan\theta$, where P is the axial compressive load limited to $0.1f'_m A_g$ to avoid possible brittle failure, and θ he resulting angle of the diagonal compression strut. The contribution of the horizontal reinforcement was considered through the term $V_{rh} = C_3 A_{hb} f_{yh} \frac{d_v}{S_h}$, with $C_3 = 0.8$ and $d_v = 0.8l_w$.

e) Voon and Ingham (2007)

Voon and Ingham (2007) proposed minor changes in the expression of the nominal shear load capacity adopted by NZS 4230 (2004). Comparing Equation 13 with Equation 15, it can be seen that the differences are in the contribution term of the horizontal reinforcement and the maximum limit for the wall capacity.

$$V_n = \left(k_\rho + \beta_r\right) k V_{bm} b_w d_v + 0.9P\tan\theta + A_{hb} f_{yh} \frac{d_v}{S_h} \leq 0.33 b_w d_v \sqrt{f'_m} \qquad \text{Eq. 15}$$

The authors considered that the horizontal reinforcement can contribute until yielding, while the standard allowed up to 80%. Contrastingly, the effective length of the wall (d_v) was reduced due to the reinforcement not being able to reach more than $0.5f_y$ at the ends of the walls; thus, $d_v = l_w - 2d' - l_{dw}$ was adopted, where d' is the distance from the edge of the wall to the nearest vertical bar, and l_{dw} is the anchorage length of the reinforcement admitted as 20Ø and 35Ø for $f_y = 300\ MPa$ and $f_y = 500\ MPa$, respectively. The lateral load capacity of the wall is now limited more conservatively to $0.33 b_w d \sqrt{f'_m}$.

f) Canadian Standards Association (CSA S304, 2014)

According to CSA S304 (2014), the nominal shear load capacity of a masonry shear wall can be calculated using Equation 16 but limited to the values obtained by Equation 17.

$$V_n = \emptyset_m \left[0.16 \left(2 - \frac{M}{\mathrm{V}d_v}\right) b_w d_v \sqrt{f'_m} + 0.25P\right] \gamma_g + \emptyset_r \left[0.6 A_{hb} f_{yh} \left(\frac{d_v}{S_h}\right)\right] \quad \text{Eq. 16}$$

$$V_{n,max} \leq \begin{cases} \emptyset_m \left(0.4 b_w d_v \sqrt{f'_m}\right) \gamma_g & \Rightarrow \quad (h_w/l_w) \geq 1.0 \\ \emptyset_m \left(0.4 b_w d_v \sqrt{f'_m}\right) \gamma_g [2 - (h_w/l_w)] & \Rightarrow \quad (h_w/l_w) < 1.0 \end{cases} \quad \text{Eq. 17}$$

The contribution of the masonry is estimated by $V_m = 0.16 \left(2 - \frac{M}{\mathrm{V}d_v}\right) b_w d_v \sqrt{f'_m}$, in which the relation $\frac{M}{\mathrm{V}d_v}$ must be contained in the range of values from 0.25 to 1.0. The influence of the axial load (V_P) is considered by an individual term and equivalent to $0.25P$, where P must be 0.9 times the dead load plus the axial load from the bending of the coupling beams of walls with openings.

The grouting type is included through the factor γ_g, which is calculated by the ratio between the effective net area and the gross area of the wall's cross-section, and must always be less than or equal to 0.5 for partially grouted walls and equal to 1.0 for fully grouted walls.

Horizontal reinforcement contributes to the wall capacity with $0.6 A_{hb} f_{yh} \left(\frac{d_v}{S_h}\right)$, so that the effective length (d_v) should not be less than the value of $0.8 l_w$ for walls with flexural reinforcement distributed along the length of the wall (l_w). For design cases, the masonry ($\emptyset_m$) and steel ($\emptyset_s$) strength reduction factors must be admitted, respectively, equal to 0.6 and 0.85.

g) Oan and Shrive (2014)

Oan and Shrive (2014) suggested some modifications to the expression of CSA S304 (2014), resulting in Equation 18. The authors tested 45 partially grouted shear walls and analyzed the data using linear regression.

$$V_n = \emptyset_m \left[0.16 \left(2 - \frac{M}{\mathrm{V}d_v}\right) b_w d_v \sqrt{f'_m}\right] \gamma_g + \emptyset_m 0.27P + \emptyset_r \left(0.05 A_v f_{yv}\right) \quad \text{Eq. 18}$$

The following modifications were suggested: only the masonry shear capacity is to be multiplied by the factor to account for partial grouting (γ_g); the contribution of the axial load (V_P) is to be increased slightly from $0.25P$ to $0.27P$, but it is limited to $0.4 f'_m A_{eh}$ to avoid compression failure of the masonry; the contribution of the vertical reinforcement is to be

included and the contribution of the horizontal reinforcement is to be neglected since it is activated only after the wall has cracked.

The final equation was verified with results from 60 partially grouted shear walls found in the literature, showing better accuracy than the equations of CSA S304 (2014), EN 1996-1 (2005), NZS 4230 (2004), and Matsumura (1988).

h) Dillon and Fonseca (2015)

Dillon and Fonseca (2015) organized a large database using test results of 353 masonry shear walls available in the literature, in which 172 were fully grouted and 181 were partially grouted. The data were synthesized and analyzed, thus independent expressions for the SLC of fully and partially grouted walls were developed.

The overall formulation was given as $V_n = V_m + V_p + V_r$, being the masonry contribution (V_m) the term that differs for the grouting type used; it is estimated $V_m = 0.083\left(1.1 + 0.9\frac{Vs_{gv}}{M}\right)A_{eh}\sqrt{f'_m}$ for PG walls, where s_{gh} is the spacing between the horizontal grouts, and $V_m = 0.083\left(1.8 + 0.7\frac{Vl_w}{M}\right)A_{eh}\sqrt{f'_m}$ for FG walls.

The contribution of the axial stress (V_p) and reinforcement (V_r) are estimated equally for both types of walls, so that $V_p = 0.15P$ and $V_r = 0.12\left[\left(\frac{A_{vib}f_{yv}}{s_v}\right)d_v + \left(\frac{A_{hb}f_{yh}}{s_h}\right)h_w\right]$. The complete expressions for fully and partially grouted walls are described by Equations 19 and 20, respectively.

$$V_n = 0.083\left(1.8 + 0.7\frac{Vl_w}{M}\right)A_{eh}\sqrt{f'_m} + 0.15P + 0.12\left[\left(\frac{A_{vib}f_{yv}}{s_v}\right)d_v + \left(\frac{A_{hb}f_{yh}}{s_h}\right)h_w\right] \quad \text{Eq. 19}$$

$$V_n = 0.083\left(1.1 + 0.9\frac{Vs_{gv}}{M}\right)A_{eh}\sqrt{f'_m} + 0.15P + 0.12\left[\left(\frac{A_{vib}f_{yv}}{s_v}\right)d_v + \left(\frac{A_{hb}f_{yh}}{s_h}\right)h_w\right] \quad \text{Eq. 20}$$

The authors stated that interior vertical reinforcement had, statistically, a significant contribution to the strength of the wall and that the expression of the Masonry Standards Joint Committee (MSJC, 2013), currently TMS 402/602 (2016), overestimates the influence of horizontal reinforcement. They also explained that since diagonal cracks are typically formed at an angle of 45°, vertical and horizontal reinforcement are essentially equally effective to restrict the opening of these cracks and to transfer tension between the masonry parts.

i) The Masonry Society (TMS 402/602, 2016)

According to TMS 402/602 (2016), the nominal shear load capacity of a masonry wall can be obtained using Equation 21, but limited to the values obtained by Equation 22 to avoid brittle failure.

$$V_n = \emptyset_m \left[0.083 \left(4 - 1.75 \frac{M}{\mathrm{V}d_v}\right) A_{eh} \sqrt{f'_m} + 0.25P + 0.5 A_{hb} f_{yh} \frac{d_v}{s_h}\right] \gamma_g \qquad \text{Eq. 21}$$

$$V_{n.max} \leq \begin{cases} \emptyset_m \left(0.5 A_{eh} \sqrt{f'_m}\right) \gamma_g & \Rightarrow \quad \left(\frac{M}{\mathrm{V}d_v}\right) \leq 0.25 \\ \emptyset_m \left(0.33 A_{eh} \sqrt{f'_m}\right) \gamma_g & \Rightarrow \quad \left(\frac{M}{\mathrm{V}d_v}\right) \geq 1.0 \end{cases} \qquad \text{Eq. 22}$$

The masonry contribution is determined by $0.083 \left(4 - 1.75 \frac{M}{\mathrm{V}d_v}\right) A_{eh} \sqrt{f'_m}$, in which the ratio $\frac{M}{\mathrm{V}d_v}$ must be greater than 0.25 and less than 1.0. The contribution of the axial load (P) to the wall capacity is considered equal to $0.25P$, while the horizontal reinforcement contributes $0.5 A_{hb} f_{yh} \frac{d_v}{s_h}$. The γ_g factor should be considered equal to 1.0 for fully grouted walls and 0.75 when partially grouted. The effective length (d_v) can be adopted equal to the length of the wall (l_w) when it is rectangular.

For design situations of masonry subjected to shear, the strength reduction factor ($\emptyset_m$) must be admitted equal to 0.8. Dillon and Fonseca (2015) commented that this reduction factor should have different values for fully grouted ($\emptyset_m$ = 0.8) and partially grouted ($\emptyset_m$ = 0.75) walls to improve the performance of the standard equation since using the same expression and a single factor for the two types of walls, the probability of failure was much higher for partially grouted walls.

j) Bolhassani et al. (2016a)

Bolhassani et al. (2016a) comment that the expression of TMS 402/602 (2016) to predict the shear load capacity of masonry walls was originally based on tests of fully grouted walls and that the reduction factor that considers partial grouting (γ_g) was only introduced later. The value of 0.75 was adopted for γ_g in the expression of TMS 402/602 (2016) from the ratio between the main results of partially and fully grouted walls reported, respectively, by Minaie et al. (2010) and Davis and Mclean (2008).

Using results available in the literature of 42 full-scale partially grouted walls, Bolhassani et al. (2016a) evaluated the accuracy of the expression of TMS 402/602 (2016) for

this wall typology. According to the authors, the results indicated that the code equation does not accurately predict the shear capacity of walls with grout spacing higher than 1.2 m, as the expression was based on a monolithic behavior model of fully grouted walls.

Given this, the authors developed an experimental and numerical study to propose a new expression for the shear load capacity of partially grouted walls based on the concrete frame mechanism with infilled masonry. As commented by Schultz (1996) and Minaie et al. (2010), the authors explain that vertical grouting points in partially grouted walls are highly vulnerable to shear failure due to shear cracks starting and propagating through the horizontal joints of the ungrouted masonry sections to the vertical grouts. Furthermore, the regions around the intersection between the horizontal and vertical grouting are especially susceptible to damage due to the interaction between the grouted and ungrouted parts near these intersections. This behavior resembles the strut mechanism observed in a concrete frame with infilled masonry.

The suggested overall equation ($V_n = V_{infill} + V_{frame}$) is therefore composed of the sum of the contribution given by each of the frames formed by the grouted cells ($V_{frame} = 4M_p/h$), and the contribution of each infill ungrouted masonry panel ($V_{infill} = V_{masonry} + V_{load}$), which considers the contributions of the masonry ($V_{masonry} = 2lt_{eff}\sqrt{f'_m}\cos\theta$) and axial load ($V_{load} = \mu P_{infill}$). The final value of the shear load capacity of the wall for the number of frames formed (n – 1) according to the distribution of the "n" vertical grouted cells can be calculated using Equations 23, 24 and 25; where, l and h are, respectively, the length and height of a infilled masonry panel; t_{eff} is the effective wall thickness; θ is the angle of the central strut formed diagonally across the infilled masonry panel; φ is the friction coefficient; M_p is the plastic moment of the frame; P is the axial load; A_{infill} is the area of a single infilled masonry panel; $A_{eh,g}$ is the area of the vertical grouted cells; A_{vb} is the area of rebars; and E_s is the modulus of elasticity of steel.

$$V_n = (n-1)\left[lt_{eff}\sqrt{f'_m}\cos\theta + \varphi P_{infill} + \frac{4M_p}{h}\right] \quad \text{Eq. 23}$$

$$P_{infill} = \frac{PA_{infill}}{(n-1)[A_{infill}+1.5A_{eh,g}]} + \frac{lt_{eff}\sqrt{f'_m}\sin\theta}{(n-1)} \quad \text{Eq. 24}$$

$$A_{eh,g} = A_{grouted\ cells} + A_{vb}\left(\frac{E_s}{A_s} - 1\right) \quad \text{Eq. 25}$$

The authors compared the accuracy of the equation suggested by them with six others found in the literature: Matsumura (1988), NZS 4230 (2004), CSA S304 (2014), TMS 402/602

(2016); Anderson and Priestley (1992), and Shing et al. (1990). The results showed that the proposed equation predicted the walls' capacity with excellent accuracy, while the other equations proved to be unconservative. The best performance among the equations in the literature was that of CSA S304 (2014), followed by Matsumura (1988).

k) Aguilar et al. (2016)

Aguilar et al. (2016) set up a database with results found in the literature of 285 shear walls of different typologies that failed by shear; 96 walls were made of concrete blocks and fully grouted, 95 walls were made of concrete blocks and partially grouted, 37 walls were made of clay blocks and fully grouted, and 57 walls were made of clay blocks and partially grouted.

With those data available, the authors analyzed the accuracy of eight expressions found in the literature to estimate the shear load capacity of masonry walls. From a statistical comparison between the estimations, it was concluded that the one proposed by Matsumura (1988) was the most accurate for fully grouted concrete masonry walls, while the equation of (Tomažević, 1999) was the most accurate for fully grouted clay masonry walls. Regarding partially grouted walls, the expression of ACI-530 (2005) was the most accurate.

Applying the technique of artificial neural networks to the data and based on the terms of the equations evaluated with the best performance, the authors proposed new expressions to predict the shear load capacity of fully grouted concrete masonry walls (Equations 26 and 27), fully grouted clay masonry walls (Equations 28 and 29), and partially grouted clay masonry walls (Equations 30 and 31). A satisfactory expression was not achieved for partially grouted concrete masonry walls. The parameters considered in the equations were the masonry strength, axial pre-compression level, amount and spacing of vertical and horizontal reinforcement, and aspect ratio. The authors concluded that the equations proposed by them predicted the experimental results more accurately and less conservatively than the other equations.

$$V_n = 3.12 A_g \left(\frac{0.7712}{1+e^{-\Omega}} + 0.0667\right) \quad \text{Eq. 26}$$

$$\Omega = 3.1329 \frac{\left(M/_{VL}\right)^{-1}\sqrt{f'_m}}{13.973} + 0.8082 \frac{\rho_h f_{yh}}{2.572} + 2.7827 \frac{\rho_v \sqrt{f_j f_{yv}}}{1.292} + 2.0651 \frac{\alpha\delta\sqrt{\rho_h f_{yh} f'_m}}{7.573} + 2.8501 \frac{\sigma}{5.87} - 3.527 \quad \text{Eq. 27}$$

$$V_n = 2.69 A_g \left(\frac{75.9867}{1+e^{-\Omega}} - 55.0746\right) \quad \text{Eq. 28}$$

$$\Omega = 0.0627 \frac{\left(M/_{VL}\right)^{-1}\sqrt{f'_m}}{9.01} + 0.0248 \frac{\rho_h f_{yh}}{2.848} + 0.0182 \frac{\rho_v \sqrt{f_j f_{yv}}}{0.689} - 0.0385 \frac{\alpha\delta\sqrt{\rho_h f_{yh} f'_m}}{8.576} + 0.0142 \frac{\sigma}{2.76} + 0.9545 \quad \text{Eq. 29}$$

$$V_n = 1.061 A_g \left(\frac{-0.5568}{1+e^{-\Omega}} - 0.9309\right) \quad \text{Eq. 30}$$

$$\Omega = -8.0997\frac{\left(M/_{VL}\right)^{-1}\sqrt{f'_m}}{7.624} - 6.9163\frac{\rho_h f_{yh}}{0.72} - 6.1045\frac{\rho_v\sqrt{f_j f_{yv}}}{1.222} + 0.4315\frac{\alpha\delta\sqrt{\rho_h f_{yh} f'_m}}{2.838} - 1.1012\frac{\sigma}{1.49} + 9.0745 \quad \text{Eq. 31}$$

where: A_g is the gross cross-sectional area of the wall; M and V are the maximum moment and shear force in the section considered; L is the wall length; f'_m is the masonry compressive strength; ρ_h and ρ_v are, respectively, the horizontal and vertical reinforcement ratio; f_y is the steel yield strength; α is the factor related to the action of the confined grout; δ is the factor related to the boundary condition; and σ is the axial stress.

l) Seif ElDin et al. (2019a)

Seif ElDin et al. (2019a) proposed an equation to predict the shear load capacity of masonry walls that considers the influence of large ductility levels. The authors comment on the controversy in the literature about the contribution of horizontal reinforcement to the wall capacity and the absence of an equation that considers this contribution accounting for the level of ductility demand.

The proposed expression (Equations 32 to 35) was developed using terms suggested in previous studies in the literature. The masonry strength was adopted proportional to $\sqrt{f'_m}$ according to that initially demonstrated by Matsumura (1988). The vertical reinforcement contribution was considered as $0.02\rho_v f_{yv}$, as indicated by Shing et al. (1990) and NZS 4230 (2004). The influence of the aspect ratio was estimated by the term $0.14\left(2.5 - \frac{h_e}{d_v}\right)$, similar to the NEHRP (1997), from which the formulation of TMS 402/602 (2016) derives. However, unlike the limits adopted, for example, by CSA S304 (2014) and TMS 402/602 (2016), the ratio h_e/d_v must not be ranged between 0.25 and 1.0 but between 1.0 and 2.0 to avoid overestimating the shear capacity of walls with high aspect ratio.

The axial load contribution was adopted as in NZS 4230 (2004), i.e., $V_p = P\,tan\,\theta$, with $\tan\theta = 0.4\,l_w/h_w$, for simplicity, and $P = 0.9P_{DL} \pm N$, as defined in CSA S304 (2014), limiting P to $0.1f'_m A_g$ to avoid unconservative results; P_{DL} is the dead load, and N is the axial load arising from bending in coupling beams. As applied in CSA S304 (2014), the modification factor γ_g was used to consider the type of grouting, being defined by the ratio between the effective net area and the gross area of the wall cross-section, which must always be less than or equal to 0.5 for partially grouted walls, and equal to 1.0 for fully grouted walls.

The horizontal reinforcement contribution was assumed to be $0.4\frac{A_{hb}}{s_h}d_e f_{yh}$, which represents 40% of the yielding capacity of the reinforcement, which can, however, be increased by the factor k_2 for large levels of wall deformation; the effective length (d_e) must be assumed to be 0.8 times the smallest value between the length (l_w) and height (h_w) of the wall.

$$V_n = \left[\left(V_m + V_p\right)\gamma_g k_1 + V_{rh}k_2\right]\delta \quad \text{Eq. 32}$$

$$V_m = \left[0.02\rho_v f_y + 0.14\left(2.5 - \frac{h_e}{d_v}\right)\right] b_w d_v \sqrt{f'_m} \quad \text{Eq. 33}$$

$$V_p = P\,tan\,\theta \quad \text{Eq. 34}$$

$$V_{rh} = 0.4\frac{A_{hb}}{s_h}d_e f_{yh} \quad \text{Eq. 35}$$

The authors used the results of nine walls tested previously (Seif ElDin and Galal, 2016) to justify and calibrate the use of the modification coefficients $k_1 = 1 - \frac{\mu_d - 1.5}{4.5}$ and $k_2 = 1 + \frac{\mu_d - 1.5}{1.65}$, which are related to the wall ductility (μ_d). It was observed in the tests that, after the appearance of diagonal cracks and vertical reinforcement yielding, the contribution conferred by the masonry and axial stress (V_{m+p}) reduces significantly, while the influence of the horizontal reinforcement (V_{rh}) increases. The horizontal reinforcement demonstrated that it could reach the yield for large levels of wall deformation and less contribution for small displacements. Thus, the coefficient k_1 assumes a linear degradation starting from 1.0 to 0 in V_{m+p} when μ_d is from 1.5 to 6.0, and the coefficient k_2 imposes a linear increase from 1.0 to 2.5 in V_{rh} when μ_d is from 1.5 to 4.0. The coefficient k_2 should only be applied to grouted walls that have a small spacing between the horizontal and vertical reinforcements.

The authors commented that the ductility parameter (μ_d) is not simple to define, and, therefore, they correlated the factors k_1 and k_2 with the seismic response modification coefficient R_d used by various design codes. For $R_d = 1.5$, it is adopted $k_1 = k_2 = 1.0$; for $R_d = 2.0$, it is adopted $k_1 = 0.75$ and $k_2 = 1.5$; for $R_d = 3.0$, it is adopted $k_1 = 0.5$ and $k_2 = 2.0$; and for $R_d = 4.0$, it is adopted $k_1 = 0.25$ and $k_2 = 2.5$.

The modification factor δ is related to the load application method and multiplies the sum of all contributions. It is adopted $\delta = 1.0$ for loading that causes a single curvature in a cantilever wall, and $\delta = 0.8$ for loading resulting in inflection point at the mid-height of walls.

Finally, the authors evaluated the accuracy of their proposed expression and nine more from literature using results from 68 shear walls. Statistical analysis showed that the authors'

equation and the equations of Matsumura (1988) and TMS 402/602 (2016) presented the lowest values of the coefficient of variation, which were 14.6%, 15.3%, and 13 .6%, respectively.

m) Izquierdo et al. (2021)

Izquierdo et al. (2021) used stepwise regression in data from 292 experimentally tested partially grouted masonry walls reported in the literature. After removing interdependencies and restricting the pool to the most suitable subset for determining the output variable, the most significant input variables were selected from a set of candidates. Among the variables studied, the axial load, wall geometry, compressive strength of mortar, and area of interior vertical reinforcement stand out. Accounting for the compressive strength of mortar is significant since it has never been included in previous shear strength equations. According to the authors, the horizontal reinforcement contribution was neglected because it had no statistical significance when compared to the other variables.

From the set of equations generated by the authors, three which maximized both accuracy and precision are presented here in Equations 36 to 38.

$$V_n = -0.0205h_w + 0.0337l_w + 6f_{mt} + 0.0917A_{vi} + 0.289P \quad \text{Eq. 36}$$

$$V_n = 0.296P + 0.255f_{mt}t_{fs}l_b + 0.291t_{fs}l_w\sqrt{f_{mt}} + 0.209A_{vi}f_{yvi} \quad \text{Eq. 37}$$

$$V_n = 0.0538l_w + 4.83f'_{mg} + 0.067A_{vf} - 0.0533s_{v,avg} + 0.245P \quad \text{Eq. 38}$$

where: l_w and h_w are the length and height of the wall; f_{mt} is the compressive mortar strength; f'_{mg} is the grouted masonry compressive strength; A_{vi} is the total area of the interior vertical reinforcement; A_{vf} is the total area of the outer vertical reinforcement; f_{yvi} is the yield strength of interior vertical reinforcement; $s_{v,avg}$ is the average spacing between interior vertical reinforcement; t_{fs} is the face shell thickness of blocks; l_b is the actual length of blocks; and P is the axial compressive load.

n) Summary of the equations presented

The parameters included in the twelve equations presented to predict the load capacity of shear-dominated masonry walls are summarized in Table 22. Note that:

- Compressive masonry strength and axial load are included in all equations;
- Compressive mortar strength is only incorporated in the expressions proposed by Izquierdo et al. (2021).

- The influence of horizontal reinforcement is not only considered in the expression proposed by Oan and Shrive (2014) and Izquierdo et al. (2021). Among the others, only the equations of Matsumura (1988) and Aguilar et al. (2016) do not include the spacing between horizontal bars;
- Vertical reinforcement was not included in the equations of Anderson and Priestley (1992) and the American (TMS 402/602, 2016) and Canadian (CSA S304, 2014) standards. In the rest, the spacing between the vertical bars was only considered by Dillon (2015), Bolhassani et al. (2016a), and Izquierdo et al. (2021);
- Aspect ratio or wall geometry was included directly or indirectly in almost all expressions, except those suggested by Shing et al. (1990) and Anderson and Priestley (1992);
- The ductility effect was integrated into the expressions of Anderson and Priestley (1992), NZS 4230 (2004), Voon and Ingham (2007), and Seif ElDin et al. (2019a);
- The distinction between concrete and clay blocks was set only in the expressions of Matsumura (1988), Anderson and Priestley (1992), and Aguilar et al. (2016);
- Most equations were developed for fully grouted walls and then adapted for partially grouted walls. The expression of Bolhassani et al. (2016a) was developed especially for partially grouted walls with grout spacing greater than 1.2 m. Also, the equation of Izquierdo et al. (2021) was designed exclusively for partially grouted walls. There is no distinguishing factor between fully and partially grouted walls in the expressions of Shing et al. (1990), Anderson and Priestley (1992), NZS 4230 (2004), and Voon and Ingham (2007). Different equations for the two types of walls were presented by Dillon (2015) and Aguilar et al. (2016).

Several authors have compared the accuracy of their equations, naturally judging theirs to be more accurate than the others. It is noteworthy that each model will show better accuracy for the data set used in its development, as it was calibrated and validated with them. Thus, the more extensive the database used, the better the equation fit.

Table 22: Summary of the parameters included in the equations presented.

Equation	Parameters included in the equation											
	Masonry Strength	Mortar Strength	Axial Load	Horizontal Reinforcement		Vertical Reinforcement		Aspect Ratio	Ductility	Block Type	Grouting	
				Amount	Spacing	Amount	Spacing				Total	Partial
Matsumura (1988)	✓		✓	✓		✓		✓		✓	✓	✓
Shing et al. (1990)	✓		✓	✓	✓	✓					✓	
Anderson and Priestley (1992)	✓		✓	✓	✓				✓	✓	✓	
NZS 4230 (2004)	✓		✓	✓	✓	✓		✓	✓		✓	
Voon and Ingham (2007)	✓		✓	✓	✓	✓		✓	✓		✓	
CSA S304 (2014)	✓		✓	✓	✓			✓			✓	✓
Oan and Shrive (2014)	✓		✓			✓		✓			✓	✓
Dillon and Fonseca (2015)	✓		✓	✓	✓	✓	✓	✓			✓	✓
TMS 402/602 (2016)	✓		✓	✓	✓			✓			✓	✓
Bolhassani et al. (2016a)	✓		✓	✓	✓	✓	✓	✓				✓
Aguilar et al. (2016)	✓		✓	✓		✓		✓		✓	✓	✓
Seif ElDin et al. (2019a)	✓		✓	✓	✓	✓		✓	✓		✓	✓
Izquierdo et al. (2021)	✓	✓	✓			✓	✓	✓				✓

Source: Author.

3.1.3 Load capacity of perforated walls

Although it is common and necessary to use doors and windows in buildings, walls with openings are less experimentally evaluated than unperforated walls (without openings). Hatzinikolas et al. (2015) comment that the behavior of masonry shear walls with openings is much more complex than that of unperforated walls.

Results of experimental tests (Calderón et al., 2017) have shown that the inclusion of openings significantly reduces the load capacity of masonry shear walls. If the mechanisms of lateral resistance depend on the second moment of area of the walls, it is evident that the decrease in stiffness due to the presence of openings will substantially alter the strength and, consequently, the behavior of the wall. Elshafie et al. (2002) state that for walls of equal dimensions, the stiffness reduction due to openings is comparable to the reduction in the load capacity, regardless of the size and location of the opening.

According to Voon and Ingham (2008), the lateral strength of walls is significantly affected by the height of the opening because the steeper the compression strut formed, the less efficient is the transfer of lateral forces. In contrast, Fortes and Parsekian (2017) and Calderón et al. (2017) concluded, based on the results of their tests, that for openings of similar length, differences in height do not affect the lateral capacity of the wall.

Walls are planar members that lose their continuity when openings are created and, thus, the general behavior of the walls becomes conditional on the behavior of the spandrels and piers defined by the dimensions of the openings (Carvalho and Oliveira, 1997). It is usual and relatively conservative to calculate the shear load capacity of masonry walls with openings as the sum of the capacity of its piers (Drysdale and Hamid, 2005; Voon and Ingham, 2008). Such an approach, however, ignores any frame action developed by the coupling of the piers and the spandrels (Calderón et al., 2019). In addition, that approach assumes that all piers reach their maximum capacity at the same displacement level, which can be adequate when the openings are identical and similar piers are formed. However, it may not be adequate when the piers have different aspect ratios and, consequently, different boundary conditions (Vargas et al., 2020).

Ingham et al. (2001) suggested that the identification of lateral load-bearing panels of walls with openings should be made according to illustrated in Figure 48. The hatched areas highlight the adopted piers with a height equal to the adjacent opening and whole panels since there is a shrinkage control joints over the entire height of the wall with a distance to the opening of more than 200 mm. The authors recommended ignoring the frame action imposed by the

beam's connection to treat the piers as individual cantilever walls. The authors cautioned that there was not enough experimental evidence that this approach could be suitable for walls with small openings.

Figure 48: Identification of load-bearing panels according to Ingham et al. (2001).

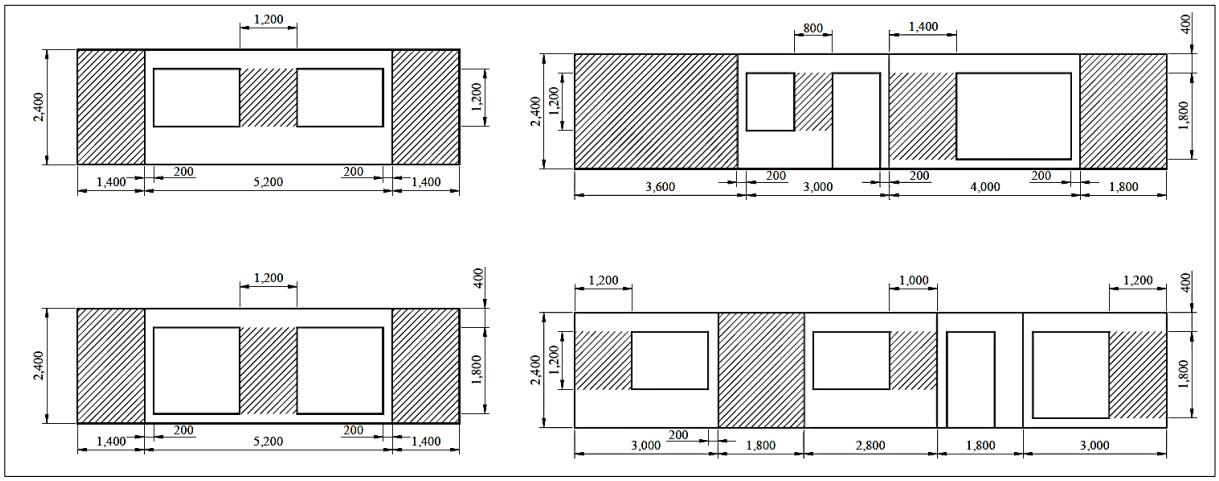

Source: Ingham et al. (2001).

Voon and Ingham (2008) tested eight shear walls with different types of openings and coupled with reinforced masonry beams. From the experimental results, the authors noticed that the available effective shear area of the piers directly affected the load distribution on the walls, increasing their capacity when the length of the piers was greater. The experimental results were used to check the approach recommended by NZS 4229 (1999) for calculating the lateral load capacity of walls. The standard says that the total capacity of a wall can be determined by the sum of the individual capacity of the piers with a vertical dimension limited to the smallest adjacent opening, as illustrated in Figure 49. The authors concluded that NZS 4229 (1999) failed to identify the resistant geometry of the wall panels, resulting in an overestimated load capacity for the wall with a small opening and more conservative as the opening height increased in the others. In walls with more than one opening, the standard underestimated the lateral load capacity by almost 90%, and, according to the authors, the extra capacity generated in the central pier should be added, given the connection made by the beam.

Yanez et al. (2004) developed an experimental study of confined masonry shear walls with different sizes of openings and reinforcement only around the openings, as shown in Figure 50. The authors concluded that the analysis methodology considering the lateral load capacity proportional to the net cross-sectional area of the walls is conservative.

Figure 49: Identification of piers on walls tested by Voon and Ingham (2008).

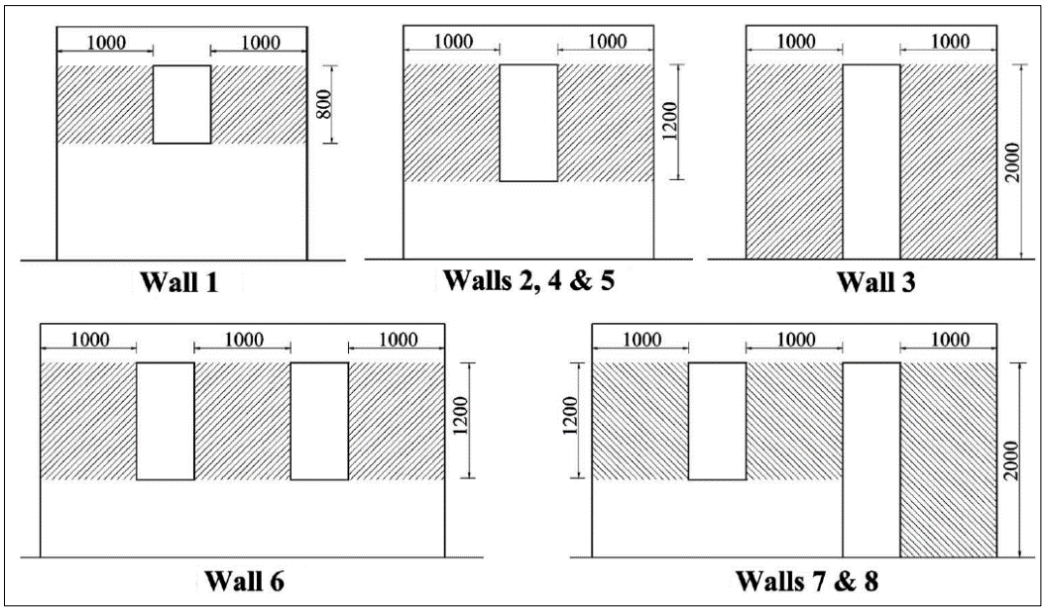

Source: Voon e Ingham (2008).

Figure 50: Arrangement of the walls tested by Yanez et al. (2004).

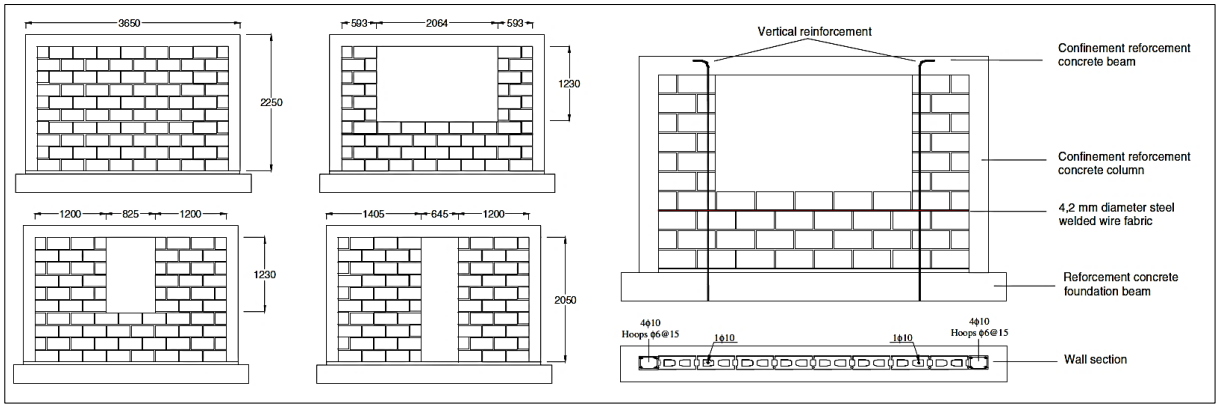

Source: Yanez et al. (2004).

Johnson and Schultz (2014) evaluated the expression of TMS 402/602 (2016) to predict the lateral load capacity of a wall experimentally tested by them. As seen in Figure 51, the wall was partially grouted with a centralized window opening, in addition to having flanges at both ends. The authors considered the total lateral capacity of the wall as the sum of the capacity of the two piers with a height equal to the opening. They did not include horizontal reinforcement because the bars were not positioned within this region. It was concluded that the standard equation adequately predicted the load capacity of the wall, presenting a ratio $V_{exp}/V_n = 1.003$. However, the authors clarify that the yielding of the horizontal bars was observed in the tests, which implies that they contributed to the capacity of the wall.

Figure 51: Detail of the wall tested by Johnson and Schultz (2014).

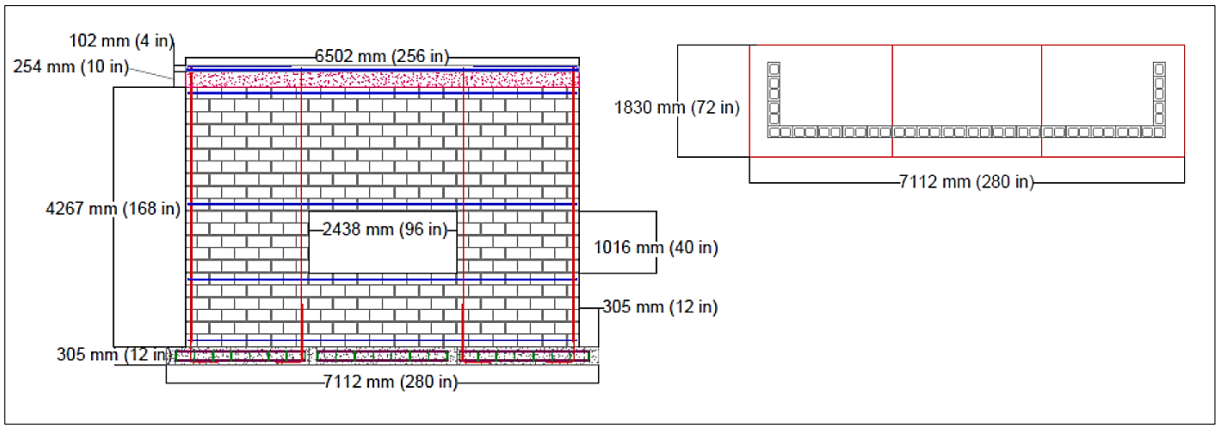

Source: Johnson e Schultz (2014).

Calderón et al. (2017) stated that the pier aspect ratio is the parameter that presented the best correlation with the results of their experimental and numerical studies. According to the authors, the lateral load capacity of walls with openings can be measured by an equivalent wall with an aspect ratio equal to that of their piers. It was observed that the shear load capacity of the walls decreased when the aspect ratio of the piers increased, but the capacity increased proportionally to the ratio of the horizontal reinforcement positioned in the region of the piers, regardless of their aspect ratio. In a later study, Calderón et al. (2019) evaluated the accuracy of the equations proposed by the CSA S304 (2014) and TMS 402/602 (2016) and by Shing et al. (1990), Psilla and Tassios (2009), and Aguilar et al. (2016) to predict the shear load capacity of the ten walls studied by them, of which three were experimentally tested, and seven were numerically modeled. The capacity of the piers, identified as depicted in Figure 52, was considered in calculating the total capacity of the walls. The authors concluded that the equation of Psilla and Tassios (2009) and TMS 402/602(2016) had the highest mean of the V_{exp}/V_n ratio and the greatest variability, while the expressions of Shing et al. (1990) and Aguilar et al. (2016) were the ones that showed the best performance and acceptable deviation.

Figure 52: Identification of piers in walls studied by Calderón et al. (2019).

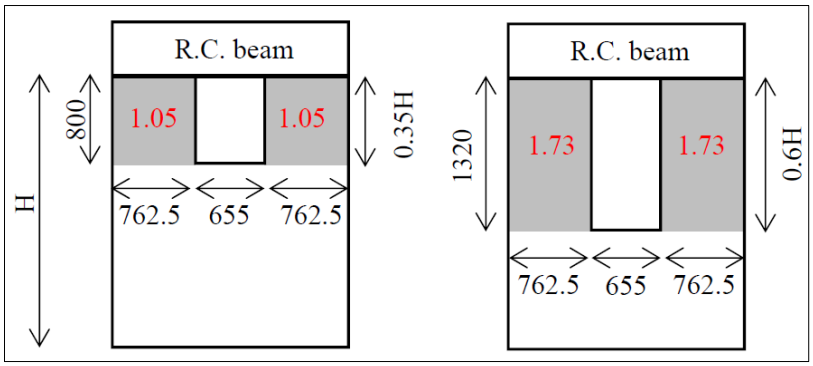

Source: Calderón et al. (2019).

Koutras and Shing (2018) commented that the equations of the American standard predicted the shear capacity of the walls of their experiment sufficiently well considering the sum of the capacity of the piers. However, the disparity between the stiffnesses of the piers and their brittle behavior can lead to an unsafe design.

3.2 DATABASE

The database used in this study is formed by 2 datasets (see Appendix C), one with 96 masonry walls simulated numerically using the finite element method (FEM) and the other with 59 experimental masonry walls reported in the literature.

3.2.1 Numerical walls

The FE model discussed in section 2.3 was adjusted and recalibrated to be used in this study. The modifications were related to the constitutive relationships of the materials available in the software, aiming to improve the hysteretic and post-peak responses. The mathematical constitutive models and the specific average properties of the materials used in the improved modeling are summarized in Table 23 and Table 24, respectively. More details regarding the adopted constitutive models are presented in Appendix A.

The model was revalidated against the experimental data from the two nominally identical wall specimens W1 and W2, and with walls D1 and D2, also nominally identical, described in section 2.2. The hysteresis and backbone curves from the experimental tests and the improved FE models are presented in Figure 53. Note that the backbone curves of the oldest FE Models are also plotted in Figure 53 to highlight the differences with the updated version.

Table 23: Constitutive models adopted to simulate the behavior of the materials.

Material	Mechanical behavior	Constitutive Model
Masonry and Concrete	Compression Pre-Peak	Hoshikuma et al. (Hoshikuma et al., 1997; Wong et al., 2013)
	Compression Post-Peak	Masonry (Park-Kent) (Priestley and Elder, 1983; Wong et al., 2013)
	Compression Softening	Vecchio 1992-A (Vecchio, 1992; Wong et al., 2013)
	Tension Stiffening	Modified Bentz 2003 (Bentz, 2000; Wong et al., 2013)
	Tension Softening	Nonlinear (Hordijk) (Hordjik et al., 1987; Wong et al., 2013)
	Cracking Criterion	Mohr-Coulomb (Stress) (Wong et al., 2013)
	Crack Slip	Masonry I (Wong et al., 2013)
	Hysteretic Response	Nonlinear with Plastic Offsets (Vecchio, 1999; Wong et al., 2013)
	Failure Criterion	Ganz (Principal Stresses) (Ganz, 1985; Wong et al., 2013)
Reinforcement	Bond	Eligehausen et al. (1983) (Eligehausen et al., 1983; Wong et al., 2013)
	Dowel Action	Tassios (Crack Slip) (He and Kwan, 2001; Wong et al., 2013)
	Buckling	Refined Dhakal-Maekawa (Wong et al., 2013; Akkaya et al., 2019)
	Hysteretic Response	Bauschinger Effect (Seckin) (Seckin, 1981; Wong et al., 2013)

Source: Author.

Table 24: Properties of materials used in the improved modeling.

Material	Parameter	Value for the material type		Reference of the used value
		(a)	(b)	
Concrete (a) Middle slabs (b) Top beam	Compressive Strength (f_c')	36.1 MPa	31.5 MPa	Test results (Fortes and Parsekian, 2017)
	Tensile Strength (f_t')	1.98 MPa	1.85 MPa	$0.33\sqrt{f_c'}$ (Wong et al., 2013)
	Initial Tangent Modulus (E_c)	33,046 MPa	30,869 MPa	$5500\sqrt{f_c'}$ (Wong et al., 2013)
	Strain at Peak Stress (ε_p)	$2.07 \cdot 10^{-3}$	$2.04 \cdot 10^{-3}$	$1.8 + 0.0075 f_c'$ (Wong et al., 2013)
	Poisson's ratio (ν)	0.15	0.15	Default value (Wong et al., 2013)
Masonry (a) Ungrouted (b) Grouted	Compressive Strength (f_m')	11.8 MPa	12.2 MPa	Test results (Fortes and Parsekian, 2017)
	Tensile Strength (f_t')	1.13 MPa	1.15 MPa	$0.33\sqrt{f_m'}$ (Wong et al., 2013)
	Joint shear strength (f_j)	0.37 MPa	0.37 MPa	Test results (Pasquantonio et al., 2020)
	Initial Tangent Modulus (E_m)	18,305 MPa	18,496 MPa	$3320\sqrt{f_m'} + 6900$ (Wong et al., 2013)
	Strain at Peak Stress (ε_p)	$1.29 \cdot 10^{-3}$	$1.32 \cdot 10^{-3}$	$(2000 f_m')/E_m$ (Wong et al., 2013)
	Poisson's ratio (ν)	0.15	0.15	Default value (Wong et al., 2013)
Reinforcement (a) Ø9.5 mm (b) Ø4.2 mm	Yield Strength (f_y)	540 MPa	743 MPa	Test results (Fortes and Parsekian, 2017)
	Ultimate Strength (f_u)	742 MPa	812 MPa	Test results (Fortes and Parsekian, 2017)
	Elastic Modulus (E_s)	203,512 MPa	222,799 MPa	Test results (Fortes and Parsekian, 2017)

Source: Author.

Figure 53: Experimental and numerical response of walls W1, W2, D1 and D2.

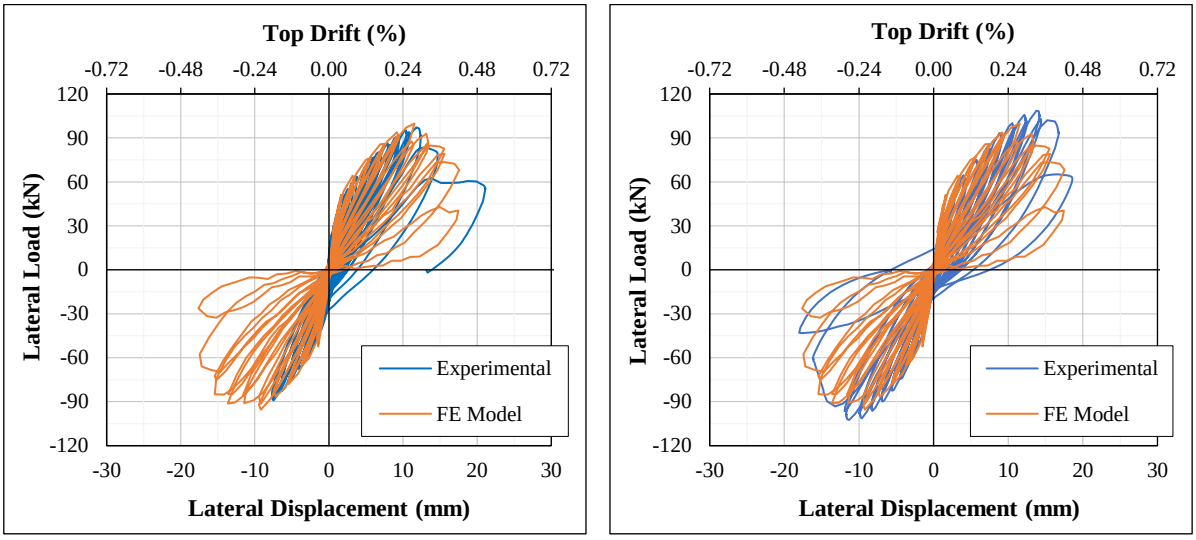

(a) Hysteresis curves of wall W1

(b) Hysteresis curves of wall W2

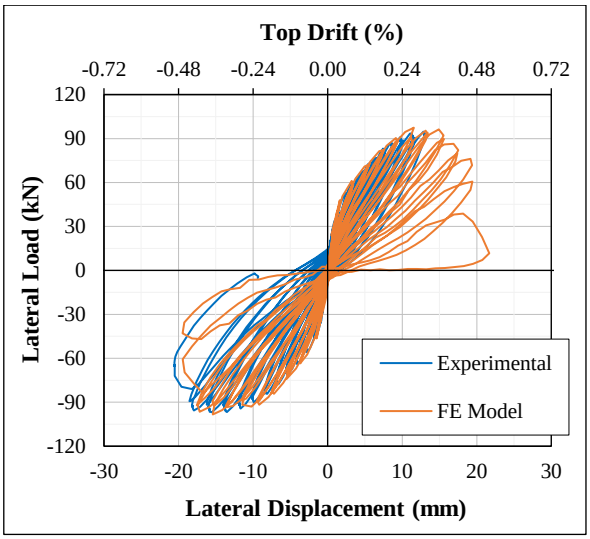

(c) Hysteresis curves of wall D1

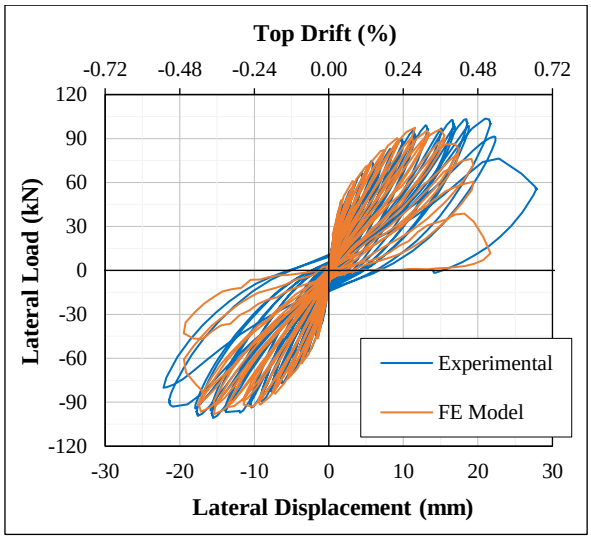

(d) Hysteresis curves of wall D2

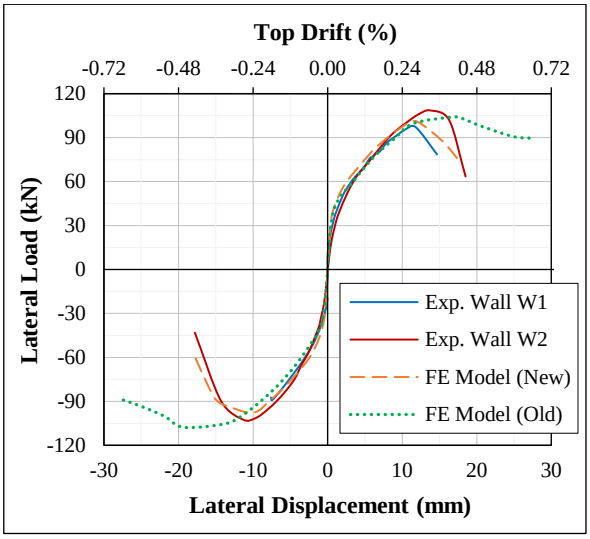

(e) Backbone curves of walls W1 and W2

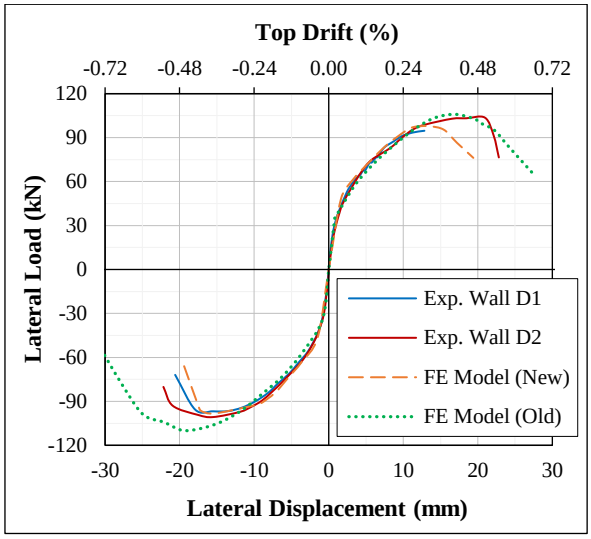

(f) Backbone curves of walls D1 and D2

Source: Author.

As can be seen in Figure 53, there was good agreement between the backbone curves of the improved FE models and the experimental walls, with remarkable enhancement in capturing the strength and stiffness degradation at the post-peak stage when compared to the oldest models. Looking at the hysteresis curves, the improved model simulated the loops well, mainly up to the peak load, although some non-agreements are still noted in the post-peak stages, especially for the residual deformations. As explained by Elmeligy et al. (2021), these divergences can be attributed to brittleness and significant anisotropy in the ungrouted parts, which induces some randomness to the post-peak response. This explanation is reinforced by the differences observed when comparing the hysteresis of the experimental walls W1 and W2, and D1 and D2, which are nominally identical but have different post-peak responses.

The average experimental maximum lateral load and the average corresponding lateral displacement of walls W1-2 were 99.3 kN and 11.1 mm, respectively. The FE model for these walls resulted in the average peak load of 99.5 kN and the average displacement of 10.8 mm, which were 0.2% higher and 2.6% smaller, respectively than the experimental results. For walls D1-2, the experimental results for the average peak load and the average corresponding displacement were 98.9 kN and 16.2 mm, respectively, against 98.8 kN (-0.1%) and 14.9 mm (-8.0%) obtained from the numerical models.

The experimental walls failed predominantly in shear with diagonal tensile cracks. This behavior was also observed in the improved numerical models in a similar pattern to that discussed previously in section 2.3.2 and illustrated in Figure 33 and Figure 34. Therefore, after comparing the lateral load capacity, lateral displacement at the top of the wall, and crack pattern against the data of the experimental tests, the improved FE model can be considered able to represent the walls' responses adequately.

After validation, other ninety-six walls were modeled aiming to assess the prediction of the SLC of PGMW varying the parameters included in the existing shear expressions or for which their influence is still questionable by researchers. Taking the experimental walls as the base, the simulated walls had changes in parameters such as the masonry compressive strength, the vertical and horizontal grouting and reinforcement, the applied axial load, the wall aspect ratio, and the dimensions of openings. A detailed list of the simulated walls is presented in Table 41 in Appendix C.

The nominal flexural load capacity of all walls was calculated to ensure shear failure. The calculation was done as explained in section 3.1.1, including the contributions of the compression reinforcement and the weight of the walls, accounted for with the axial load. Even in the worst case, the nominal flexural load capacity was at least 43% higher than the maximum lateral load reached for that wall. In addition, the failure mode of all walls was examined and confirmed to be a shear failure because of the diagonal shear cracks, the absence of the vertical reinforcement yielding, and because toe crushing was not observed.

The reduced-scale numerical walls were converted to equivalent full-scale walls to proceed with the analyses and to be used in the assessment of the shear strength prediction equations. The simple model similarity approach (Tomaževič and Velechovsky, 1992) was employed, in which the geometric properties are scaled by a factor of S_L (the ratio of the reduced-scale to the equivalent full-scale size), areas and forces are scaled by a factor of S_L^2,

and the material strengths are scaled by a factor of 1 (Long, 2006; Dillon and Fonseca, 2015; Izquierdo et al., 2021). Taking the dimensions in the length for a block plus a joint in the reduced-scale as 185 + 5 = 190 mm, and in the full-scale as 390 + 10 = 400 mm, the factor S_L (190/400) = 0.475 for the walls in this study.

3.2.2 Experimental walls from the literature

Some criteria were established for the data collection from tests reported in the literature to avoid inconsistencies and high variation. The scope was restricted to masonry walls made of concrete blocks, partially grouted, subjected to in-plane reverse cyclic load or phased-sequential, quasi-static loading rate, which failed in a shear mode. Since the first numerical walls modeled considered half-scale walls experimental data, another criterion was to choose experimental walls constructed with full-scale units.

The data reported by Meli et al., (1968), Schultz (1996), Minaie et al. (2010), Elmapruk and ElGawady (2010), Nolph and ElGawady (2012), Hoque and Lissel (2013), and Rizaee and Lissel (2015) were selected to compose the experimental database. The data were extracted from the respective research and checked in the database assembled by Dillon and Fonseca (2015), and Izquierdo and Cruz-Noguez (2021). A detailed list of the selected walls is presented in Table 42 in Appendix C.

3.3 SHEAR LOAD CAPACITY PREDICTION OF UNPERFORATED PARTIALLY GROUTED MASONRY WALLS

3.3.1 Equations from the literature

Among the several equations presented and detailed in section 3.1.2, those proposed by Matsumura (1988), CSA S304 (2014), Oan and Shrive (2014), Dillon and Fonseca (2015), TMS 402/602 (2016), Seif ElDin et al. (2019a), and Izquierdo et al. (2021) were chosen to evaluate the shear load capacity of the walls. The equations are summarized in Table 25 showing separately the contribution of the masonry (V_m), the axial load (V_p) and the reinforcement (V_r) to the nominal SLC of the wall. The equation of Dillon and Fonseca (2015) presented in Table 25 is the one specific for PGMW, and the equation of Izquierdo et al. (2021) is the one that had the best performance among the various proposed.

Table 25: Factored contribution in shear load capacity equations.

Equation	V_m – Masonry	V_p – Axial Load	V_r – Reinforcement
Matsumura (1988)	$k_u k_\rho \left(\frac{0.76}{h_w/d_v + 0.7} + 0.012\right) 0.875 b_w d_v \sqrt{f'_m}$	$0.175\sigma_0 b_w d_v$	$0.1575\gamma\delta b_w d_v \sqrt{\rho_h f_{yh} f'_m}$
CSA S304 (2014)	$\gamma_g \left[0.16\left(2 - \frac{h_e}{d_v}\right) b_w d_v \sqrt{f'_m}\right]$	$\gamma_g(0.25P)$	$0.6 A_{hb} f_{yh} \frac{d_v}{s_h}$
Oan and Shrive (2014)	$\gamma_g \left[0.16\left(2 - \frac{h_e}{d_v}\right) b_w d_v \sqrt{f'_m}\right]$	$0.27P$	$0.05 A_v f_{yv}$
Dillon and Fonseca (2015)	$0.083\left(1.1 + 0.9\frac{V s_{gv}}{M}\right) A_{eh}\sqrt{f'_m}$	$0.15P$	$0.12\left[\left(\frac{A_{vib} f_{yv}}{s_v}\right) d_v + \left(\frac{A_{hb} f_{yh}}{s_h}\right) h_w\right]$
TMS 402/602 (2016)	$0.083\gamma_g \left[\left(4 - 1.75\frac{h_e}{d_v}\right) A_{eh}\sqrt{f'_m}\right]$	$\gamma_g(0.25P)$	$\gamma_g \left(0.5 A_{hb} f_{yh} \frac{d_v}{s_h}\right)$
Seif ElDin et al. (2019a)	$\gamma_g k_1 \delta \left[0.02\rho_v f_{yv} + 0.14\left(2.5 - \frac{h_e}{d_v}\right)\right] b_w d_v \sqrt{f'_m}$	$\gamma_g k_1 \delta (P \tan\theta)$	$k_2 \delta \left(0.4 \frac{A_{hb}}{s_h} d_e f_{yh}\right)$
Izquierdo et al. (2021)	$-0.0205 h_w + 0.0337 l_w + 6 f_{mt}$	$0.289P$	$0.0917 A_{vi}$

Note: The shear span ratio presented originally in some equations as $M/(\mathrm{V}d_v)$ was rewritten here as h_e/d_v, where $h_e = M/\mathrm{V}$.

Source: Author.

3.3.2 New proposed equation

The proposed equation is focused on predicting the nominal SLC of PGMW made with hollow concrete masonry units. The influence of various parameters was included in the equation adapting terms suggested in previous studies and through mathematical regressions using the results of the walls in the database. The general form is given in Equation 39.

$$V_n = k_{gv} k_{gh} V_m + V_p + V_{rv} + V_{rh} \qquad \text{Eq. 39}$$

a) Contribution of the vertical reinforcement

It was possible to model walls without external axial loading and any horizontal reinforcement to isolate the influence of the masonry in the shear strength, but the presence of vertical reinforcement was inevitable due to the necessity to ensure that the wall would not fail in flexure. Hence, the first step was to adopt a term for the contribution of the anchorage of the vertical reinforcement, Equation 40, which was based on the expression of Oan and Shrive (2014). The authors considered the contribution of dowel action as $0.05 A_v f_{yv}$ after some modifications to the term suggested by Shing et al. (1990), which was $0.0217 \rho_v f_{yv} A_{eh} \sqrt{f'_m}$. Oan and Shrive (2014) simplified the term using directly $A_v f_{yv}$ instead of the $\rho_v f_{yv} A_{eh}$ and multiplying 0.0217 by the lowest f'_m found in the dataset used by them.

$$V_{rv} = 0.02 A_v f_{yv} \sqrt{f'_m} \quad \left(\text{in N, for } f_{yv} \text{ and } f'_m \text{ in MPa, and } A_v \text{ in mm}^2\right) \qquad \text{Eq. 40}$$

b) Contribution of the masonry

The next step was, therefore, to study the contribution of the masonry. Like most of the existing equations, proportionality was assumed between the shear capacity and $\sqrt{f'_m}$. However,

unlike others, the effective horizontal cross-sectional area of masonry (A_{eh}) was adopted instead of the gross area $(b_w d_v)$ since it permits greater precision in the calculation of the actual section, which may be significantly impacted by the number of voids in PGMW. Here, A_{eh} is defined as the area comprising all the mortared area and the area of grouted voids. Moreover, f'_m is standardized with a height-to-thickness ratio of prism equal to 5 as used by some design codes (BS 5628-2, 2000; AS 3700, 2011; CSA S304, 2014). As mentioned by Dillon and Fonseca (2015), researchers (Hegemier et al., 1978; Boult, 1979) have revealed that the ratio of 5 better reflects the compressive strength of the masonry in the field. Thus, the correction factor k_c, Equation 41 (Dillon and Fonseca, 2015), must be used multiplying f'_m to adjust different prism height-to-thickness ratios to 5:1 before proceeding with all steps in the proposed equation.

$$k_c = 1 - 0.058\left(5 - {}^{h}/_{t}\right)^{1.07} \qquad \text{Eq. 41}$$

The equations proposed by TMS 402/602 (2016), CSA S304 (2014), and Oan and Shrive (2014) limit the shear span ratio h_e/d_v in a range from 0.25 to 1.0, whereas Seif ElDin et al. (2019a) impose a range from 1.0 to 2.0 as a limit. The upper limit of 1.0 may overestimate the SLC of slender walls and, in contrast, the bottom limit of 1.0 may underestimate the SLC of squat walls. To avoid false predictions, the suggestion for the new proposed equation is a range for the shear span ratio from 0.25 to 2.0, which was investigated using the simulated walls 9 to 21. These walls had the same masonry strength and the same vertical grouting and reinforcement, except wall 11; none of them had external axial loading nor any horizontal grouting and reinforcement, thus the aspect ratio was the main variable. The graph in Figure 54 correlates the shear span ratio with the contribution of the masonry V_m normalized by $A_{eh}\sqrt{f'_m}$, taking $V_m = V_{max,avg} - V_{rv}$ and assuming $d_v = l_w$.

Figure 54: Relation between the normalized contribution of the masonry and the shear span ratio.

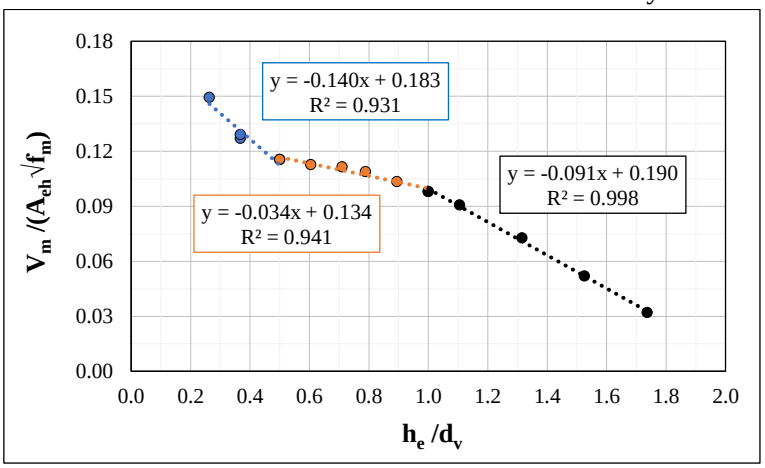

Source: Author.

As shown in Figure 54, the tendency of the correlation between the contribution of the masonry and the shear span ratio was well fitted by separating it into three linear regression curves. Therefore, the contribution of the masonry to the nominal SLC should be calculated using Equation 42 depending on the value of the shear span ratio, Equation 43. It is strongly recommended also to verify the flexural capacity of the wall, especially for walls with shear span ratios higher than 1.5 since for this condition the wall may already present a mixed failure mode tending to more flexural dominated behavior with increasing ratio.

$$V_m = \beta_r A_{eh} \sqrt{f'_m} \quad (\text{in N, for } f'_m \text{ in MPa, and } A_{eh} \text{ in mm}^2) \qquad \text{Eq. 42}$$

$$\beta_r = \begin{cases} 0.183 - 0.14(h_e/d_v) & if \quad 0.25 \leq h_e/d_v < 0.5 \\ 0.134 - 0.034(h_e/d_v) & if \quad 0.5 \leq h_e/d_v < 1.0 \\ 0.19 - 0.091(h_e/d_v) & if \quad 1.0 \leq h_e/d_v < 2.0 \end{cases} \qquad \text{Eq. 43}$$

c) Contribution of the horizontal grouting

Analyzing the response of the simulated walls 38 to 42, the SLC increases as the spacing between the horizontal grouting decreases, Figure 55. Therefore, the factor k_{gh} multiplying the masonry contribution (V_m) is suggested to account for this effect using Equation 44. As detailed in Table 41, these walls were modeled without external axial loading and any horizontal reinforcement, keeping the other aspects constant, so that only the influence of horizontal grouting could be evaluated. The average spacing between the horizontal grouting $s_{gh,avg}$ should be calculated as h_w/n_{ugph}, where n_{ugph} is the number of the horizontal ungrouted panels formed along the height of the wall h_w.

$$k_{gh} = 1.633 - 0.079 \ln(s_{gh,avg}) \geq 1.0 \quad (for\ s_{gh,avg} \text{ in mm}) \qquad \text{Eq. 44}$$

Figure 55: Relation between the normalized contribution of the masonry and the spacing between the horizontal grouting.

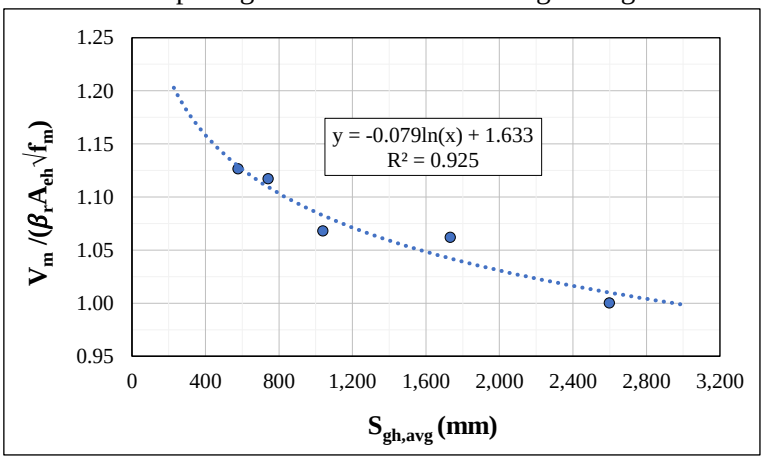

Source: Author.

d) Contribution of the axial load

The interrelation between variables makes the prediction of the shear behavior of masonry walls all the more difficult. Researchers (Ramírez et al., 2016; Hung et al., 2018; Sandoval et al., 2018; Calderón et al., 2021c) have shown that the effect of axial loading on the shear strength is less pronounced as the aspect ratio increases: however, various existing shear equations ignore this interaction. Zhang et al. (2021) suggested accounting for this effect using a factor based on the inverse of the effective aspect ratio of the wall. Here, the contribution of the axial loading, Equation 45, was included in the new proposed equation by the horizontal component of the diagonal compression strut (NZS 4230, 2004; Voon and Ingham, 2007; Seif ElDin et al., 2019a). The horizontal component can be calculated as $P\,tan\,\theta$ since the compression strut is formed between the points of the applied axial load and the resultant compression force of the flexural compression zone (Seif ElDin et al., 2019a). However, considering the dispersion of the strut in a fan shape and the uplift effect caused by the lateral load, the contribution of the axial load should be reduced by 0.4 and, simultaneously, P should be taken as 0.9 times the dead load to avoid overestimation. This assumption agrees with the results of Chapter 2, in which it was found that the SLC of a wall was only slightly sensitive to the axial stress. For simplicity, $tan\,\theta$ can be estimated as $0.4l_w/h_w$ (Seif ElDin et al., 2019a).

$$V_p = 0.4P\,tan\,\theta \quad \text{(in N, for } P \text{ in N)} \qquad \text{Eq. 45}$$

e) Contribution of the horizontal reinforcement

Concerning the horizontal reinforcement, the results of simulated walls 1 and 27 confirm that the horizontal bar placed in the top bond beam does not contribute to the wall shear capacity since the difference between these walls was only this aspect and the average maximum lateral load was the same. Similar findings are reported by Blondet et al. (1989) and Shing et al. (1990).

To avoid unconservative predictions, the influence of the horizontal reinforcement was carefully included in the new proposed equation. It was assumed that horizontal reinforcement provides the same behavior as the vertical reinforcement restricting the opening of cracks and transferring tensions between the masonry parts since diagonal cracks are usually formed at 45° (Dillon and Fonseca, 2015). Thus, based in Equation 40, the contribution of the horizontal reinforcement would be calculated as $0.02A_h f_{yv}\sqrt{f'_m}$. Nevertheless, the results of simulated walls 1, 24, 25, 26, 28, and 29 show that this contribution is limited by a certain reinforcement ratio, as also stated by others (Fattal, 1993; Elmapruk and ElGawady, 2010; Nolph and ElGawady, 2012). There is a small variation decreasing the average maximum lateral load when

the net horizontal reinforcement ratio decreased from 0.14% in wall 1 to 0% in wall 28, and from 0.18% in wall 25 to 0% in wall 29, but it did not increase when the net horizontal reinforcement ratio increased from 0.14% in wall 1 to 0.25% in wall 24, and from 0.18% in wall 25 to 0.25% in wall 26. Therefore, the contribution of the horizontal reinforcement (V_{rh}) should be estimated with Equation 46 using the net horizontal reinforcement ratio instead of the area to ease the imposition of the maximum reinforcement ratio, which is suggested here as 0.20%. It is important to state that the term V_{rh} is based on the results of walls with horizontal reinforcement in bond beams and hooked around the vertical bars, and does not include bed joint reinforcement.

$$V_{rh} = 0.02\rho_h A_{ev} f_{yh}\sqrt{f'_m} \quad \left(\text{in N, for } f_{yh} \text{ and } f'_m \text{ in MPa, and } A_{ev} \text{ in mm}^2\right) \qquad \text{Eq. 46}$$

f) Contribution of the vertical grouting

The influence of the vertical grouting spacing was also considered since it was found that the shear capacity increases as the spacing decreases (Elmapruk and ElGawady, 2010; Nolph and ElGawady, 2012; Elmapruk et al., 2020). The experimental dataset was used to develop the factor k_{gv}, Equation 47, that accounts for this behavior multiplying the masonry contribution V_m. The walls were grouped according to the vertical grouting spacing and then an average contribution of the masonry V_m was plotted, as shown in Figure 56, by normalizing it by $k_{gh}\beta_r A_{eh}\sqrt{f'_m}$, taking $V_m = V_{max,avg} - V_p - V_{rv} - V_{rh}$ and assuming $d_v = l_w$. The average spacing between the vertical grouting $\left(s_{gv,avg}\right)$ should be calculated as l_w/n_{ugpv}, where n_{ugpv} is the number of the vertical ungrouted panels formed along the length of the wall l_w.

$$k_{gv} = 5.539 - 0.583\ln\left(s_{gv,avg}\right) \quad \left(for\ s_{gv,avg} \text{ in mm}\right) \qquad \text{Eq. 47}$$

Figure 56: Relation between the normalized contribution of the masonry and the spacing between the vertical grouting.

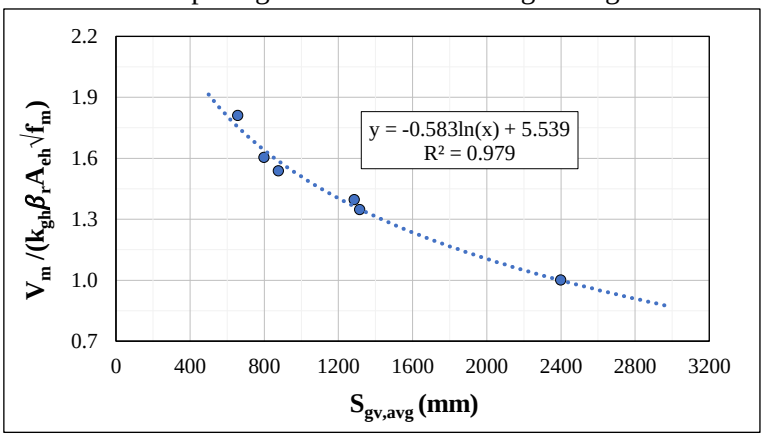

Source: Author.

g) Complete expression

Finally, the complete expression for the nominal SLC including the contributions of masonry, aspect ratio, horizontal and vertical grouting, horizontal and vertical reinforcement, and axial loading is presented in Equation 48. A limit for the SLC adapted from that of CSA S304 (2014) and equal to $0.4A_{eh}\sqrt{f'_m}$ was checked for all 155 walls in the datasets, but was not the critical value; therefore, it was not imposed for Equation 48.

$$V_n = k_{gv}k_{gh}\beta_r A_{eh}\sqrt{f'_m} + 0.4P\,tan\,\theta + 0.02A_v f_{yv}\sqrt{f'_m} + 0.02\rho_h A_{ev} f_{yh}\sqrt{f'_m} \quad \text{Eq. 48}$$

To show the relevance of each term in the total predicted values, the factored contribution of the masonry (including the horizontal and vertical grouting), axial load, and vertical and horizontal reinforcement to the nominal SLC of the wall is presented in Table 43 and Table 44 in Appendix D for the numerical and the experimental datasets. The minimum, maximum, and average percentual values for both datasets are summarized in Table 26.

Table 26: Summary of the factored contributions in the percentage of total nominal capacity.

Result	Numerical Dataset				Experimental Dataset				Average			
	$k_{gv}k_{gh}V_m$	V_p	V_{rv}	V_{rh}	$k_{gv}k_{gh}V_m$	V_p	V_{rv}	V_{rh}	$k_{gv}k_{gh}V_m$	V_p	V_{rv}	V_{rh}
Minimum	37%	0%	13%	0%	53%	0%	8%	0%	45%	0%	10%	0%
Maximum	80%	25%	62%	13%	92%	31%	33%	6%	86%	28%	47%	9%
Average	60%	9%	29%	2%	69%	16%	13%	2%	64%	12%	21%	2%

Source: Author.

The masonry and horizontal reinforcement terms provide the most and least important contributions to the SLC in all scenarios analyzed. The axial load and vertical reinforcement terms take turns in their importance depending on each case. Considering an average of the minimum and maximum contributions between the two datasets, the masonry term ranged from 45% to 86%, the vertical reinforcement term contributed with 10% to 47%, the axial load term varied from 0% to 28%, and the horizontal reinforcement term contributed with 0% to 9%.

3.3.3 Accuracy of the equations

The accuracy of the equations on predicting the SLC of the walls without openings was evaluated in terms of the minimum, maximum, average, standard deviation, coefficient of variation (CoV), 5th percentile, and 95th percentile of the ratio between the predicted value ($V_{n,pred}$) and the average maximum lateral load ($V_{max,avg}$) for each wall. Note that if $V_{n,pred}/V_{max,avg}$ < 1.0, it means underprediction, and if $V_{n,pred}/V_{max,avg}$ > 1.0, it means overprediction. The 5th percentile represents the value exceeded by 95% of the samples whereas the 95th percentile is the value exceeded by only 5% of the samples. These values can also be interpreted as the lower

and upper limits, respectively, of a range contained 95% of the samples. Furthermore, the Mean Error (ME) and the Root Mean Squared Error (RMSE) were used to designate the levels of accuracy and precision of the shear equations. Values of the ME and RMSE closer to zero indicate smaller errors, and while the RMSE is always a positive number, the ME can be negative or positive, which means over or underestimation, respectively.

The results for the numerical dataset (walls 1 to 58 in Table 41) and for the experimental dataset (walls 1 to 59 in Table 42) using each of the shear equations are summarized statistically in Table 27 and Table 28, and presented graphically in Figure 57 and Figure 58, respectively. These results do not consider any strength-reduction factors.

Table 27: Statistical comparison between the shear equations for the numerical dataset.

Equation	$V_{n,pred}/V_{max,avg}$							ME	RMSE
	Min.	Max.	Avg.	STDV	CoV (%)	5th PCTL	95th PCTL	(kN)	(kN)
Matsumura (1988)	0.46	1.04	0.71	0.18	25.4	0.51	0.99	224.7	201.4
CSA S304 (2014)	0.53	1.46	0.85	0.27	32.1	0.54	1.30	62.5	148.4
Oan and Shrive (2014)	0.68	1.45	0.88	0.10	11.7	0.79	0.99	62.3	75.2
Dillon and Fonseca (2015)	0.75	1.26	1.03	0.08	8.1	0.91	1.12	-12.8	42.2
TMS 402/602 (2016)	0.98	1.85	1.29	0.20	15.6	1.03	1.65	-143.7	175.6
Seif ElDin et al. (2019a)	0.67	1.73	0.92	0.20	21.8	0.71	1.35	41.2	103.0
Izquierdo et al. (2021)	0.95	1.49	1.11	0.10	9.0	1.00	1.29	-46.8	60.2
Proposed Equation	0.86	1.10	0.99	0.05	4.7	0.92	1.07	2.0	25.1

Source: Author.

Table 28: Statistical comparison between the shear equations for the experimental dataset.

Equation	$V_{n,pred}/V_{max,avg}$							ME	RMSE
	Min.	Max.	Avg.	STDV	CoV (%)	5th PCTL	95th PCTL	(kN)	(kN)
Matsumura (1988)	0.49	1.78	1.02	0.25	24.3	0.63	1.48	1.1	58.9
CSA S304 (2014)	0.62	1.84	1.16	0.27	23.4	0.73	1.61	-30.4	68.2
Oan and Shrive (2014)	0.65	1.64	1.15	0.24	21.0	0.76	1.51	-25.4	58.7
Dillon and Fonseca (2015)	0.46	1.51	0.90	0.22	24.9	0.52	1.25	29.8	65.6
TMS 402/602 (2016)	0.72	1.59	1.17	0.23	19.8	0.78	1.56	-31.3	59.4
Seif ElDin et al. (2019a)	0.68	1.80	0.99	0.22	21.9	0.72	1.47	8.8	43.1
Izquierdo et al. (2021)	0.54	1.96	1.03	0.23	22.2	0.79	1.49	1.5	45.4
Proposed Equation	0.76	1.39	1.05	0.15	14.0	0.81	1.28	-6.0	33.9

Source: Author.

Figure 57: Results of the shear equations for the numerical dataset.

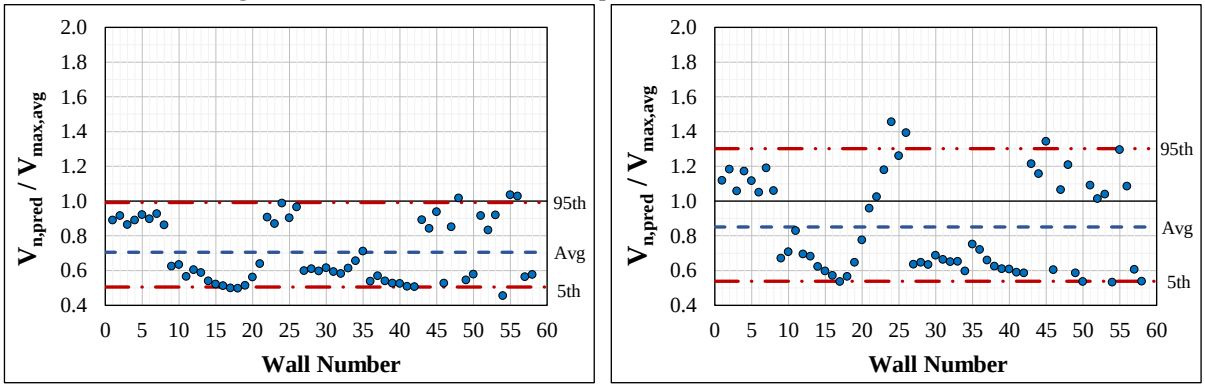

(a) Matsumura (1988) (b) CSA S304 (2014)

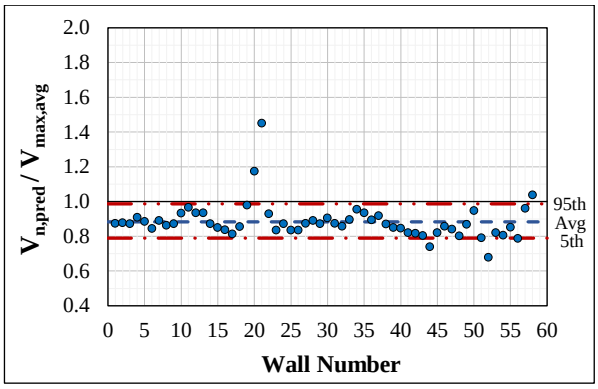

(c) Oan and Shrive (2014)

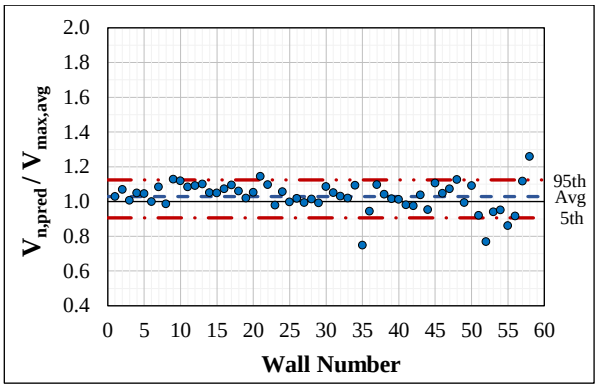

(d) Dillon and Fonseca (2015)

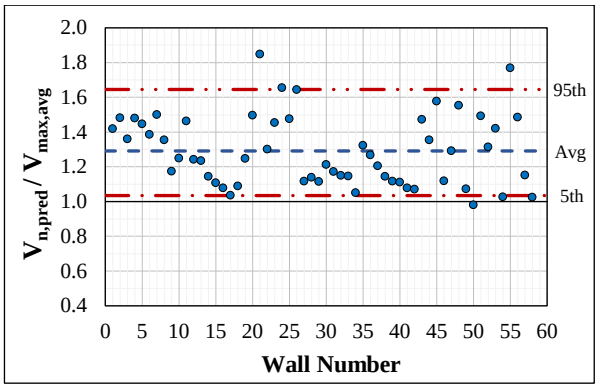

(e) TMS 402/602 (2016)

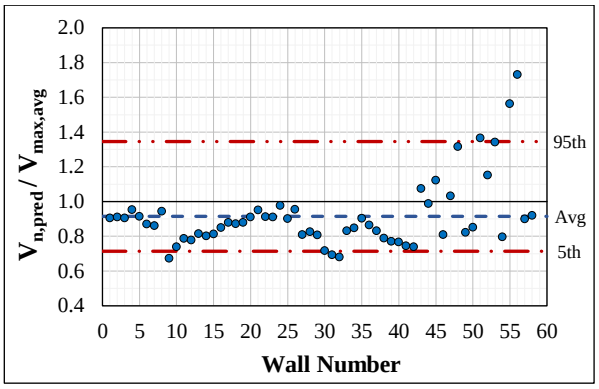

(f) Seif ElDin et al. (2019a)

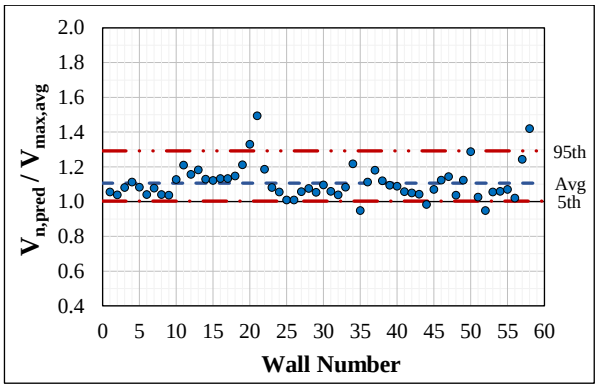

(g) Izquierdo et al. (2021)

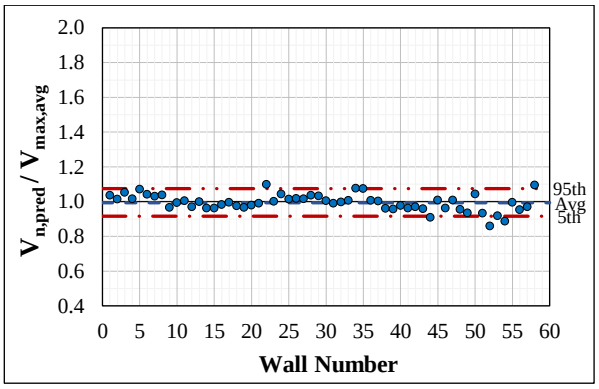

(h) Proposed Equation

Source: Author.

Figure 58: Results of the shear equations for the experimental dataset.

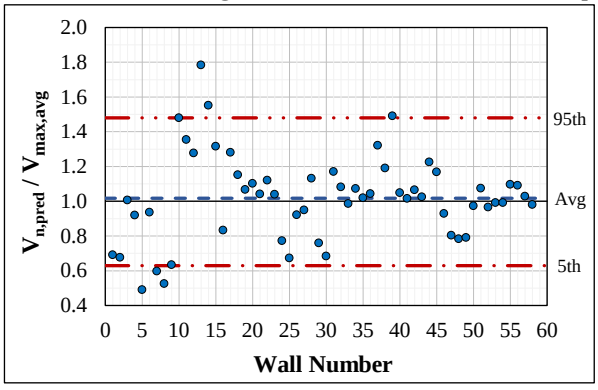

(a) Matsumura (1988)

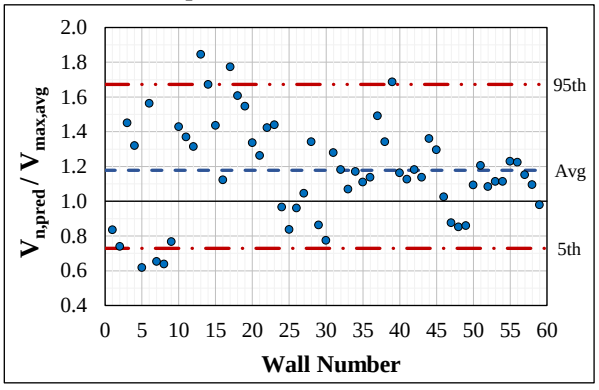

(b) CSA S304 (2014)

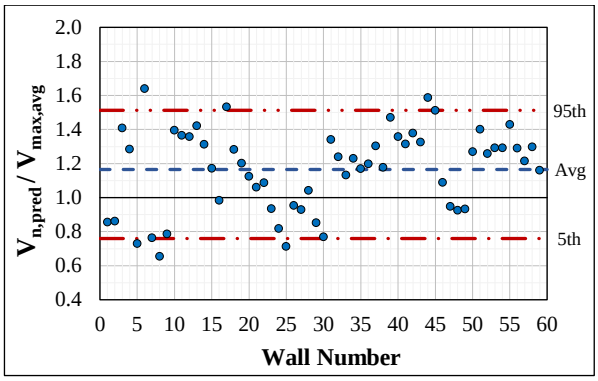

(c) Oan and Shrive (2014)

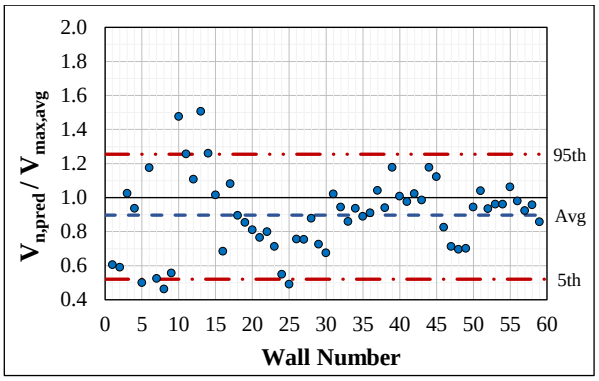

(d) Dillon and Fonseca (2015)

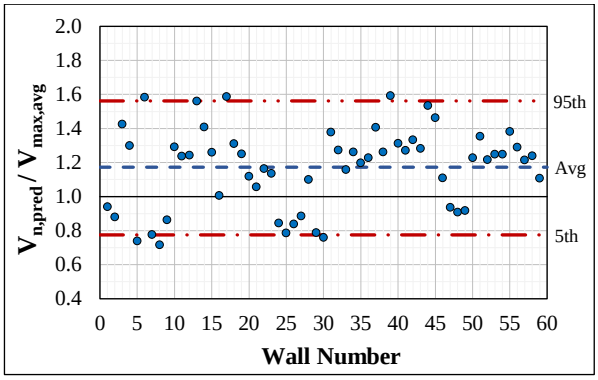

(e) TMS 402/602 (2016)

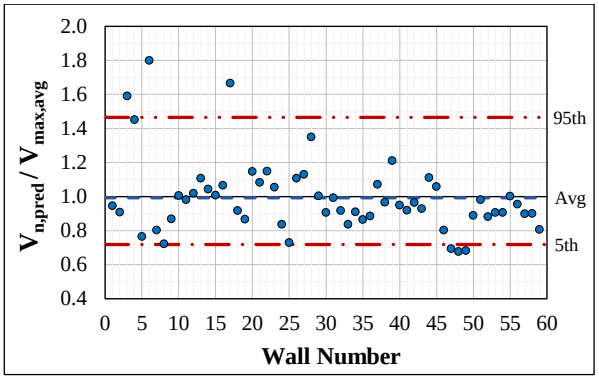

(f) Seif ElDin et al. (2019a)

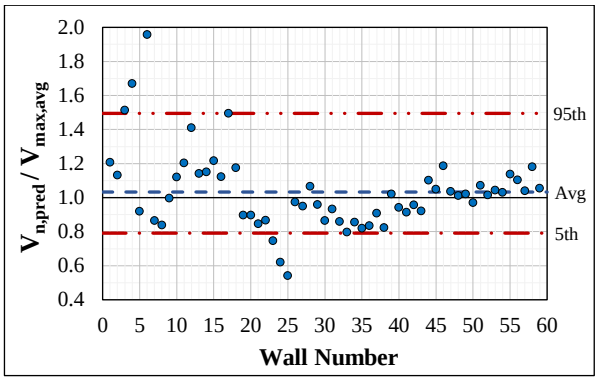

(g) Izquierdo et al. (2021)

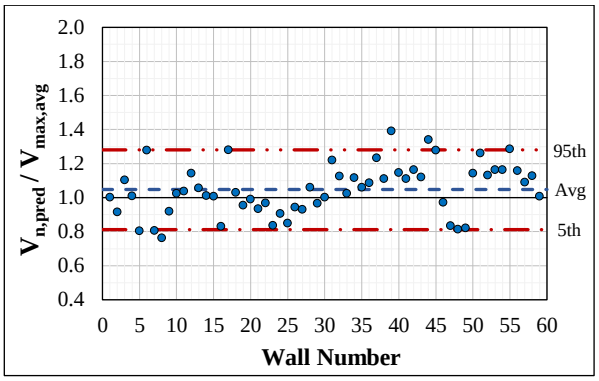

(h) Proposed Equation

Source: Author.

h) Discussion of the results for the numerical dataset

The results of the walls from the numerical dataset show that the code-based shear equations had the worst performance. The equation of TMS 402/602 (2016) estimated the SLC of walls with an average ratio $V_{n,pred}/V_{max,avg}$ of 1.29, with the 5th percentile value of $V_{n,pred}/V_{max,avg}$ equal to 1.03, which implies that most of the walls had their shear capacity overpredicted. This overestimation was more prominent for walls with horizontal reinforcement (walls 1 to 8, 22 to 26, 43 to 45, 47, 48, 51 to 53, 55, and 56) and walls with a high h_e/d_v (walls 20 and 21). The ME equal to -143.7 kN for the American code was the highest negative value among all equations, which indicates many unsafe predictions.

The average ratio $V_{n,pred}/V_{max,avg}$ calculated as 0.85 using the equation of CSA S304 (2014) was apparently safe, but the Canadian standard had the greatest dispersion among all equations. This is shown by the highest value of CoV (32.1%) and the highest range between the 5th percentile (0.54) and 95th percentile (1.30) of the ratio $V_{n,pred}/V_{max,avg}$. Also, the high value for the RMSE (148.4 kN) confirms the low precision of the equation, which was affected mainly by the contribution of the horizontal reinforcement; the SLC was over and under predicted, respectively, for walls with and without reinforcement.

Contrary to the equation of TMS 402/602 (2016), the equation of Matsumura (1988) estimated the shear capacity of most of the walls on the safe side, i.e., the 95th percentile value of $V_{n,pred}/V_{max,avg}$ was equal to 0.99. Nevertheless, the low precision of the equation was also strongly affected by the presence or absence of horizontal reinforcement. The good predictions for the walls with horizontal reinforcement (walls 1 to 8, 22 to 26, 43 to 45, 47, 48, 51 to 53, 55, and 56) can be considered as "false positives" since the predictions for the walls without horizontal reinforcement were at least 30% smaller than expected.

The equation of Seif ElDin et al. (2019a) estimated conservatively the SLC of walls with $h_e/d_v < 1.0$, but overestimated the SLC in some cases of walls with $h_e/d_v > 1.0$, specifically for walls with horizontal reinforcement (walls 51 to 53, 55, and 56). This fact caused a large difference between the 5th and 95th percentiles of the ratio $V_{n,pred}/V_{max,avg}$. It appears that the overestimation of the contribution of the horizontal reinforcement was offset by the underestimation of the contribution of the masonry in walls with small h_e/d_v since this equation imposes $h_e/d_v \geq 1.0$. The SLC of Wall 48 is overpredicted even with $h_e/d_v < 1.0$; in that case the high estimation was caused by the greater amount of horizontal reinforcement.

The equation of Oan and Shrive (2014) and the equation of Izquierdo et al. (2021) predicted the SLC of the walls with an average error of 10%, and with a CoV of less than 12%. An important difference between the results of these two equations is the lower and upper bounds of the predictions, i.e., the equation of Oan and Shrive (2014) estimated most of the shear walls capacity with $V_{n,pred}/V_{max,avg} < 1.0$ (95th percentile equal to 0.99) whereas the equation of Izquierdo et al. (2021) estimated it with $V_{n,pred}/V_{max,avg} > 1.0$ (5th percentile equal to 1.0). Neither equation estimated the shear capacity of walls 20 and 21 accurately, which had a high aspect ratio.

The equation of Dillon and Fonseca (2015) gave the best predictions compared to the other equations. The SLC of the walls was estimated with an average ratio $V_{n,pred}/V_{max,avg}$ of

1.03 with low variation, confirmed by a CoV of 8.1% and the 5th and 95th percentiles being equal to 0.91 and 1.12, respectively. Also, this equation resulted in small errors, with results of ME and RMSE equal to -12.8 kN and 42.2 kN, respectively. Walls 35, 52, and 58 had their shear capacity estimated out of the range between the 5th and 95th percentiles; wall 35 did not have internal vertical reinforcement, wall 52 had high masonry compressive strength, and wall 58 had a high amount of vertical reinforcement.

The proposed equation has the best statistical indicators among all the equations examined. The average ratio $V_{n,pred}/V_{max,avg}$ was equal to 0.99 with a CoV of only 4.7% and with values of the 5th and 95th percentiles close to 1.0 (0.92 and 1.07, respectively). The ME of 2.0 kN and the RMSE of 25.1 kN for the proposed equation were the smallest errors among all the equations assessed.

i) Discussion of the results for the experimental dataset

The equations of CSA S304 (2014) and TMS 402/602 (2016) resulted in the most unsafe predictions for the SLC of the walls, presenting a RMSE of 68.2 kN and 59.4 kN, respectively, and a ME of -30.4 kN and -31.3 kN, respectively. Moreover, the average ratio $V_{n,pred}/V_{max,avg}$ was 1.16 (CoV = 23.4%) with the 95th percentile equal to 1.61 for the Canadian code, and 1.17 (CoV = 19.8%) with the 95th percentile equal to 1.56 for the American code. The equation of Oan and Shrive (2014) estimated the shear capacity of the walls with similar statistical indicators to the codes.

It can be noted that these equations tend to overestimate the SLC of walls in which the grout is more spaced (e.g., walls 3, 4, 6, 10-15) and led to more conservative results for walls with more points of grout (e.g., walls 1, 2, 5, 7-9, 24, 25, 29, 30). Similar findings are reported in other studies (Nolph and ElGawady, 2012; Elmapruk et al., 2020) and can be attributed to the fact that the code equations were developed for FGMW and further adjusted for PGMW using a constant reduction factor, which does not reflect the actual non-linear behavior shown in Figure 56.

In contrast to the results for the numerical dataset, the equation of Dillon and Fonseca (2015) did not present the best predictions among the other existing shear equations for the experimental dataset. Their equation showed a tendency of making safer predictions with an average ratio $V_{n,pred}/V_{max,avg}$ of 0.90 with the 95th percentile equal to 1.25, but the variance (CoV = 24.9%) and the errors (RMSE = 65.6 kN and ME = 29.8 kN) were higher than for other equations. The equation of Dillon and Fonseca (2015) overestimated the SLC of walls with

grout only at the ends (walls 10-14), being the error higher as long as the length of the wall. Contradistinctively, this equation predicted highly conservative values for the SLC of walls with lower spacing between grouted cores (walls 1, 2, 5, 7-9, 24, 25, 29, 30) when compared to other walls in the same subset.

Among the existing shear equations, the best estimations for the SLC of the experimental walls were made using the equations of Izquierdo et al. (2021) and Seif ElDin et al. (2019a). These equations estimated similarly the shear capacity of the walls with an average ratio $V_{n,pred}/V_{max,avg}$ close to 1.0 with a CoV of approximately 22%. The values for the 5th and 95th percentiles were approximately 0.75 and 1.5, respectively, and the RMSE was approximately 45 kN. Using these two equations, the most unsafe predictions were for walls 3, 4, and 6, which had a large spacing between grouted cores.

As with the numerical dataset, the proposed equation presented the best statistical indicators among all studied shear equations for the experimental dataset. The SLC of the walls was estimated with an average ratio $V_{n,pred}/V_{max,avg}$ of 1.05 with a CoV of 14%, and with the smallest range between the 5th percentile (0.81) and the 95th percentile (1.28). The ME of -6.0 kN and the RMSE of 33.9 kN for the proposed equation were also the lowest errors among all equations examined.

3.4 SHEAR LOAD CAPACITY OF PERFORATED PARTIALLY GROUTED MASONRY WALLS

Some walls with openings were simulated intentionally with the same dimensions and characteristics of the unperforated walls to evaluate the changes in the shear capacity. As observed in Table 41, the average maximum lateral load $V_{max,avg}$ decreased approximately 9%, 16%, and 21% from wall 1 to walls 59, 60, and 61, respectively. This difference can be attributed to the presence of window openings that had the same height but different lengths. Walls 59 and 60 had a centralized opening whereas wall 61 had two openings symmetrically positioned; both were single-story walls. These openings implied a reduction on the effective horizontal cross-sectional area of 10%, 19%, and 23% for walls 59, 60, and 61, respectively, compared to wall 1.

Making the same comparison for wall 43 with walls 75, 76, and 77, which all had two stories, the decrease in the $V_{max,avg}$ was smaller: 7%, 10%, and 15%, respectively. The decrease in the $V_{max,avg}$ was even smaller for walls with three stories, wall 51 compared to walls 86, 87,

and 88: 2%, 8%, and 8%, respectively. The reduction in the $V_{max,avg}$ was smaller for walls with more stories probably because the diagonal struts found more regions of masonry between the stories to spread out, reducing relatively the influence of the openings. It is important to mention that the lateral load was applied at the top of the highest story; thus, the main diagonal strut starts from the point of application of the load and goes through the stories until the base of the wall. If the lateral load was applied at the level of each story, struts would form at each story, which would probably increase the influence of the openings.

Variations on the height of the openings also impacted the SLC of the walls. Decreases in $V_{max,avg}$ of approximately 6%, 9%, and 7% are observed when comparing respectively, walls 59 and 64, 60 and 65, and 61 and 66. Walls 59, 60 and 61 were single-story with six course-high window openings whereas walls 64, 65, and 66 were the same but with 11 course-high door openings. Making the same comparison for the two-story walls 75 and 78, 76 and 79, and 77 and 80, the $V_{max,avg}$ decreased by 7%, 11%, and 15%, respectively. For the three-story walls (86 and 89, 87 and 90, and 88 and 91) the $V_{max,avg}$ decreased 4%, 5%, and 15%, respectively. It appears that as the height of the openings increases, the wall panel behavior becomes more independent and, consequently, the diagonal struts concentrate in the shorter piers.

3.4.1 Examined approaches for predicting the shear capacity

Current shear equations consider only walls without openings: thus, four different approaches using the new proposed equation were examined to predict the SLC of perforated walls. The approaches are based on the strength of the wall piers with dimensions limited by different possibilities for the diagonal shear cracks.

The first approach (SA1) considers the full wall with a diagonal shear crack formed from the top of the bond beam of the last story to the base of the first course of the first story, Figure 59(a). The horizontal effective cross-sectional area is subtracted from the cross-sectional area of the openings.

In the second (SA2), third (SA3), and fourth (SA4) approaches, the openings are assumed to separate the wall into identical panels, rigidly connected and with the same strength. The distinction between these approaches is where the diagonal shear crack is assumed to start and finish in the panels, which implies different dimensions for them. SA2 considers the diagonal shear crack to form from the top of the bond beam of each story to the base of the first course of the same story, Figure 59(b). In SA3, the diagonal crack is assumed to run from the top of the bond beam of each story to the bottom corner of the opening of the same story,

Figure 59(c). In SA4 the diagonal crack is taken to form from the upper corner of the opening to the lower corner of the opening of the same story, Figure 59(d).

Figure 59: Layout types that are considered on the four approaches.

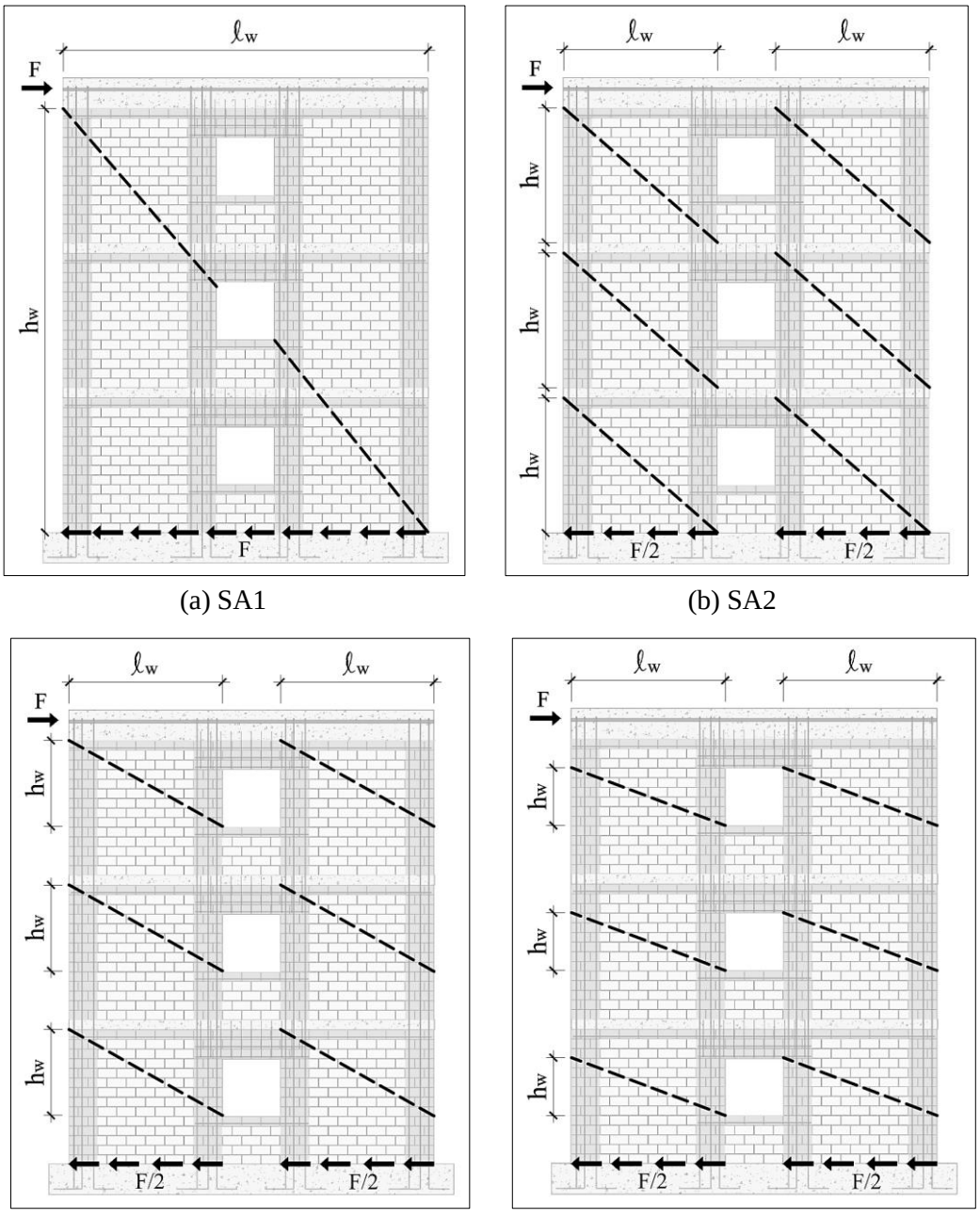

(a) SA1 (b) SA2

(c) SA3 (d) SA4

Source: Author.

With approaches SA2, SA3 and SA4 the lateral load capacity is calculated as the sum of the capacities of the piers placed at the same horizontal alignment since it is the direction of the shear action. The sum of the capacities of the piers superposed vertically must not be included since this will overestimate the actual capacity of the wall. The most unfavorable case can be considered for the piers in the first story, and, therefore, the total axial load should be

divided between them in the calculation of the lateral load capacity. Only the reinforcement included in the piers was considered in the calculations using these approaches.

In addition to walls with only an opening positioned symmetrically in each story, the assessed dataset (walls 59 to 96 in Table 41) also included walls with two identical openings positioned symmetrically in each story (walls 61, 66, 77, 80, 88, and 91) and walls with two different openings positioned symmetrically in each story (walls 67, 81, and 92). The definition of the piers for these walls using the approaches SA3 and SA4 is conditioned by the dimension of the smallest opening.

3.4.2 Accuracy of the approaches for predicting the shear capacity

The results of the four approaches using the new proposed equation for predicting the SLC of the simulated walls with openings are presented in Table 29 and Figure 60. As before, the accuracy was evaluated in terms of the minimum, maximum, average, standard deviation, coefficient of variation (CoV), 5th percentile, and 95th percentile of the ratio $V_{n,pred}/V_{max,avg}$ for each wall. The Mean Error (ME) and the Root Mean Squared Error (RMSE) were also calculated to evaluate the levels of precision of the approaches. These results do not consider any strength-reduction factors.

Figure 60: Results of the approaches for the shear capacity of the perforated walls.

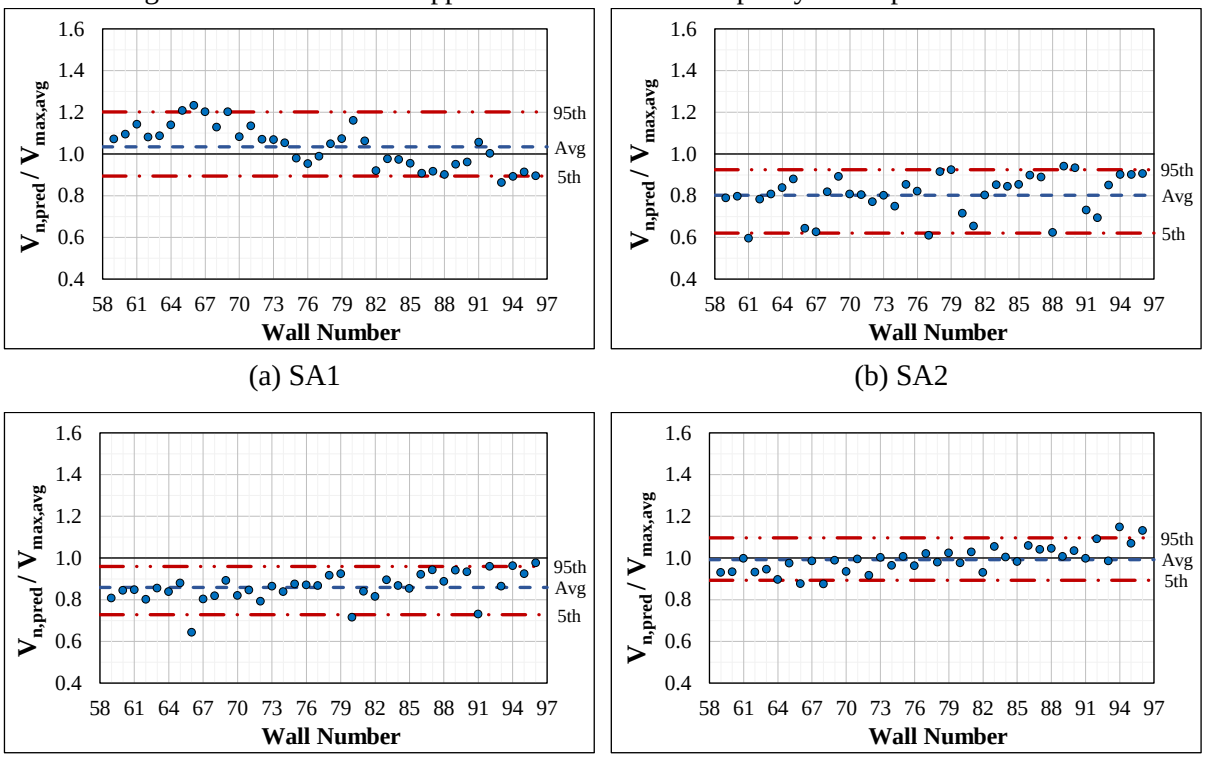

(a) SA1 (b) SA2

(a) SA3 (b) SA4

Source: Author.

Table 29: Statistical comparison between the approaches for the shear capacity of the perforated walls.

Approach	$V_{n,pred}/V_{max,avg}$							ME	RMSE
	Min.	Max.	Avg.	STDV	CoV (%)	5th PCTL	95th PCTL	(kN)	(kN)
SA1	0.86	1.23	1.03	0.10	9.7	0.89	1.20	-15.2	48.9
SA2	0.59	0.94	0.80	0.10	12.1	0.62	0.92	91.2	100.4
SA3	0.64	0.97	0.86	0.07	7.8	0.73	0.94	66.5	73.2
SA4	0.87	1.15	0.99	0.06	6.2	0.89	1.10	4.8	29.8

Source: Author.

SA1 estimated the SLC of the perforated walls with an average ratio $V_{n,pred}/V_{max,avg}$ of 1.03 (CoV = 9.7%) and with the 5th and 95th percentiles equal to 0.89 and 1.20, respectively, which were close to 1.0, but with a slight tendency for overestimation, confirmed by a negative value of the ME (-15.2 kN). The main deficiency of this approach is to consider only the reduction of the effective horizontal cross-sectional area and not to consider the opening height.

The results show that SA2 made the worst predictions among the four approaches. The average and maximum ratio of $V_{n,pred}/V_{max,avg}$ of 0.80 and 0.94 indicate that all walls had their shear capacity underpredicted. This underestimation reached up to 41%, being larger for walls with two openings in the same story (walls 61, 66, 67, 77, 80, 81, 88, 91, and 92). The ME and the RMSE of 91.2 kN and 100.4 kN, respectively, were the highest among all approaches.

SA3 also underpredicted the shear capacity of all walls, but the values of the ratio $V_{n,pred}/V_{max,avg}$ were closer to 1.0 and the variation and errors were smaller compared to SA2. The average and the maximum ratio of $V_{n,pred}/V_{max,avg}$ were 0.86 and 0.97, respectively, with a CoV of 7.8%. This approach also did not predict accurately the shear capacity of walls 66, 80, and 91, which had two door openings in the same story. The inaccuracy in predicting the shear capacity of walls with two openings with SA2 and SA3 may be related to the simplified assumption that the load carried by each pier and the strength of each pier are identical.

SA4 has the best statistical indicators among the four approaches assessed for the prediction of the SLC of perforated walls. The average ratio of $V_{n,pred}/V_{max,avg}$ was equal to 0.99 with a CoV of only 6.2% and with values of the 5th and 95th percentiles varying only approximately ±10%. The ME of 4.8 kN and the RMSE of 29.8 kN for SA4 were the smallest errors among all approaches. SA4 also predicted the SLC of the walls with two openings in the same story accurately, even when the openings were different (walls 67, 81, and 92). It can be noted that the predictions passed from a condition of underestimation (walls 59 to 74) to a condition of overestimation (walls 75 to 96) as the number of stories was increased. This might be explained by the fact that this approach is based on the strength of the piers and does not account for the global aspect ratio of the wall.

3.5 CONCLUDING REMARKS

A new shear equation was proposed, and some relevant existing expressions were evaluated aimed at determining the most accurate in predicting the SLC of unperforated PGMW. Furthermore, different approaches were studied to determine the most consistent way of predicting the SLC of single and multi-story PGMW with openings. According to the results, the following comments and conclusions can be made:

- The use of numerical simulations was very useful to create specific situations by varying parameters for which there is no consensus in the literature concerning their contribution to the shear resistance of walls. These situations could show that some good predictions using the existing shear equations are actually false positives. In many cases, the overestimation of the contribution of the horizontal reinforcement was offset by the absence of a term for the contribution of the vertical reinforcement and/or by the underestimation of the contribution of the masonry imposed by limits on the aspect ratio and vice-versa;
- The shear equations of TMS 402/602 (2016) and CSA S304 (2014) resulted in the most inaccurate predictions of the shear load capacity of unperforated PGMW of both the numerical and experimental datasets, of all the equations assessed. The TMS 402/602 (2016) equation presented a tendency to overpredict insecurely the SLC of walls with horizontal reinforcement. The CSA S304 (2014) equation also predicted with high variability the SLC of walls involving horizontal reinforcement. The code equations tend to overestimate and underestimate, respectively, the SLC of walls with large and small horizontal spacing between grouted cores, mainly because these equations were developed for FGMW and further adjusted for PGMW using a simple constant reduction factor;
- Between the evaluated existing shear equations, the equation of Dillon and Fonseca (2015) performed the best predictions for the walls of the numerical dataset, whereas the equations of Izquierdo et al. (2021), and Seif ElDin et al. (2019a) were the most accurate for the walls of the experimental dataset;
- The influences of the aspect ratio, vertical and horizontal grouting and reinforcement, and axial loading, were incorporated in the new proposed equation, ensuring a suitable accuracy in predicting the SLC of the walls. Thus, the proposed equation

presented the best statistical indicators among all the shear equations studied for unperforated PGMW of both the numerical and experimental datasets;

- The significant decrease in the SLC of the single-story walls caused by the presence of openings can be correlated with the reduction of the effective horizontal cross-sectional area. Even in a smaller proportion, the SLC of the walls also decreased when the window openings were replaced with door openings. The influence of the openings was smaller for walls with more stories since the lateral load was applied at the top of the highest story and, consequently, the diagonal struts found more regions of masonry between the stories to pass through. Further studies are necessary to evaluate the influence of the openings in multi-story PGMW when the lateral load is applied at the level of each story;
- The approach of predicting the SLC of perforated PGMW by only reducing the effective horizontal cross-sectional area in the shear equation did not produce accurate results since this approach ignores the influence of the opening height. The most accurate predictions were made using the approach which considered the strength of the wall as the sum of the strengths of the wall piers with dimensions limited by the diagonal shear crack forming from the upper corner of the opening to the lower diagonally opposite corner of the opening of the same story. Further research is needed to investigate the applicability of this approach using the new proposed shear equation for cases of walls with openings positioned asymmetrically.

Finally, besides proposing a new accurate and complete shear equation for PGMW, this study highlights the necessity of updating the shear expression of the TMS 402/602 (2016) and CSA S304 (2014). It is suggested to reduce the influence of the horizontal reinforcement, include the effect of the vertical reinforcement, revise the limits for the aspect ratio, consider the interrelation between the applied axial loading and aspect ratio, and separate equations for FGMW and PGMW or, at least, account for the non-linear influence of the grout spacing instead of using a constant reduction factor. Furthermore, a simple approach was checked and confirmed as useful in predicting the SLC of single and multi-story PGMW with openings positioned symmetrically.

4. SEISMIC BEHAVIOR AND PERFORMANCE

Buildings must be designed to preserve human lives so that structures maintain their integrity after seismic events. To meet this requirement, it is necessary to know the behavior and aspects like strength, ductility, and degradation of the structural components in the face of the seismic actions to limit the spread of damage and ensure continuity in the safe operation of the establishment.

Compared to FG masonry structures, PG masonry can be considered a good alternative in economic terms for situations with low and mid-intensity wind and/or seismic loads. Because of that, this typology is widely used in Brazil and many other regions around the world and, thus, its behavior must be better understood.

No studies have explored the seismic behavior and performance of partially grouted walls that are simultaneously multi-story, with openings, and with grout and reinforcement concentrated at the ends of the wall piers. In this context, the research presented herein aims to expand the knowledge about the in-plane behavior of this type of PG masonry shear walls by analyzing the walls' responses qualitatively and quantifying their seismic performance.

The study presented in this chapter led to the following publication:

- Medeiros, K. A. S., Palhares, R. A., Parsekian, G. A., Shrive, N. G., Fonseca, F. S., 2022, In-plane behavior and seismic performance of differently detailed, multi-story, perforated, partially grouted masonry walls. Engineering Structures, 271, 114941. https://doi.org/10.1016/j.engstruct.2022.114941

4.1 LITERATURE REVIEW

4.1.1 Brazilian seismic context

The damage caused by earthquakes is often irreparable since they can cause, in addition to material damage, human losses, affecting the entire economic and social context. Among the seismic events that have already happened around the world, BBC – Brazil (2014) lists the five most relevant in terms of magnitudes and effects: Chile, 1960; Alaska (USA), 1964; Sumatra (Indonesia), 2004; Honshu (Japan), 2011, and; Kamchatka (Russia), 1952. All these events had magnitudes greater than or equal to 9.0 points on the Richter scale and caused thousands of deaths and billions of losses

Several other events could be cited as relevant, such as the one that occurred in Haiti in January 2010. In this case, there was a succession of three earthquakes with magnitudes, respectively, of 7.0, 5.9, and 5.5 degrees, which, according to data published in the press (Francisco, 2020), resulted in the destruction of thousands of homes and commercial properties, as well as more than 200,000 deaths and about 250,000 injuries. The aggravating factors were the proximity to the surface where the phenomenon occurred, only 10 kilometers deep, and the total unpreparedness of the nation's constructions, which was already considered the poorest in the Americas.

The number of occurrences in Brazil, compared to countries with high seismic activity, is reduced and has lesser consequences. However, important records have already been made, such as those listed by Baptista (2015):

1) Mato Grosso (1955): More precisely in Serra do Tombador, an earthquake with a magnitude of 6.6 was detected, the largest recorded in the country's history. The event occurred in an uninhabited region, causing no deaths or material damage;

2) Espírito Santo (1955): Vitória city was hit by an earthquake measuring 6.3 points on the Richter scale. The people's reaction was one of fright, and the houses just shook, with no record of injuries or damage;

3) Rio Grande do Norte (1986): João Câmara city was hit by a series of earthquakes at that time, the most severe being a 5.1 magnitude tremor, causing the partial or total destruction of 4,000 properties;

4) Ceará (1980): Pacajus and the metropolitan region of Fortaleza felt the effects of an earthquake with a magnitude of 5.2 points;

5) Minas Gerias (2007): The tremor in the locality of Caraíbas, in Itacarambi city, reached 4.7 degrees on the Richter scale. Despite a not-so-great magnitude, some houses collapsed, six people were injured, and a five-year-old child died.

As noticed, most earthquakes in Brazil happen in sparse or uninhabited areas, which, fortunately, has not caused major catastrophes. Despite this, the population expansion in the country is demanding unpopulated areas, in addition to the seismic unpredictability of nature. Furthermore, earthquakes with smaller magnitudes cannot be ruled out in the risk analysis, as they can also cause serious consequences due to their way of propagation through the ground, the focal distance, and the weaknesses of some constructions.

Assumpção et al. (2016) point out, through the map in Figure 61, that small and moderate earthquakes are not so occasional in Brazil. The map presented includes ancient historically reported earthquakes and recent earthquakes detected by seismographs. The authors commented that there are probably a large number of ancient tremors that were not recorded because they occurred in uninhabited regions and, therefore, were not felt or detected in seismographic stations because they were small. This fact justifies the Southeast region appearing more active than the Amazon region, known for its higher population density and seismographic stations operating for a longer time.

Figure 61: Shallow earthquakes (depth < 50 km) in Brazil, 1720-04/2016.

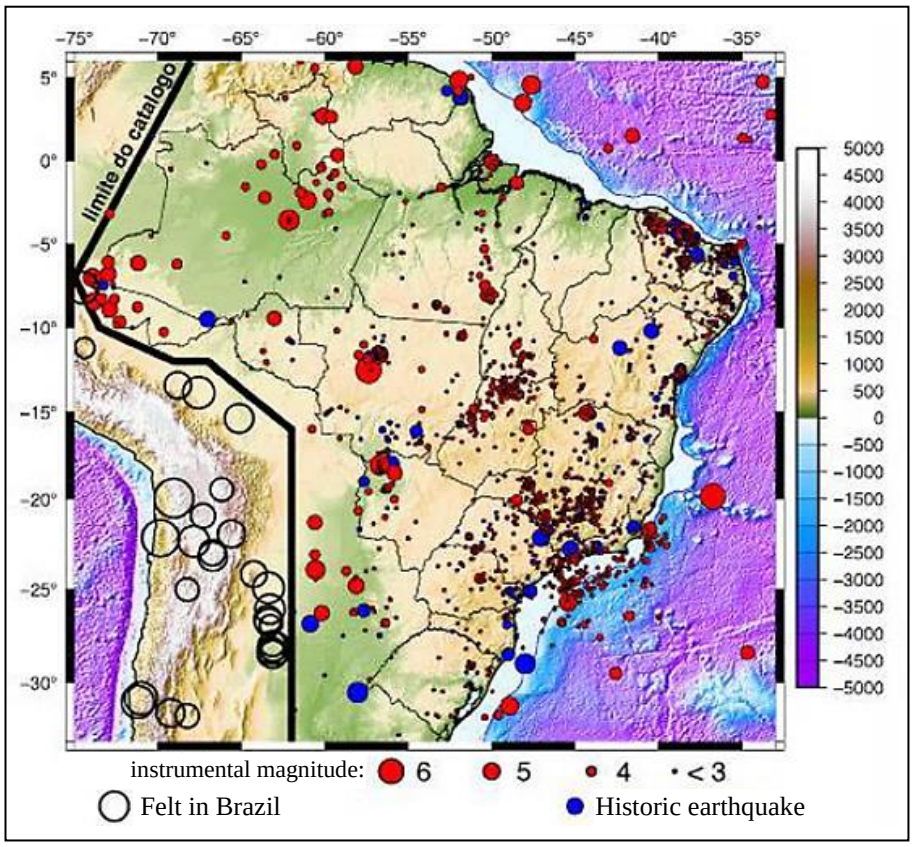

Source: Adapted from Assumpção et al. (2016).

Seismic activity involves concepts related to the movement of tectonic plates, geological faults, distance and depth of occurrence of events, and the pattern and propagation of the seismic waves. These aspects make the phenomenon of great complexity, making it difficult to predict actual events and consequences.

Based on tectonic theory, it is known that the most intense seismic activities on the planet occur in the regions near plate boundaries. Even so, places far from these borders, called intraplate regions, may also be subject to this phenomenon due to geological faults. Brazil is

located near the center of the South American plate, presumably generating a lower occurrence of events and promoting an apparent sense of security.

Assumpção et al. (2014, 2016) comment that most earthquakes in Brazil have a focus shallower than 10 km; however, although intraplate earthquakes occur mainly in the upper crust, their causes can be much deeper. Therefore, understanding intraplate seismicity is a great challenge, with several models proposed to elucidate this activity.

The main seismic events in Brazil are related to vibration diffusion, resulting from earthquakes along old fractures, arising in different locations, such as the southeast coast, the south, central Minas Gerais, and the northeast (Montardo, 2006). Additionally to those occurring in our territory, vibration diffusion causes large earthquakes focused on neighboring countries also to be felt in Brazilian states, as reported in Figure 61.

Earthquakes are practically impossible to predict or avoid. The best way to prevent them is to design buildings with attention to seismic hazard maps, in which the areas of greatest activity and probability of occurrences are identified based on the frequency and magnitude of earthquakes already registered. These maps indicate the levels of ground motion for a specific return period, considering at any point on the map a slight tremor occurring close to the location or a more significant and distant tremor.

The expression “seismic risk” is often linked to this type of map, but Assumpção et al. (2016) explained that this term is technically the result of the product of hazard and vulnerability, which describes the potential for damage due to the fragility of buildings, probable number of victims, etc. Therefore, a highly active seismic area may have a high degree of hazard, but if it is uninhabited, like much of the Amazon region, the seismic risk will be almost null. On the other hand, small earthquakes have a low degree of hazard, but if they occur in places with very precarious constructions, as happened in Itacarambi-MG or Haiti, the risk can be significant.

ABNT NBR 15421 (2006) adopts the seismic zoning shown in Figure 64 to define the seismic actions to be considered in the design. The map in Figure 64 shows the peak ground accelerations in fractions of the gravity acceleration, in a hard rock site Class, with a 10% exceedance probability over 50 years, corresponding to a return period of 475 years. The standard considers some seismic force-resisting systems, but structural masonry is not included until now. It should be noted that the standard is currently undergoing a review process in which the seismic hazard map will probably be updated, and more resistant systems may be included.

Figure 62: Mapping of the characteristic horizontal seismic acceleration in Brazil.

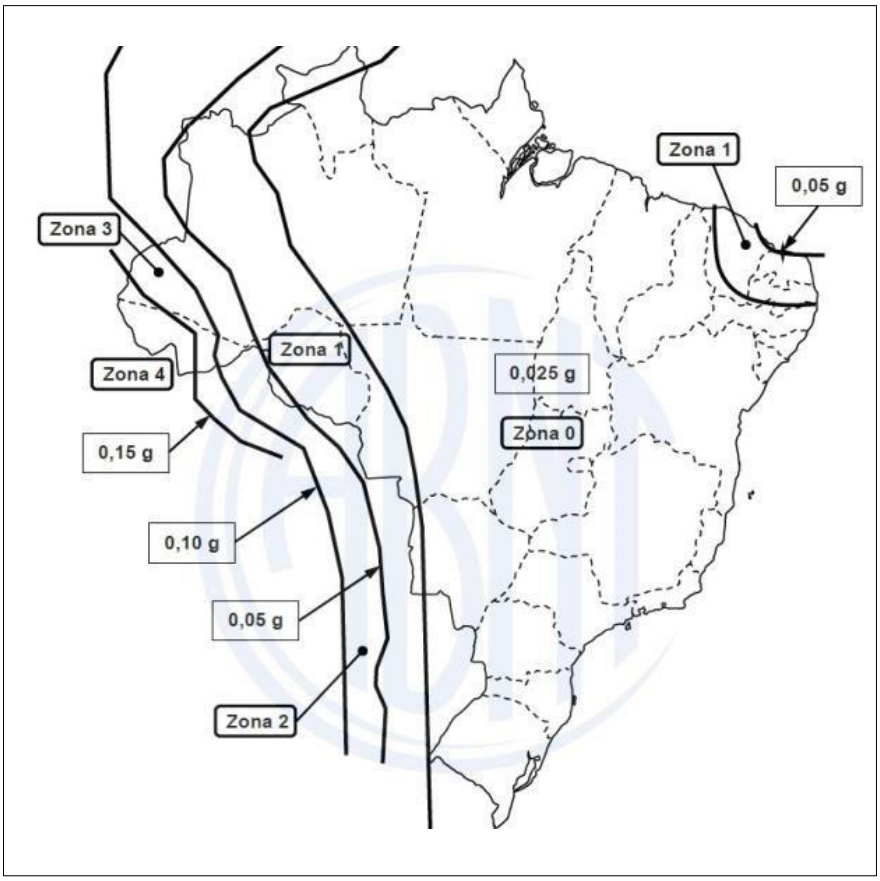

Source: ABNT NBR15421 (2006).

4.1.2 Seismic analysis methods

Seismic waves propagate in both vertical and horizontal directions, and special attention should be paid to the horizontal vibrations because traditional calculation models do not consider this type of action in design. Vertical vibrations are less worrying, as they act in the direction of the structure's self-weight, which, in general, with design considering the proper calculation coefficients, sufficient safety is already provided.

According to Dantas (2013), the main parameters involved in seismic analyzes are the duration of the event and the predominant period, with fundamental importance in the non-linear analysis of structures, and the maximum values of the acceleration (PGA - Peak Ground Acceleration), velocity (PGV – Peak Ground Velocity) and displacement (PGD – Peak Ground Displacement), which depend on the characteristics of the fault distance, the nature of the soil formations traversed by the seismic waves and the local geological conditions. Regarding civil constructions, regulatory texts treat maximum acceleration as the most important parameter.

The response of structures to seismic action involves qualitative and quantitative parameters and can be evaluated through different approaches. Among the type of analysis, it

can be cited the linear elastic, nonlinear static, and nonlinear dynamic with time-integration, which may present modal characteristics and rely on the aid of numerical simulations.

It is necessary to determine the forces that represent the seismic action on the building and the consequences they produce before the effective design of the structural members. Most regulatory standards define seismic loading via the elastic acceleration response spectrum, Figure 63, equivalent to a 10% probability of being exceeded over a 50-year return period.

Figure 63: Response spectrum depending on the period.

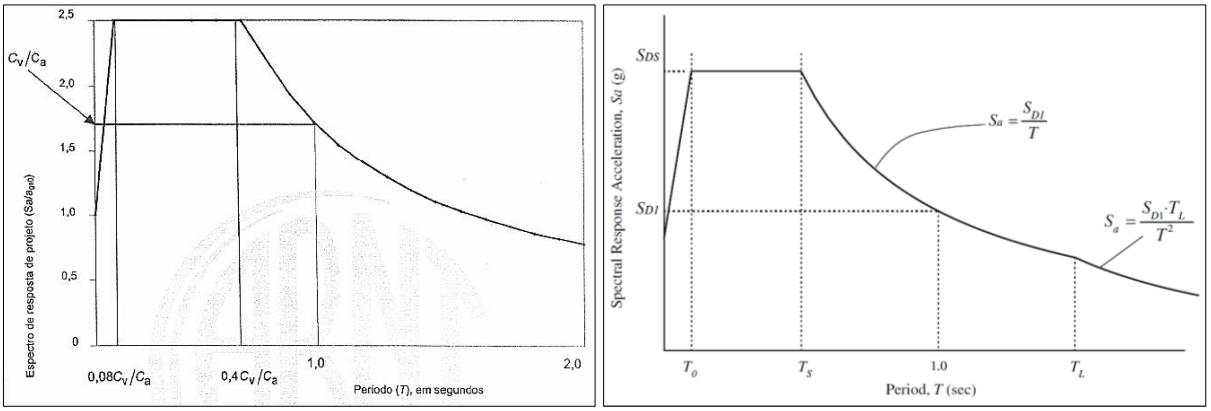

(a) ABNT NBR 15421 (2006) (b) ASCE/SEI 7 (2016)

Source: Adapted from ABNT NBR 15421 (2006) and ASCE/SEI 7 (2016).

Despite the development of advanced analysis tools, simplified methodologies are still preferred by engineers. In this context, most standards allow, for its better understanding, the method of equivalent lateral forces, in which total horizontal forces are applied at the base of the structure and on each floor for each of the main directions. These forces depend on the response modification factors, the system's total weight, spectral acceleration, and the structure's natural period.

In the method of equivalent horizontal forces, a reduced elastic response spectrum is considered by employing behavior coefficients, which allows for accounting for the inelastic capacity of the structure to dissipate energy through deformations and induced damage (Mohammadi and Naggar, 2004). The behavior coefficients vary depending on the building typology, and they are generally presented in the regulatory standards as the response modification, overstrength, and deflection amplification factors for each type of seismic force-resisting system.

Non-linear static analysis methods (pushover analysis) can be used to include inelastic parameters in safety assessments. These methods are based on controlling damage and deformation mechanisms for specific performance levels. Marques and Lourenço (2012)

clarifies that it is necessary to predict the capacity curve of buildings, which represents the relationship between the horizontal seismic force and the displacement of a significant control point of the structure. The curve is calculated by simulating an incremental static lateral load on the structure by assuming a uniform distribution of forces proportional to the inertia masses or modal distribution, in which seismic forces proportional to the inertia masses multiplied by the displacements of the first mode of vibration of the structure are used. The process is incremental and iterative, making its application difficult if computational resources are not used. It is indicated to use models with finite macro-elements, as illustrated in Figure 64, in which the damage progression on the panels can be observed, controlling the evolution of the capacity curve (Marques and Lourenço, 2012).

Figure 64: Structural masonry building pushover analysis.

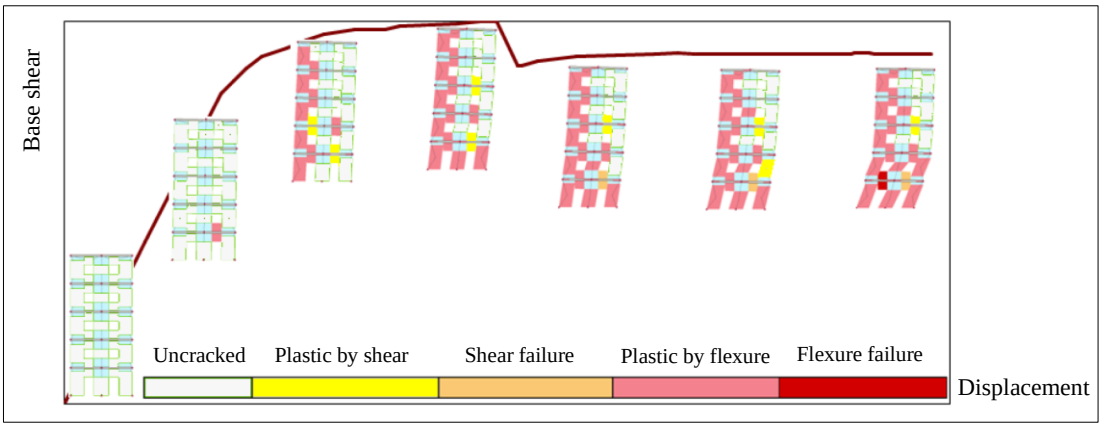

Source: Adapted from Marques and Lourenço (2012).

In the dynamic analysis of structures, the equilibrium is governed by the Equation 49, considering the inertia forces dependent on the acceleration imposed (vector $\ddot{u}$) to the mass (matrix m) in each of the degrees of freedom, the forces on the elastic elements calculated by multiplying the stiffness (matrix k) by the displacements (vector u), and the viscous damping forces expressed as the product of the damping (matrix c) by the velocities (vector $\dot{u}$). The balance is made by equating it to the product of the mass and the acceleration at the base of the building (vector $\ddot{s}(t)$).

$$m\ddot{u} + c\dot{u} + ku = -m\ddot{s}(t) \qquad \text{Eq. 49}$$

Depending on the desired precision level, the structure's dynamic analysis can be performed using different methods, varying the consideration of the inelastic behavior, the way of defining the seismic excitation, and the calculation procedure. In order to consider nonlinearity, it is necessary to modify the dynamic equilibrium equations, usually adopting a hysteretic rule simulating the cycles of loading, unloading, and reloading of the elements

(Marques and Lourenço, 2012). According to Paulay and Priestly (1992), the inelastic time-integration method is considered one of the most sophisticated for predicting forces and displacements under seismic action, as it involves step-by-step resolution in the time domain of the equations of motion, considering multiple degrees of freedom to represent the response of a multi-story building. This analysis model is not usual because it involves complex concepts that designers find challenging to interpret and apply.

4.1.3 Seismic parameters

4.1.3.1 Conceptualization and methods

The seismic behavior coefficients allow incorporating the inelastic response capacity in terms of strength and deformation to seismic force-resisting systems when they are dimensioned using linear analysis methods (NIST, 2010).

Most literature and design codes consider response modification, overstrength, and deflection amplification coefficients. Dantas (2013) explains that the response modification coefficient is related to the overall ductility of the structure, implying the ability to absorb and dissipate energy as a function of displacements in the plastic regime. The overstrength coefficient represents the ratio between the real strength of the structure and the strength assumed in design. The deflection amplification coefficient adds the capacity for inelastic deformation to the displacement initially assumed to be elastic. All these coefficients are dependent, among other things, on the type of structure, redundancy level, and materials used.

According to the National Earthquake Hazards Reduction Program (NEHRP, 1988), the response modification coefficients were, until then, obtained empirically by observing structures that had already been subjected to earthquakes or in comparisons with similar systems that already had their capacity known. Therefore, Uang (1991) determined well-defined relationships for the seismic parameters described in Equations 50 to 56. The author exemplified, through the graph in Figure 65, the actual behavior of a ductile structure and its respective response with bilinear elastoplastic idealization, in which the linear elastic phase incorporates part of the inelastic capacity of the structure. The vertical axis expresses the base shear on the structure normalized by its seismic weight, while the horizontal axis refers to the story drift, which is the ratio of the displacement at the top of the story to the wall height. For design using stress-based methods, the lateral force (C_y) corresponding to the maximum displacement (Δ_{max}) is reduced to the force level (C_s) at which the formation of the first plastic

hinge occurs or to the design load level (C_w), so that simply elastic analyzes can be conducted. The author commented that this reduction was usually made in a non-explicit way; thus, the structure's performance could be unsatisfactory for severe earthquakes since the actual reserve of strength and ductility that the structure would present in these conditions was unknown.

Figure 65: General seismic response with bilinear elastoplastic idealization.

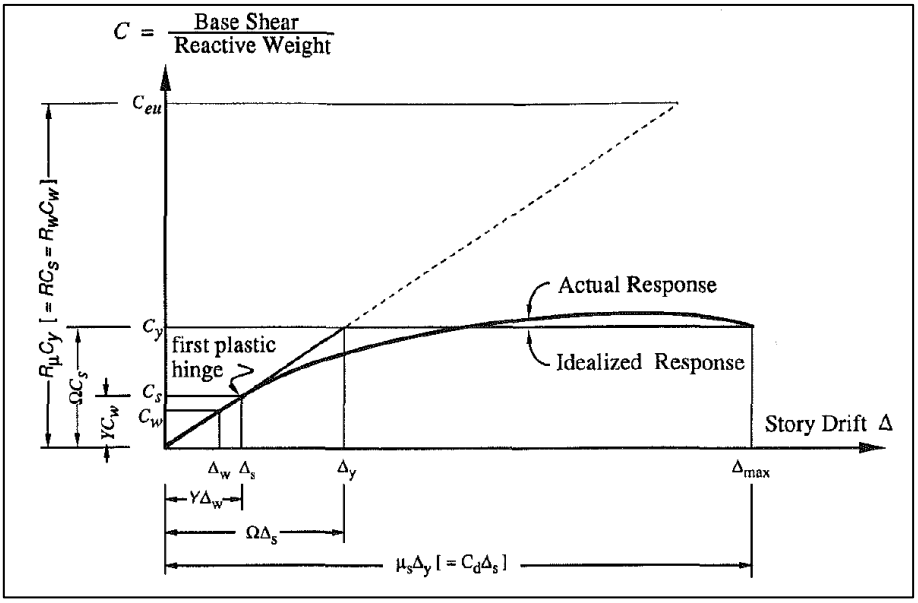

Source: Uang (1991).

The structural ductility factor (μ_s) is estimated by the ratio between the maximum drift (Δ_{max}) and the drift (Δ_y) corresponding to the end of the linear branch of the perfect elastoplastic graph.

$$\mu_s = \frac{\Delta_{max}}{\Delta_y} \qquad \text{Eq. 50}$$

The ductility reduction factor (R_μ) reduces the response from the force level C_{eu}, which considers that the structure would continue to behave elastically until failure, to the force level C_y, which is related to the idealized structural yield level.

$$R_\mu = \frac{C_{eu}}{C_y} \qquad \text{Eq. 51}$$

The overstrength factor (Ω) refers to the reserve of strength that exists between the force level C_y and the first significant yield level (C_s).

$$\Omega = \frac{C_y}{C_s} \qquad \text{Eq. 52}$$

The allowable stress factor (Y) reduces the capacity of the structure from the force level C_s to the design force level (C_w).

$$Y = \frac{C_s}{C_w} \quad \text{Eq. 53}$$

The response modification factor (R or R_w) changes the response from the force level C_{eu} to the force level C_s or C_w.

$$R = \frac{C_{eu}}{C_s} = \frac{R_\mu C_y}{C_y/_\Omega} \quad \therefore \quad R = R_\mu \Omega \quad \text{Eq. 54}$$

$$R_w = \frac{C_{eu}}{C_w} = \frac{R_\mu C_y}{C_s/_Y} = \frac{R_\mu C_y Y}{C_y/_\Omega} \quad \therefore \quad R_w = R_\mu \Omega Y \quad \text{Eq. 55}$$

The displacement amplification factor (C_d) is the ratio between the maximum drift (Δ_{max}) and the drift corresponding to the first significant yield (Δ_s).

$$C_d = \frac{\Delta_{max}}{\Delta_s} = \frac{\mu_s \Delta_y}{(C_s \Delta_y)/_{C_y}} = \frac{\mu_s C_y}{C_s} \quad \therefore \quad C_d = \mu_s \Omega \quad \text{Eq. 56}$$

Since the displacement amplification and response modification factors depend on the level of reduction in the seismic design force admitted in each design code, the ratio between them, Equation 57, is a better way of comparing these parameters (Uang and Maarouf, 1994).

$$\frac{C_d}{R} = \frac{\mu_s \Omega}{R_\mu \Omega} = \frac{\mu_s}{R_\mu} \quad \text{Eq. 57}$$

As can be seen in Figure 65, the idealized elastoplastic response of a structure is characterized by the initial stiffness and by the ultimate and yield displacements. According to Seif ElDin et al. (2019b) the effective elastic stiffness can be defined by the secant stiffness of the wall when experimentally observing the first major diagonal crack or by the secant stiffness determined by the ratio between the load and the wall displacement referring to the beginning of the vertical reinforcement yielding. The first and second approaches are more representative of walls with failure modes dominated by shear and flexure, respectively. The ultimate displacement of the plastic plateau can be adopted equal to the experimental displacement corresponding to the maximum load, which can result in conservative values, or as the displacement corresponding to the load with 20% decay after the peak or even equivalent to a drift of 1% when the structure is highly ductile. The yield displacement is determined by the intersection between the lines of the elastic and plastic branches or by equating the areas below the actual and idealized force-displacement curves.

Regardless of the ductility factor, structures with natural frequencies between 0.3 Hz and 2 Hz show similar ultimate displacements, whereas structures with natural frequencies between 2 Hz and 8 Hz show the same energy with a corresponding relationship between

displacements and forces or accelerations (Newmark and Hall, 1982). Based on this statement, Seif ElDin et al. (2019b) explain two approaches for determining the ductility-related seismic force modification factor (R_d), which reduces the maximum lateral load of the elastic response (V_e) to the elastoplastic equivalent load (V_i), equal to the ductility reduction factor (R_μ) presented by Uang (1991).

In the first approach, which is indicated for structures with lower frequencies or longer periods ($\omega_n < 2\ Hz;\ T > 0.5\ s$), it is considered, as shown in Figure 66(a), the ultimate displacement of the elastic response (Δ_u^e) equal to that of the idealized elastoplastic (Δ_u^{ep}), in addition to the same initial stiffness for both responses. Thus, due to the similarity of triangles shown in Equation 58, it is determined that the R_d factor is equal to the ratio between the ultimate displacement (Δ_u^{ep}) and yield displacement (Δ_y^{ep}) of the idealized curve, i.e., equal to the displacement ductility factor of the idealized elastoplastic response (μ_d^{ep}). The ratio between the displacement amplification (C_d) and response modification (R) factors have, therefore, a unit value, as shown in Equation 59. For simplicity, the natural period of vibration can be calculated using Equation 60, where *W* is the seismic weight, i.e., the applied vertical load on the wall, including the self-weight, g is the gravitational acceleration, and *K* is the idealized stiffness of the wall.

$$R_d = \frac{V_e}{V_i} = \frac{\Delta_u^{ep}}{\Delta_y^{ep}} \quad \therefore \quad R_d = \mu_{\mathrm{d}}^{ep} \qquad \text{Eq. 58}$$

$$\frac{C_d}{R} = \frac{\mu_{\mathrm{d}}^{ep}}{R_d} = 1 \qquad \text{Eq. 59}$$

$$T_n = 2\pi\sqrt{\frac{W}{g \cdot K}} \qquad \text{Eq. 60}$$

The second approach is suitable for structures with higher frequencies or lower periods ($\omega_n \geq 2\ Hz;\ T \leq 0.5\ s$), and also adopts equal initial stiffness for the elastic and elastoplastic responses. The energy equivalency between the responses is made by equating the area under the curves in Figure 66(b); thus, it is determined $R_d = \sqrt{2\mu_d^{ep} - 1}$, as demonstrated in Equations 61 to 63. In this method, the ratio between the displacement amplification (C_d) and response modification (R) factors can be obtained by Equation 64.

$$A_e = A_{ep} \quad \therefore \quad \frac{\Delta_u^e V_e}{2} = \frac{\Delta_y^{ep} V_i}{2} + (\Delta_u^{ep} - \Delta_y^{ep}) V_i \qquad \text{Eq. 61}$$

$$\Delta_u^e V_e = V_i\left(\Delta_y^{ep} + 2\Delta_u^{ep} - 2\Delta_y^{ep}\right) \;\therefore\; \frac{\Delta_u^e V_e}{V_i} = 2\Delta_u^{ep} - \Delta_y^{ep} = 2\mu_{\mathrm{d}}^{ep}\Delta_y^{ep} - \Delta_y^{ep} \qquad \text{Eq. 62}$$

$$\frac{\Delta_u^e}{\Delta_y^{ep}}\frac{V_e}{V_i} = 2\mu_{\mathrm{d}}^{ep} - 1 \;\therefore\; R_d^2 = 2\mu_d^{ep} - 1 \;\therefore\; R_d = \sqrt{2\mu_{\mathrm{d}}^{ep} - 1} \qquad \text{Eq. 63}$$

$$\frac{C_d}{R} = \frac{\mu_{\mathrm{d}}^{ep}}{R_d} = \frac{\mu_d^{ep}}{\sqrt{2\mu_{\mathrm{d}}^{ep} - 1}} \qquad \text{Eq. 64}$$

Figure 66: Equal displacement and equal energy approaches for determining R_d.

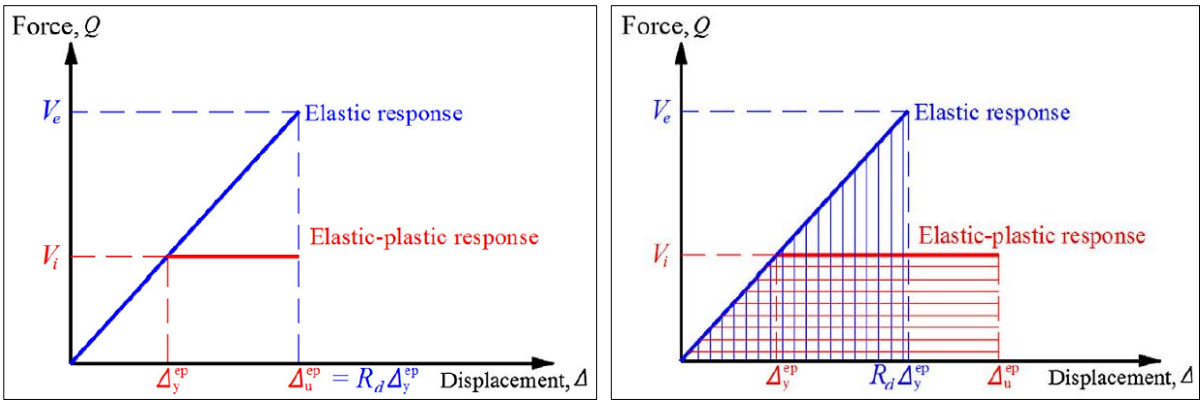

(a) Equal displacement (b) Equal energy

Source: Seif ElDin et al. (2019b).

The Federal Emergency Management Agency (FEMA) presented in FEMA P695 (2009) a methodology developed by the Applied Technology Council (ATC) under Project ATC-63 to determine the seismic response parameters to be used in the design of structures. The objective was to establish a standard logical procedure that could evaluate the performance and seismic parameters of seismic force-resisting systems already considered in design codes and of new systems that might be proposed. Minimum criteria were provided to guarantee the protection and safety of users' lives, in which the structure must have a low probability of collapse in the face of the Maximum Considered Earthquake (MCE).

FEMA P695 (2009) uses the graphs in Figure 67 to illustrate and explain how the response modification (R), overstrength (Ω), and deflection amplification (C_d) factors are considered in the methodology. The parameters are presented in Figure 67(a) by ratios between forces or displacements with concepts similar to those previously discussed. The seismic parameters are correlated with the ground movement corresponding to the MCE in the graph with spectral coordinates shown in Figure 67(b). The conversion to spectral coordinates is based on adopting the total effective seismic weight of the structure *(W)* included in the fundamental mode of the system period *(T)* and an effective damping level equal to 5%.

Figure 67: Illustration of seismic behavior parameters.

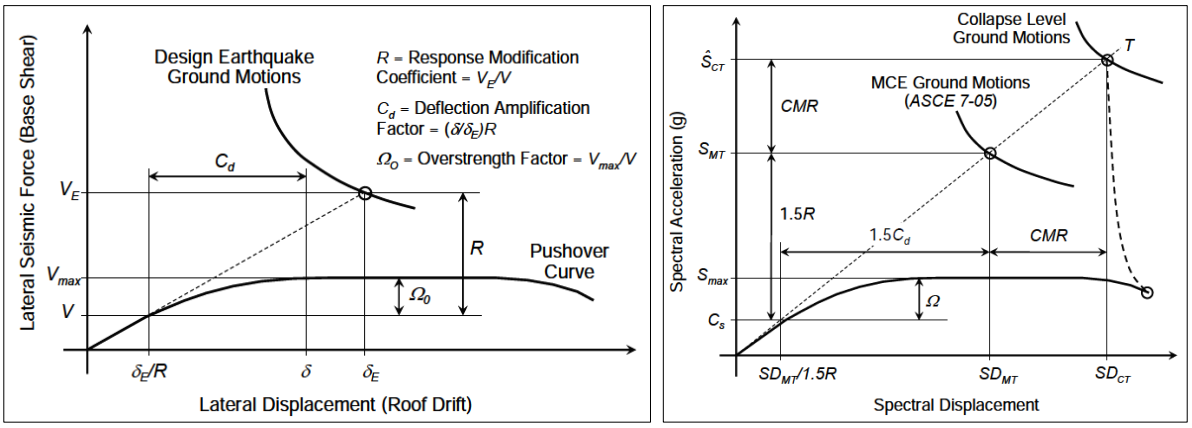

(a) Regular coordinates (b) Spectral coordinates

Source: FEMA 450-1 (2004); FEMA P695 (2009).

The seismic response coefficient (C_s) is related to the seismic base shear required for design (V) normalized by the effective seismic weight *(W)*; thus, $C_s = V/W$. As can be seen in Equation 65, the ratio between the MCE spectral acceleration (S_{MT}) at the period of the system *(T)* and C_s corresponds to 1.5 times the R factor.

$$1.5R = \frac{S_{MT}}{C_s} \quad \text{Eq. 65}$$

The overstrength factor (Ω) is defined by the ratio between the spectral acceleration corresponding to the maximum load of the idealized curve (S_{max}) and C_s, Equation 66. The analysis must be non-linear static (pushover) to determine the overstrength coefficient.

$$\Omega = \frac{S_{max}}{C_s} \quad \text{Eq. 66}$$

Based on the principle of equal displacements (Newmark and Hall, 1982), the displacement amplification factor (C_d) can be considered equal to the response modification factor (R), Equation 67.

$$C_d = R \quad \text{Eq. 67}$$

The safety criterion is expressed by the Collapse Margin Ratio (CMR), Equation 68, which relates the ground movement that would result in a life-threatening collapse in half of the seismic-resisting structures and the maximum considered earthquake. The CMR can be obtained through the ratio between the spectral accelerations (S_{CT}/S_{MT}) or between the corresponding spectral displacements (SD_{CT}/SD_{MT}).

$$CMR = \frac{S_{CT}}{S_{MT}} = \frac{SD_{CT}}{SD_{MT}} \quad \text{Eq. 68}$$

4.1.3.2 Regulatory values and case studies

As aforementioned, the Brazilian standard ABNT NBR 15421 (2006) does not present seismic response parameters for structural masonry systems. The Canadian standard (NBCC, 2015) adopts, based on the method of equal displacements, values between 1.5 and 3.0 for the ductility-related seismic force modification factor (R_d) and, through statistical analysis, an overstrength factor (R_o) equal to 1.5 for systems with masonry shear walls. The American standard (ASCE/SEI 7, 2016) indicates, as highlighted in Figure 68, more than ten options of seismic force-resisting systems of structural masonry with values of the response modification factor (R) ranging from 1.5 to 5.5 and overstrength factor (Ω_o) fixed at 2.5. ASCE/SEI 7 (2016) also presents values for the deflection amplification factor (C_d), which are not directly mentioned in NBCC (2015). The American standard adopts the FEMA P695 (2009) methodology for determining seismic parameters of new systems.

Figure 68: Coefficients for seismic force-resisting systems in ASCE/SEI 7 (2016).

Seismic Force-Resisting System	Response Modification Coefficient, R^a	Overstrength Factor, $\Omega_0{}^b$	Deflection Amplification Factor, $C_d{}^c$
A. BEARING WALL SYSTEMS			
1. Special reinforced concrete shear walls[g,h]	5	2½	5
…	…	…	…
7. Special reinforced masonry shear walls	5	2½	3½
8. Intermediate reinforced masonry shear walls	3½	2½	2¼
9. Ordinary reinforced masonry shear walls	2	2½	1¾
10. Detailed plain masonry shear walls	2	2½	1¾
11. Ordinary plain masonry shear walls	1½	2½	1¼
12. Prestressed masonry shear walls	1½	2½	1¾
13. Ordinary reinforced AAC masonry shear walls	2	2½	2
14. Ordinary plain AAC masonry shear walls	1½	2½	1½
…	…	…	…
B. BUILDING FRAME SYSTEMS			
1. Steel eccentrically braced frames	8	2	4
…	…	…	…
16. Special reinforced masonry shear walls	5½	2½	4
17. Intermediate reinforced masonry shear walls	4	2½	4
18. Ordinary reinforced masonry shear walls	2	2½	2
19. Detailed plain masonry shear walls	2	2½	2
20. Ordinary plain masonry shear walls	1½	2½	1¼
21. Prestressed masonry shear walls	1½	2½	1¾

Source: Adapted from ASCE/SEI 7 (2016).

The differences between the different masonry systems in the American and Canadian standards are associated with the reinforcement details. The American standard classifies shear walls into ordinary, intermediate, and special, while the Canadian standard categorizes them

into conventional, moderately ductile, and ductile. The standards specify limits for the maximum uniform reinforcement spacing and the minimum rebar diameter for each category.

The Chilean standard (NCh 433, 2012) presents values for the response modification factor to be used in the static analysis (R) and spectral modal analysis (R_o). As highlighted in Figure 69, the R value must be adopted equal to 3 and 4, respectively, for reinforced masonry made of clay and concrete block. For seismic force-resisting masonry systems, R_o values must be adopted the same as R values. Unlike the American standard, NCh 433 (2012) does not specify the displacement amplification coefficient (C_d^*) for each type of system, but depending on the type of soil and the structure's natural period, as can be seen in Figure 70.

Figure 69: Maximum values for the response modification factors for seismic force-resisting masonry systems in NCh 433 (2012).

Sistema estructural	Material estructural	R	R_o
Muros y sistemas arriostrados	...	...	...
	Madera	5,5	7
	Albañilería confinada	4	4
	Albañilería armada		
	- De bloques de hormigón o unidades de geometría similar en las que se llenan todos los huecos, y albañilería de muros doble chapa	4	4
	- De ladrillos cerámicos tipo rejilla con y sin relleno de huecos y albañilería de bloques de hormigón o unidades de geometría similar en que no se llenan todos los huecos	3	3
Cualquier tipo de estructuración o material que no pueda ser clasificado en alguna de las categorías anteriores[3)]		2	-

Source: Adapted from NCh 433 (2012).

Figure 70: Values for the displacement amplification factor in NCh 433 (2012).

Tipo de Suelo	C_d^*	Rango Períodos
A	1.0	$T_n \leq 0.23$ seg
	$-0.055T_n^2 + 0.36T_n + 0.92$	0.23 seg $< T_n \leq 2.52$ seg
	$0.08T_n^2 - 0.9T_n + 3.24$	2.52 seg $< T_n \leq 5.00$ seg
B	1.0	$T_n \leq 0.47$ seg
	$0.95T_n + 0.55$	0.47 seg $< T_n \leq 2.02$ seg
	$0.065T_n^2 - 0.75T_n + 3.72$	2.02 seg $< T_n \leq 5.00$ seg
C	1.0	$T_n \leq 0.65$ seg
	$0.57T_n + 0.63$	0.65 seg $< T_n \leq 2.02$ seg
	$0.055T_n^2 - 0.63T_n + 2.83$	2.02 seg $< T_n \leq 5.00$ seg
D	1.0	$T_n \leq 0.90$ seg
	$1.1T_n$	0.90 seg $< T_n \leq 1.75$ seg
	1.93	1.75 seg $< T_n \leq 5.00$ seg

Source: Adapted from NCh 433 (2012).

Some studies have been conducted to determine the seismic behavior parameters of new or other commonly used masonry systems. The National Institute of Standards and Technology (NIST, 2010) evaluated the FEMA P695 (2009) methodology applied to structures with reinforced masonry shear walls. The wall configurations varied concerning the number of stories (2, 4, 8, and 12), wall aspect ratio, axial loading, seismic category, total or partial grouting, and reinforcement spacing. The archetype adopted was distinguished for buildings with a single story, Figure 71(a), and with multiple stories, Figure 71(b). The design and verification did not consider flanges and coupling between piers in walls with openings.

Figure 71: Plan view of the typical archetypes used in the NIST (2010) study.

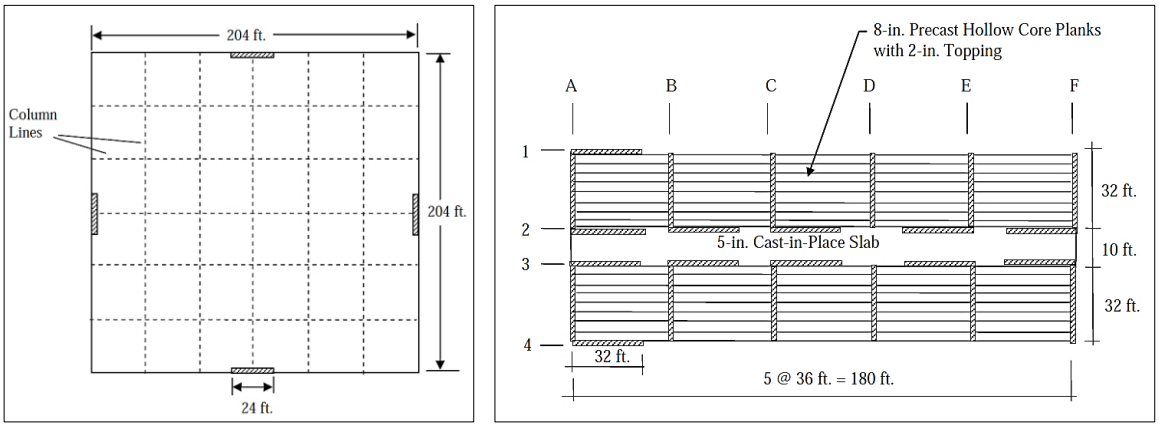

(a) Single story (b) Multiple stories

Source: NIST (2010).

The analyzes conducted by NIST (2010) were not intended to find new values for the seismic factors of this system but rather to assess whether the performance met the acceptance criteria established by the methodology and possible considerations to be adopted in future analyses. $C_d = R$ and equal to 5 or 2 were adopted as recommended by the American standard in Figure 68 for special and ordinary reinforced masonry, respectively. The general results indicated that the adopted configurations did not meet the acceptance criteria but that the overstrength factor found ($\Omega \cong 2.1$) was compatible with the value already established in by the American standard for this seismic-resisting system. If analyzed individually, the configurations with few stories did not satisfy the safety conditions, but those with more stories were consistent with the criteria. Since the acceptance is made statistically based on the whole set of responses, the report contests the use of the same collapse criterion and the R factor for low and high buildings since the literature has already demonstrated different seismic behavior for structures of short and long natural periods. Additionally, it was commented that the methodology is sensitive to the predicted failure mode and the hypotheses assumed in the non-linear modeling.

Shedid et al. (2011) applied the concepts defined by Uang (1991), the methodology of FEMA P695 (2009), and the principle of equal displacements to determine the seismic response parameters of fully grouted masonry shear walls with a rectangular section, and partially grouted masonry walls with flanges or end-confined, as shown in Figure 72. The authors commented that although the methodology of FEMA P695 (2009) is directed to buildings, the application to shear walls can represent a general system response since identical and equally spaced walls with neglected coupling are generally used in the analyses. Also, it is mentioned that the bilinear elastoplastic idealization associated with the equal displacement approach is a technique that engineers can easily implement in design situations, unlike the complexity imposed by pushover and dynamic analyses.

Figure 72: Arrangement of the walls studied by Shedid et al. (2011).

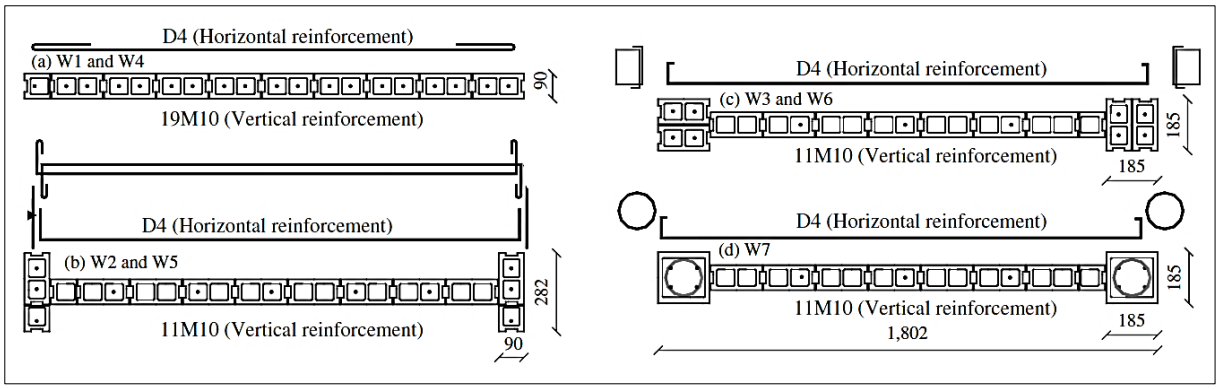

Source: Shedid et al. (2010, 2011).

The Shedid et al. (2011) analysis showed good coherence between the value of the response modification factor *(R)* calculated for the fully grouted wall of a rectangular section with the value estimated by the American standard, defined as 5. However, the deflection amplification factor (C_d) was 45% higher than that admitted in the standard. The value found for the ductility-related seismic force modification factor (R_d) for the fully grouted wall was significantly higher than that stipulated by the Canadian standard. The walls with flanges and those end-confined showed, respectively, gains around 30% and 90% for the R e R_d factors compared to the rectangular wall, demonstrating that even with reduced grouting and reinforcement, there was a gain in ductility. It is also evident that different aspect ratios and, consequently, different natural periods caused significant changes in the seismic coefficients.

Ezzeldin et al. (2016) adopted the same archetype, Figure 71, and the same number of stories as the NIST (2010) study to evaluate the performance of the seismic-resisting wall system with boundary members. The configuration of the walls was similar to the walls with ends confined by masonry columns analyzed by Shedid et al. (2011), shown in Figure 72. The

authors used the FEMA P695 (2009) methodology with $R = 5$ for all variations, a value indicated by the American standard for special reinforced masonry shear walls with rectangular sections. As specified in the methodology, $C_d = R$ was considered. The results showed that, unlike the evaluation made by NIST (2010) for walls of a rectangular section, the adoption of confining members at the ends made the system meet the acceptance criteria of the methodology for the configurations with 1 and 2 stories. Furthermore, higher ratios of collapse margin were obtained for taller buildings when boundary members were used, which implies that the response modification factor (R) may be higher than that adopted in the analyses.

Bolhassani et al. (2016b) proposed a different detailing so that partially grouted walls had their seismic performance improved. The authors studied the replacement of conventional detailing with single reinforcement, Figure 73(a), by the use of double reinforcement vertically and horizontally, Figure 73(b), and by double reinforcement vertically with joint reinforcement at every course, Figure 73(c). The authors argued that, as observed by Koutromanos and Shing (2010), systems with masonry shear walls with the usual detailing applying the seismic coefficients adopted by the American standard ($R = 2$, $\Omega = 2.5$ e $C_d = 1.75$) do not meet FEMA P695 (2009) safety criteria. Therefore, coefficients with lower values should be used, or the reinforcements' detailing should be improved.

Initially, Bolhassani et al. (2016b) determined the ductility factor (μ_d) and the ductility-related modification factor (R_d) using the equal energies approach and idealized elastoplastic diagram. Then, the FEMA P695 (2009) methodology was used to evaluate the seismic performance of the proposed details applied to the building configuration illustrated in Figure 73(d). The data confirmed greater ductility when using the suggested details and that these significantly improved the seismic performance of the building, which may be a good alternative for regions of more intense earthquakes.

In addition to the studies detailed here, research that encompasses seismic performance coefficients of masonry systems is found in Tomaževič and Weiss (1994), Benedetti et al. (1998), Tomaževič et al. (2004), Benedetti (2004), Morandi (2006), Tomaževič (2007), Frumento et al. (2009), Shahzada et al. (2012), Hassanli et al. (2015), Eixenberger (2017), and Sandoval et al. (2018).

Figure 73: Arrangement of walls and building studied by Bolhassani et al. (2016b).

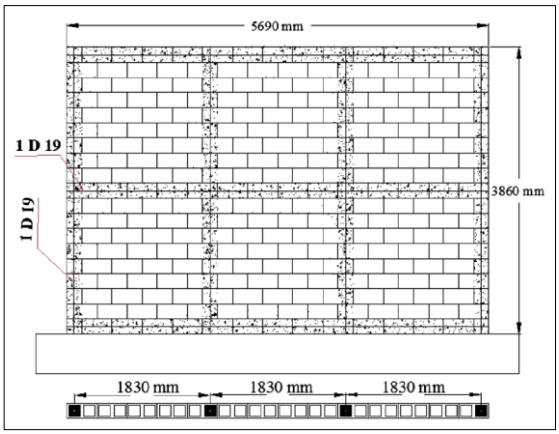

(a) Single reinforcement

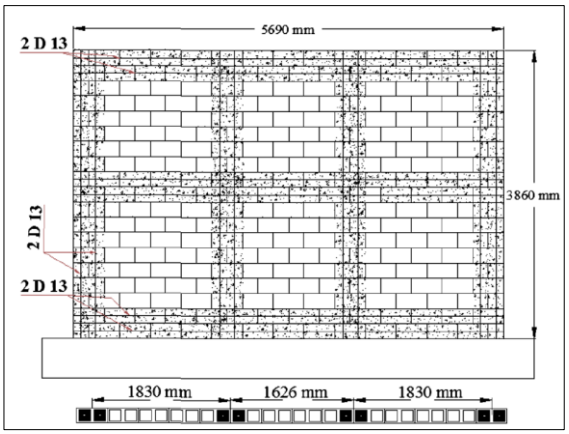

(b) Double reinforcement (DR)

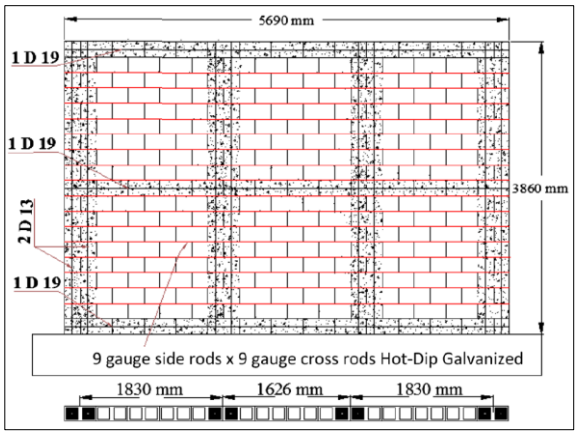

(c) DR vertically and joint reinforcement

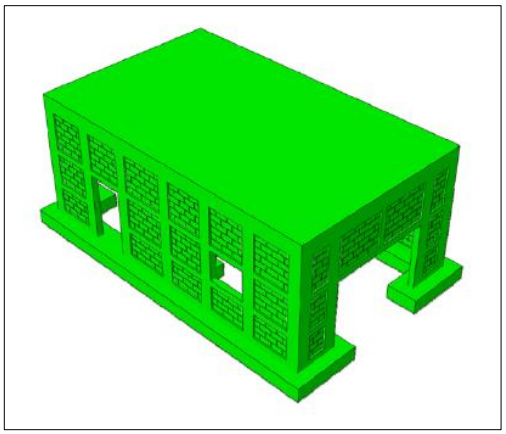

(d) Building configuration

Source: Bolhassani et al. (2016b).

4.2 NUMERICAL MODELING

The finite element model recalibrated and revalidated previously in Chapter 3 is used here to investigate the in-plane behavior and seismic performance of the walls. Further comparisons between the responses of the experimental and numerical walls W1, W2, D1, and D2 are performed in this chapter to ensure a suitable model for a more specific analysis. Comparisons are made with data collected from some Strain-Gauges (SGs) bonded to reinforcing bars and String-Potentiometers (SPs) placed on the masonry and external to it. The SGs and SPs on the first story were chosen since they are located at critical regions of the walls.

To obtain the diagonal displacements of the panels in the numerical models, the displacements in the horizontal and vertical directions of the plane elements at locations corresponding to the instrumentation were extracted. Then, these displacements were transformed to the SP direction, and the relative displacement thus calculated. The deformation of the reinforcement was obtained directly from the corresponding linear element.

The hysteresis and backbone curves from the instrumentation of the experimental tests and the respective FEM are presented in Figure 74 for walls D1-2, and in Figure 75 for walls W1-2; the location of the SG or SP is shown in each graph. The lateral displacement along the height of wall W1 is shown in Figure 76 for some levels of the maximum lateral load in the push direction (from left to right): $0.2V_{max}$, $0.4V_{max}$, $0.6V_{max}$, $0.8V_{max}$, V_{max}, and $0.8V_{max}$*, this last one corresponding to the instant when the load had dropped 20% after the peak.

Figure 74: Experimental and numerical response of SG and SP in walls D1 and D2.

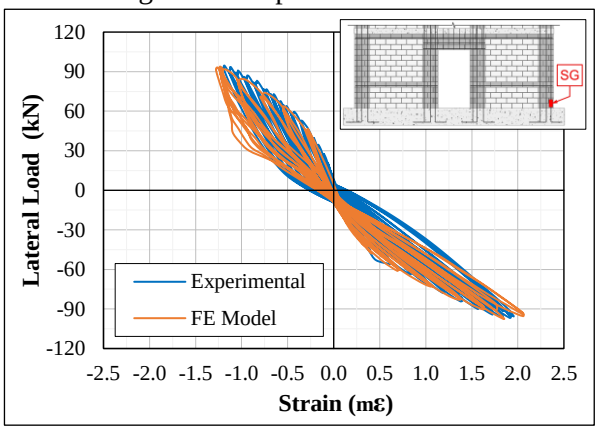

(a) Hysteresis curves of SG8 in wall D1

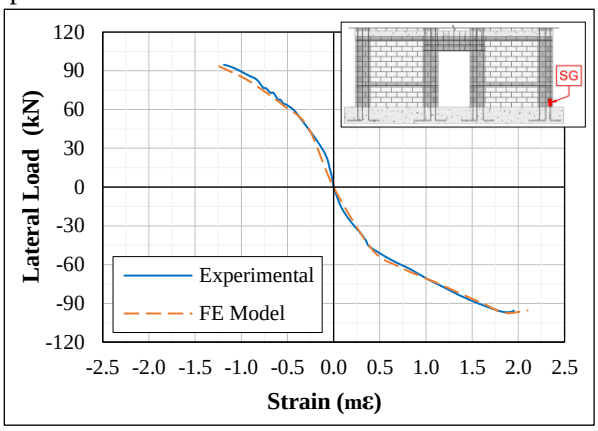

(b) Backbone curves of SG8 in wall D1

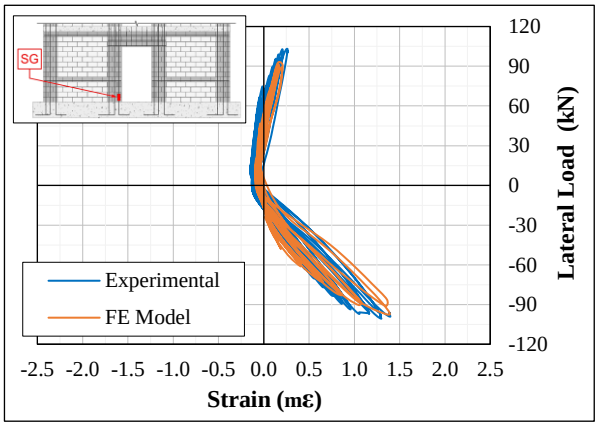

(c) Hysteresis curves of SG4 in wall D1

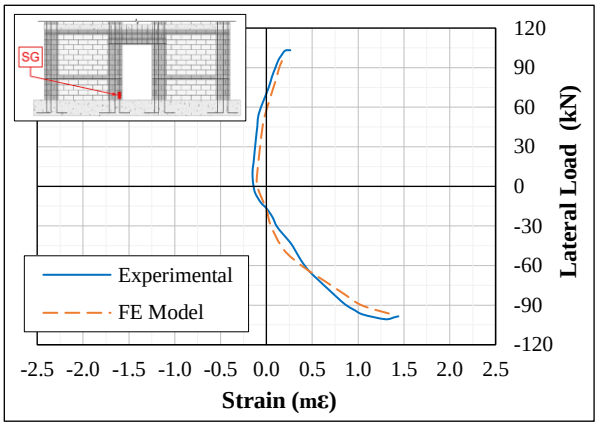

(d) Backbone curves of SG4 in wall D1

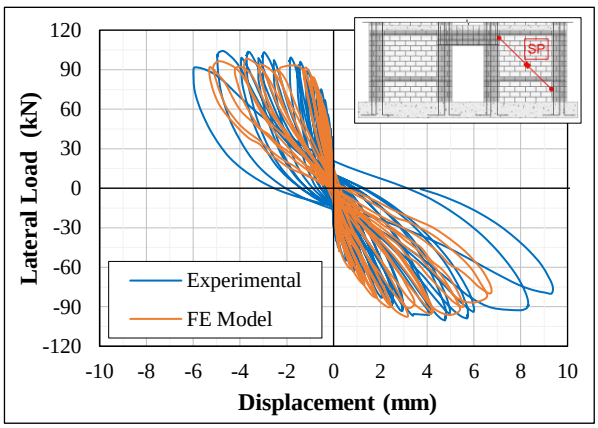

(e) Hysteresis curves of SP43 in wall D2

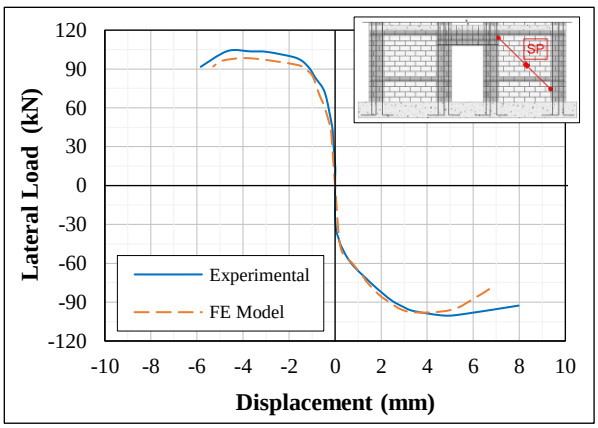

(f) Backbone curves of SP43 in wall D2

Source: Author.

Figure 75: Experimental and numerical response of SG and SP in walls W1 and W2.

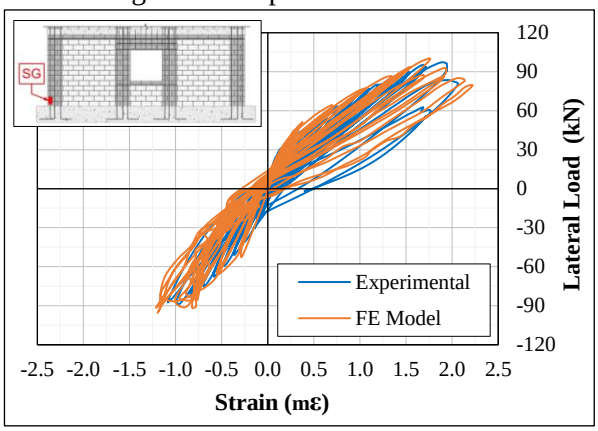

(a) Hysteresis curves of SG29 in wall W1

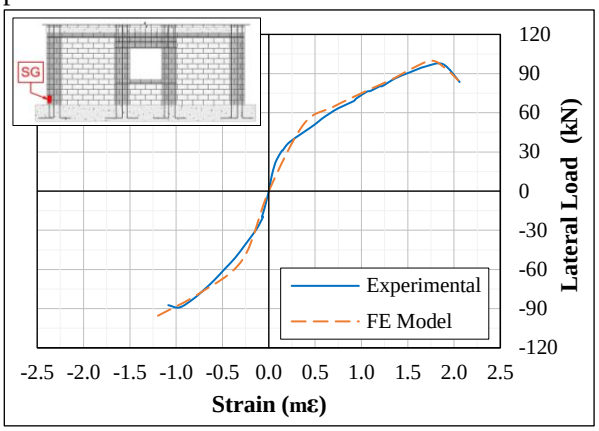

(b) Backbone curves of SG29 in wall W1

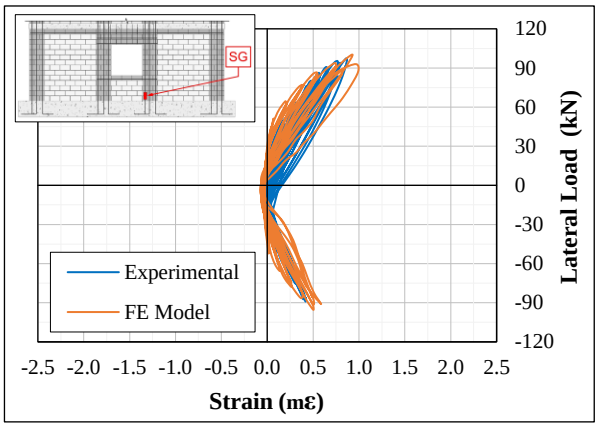

(c) Hysteresis curves of SG10 in wall W1

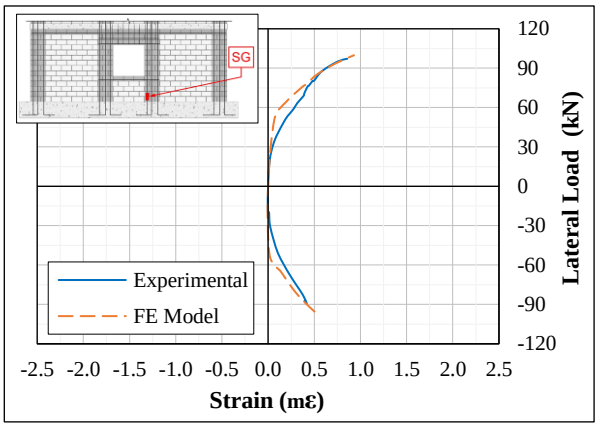

(d) Backbone curves of SG10 in wall W1

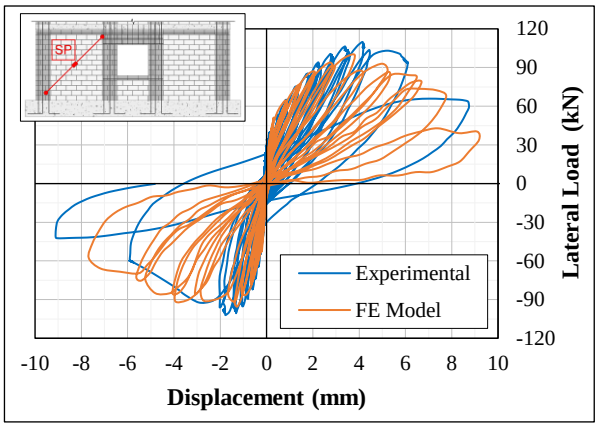

(e) Hysteresis curves of SP37 in wall W2

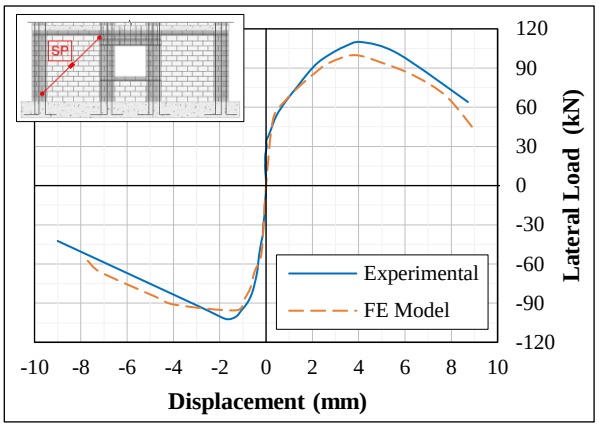

(f) Backbone curves of SP37 in wall W2

Source: Author.

The comparisons in Figure 74, Figure 75, and Figure 76 show again a good agreement between the finite element models and the experimental walls. These results confirm that the FEM can describe beyond the general behavior of the walls since it was able to simulate particulars such as the load-strain response of reinforcing bars, the load-displacement response of diagonal segments of the wall, and the lateral displacement along the wall height for different levels of lateral load.

Figure 76: Experimental and numerical lateral displacement profiles of wall W1 for different load levels.

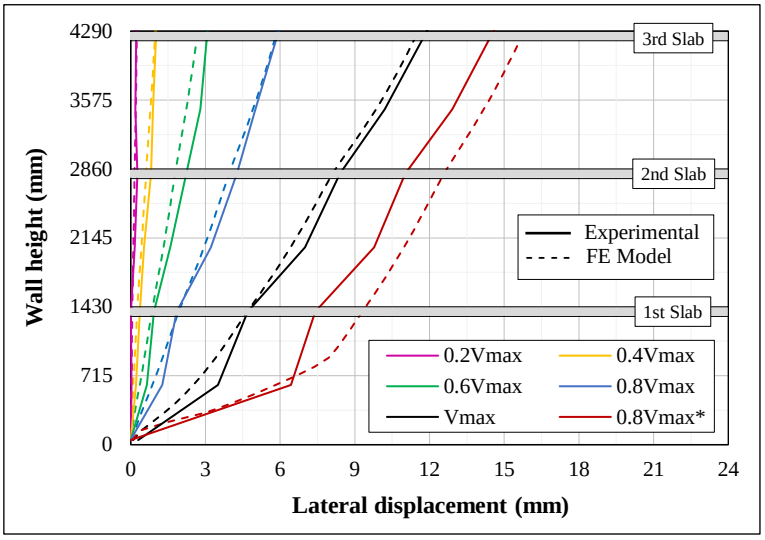

Source: Author.

4.3 DESCRIPTION OF THE BEHAVIOR OF THE WALLS

The load-strain responses of SG8 and SG4 in wall D1 and SG29 and SG10 in wall W1 confirm the significance of the reinforced masonry beam coupling the piers in frame action. SG8 and SG29 were bonded to a rebar at an extremity of the walls, and the bars deformed in compression and tension when the wall was subjected to displacements in the push and pull regimes, see Figure 74(a) and Figure 75(a). Differently, SG4 and SG10 were connected to a rebar adjacent to the opening and deformed only in tension with less elongation than SG8 and SG29, as seen in Figure 74(c) and Figure 75(c), for both regimes. This behavior is commonly neglected in simple design methods since the piers are considered isolated and, consequently, each pier has symmetrical flexural deformations at the ends.

The lateral displacement profiles shown in Figure 76 present a linear approximation from the base to the top of the wall up to close to the maximum lateral load. This linearity implies that the wall behaved, for these load stages, like a solid composite with shear deformations and a linear distribution of the lateral load along the wall height. As the lateral load increases to the maximum and further, the lateral displacement profile becomes non-linear, with predominantly horizontal displacement at the first story caused mainly by the major cracks on the ungrouted masonry in this region, as seen in the evolution of the deformed and cracked shape in Figure 77.

The vertical strain along the length of the first course was plotted in Figure 78 for the numerical walls with window and door openings aiming to examine the deformation along the

horizontal section. As in Figure 76, the graphs include results for different proportions of the maximum lateral load in the push direction (from left to right) before and after the peak.

Figure 77: Numerical deformed and cracked shape of wall W1 for different load levels.

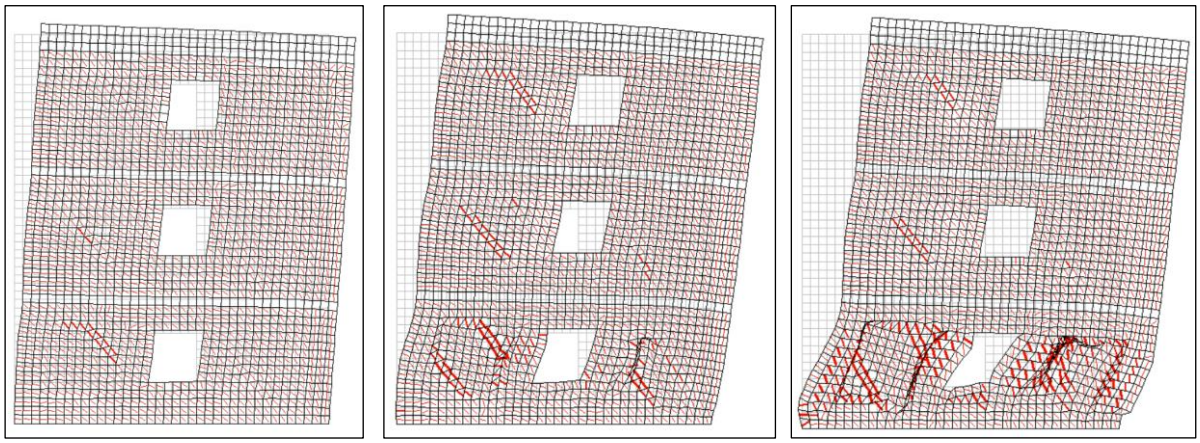

(a) $0.8V_{max}$ (b) V_{max} (c) $0.8V_{max}$*

Source: Author.

Figure 78: Vertical strain distribution along the length of the wall for a section crossing the first course.

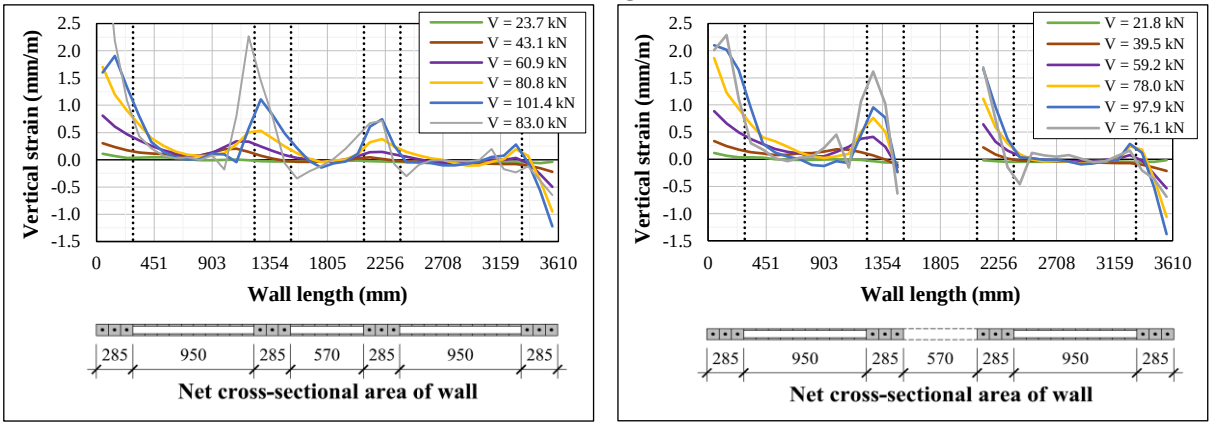

(a) Wall with window openings (b) Wall with door openings

Source: Author.

Analyzing both cases in Figure 78, it can be seen that the sections remain almost plane only for low levels of the lateral load. Also, the differences between the deformations in the ungrouted and grouted/reinforced regions is evident as the lateral load increases. This contrast can be attributed to the difference in the stiffnesses as the grouted region is significantly stiffer and, consequently, attracts the loads. It appears that the concentration of material area and reinforcement at the ends of the wall piers induced the system to perform like a continuous frame, with the grouted regions behaving like columns and the ungrouted regions acting like confined masonry.

4.4 NUMERICAL INVESTIGATION OF DIFFERENT DETAILING TYPES

In order to investigate variations of the detailing used in the tests, new walls were modeled taking the wall with window openings (walls W1-2) as the reference, named now as Wall M1. The description and illustration of the effective net sectional area crossing the opening of each one of the walls are presented in Figure 79. Walls M2 to M7 differ from Wall M1 in the vertical grouting and reinforcement amount at the ends of the wall piers aiming to examine the influence of different stiffnesses in the grouted masonry columns. The changes in Walls M8 and M9 relate to the vertical grouting and reinforcement spacing, keeping the effective net cross-sectional area and reinforcement ratio constant.

Figure 79: Configurations of walls for the different detailing types; dimensions in mm.

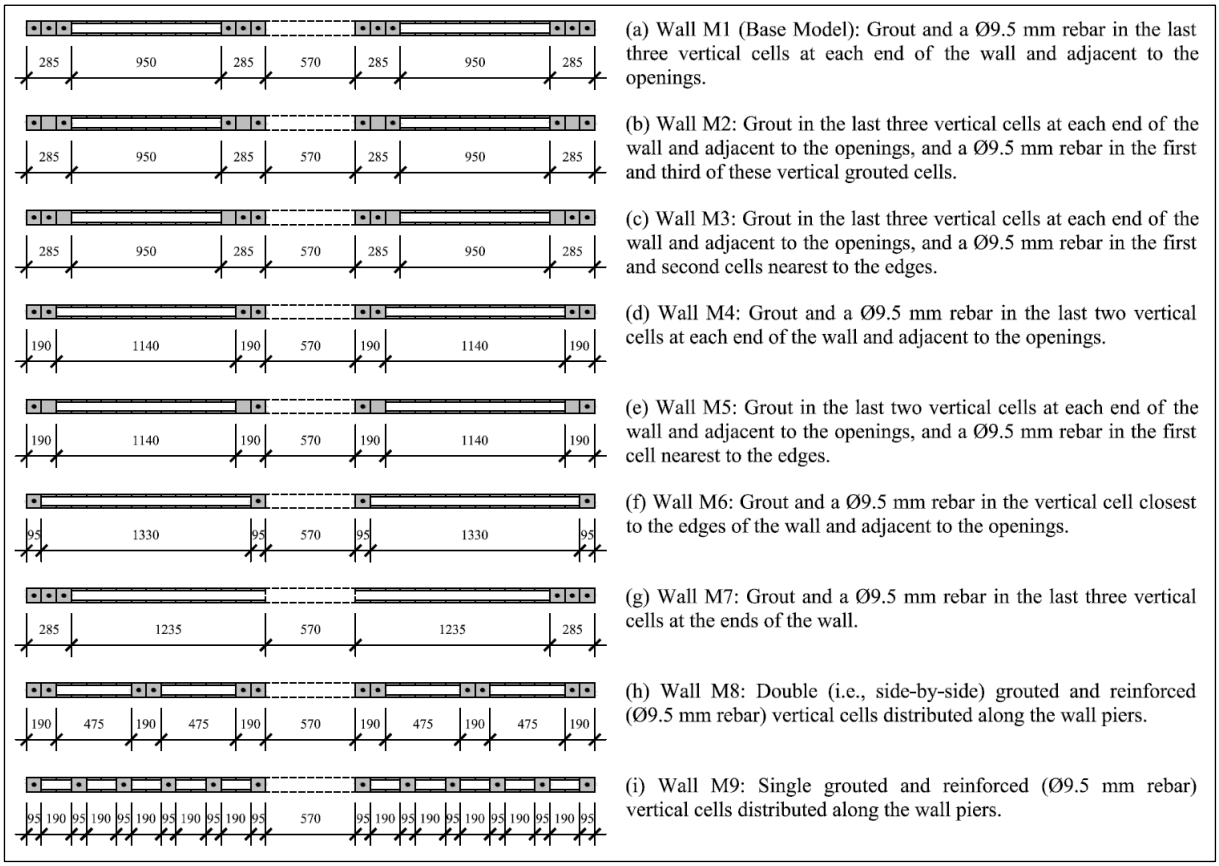

Source: Author.

The level of vertical pre-compression significantly impacts wall behavior, especially the lateral load capacity and ductility: higher axial load increases capacity and decreases ductility. The experimental walls were tested only with an axial load of 50 kN, which, added to the self-weight, implied a compressive stress equal to 4% of the masonry compressive strength at the base of the wall. Therefore, seeking a wider investigation in this study, Walls M1 to M9 had duplicated models, one with the axial load as used in the experimental walls and another with

a higher axial load, specifically 390 kN, resulting in a compressive stress of approximately 20% of the masonry compressive strength. This level of compressive stress of $0.2f'_m$ represents circumstances closer to actual design practice for mid and/or high-rise masonry buildings.

4.4.1 Seismic performance assessment

4.4.1.1 Strength and ductility

a) Idealized response

The idealized load-displacement response of masonry is usually simplified via bilinear or trilinear elastoplastic curves characterized by the initial elastic stiffness (K_{el}), maximum lateral load (V_{max}), ultimate lateral load (V_u), yield displacement (d_y), and ultimate displacement (d_u). Many different strategies to define the idealized response and its parameters have been used by researchers (Shedid et al., 2008; Banting and El-Dakhakhni, 2014; Bolhassani et al., 2016b; Ramírez et al., 2016; Calderón et al., 2017; Sandoval et al., 2018; Seif ElDin et al., 2019b; Calderón et al., 2021a; Calderón et al., 2021b), but there is still no consensus. Thus, three approaches are discussed in detail here to show the impact on the seismic performance factors. The equal energy principle was invoked in the process since all the walls analyzed here have $T_n < 0.5\ s$ calculated using the aforementioned Equation 60, assuming the stiffness in the backbone response when it deviates significantly from the elastic phase.

In the first bilinear approach (BL1), Figure 80(a), the actual response is idealized as a bilinear elastic-perfectly plastic curve with a yielding load plateau $V_y = V_{max}$ and d_u equal to the displacement at a load of $0.8V_{max}$ in the post-peak stage. The yield displacement is found using Equation 69 by equalizing the total energy (U_t), i.e., the area, under the actual and idealized curves. Consequently, the elastic stiffness is estimated as $K_{el} = V_y/d_y$. The seismic factors are calculated using Equations 70 to 74, where V_{el} is the load for which the actual response deviates significantly from the elastic stage, and d_{el} is the corresponding displacement in the idealized curve computed as $d_{el} = V_{el}/K_{el}$.

$$d_y = 2\left(d_u - {U_t}/{V_{max}}\right) \quad \text{Eq. 69}$$

$$\mu_d = {d_u}/{d_y} \quad \text{Eq. 70}$$

$$\Omega = {V_y}/{V_{el}} \quad \text{Eq. 71}$$

$$C_d = {d_u}/{d_{el}} = \mu_d \cdot \Omega \quad \text{Eq. 72}$$

$$R_d = {V_e}/{V_y} = \sqrt{2\mu_d - 1} \quad \text{Eq. 73}$$

$$R = {V_e}/{V_{el}} = R_d \cdot \Omega \quad \text{Eq. 74}$$

The second bilinear approach (BL2) is illustrated in Figure 80(b). This idealized response is also a bilinear elastic-perfectly plastic curve with d_u corresponding to $0.8V_{max}$ in the post-peak stage. However, the initial elastic stiffness is defined by the point where the actual response starts to deviate significantly from the elastic phase, $K_{el} = V_{el}/d_{el}$. The yielding load plateau is calculated as $V_y = K_{el} \cdot d_y$, where d_y is obtained from Equation 75 by equalizing the energy under the actual and idealized curves. Like the BL1 approach, the seismic factors are calculated using Equations 70 to 74.

$$d_y = d_u - \sqrt{{d_u}^2 - 2\left({U_t}/{K_{el}}\right)} \quad \text{Eq. 75}$$

The trilinear approach (TL), Figure 80(c), idealizes the actual response as a trilinear elastic-plastic curve with the same peak load point and d_u corresponding to $0.8V_{max}$ in the post-peak phase. As in the BL2 approach, K_{el} is defined by the point where the actual response deviates significantly from the elastic stage. There is no yielding load plateau in this approach. The idealized linear elastic part ends at $V_y = K_{el} \cdot d_y$ with d_y calculated using Equation 76 from the energy equality under the actual and idealized curves. Calculation of μ_d and R is the same as in previous approaches, but Ω, C_d, and R_d are estimated differently. Equations 77 to 79 were deduced for these factors considering the auxiliary variables $\eta = V_y/V_{max}$ and $\Delta_d = d_{Vmax}/d_y$.

$$d_y = \frac{2U_t + V_{max}\left(0.8d_{V_{max}} - 1.8d_u\right)}{K_{el} \cdot d_{V_{max}} - V_{max}} \quad \text{Eq. 76}$$

$$\Omega = {V_{max}}/{V_{el}} \quad \text{Eq. 77}$$

$$C_d = {d_u}/{d_{el}} = \mu_d \cdot \Omega \cdot \eta \quad \text{Eq. 78}$$

$$R_d = {V_e}/{V_{max}} = \sqrt{\eta^2\Delta_d + \eta(1.8\mu_d - 0.8\Delta_d - 1)} \quad \text{Eq. 79}$$

The post-peak response can be ignored for a more conservative analysis, as used by other authors (Calderón et al., 2017; Calderón et al., 2021b). In this situation, in each of the approaches in Figure 80, V_u and d_u must be taken equal to V_{max} and d_{Vmax}, and the total energy

under the actual and idealized curves must be limited to the peak load point. The idealized curves for the three approaches are shown with the actual response of Wall M1 for the push direction in Figure 81. Furthermore, the graphs in Figure 82 present the average values between the push and pull directions of the seismic performance factors for all approaches with and without considering the post-peak stage.

Figure 80: Approaches for equivalent elastoplastic response idealization.

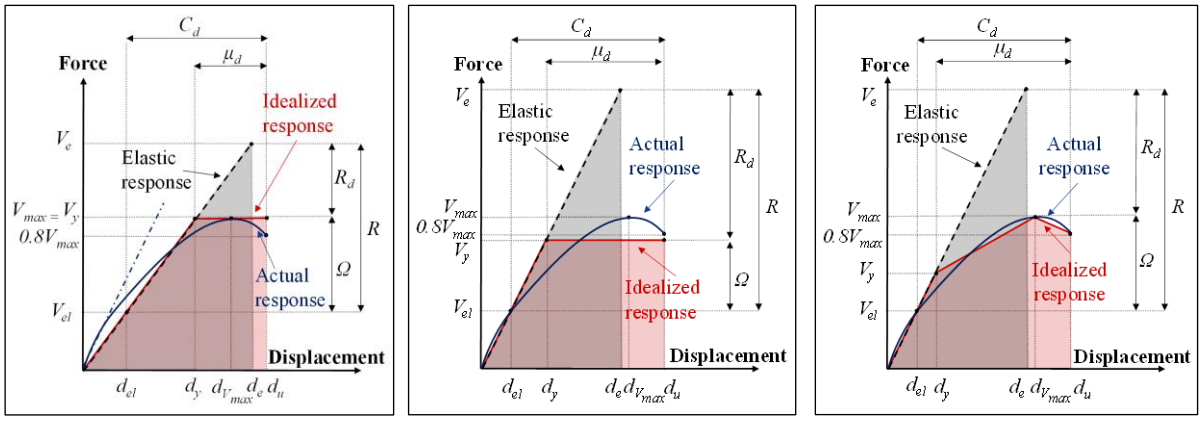

(a) BL1 (b) BL2 (c) TL

Source: Author.

Figure 81: Actual and idealized responses for Wall M1.

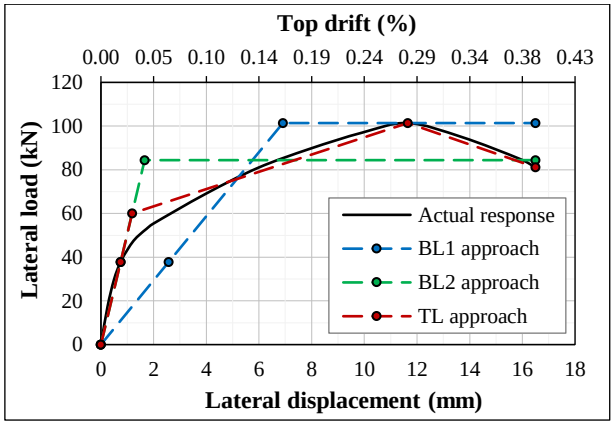

Source: Author.

Figure 82: Seismic performance factors of Wall M1 for the three approaches.

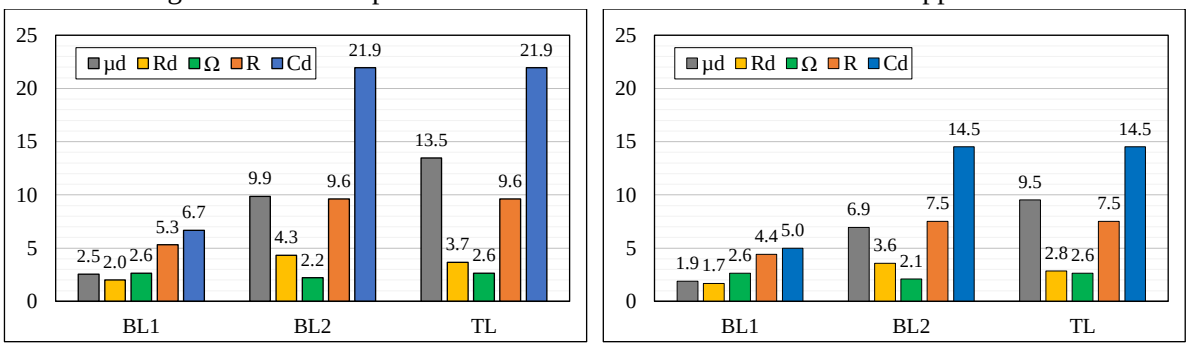

(a) Considering the post-peak stage (b) Without considering the post-peak stage

Source: Author.

Figure 81 reveals remarkable differences between the idealized responses. The BL1 approach shifts the initial behavior of the wall substantially, implying an initial elastic stiffness 70% smaller and, consequently, a less ductile response than actual. The BL2 approach uses the same initial elastic stiffness as the actual response but penalizes the lateral load capacity of the wall by approximately 20%. The TL approach fits the actual response more closely, preserving the three essential characteristics: the initial elastic stiffness, the lateral load capacity, and the decay in the post-peak phase.

Comparing the seismic performance factors in Figure 82, it may be seen that the BL1 approach is the most conservative, presenting a μ_d up to five times smaller, R_d and R two times smaller, and C_d three times smaller than the other two approaches. The BL2 and TL approaches have the same value for R and C_d but different μ_d, R_d, and Ω; while the BL2 approach has a higher R_d, the TL approach has higher μ_d and Ω.

The seismic factors R_d and R present a decrease of 17% to 22%, while μ_d and C_d demonstrate a reduction of 25% to 34% when comparing the approaches with and without considering the post-peak response, Figure 82(a) and Figure 82(b), respectively. These differences can be seen favorably as being more conservative but ignore the wall's actual extra ductility from the post-peak behavior.

b) Comparison of wall responses

The backbone curves of all walls with the two different vertical pre-compression levels were generated and plotted in Figure 83 to provide an overall assessment. While the load-displacement behavior is presented in Figure 83(a), the stress-displacement behavior is shown in Figure 83(b), where stress is defined as the load divided by the effective net sectional area crossing the opening. Since there are many walls, and the difference between the responses of the push and pull regimes is minimal, only the response for the push regime is shown, limiting the curves to the stage when the peak load dropped 20%. The suffixes L (low) and H (high) were used in the name of walls to differentiate the axial load cases. Furthermore, graphs for certain wall subgroups are exhibited separately in Figure 84 for more specific comparisons.

The seismic performance factors were calculated for all walls considering the idealized trilinear response with the post-peak contribution since this approach is considered the most realistic in reproducing the wall behavior. The data and results are presented in Table 30 for both the push and pull regimes (also the average) of each wall. To differentiate the load cases, the prefixes L (low) and H (high) were used in the names of the walls once again.

Figure 83: Push backbone curves of all walls.

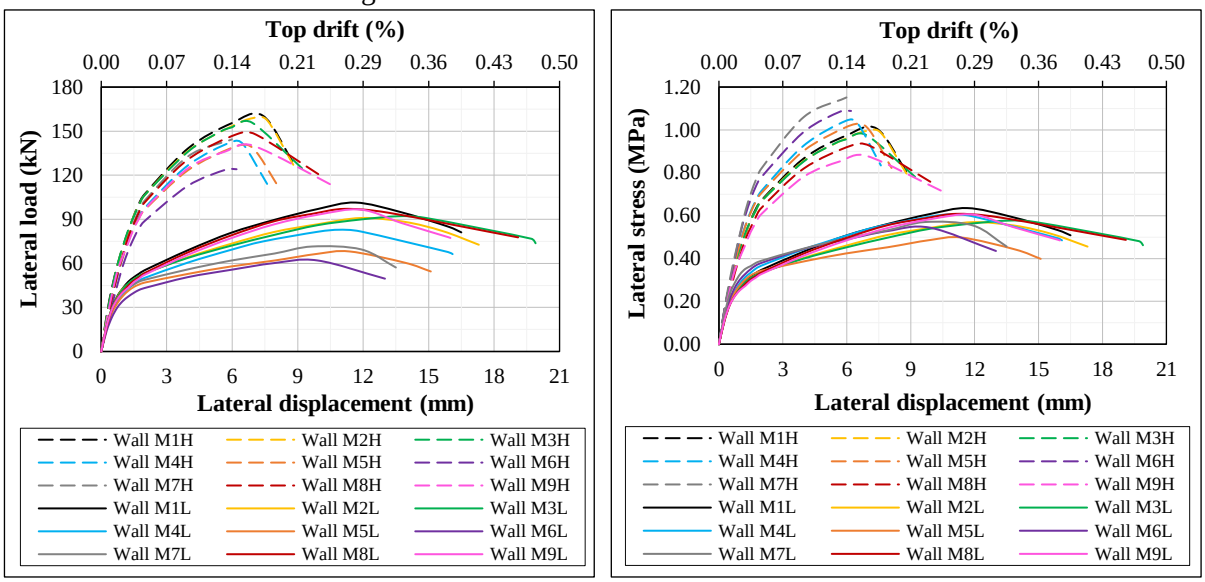

(a) Load-displacement graph (b) Stress-displacement graph

Source: Author.

Figure 84: Push backbone curves of specific wall subgroups.

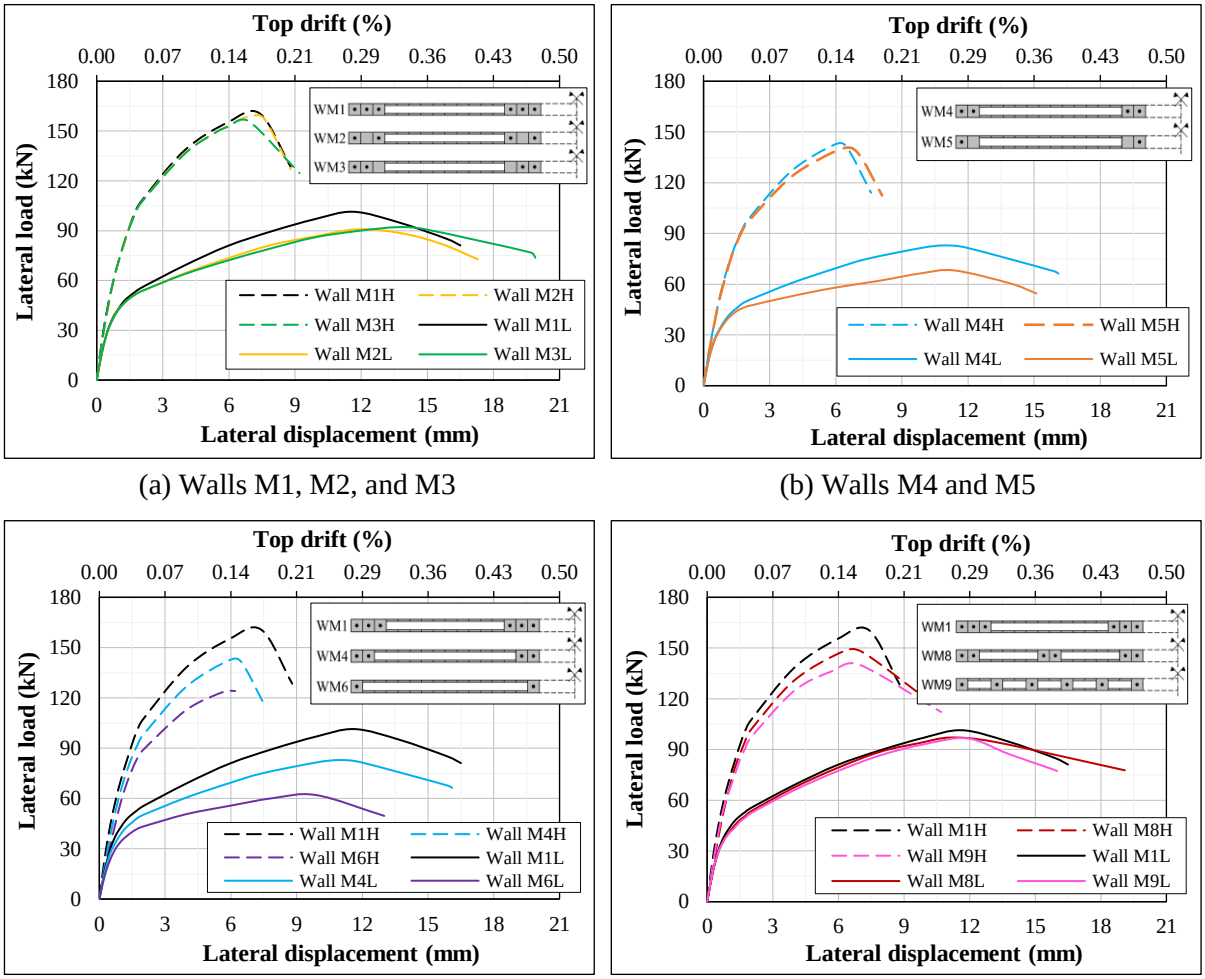

(a) Walls M1, M2, and M3 (b) Walls M4 and M5

(c) Walls M1, M4, and M6 (d) Walls M1, M8, and M9

Source: Author.

Table 30: Seismic performance data and results for all walls.

Wall Model	W (kN)	Area (mm²)	Load Direction	V_{max} (kN)	τ_{max} (MPa)	$\sigma_{s_{Vmax}}$ (mm)	d_{Vmax} (mm)	d_{Vu} (mm)	U_{Vmax} (kN·mm)	U_{Vu} (kN·mm)	K_{el} (kN/mm)	T_n (s)	μ_d	R_d	Ω	R	C_d
Wall M1L	81.2	159600	Push	101.4	0.64	369.5	11.7	16.5	874.1	1322.9	50.9	0.08	14.0	3.6	2.7	9.7	22.2
			Pull	97.7	0.61	343.0	9.9	16.1	712.4	1280.6	49.0	0.08	13.0	3.7	2.6	9.5	21.7
			Avg.	99.6	0.62	356.3	10.8	16.3	793.3	1301.8	50.0	0.08	13.5	3.7	2.7	9.6	22.0
Wall M1H	420.5	159600	Push	160.6	1.01	219.4	7.2	8.8	894.1	1096.4	62.0	0.17	4.4	2.3	1.7	4.0	5.9
			Pull	155.2	0.97	184.0	5.9	8.8	681.6	1082.0	59.9	0.17	4.2	2.4	1.7	4.0	5.9
			Avg.	157.9	0.99	201.7	6.6	8.8	787.9	1089.2	61.0	0.17	4.3	2.4	1.7	4.0	5.9
Wall M2L	81.2	159600	Push	90.9	0.57	421.0	11.9	17.3	823.1	1279.2	50.1	0.08	14.7	3.9	2.4	9.6	23.3
			Pull	87.8	0.55	400.2	10.1	17.1	658.2	1255.4	48.4	0.08	13.4	4.0	2.4	9.5	22.9
			Avg.	89.4	0.56	410.6	11.0	17.2	740.7	1267.3	49.2	0.08	14.1	4.0	2.4	9.6	23.1
Wall M2H	420.5	159600	Push	158.9	1.00	242.4	6.9	8.8	812.8	1086.9	61.9	0.17	4.4	2.3	1.7	4.0	5.9
			Pull	153.0	0.96	201.4	5.9	7.6	662.5	892.2	59.6	0.17	3.9	2.2	1.7	3.6	5.1
			Avg.	156.0	0.98	221.9	6.4	8.2	737.7	989.6	60.8	0.17	4.2	2.3	1.7	3.8	5.5
Wall M3L	81.2	159600	Push	92.1	0.58	460.8	13.6	19.9	971.7	1504.8	49.7	0.08	16.3	4.2	2.5	10.5	26.8
			Pull	92.3	0.58	434.2	13.4	18.2	958.1	1350.0	49.8	0.08	15.7	4.0	2.5	9.9	24.5
			Avg.	92.2	0.58	447.5	13.5	19.1	964.9	1427.4	49.8	0.08	16.0	4.1	2.5	10.2	25.7
Wall M3H	420.5	159600	Push	155.9	0.98	224.2	6.7	9.2	804.1	1126.8	61.7	0.17	4.7	2.4	1.7	4.1	6.2
			Pull	153.0	0.96	192.3	5.9	8.1	678.4	976.8	60.6	0.17	3.8	2.3	1.7	3.8	5.4
			Avg.	154.5	0.97	208.3	6.3	8.7	741.3	1051.8	61.1	0.17	4.3	2.4	1.7	4.0	5.8
Wall M4L	79.4	136800	Push	82.9	0.61	379.3	10.9	16.1	689.7	1084.0	45.5	0.08	13.6	3.8	2.5	9.3	21.7
			Pull	81.0	0.59	345.0	9.9	16.0	610.7	1089.0	44.5	0.08	12.1	3.9	2.4	9.3	21.5
			Avg.	82.0	0.60	362.2	10.4	16.1	650.2	1086.5	45.0	0.08	12.9	3.9	2.5	9.3	21.6
Wall M4H	418.6	136800	Push	142.6	1.04	193.4	6.0	7.6	608.3	826.0	56.9	0.17	3.9	2.1	1.7	3.6	5.1
			Pull	142.7	1.04	184.8	5.9	7.2	624.7	787.8	56.9	0.17	3.5	2.1	1.7	3.5	4.8
			Avg.	142.7	1.04	189.1	6.0	7.4	616.5	806.9	56.9	0.17	3.7	2.1	1.7	3.6	5.0
Wall M5L	79.4	136800	Push	68.1	0.50	424.8	11.4	15.1	620.5	850.8	44.4	0.08	14.0	4.0	2.1	8.3	20.3
			Pull	66.2	0.48	400.3	9.9	14.7	520.3	819.8	43.2	0.09	13.3	4.1	2.0	8.2	19.8
			Avg.	67.2	0.49	412.6	10.7	14.9	570.4	835.3	43.8	0.09	13.7	4.1	2.1	8.3	20.1
Wall M5H	418.6	136800	Push	140.6	1.03	257.5	6.7	8.1	698.8	878.7	56.3	0.17	4.2	2.2	1.7	3.7	5.4
			Pull	136.2	1.00	186.6	5.4	6.8	529.3	702.4	54.5	0.18	3.5	2.1	1.6	3.3	4.6
			Avg.	138.4	1.01	222.1	6.1	7.5	614.1	790.6	55.4	0.17	3.9	2.2	1.7	3.5	5.0
Wall M6L	77.7	114000	Push	62.0	0.54	368.8	9.9	13.0	494.1	666.7	40.5	0.09	11.8	3.7	2.1	7.7	17.5
			Pull	61.7	0.54	406.1	9.7	14.0	480.4	733.1	40.3	0.09	11.9	3.9	2.0	8.1	18.8
			Avg.	61.9	0.54	387.5	9.8	13.5	487.3	699.9	40.4	0.09	11.9	3.8	2.1	7.9	18.2
Wall M6H	417.0	114000	Push	124.1	1.09	177.8	6.2	6.2	572.9	572.9	51.7	0.18	3.2	2.0	1.6	3.2	4.2
			Pull	126.1	1.11	213.7	5.9	5.9	541.9	541.9	52.5	0.18	3.2	1.9	1.6	3.1	4.0
			Avg.	125.1	1.10	195.8	6.1	6.1	557.4	557.4	52.1	0.18	3.2	2.0	1.6	3.2	4.1
Wall M7L	79.1	125400	Push	71.5	0.57	348.3	9.7	13.5	538.6	797.4	48.3	0.08	13.0	3.9	2.0	7.7	18.1
			Pull	68.9	0.55	325.3	9.7	12.9	541.9	747.3	46.5	0.08	12.0	3.9	1.9	7.5	17.3
			Avg.	70.2	0.56	336.8	9.7	13.2	540.3	772.4	47.4	0.08	12.5	3.9	2.0	7.6	17.7
Wall M7H	418.4	125400	Push	144.4	1.15	132.6	6.0	6.0	633.5	633.5	58.9	0.17	3.1	1.9	1.6	3.1	4.0
			Pull	141.7	1.13	112.9	5.7	5.7	592.4	592.4	57.8	0.17	2.8	1.9	1.6	3.0	3.8
			Avg.	143.1	1.14	122.8	5.9	5.9	613.0	613.0	58.3	0.17	3.0	1.9	1.6	3.1	3.9
Wall M8L	81.2	159600	Push	97.1	0.61	343.1	11.2	19.1	803.8	1507.4	48.5	0.08	15.6	3.9	2.7	10.6	25.7
			Pull	95.5	0.60	343.9	9.9	18.9	705.5	1502.1	47.7	0.08	14.2	4.0	2.7	10.6	25.4
			Avg.	96.3	0.60	343.5	10.6	19.0	754.7	1504.8	48.1	0.08	14.9	4.0	2.7	10.6	25.6
Wall M8H	420.5	159600	Push	147.9	0.93	184.8	6.2	10.2	661.7	1206.6	58.3	0.17	5.0	2.5	1.7	4.3	6.9
			Pull	145.6	0.91	167.9	5.4	10.8	558.4	1285.8	57.4	0.17	4.9	2.7	1.7	4.5	7.3
			Avg.	146.8	0.92	176.4	5.8	10.5	610.1	1246.2	57.8	0.17	5.0	2.6	1.7	4.4	7.1
Wall M9L	81.2	159600	Push	96.6	0.61	384.8	11.9	16.0	859.3	1215.0	48.0	0.08	13.4	3.5	2.7	9.6	21.5
			Pull	93.1	0.58	355.2	9.9	15.3	674.3	1142.0	46.3	0.08	12.8	3.6	2.6	9.3	20.6
			Avg.	94.9	0.59	370.0	10.9	15.7	766.8	1178.5	47.1	0.08	13.1	3.6	2.7	9.5	21.1
Wall M9H	420.5	159600	Push	140.2	0.88	217.3	6.9	10.7	736.5	1209.9	59.7	0.17	5.9	2.7	1.9	5.1	8.6
			Pull	141.1	0.88	182.0	5.7	9.3	576.0	1030.3	60.1	0.17	5.4	2.5	1.9	4.7	7.5
			Avg.	140.7	0.88	199.7	6.3	10.0	656.3	1120.1	59.9	0.17	5.7	2.6	1.9	4.9	8.1

Source: Author.

Differences between the responses of walls subjected to the two levels of axial load can be clearly seen in Figure 83. Walls with the lower vertical pre-compression presented a more ductile behavior but a lower lateral load capacity. Otherwise, walls with the higher axial load had a higher lateral capacity but a more brittle response, especially Walls M6 and M7, which achieved failure at the peak load without the capacity to continue deforming in a post-peak phase. The results in Table 30 confirm this perception: V_{max} increased between 48% (Wall M9) and 106% (Wall M5), whereas μ_d decreased between 57% (Wall M9) to 76% (Wall M7) when comparing the walls with the higher axial load against the same walls with the lower axial load. The seismic factors of R_d, Ω, R, and C_d reduced up to 51%, 37%, 62%, and 78%, respectively.

The comparisons between the responses of Walls M1, M2, and M3 in Figure 84(a) and Walls M4 and M5 in Figure 84(b), assisted by the results in Table 30, indicate that changing the amount of vertical reinforcement at the wall pier ends influenced the V_{max}, Ω, and R of the walls up to 18%, 16%, and 11%, respectively, in the situation with the lower axial load. Related to ductility, Wall M3L presents increases of 19%, 12%, and 17% in μ_d, R_d, and C_d, respectively, and a smaller peak load than Wall M1L. Also, M3L is more ductile than M2L, indicating that placing the reinforcement closest to the ends is more effective for achieving ductility. In contrast, the responses of these walls did not present differences greater than 3% in the higher pre-compression cases.

Examining Figure 84(c), it is observed that reducing the number of grouted/reinforced cells at the wall pier ends from three in Wall M1 to two in Wall M4 and one in Wall M6 provoked, as expected, a worsening in the in-plane response of the walls for both levels of vertical pre-compression. The reduction of the lateral load capacity was greater for the lower level of axial load, being 18% for Wall M4 and 38% for Wall M6; in comparison, the decrease was 10% and 21% for these walls, respectively, in the case with the higher axial load. The ductility, in its turn, reduced less for Walls M4L and M6L, 5% and 12%, respectively, than for Walls M4H and M6H, 14% and 26%, respectively.

The graph in Figure 83(b) shows that walls with less grout, i.e., smaller net cross-sectional area, are subjected to higher stress than others for the same displacement. This implies that the material strength limit was achieved at a lower lateral load.

No lateral capacity gains were noted for the walls that had the grouting and reinforcement spaced along the wall piers (Walls M8 and M9) when compared to concentrating them at the wall pier ends (Wall M1), see Figure 84(d). In fact, Walls M8 and M9 had lateral

capacities 3.3% and 4.7% less than Wall M1 with the lower axial load and 7.1% and 10.9% less with the higher axial load. Wall M8 has an advantage on the SPFs for both levels of vertical pre-compression, whereas Wall M9 performed better than Wall M1 only in the case of the higher axial load. About the values, the seismic factors of μ_d, R_d, R, and C_d were up to 15%, 11%, 10%, and 20% higher comparing Wall M8H with Wall M1H, and 31%, 11%, 23%, and 36% higher comparing Wall M9H with Wall M1H.

Since Walls M1, M8, and M9 have the same amount of grout and reinforcement, a simple comparison is made here to measure the efficiency of the detailing using the parameter $V_e = V_{max} \cdot R_d$, which is the maximum load capacity a wall should have, assuming linear elastic behavior, as illustrated in Figure 80. The ductility parameters are incorporated into the calculation of R_d (Equation 79), and, therefore, using V_e as a comparison index implies simultaneous consideration of the load capacity and ductility. As shown in Table 42, the difference varied from -7.3% to 4.7%, which suggests that those distinct details examined here have similar efficiency. These results indicate that the reinforcement spacing limits for shear walls specified by ASCE/SEI 7 (2016) and NBCC (2015) can be relaxed at the center of the walls as long the total amount of grout and reinforcement are respected and concentrated at the wall ends, giving some differences in the SPFs but similar design efficiency.

Table 31: Comparison between the detailing efficiency of Walls M1, M8, and M9.

Wall Model	V_{max} (kN)	ΔV_{max} (%)	R_d	ΔR_d (%)	V_e (kN)	ΔV_e (%)
Wall M1L	99.6	---	3.7	---	363.4	---
Wall M8L	96.3	-3.3	4.0	8.2	380.4	4.7
Wall M9L	94.9	-4.7	3.6	-2.7	336.7	-7.3
Wall M1H	157.9	---	2.4	---	371.1	---
Wall M8H	146.8	-7.1	2.6	10.6	381.6	2.8
Wall M9H	140.7	-10.9	2.6	10.6	365.7	-1.4

Source: Author.

Regarding the failure mode of walls, the stress in the reinforcing bars was not a determinant since the stress in the outmost rebar was less than the yield strength ($\sigma_{s_{Vmax}} < 540$ MPa) at the peak load for all cases analyzed, as reported in Table 30. Furthermore, it can be noted that the reinforcement stress at peak load was lower when the higher precompression was applied to the walls. This fact is associated with a lower lateral displacement corresponding to the peak load when compared to the situation with lower axial load.

The cracking pattern differs among the walls with the grout and reinforcement concentrated at the pier ends (M1 to M7) and the walls with them distributed along the piers (M8 and M9). In Walls M1 to M7, noticeable cracks develop diagonally in the ungrouted region

on each pier, increasing in width gradually until the peak load; Figure 85(a) and Figure 85(d). The double grouted cells in the middle of Wall M8 piers induce a subdivision of the diagonal shear cracks to the subsequent ungrouted regions, resulting in cracks with smaller widths than in Wall M1; Figure 85(b) and Figure 85(e). With M9, cracking starts at higher loads, being more distributed and of smaller widths than in the other cases. Also, the main cracks develop almost vertically at the transition between the ungrouted masonry panels and the grouted cells; Figure 85(c) and Figure 85(f). As noted in Figure 85, a similar influence of the reinforcement detailing in the cracking pattern is observed when the walls are subjected to the higher precompression but with less damage.

Figure 85: Damage pattern in the pull direction displayed by the principal strain at V_{max}.

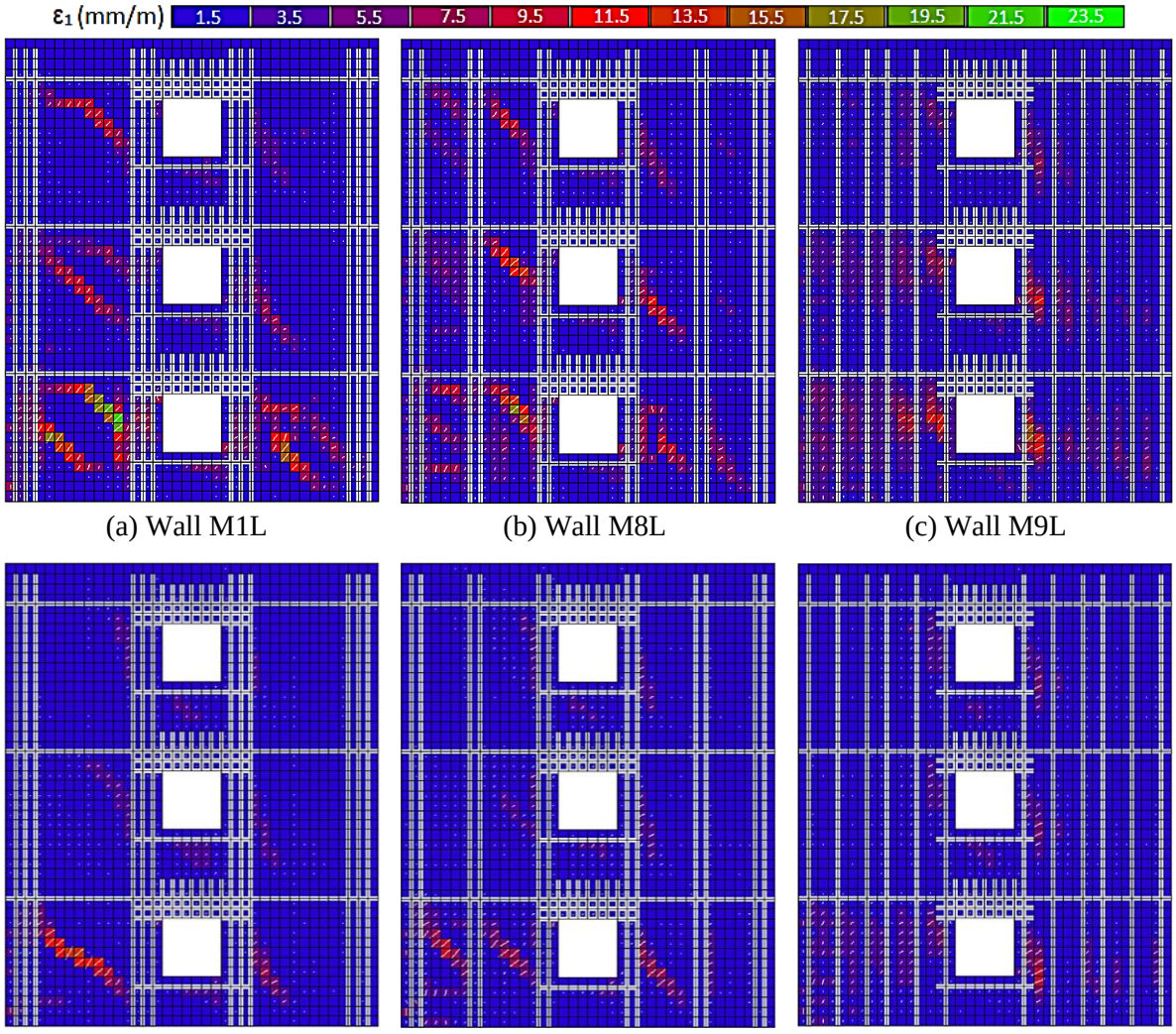

(a) Wall M1L (b) Wall M8L (c) Wall M9L

(d) Wall M1H (e) Wall M8H (f) Wall M9H

Source: Author.

The differences in the cracking patterns did not significantly impact the lateral load capacity of the walls since the masonry compression strength was reached at the toe of the walls close to the peak load, thus limiting the wall capacity. Regarding ductility, the cracking pattern

of the walls influenced it favorably towards the walls with more distributed reinforcement. This impact was only not observed in Wall M9L, which achieved a ductility equivalent to Wall M1L.

It is important to clarify that the seismic performance factors presented here are specific to the walls examined and do not directly represent the overall building system response. Further analyses are needed to suggest SPFs for buildings using the detailing type studied here.

4.4.1.2 Lateral stiffness degradation

The stiffness degradation as a function of lateral displacements of all walls with the two different vertical pre-compression levels is presented graphically in Figure 86 in a non-dimensional form. The secant stiffness ($K_{s,i} = V_i / d_i$) and the top lateral displacement (d_i) for each cycle are normalized, respectively, by the elastic stiffness (K_{el}) and the displacement corresponding to the maximum lateral load (d_{Vmax}) reported in Table 30. The K_{el} and d_{Vmax} were chosen instead of the initial tangent stiffness (K_0) and d_u in the normalization to show how much stiffer the wall can be in the initial cycles and how much more displacement it can achieve in the post-peak stage.

Figure 86: Lateral stiffness degradation of all walls.

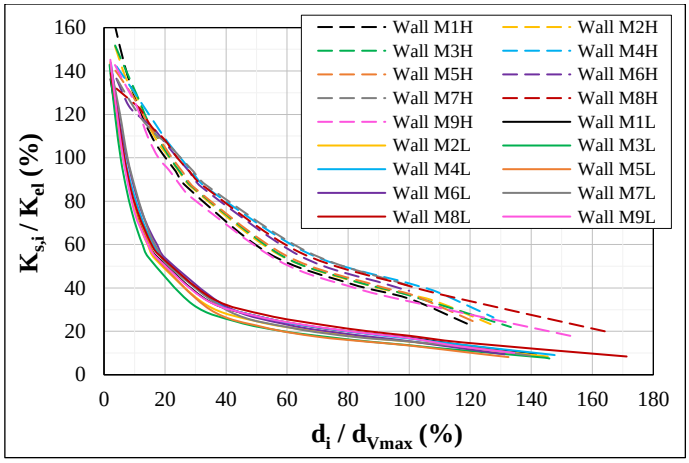

Source: Author.

It can be seen in Figure 86 that the stiffness degradation was more intense when the walls were subjected to the lower axial load, quickly reducing by 50% and 70% of the elastic secant stiffness before reaching, respectively, 20% and 40% of d_{Vmax}; thereafter, the degradation occurred more gradually as the deformation increased. In comparison, when the walls were subjected to the higher axial load, the K_{el} degraded by 50% and 70% only after the displacement achieved, respectively, 60% and 100% of d_{Vmax}. The reason for this behavior is that a higher level of pre-compression delays the development of cracking in the masonry and increases the frictional component post-cracking, consequently reducing the level of stiffness degradation.

All the masonry walls assessed here with the same vertical pre-compression level have a similar shape for the stiffness degradation curve, see Figure 86. Ramírez et al. (2016) used, as suggested by Tomažević (1999), a power function to represent the curves, which proved suitable through Equation 80 for the walls with the lower axial load analyzed here. However, the best fit found for the walls with the higher axial load was the logarithmic function shown in Equation 81. The terms *a* and *b* in Equations 80 and 81 are the stiffness degradation parameters, and their values are listed in Table 32, together with the correlation factor R^2 for all walls. Also, a dispersion graph is plotted in Figure 87 to illustrate the best function common to all walls grouped in the two data sets according to the pre-compression level.

$$\frac{K_{s,i}}{K_{el}} = a\left(\frac{d_i}{d_{V_{max}}}\right)^b \quad \text{Eq. 80}$$

$$\frac{K_{s,i}}{K_{el}} = a \cdot \ln\left(\frac{d_i}{d_{V_{max}}}\right) + b \quad \text{Eq. 81}$$

Table 32: Stiffness degradation function parameters and correlation factor R² of all walls.

Wall Model	Lower axial load case (Power function)			Higher axial load case (Logarithmic function)		
	a	***b***	***R²***	***a***	***b***	***R²***
Wall M1	314.97	-0.65	0.93	-39.85	217.52	1.00
Wall M2	330.66	-0.68	0.94	-37.90	211.94	0.99
Wall M3	310.14	-0.69	0.93	-34.48	214.52	0.99
Wall M4	355.77	-0.68	0.93	-35.89	209.43	0.97
Wall M5	370.74	-0.72	0.91	-36.36	206.33	0.97
Wall M6	375.57	-0.69	0.91	-32.73	196.49	0.95
Wall M7	398.85	-0.71	0.91	-31.24	194.19	0.95
Wall M8	315.60	-0.63	0.94	-33.51	199.03	0.95
Wall M9	317.39	-0.65	0.95	-36.24	202.29	0.98
Common to all	**340.03**	**-0.68**	**0.92**	**-36.17**	**206.81**	**0.97**

Source: Author.

Figure 87: Lateral stiffness degradation for the walls grouped according to the axial load.

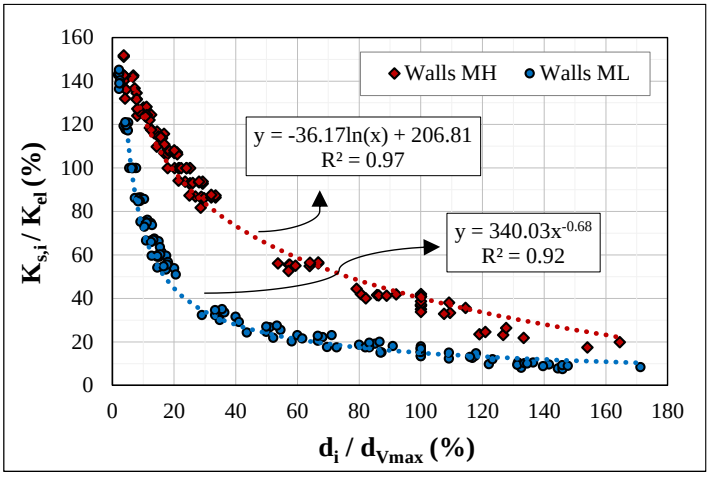

Source: Author.

4.5 CONCLUDING REMARKS

The FEM developed previously was further validated in this chapter and employed to assess the in-plane behavior and seismic performance of multi-story perforated walls with grout and reinforcement concentrated at the wall piers ends. According to the analysis, the following observations and conclusions can be drawn:

- The FEMs proved to be able also to simulate the more specific behavior of the experimental walls analyzed, achieving an excellent fit in the lateral and diagonal displacements, and SG and SP readings;
- Experimental and numerical readings confirmed that the reinforced masonry beam over the openings effectively coupled the wall piers imposing a frame-type action. It is crucial to achieve this behavior for a more economical design when high lateral loads act on the structure;
- In general, the lateral displacement profile along the wall height was linear up to close to the maximum lateral load, i.e., the wall behaved like a solid composite with shear deformations and a linear distribution of the lateral load along the height. It became non-linear after the peak load with predominantly horizontal displacement at the first story caused by the major cracks in the ungrouted masonry in this region;
- The concentration of grout and reinforcement at the wall piers ends seems to have induced the structure to perform as a continuous frame, with the grouted portions acting like columns and the ungrouted parts acting like confined masonry;
- In contrast to the bilinear elastoplastic idealizations, the trilinear approach fits the actual response of the walls preserving the three essential characteristics: initial elastic stiffness, lateral load capacity, and decline in the post-peak phase. Adopting the bilinear methods and disregarding the post-peak stage led to SPFs that can be seen as favorably conservative but ignoring the wall's actual extra ductility;
- The results confirmed that a high vertical pre-compression level could increase the lateral load capacity but lead to a brittle response. The loss of ductility is evidenced in the reduction of the SPFs values. This failure mode is undesirable and, therefore, it is suggested to use a greater quantity of walls in a building to keep a low level of pre-compression, guaranteeing a ductile behavior;

- Particular attention should be given to the wall with only one grouted/reinforced cell at the pier ends and to the wall without grout/reinforcement near the openings. When subjected to the higher pre-compression, these walls failed at the peak load without the capacity to continue carrying load and deforming further in a post-peak phase. Hence, it is suggested to avoid this detailing to resist seismic actions;
- The changes in the amount of vertical reinforcement at the wall pier ends influenced the behavior and seismic performance of walls in the situation with the lower axial load but did not have a significant impact in the higher pre-compression cases. Considering the lower axial load circumstance, placing the reinforcement closest to the ends was more effective;
- Reducing the number of grouted/reinforced cells at the wall pier ends caused, as expected, a worsening in the in-plane response of the walls. The reduction of the lateral load capacity was greater for the lower level of axial load, whereas the ductility decreased more in the higher axial load situation;
- Compared to uniformly distributing the grouting and reinforcement along the wall piers, concentrating them at the ends yielded a reduction of the ductility and SPFs but an increase in the lateral load capacity was observed. In terms of the detailing efficiency measured by the product $V_{max} \cdot R_d$, these options are equivalent. This finding suggests that the ASCE/SEI 7 (2016) and NBCC (2015) reinforcement spacing limits for shear walls can be relaxed at the center of the walls as long as the total amount of grout and reinforcement is maintained and concentrated at the wall ends, resulting in similar design efficiency. Experimental comparisons would be pertinent to confirm these numerical results;
- The stiffness degradation was more intense when the walls were subjected to the lower pre-compression level, quickly reducing in the initial stages and gradually decreasing thereafter. All walls with the same axial load have a similar shape for the stiffness degradation curve, being the best fit made with a power function for walls with the lower axial load and a logarithmic function for the higher pre-compression.

5. SIMPLIFIED FRAME MODELS

Different methods can be used to assess the in-plane behavior of shear walls, from the most simplified ones that consider the walls as individual cantilever elements to more complex models of full discretization with finite elements.

An important issue for the more simplified methods is the non-consideration of the coupling between wall piers by the beams. Neglecting the contribution of strong coupling beams between wall piers may generate conservatively acceptable results for structures subjected to low-intensity lateral loads. However, it may be an uneconomical procedure for tall buildings with wind and/or seismic incidents or even for low-rise buildings subjected to high seismic actions. Finite element models present a higher computational cost and complex task in adequately estimating the material properties and proceeding with the non-linear analysis. Thus, equivalent frame models can be an alternative that is relatively simpler to use, have a low computational cost, and it is easy to interpret the results.

Within this context, the study presented in this chapter employs linear and non-linear frame models to predict the in-plane load-displacement response of the multi-story, perforated, partially grouted masonry walls experimentally tested.

5.1 LITERATURE REVIEW

5.1.1 Behavior and structural idealization

Openings delimit and condition the wall behavior to the beams and piers, which differ not only by the orientation of their longitudinal axis, horizontal in the first and vertical in the second, but also in the level of axial force introduced by the loads, much lower for the beams, or even neglected. Despite the differences, they present dependent behavior since the beams promote the connection between the piers. The greater the number of floors, the greater the influence of these members on the wall behavior (Candeias et al., 2008).

According to Paulay and Priestley (1992), shear walls with openings can be classified into three main categories depending on their configuration and structural behavior: walls fixed only at the base and connected by flexible slabs, Figure 88, coupled walls with piers of low resistance, Figure 89, and walls coupled with low resistance beams, Figure 90. Augenti (2004)

adds that once the type of behavior is recognized, the walls can be modeled with certain simplifications concerning the connections between the members.

The walls illustrated in Figure 88 are connected by slabs that are in-plane flexible but rigid in the orthogonal direction, which guarantees a distribution of lateral loads proportional to the stiffness of walls without transferring bending moments between them. Thus, the walls can be considered independent of each other and with large moments developed on the lower stories (Tomaževič, 1999). According to Paulay and Priestley (1992), the ductility (μ_Δ) of these walls is controlled by the rotation capacity (θ_p) of the plastic hinges formed at their bases, according to Equation 82; where Δ_y is the lateral elastic displacement at the wall top with height h_w and plastic hinge assumed to be formed at half height ($l_p/2$) of the first story.

$$\mu_\Delta = 1 + \frac{\theta_p}{\Delta_y}\left(h_w - \frac{l_p}{2}\right) \qquad \text{Eq. 82}$$

Figure 88: Structural model of masonry shear walls fixed at the base and connected by flexible slabs.

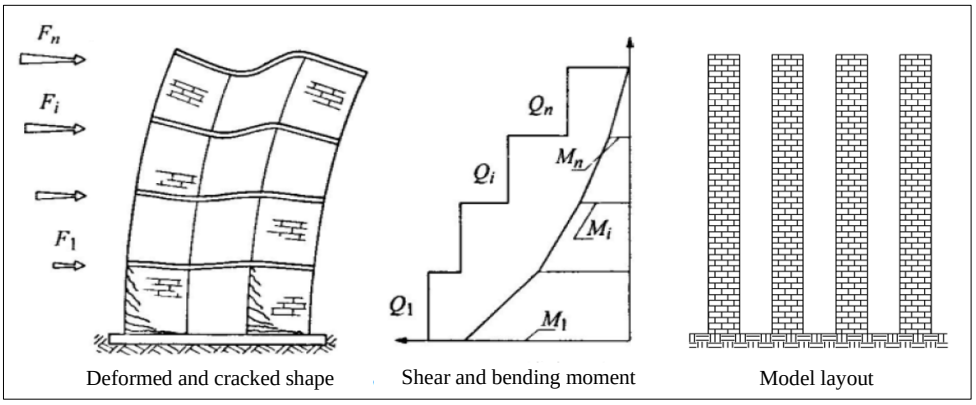

Source: Adapted from Tomaževič (1999) and Augenti (2004).

In most cases for unreinforced masonry coupled shear walls, the piers are weaker than the beams, as illustrated in Figure 89. Thus, the piers present the first cracks when required by the displacements imposed on the wall and may fail either by flexure or shear (Tomaževič, 1999). Inevitably, the greatest demand for ductility occurs in the piers of the first story so that the limit condition of displacement of the wall with *n* stories is conditioned to the ductile capacity of the piers ($\mu_{\Delta p}$), as presented in Equation 83 (Paulay and Priestley, 1992).

$$\mu_\Delta = 1 + 0{,}5\frac{(\mu_{\Delta p} - 1)}{n} \qquad \text{Eq. 83}$$

Marques and Lourenço (2012) clarify that piers can be considered fixed at the lower and upper ends if the beams are rigid and, thus, double curvature can be admitted for the deformation of the piers with elastic stiffness (k_1) calculated by Equation 84.

$$k_1 = \frac{G \cdot d \cdot t}{\chi \cdot h} \frac{1}{1+\frac{G}{\chi \cdot E}\left(\frac{h}{d}\right)^2} \quad \text{Eq. 84}$$

where: *E* and G are, respectively, the longitudinal and transversal modulus of elasticity of masonry; *d*, *h* and *t* are, respectively, the length, height, and thickness of the panel; χ is the shear factor, assumed equal to 1.2 for rectangular sections.

Figure 89: Structural model of masonry coupled shear walls with piers of low resistance.

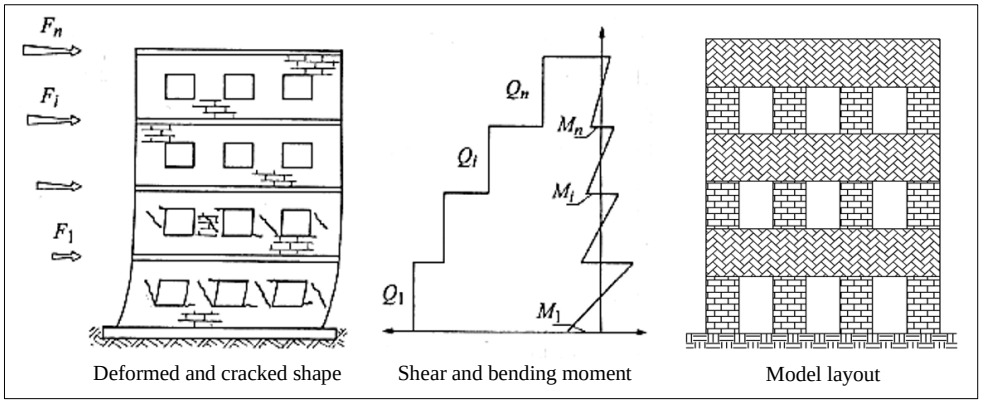

Source: Adapted from Tomaževič (1999) and Augenti (2004).

In cases where piers are more resistant, Figure 90, rapid degradation of strength and stiffness tends to happen in the coupling beams, mainly on the upper stories, due to the larger displacements. The transfer of bending moments occurs between the piers by the beams until they yield, implying an increase of moments at the wall base and starting to behave like isolated piers (Paulay and Priestley, 1992). In this situation, according to Marques and Lourenço (2012), the damage will occur both in the piers and beams with a predominant flexural response, assuming elastic stiffness (k_1) for a pier calculated using Equation 85.

$$k_1 = \frac{G \cdot d \cdot t}{\chi \cdot h} \frac{1}{1+\frac{4G}{\chi \cdot E}\left(\frac{h}{d}\right)^2} \quad \text{Eq. 85}$$

The functioning mechanism of beams starts with them being subjected to shear, Figure 91(a), until they reach the rupture, Figure 91(b), leaving the wall to depend only on the piers. If the beams were adequately reinforced to resist the tensile forces, Figure 91(c), a compression strut and, consequently, higher resistance to flexure is imposed. The failure of the beams then happens by crushing the strut or by diagonal tension (Magenes et al., 2000; Candeias et al., 2008).

Masonry walls coupled with ductile members (reinforced beams) have a more economical design because the coupling forces reduce the moment demands. However, it is noteworthy that walls dominated by flexure require high ductility of the beams, as they can

present large local rotations derived from wall rotation (Paulay and Priestley, 1992). Therefore, as Parsekian et al. (2012) highlighted, coupling members must have their demands checked carefully to ensure efficiency.

Figure 90: Structural model of masonry shear walls coupled with low resistance beams.

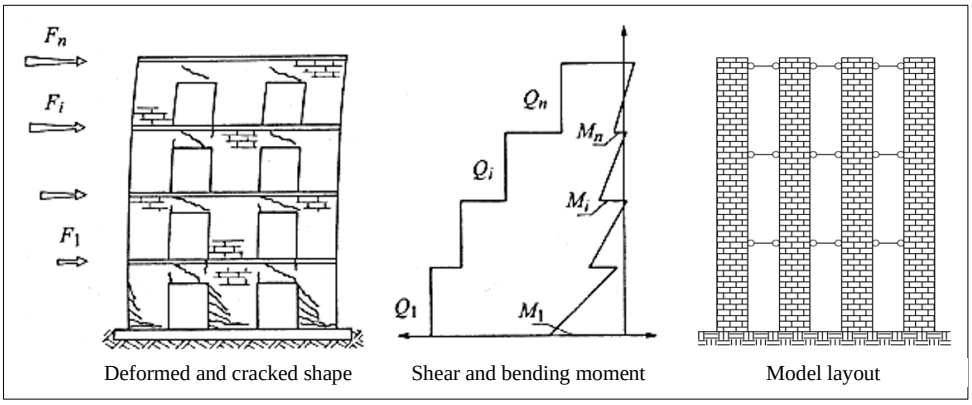

Source: Adapted from Tomaževič (1999) and Augenti (2004).

Figure 91: Functioning mechanism of beams.

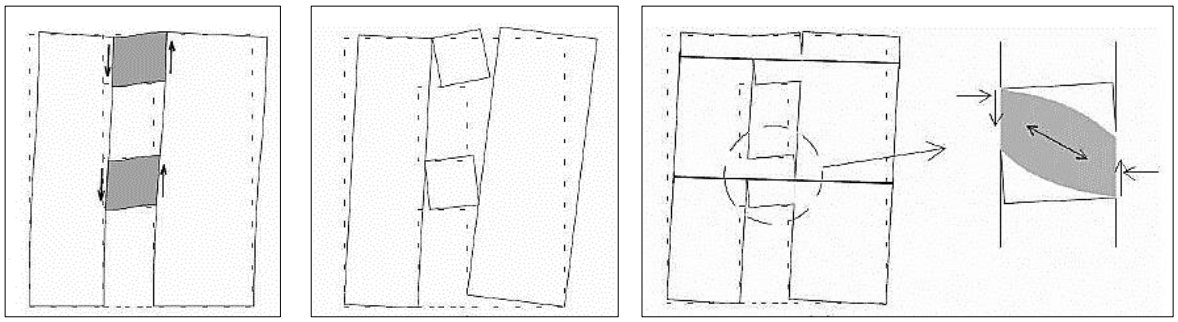

(a) Shear (b) Failure (c) Tensile resistance

Source: Adapted from Magenes et al. (2000).

Kingsley et al. (2014) stated that coupling members must be designed to be structurally integrated with the walls, and the analysis should consider their stiffness. These authors also commented that, in general, masonry beams are more challenging to be reinforced to achieve high ductility than concrete beams, and, therefore, the coupling effects conferred by them should not be trusted. In contrast, Fortes and Parsekian (2017) demonstrated experimentally that reinforced masonry beams could guarantee coupling as well as reinforced concrete beams in masonry walls with openings since they presented a similar response in terms of load capacity and deformability in response to lateral actions. Voon and Ingham (2008) also verified that coupling masonry beams properly reinforced in walls with openings guaranteed the frame action, even in advanced stages of the tests, providing a considerable inelastic displacement.

Tomaževič (1999) states that shear walls can be, in a practical way, modeled by using the idealization of a frame structure with induced forces in the piers and beams, as shown in

Figure 92. The overturning moment caused by the lateral force causes an increase or decrease, depending on the direction of action, of axial forces on the piers. If the masonry beam is appropriately reinforced to ensure the transfer of moments between piers, the resulting lateral force on each story can be distributed to the wall members according to their stiffness.

Figure 92: Force distribution in a shear wall modeled as a frame.

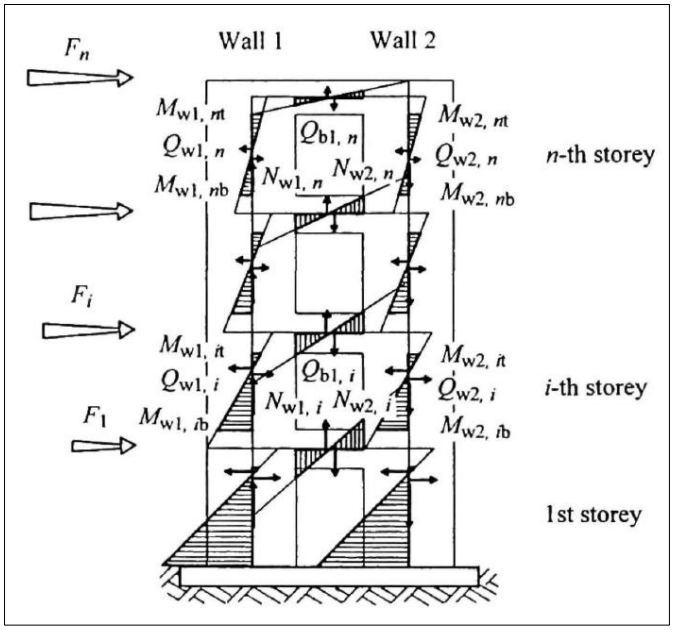

Source: Tomaževič (1999).

More simplistic approaches conservatively neglect the contribution of coupling beams to wall stiffness and overall building stiffness. Therefore, the resulting lateral force *(F)* on each story must be distributed as a function of the relative stiffness $(K_i/\sum K_i)$ of the isolated walls in the considered direction, as demonstrated in Equation 86.

$$F_i = \frac{K_i}{\sum K_i} F \qquad \text{Eq. 86}$$

Many software packages can simulate the elastic and plastic behavior of masonry shear walls using two or three-dimensional finite elements. The main advantage of these forms of modeling is the possibility of capturing more accurately the flexural and shear responses and the stress distribution along the wall parts. However, it is warned that using shell elements with elastic behavior can overestimate the stiffness of cracked walls and that the level of mesh refinement strongly impacts the results of nonlinear shell models. Meshes with too large elements can overestimate the wall's strength. Nonlinear shell models generally present a higher computational cost and complex task in adequately estimating the material properties and proceeding with the non-linear analysis, processes that most engineers are unfamiliar with.

Therefore, nonlinear shell models are indicated for more specific situations in which they can be calibrated and validated against experimental results (Kingsley et al., 2014).

Equivalent frame models are an alternative that are relatively simpler to use, have a low computational cost, and it is easy to interpret the results. The frame elements can incorporate both flexural and shear deformations and also represent linear and non-linear characteristics of the structure. Thus, this type of model can be used to evaluate the main design parameters, such as load capacity, maximum displacement, and even failure modes (Knox and Ingham, 2012a, 2012b; Peruch et al., 2019).

Walls with openings have connection areas between the vertical and horizontal elements that, despite not being completely rigid zones, can be treated as such in a frame model (Sangirardi et al., 2019). This consideration increases the rotational constraint at the ends of the segments and decreases their aspect ratio, conservatively requiring a greater shear capacity in design. For a consistent model, the vertical and horizontal segments must be modeled with appropriate elements of columns and beams accounting for the likely location of shear forces and critical moments. Given the critical actions and the corresponding reinforcements for the wall segments, the rigid zones must be dimensioned and detailed to resist the forces of the adjacent sections (Kingsley et al., 2014).

Different configurations of coupled walls represented by the frame idealization are shown in Figure 93. Weakly coupled walls, joined only by slabs, for example, can be modeled as isolated vertical bars or, as shown in Figure 93(a), as vertical bars connected by a rigid horizontal link pinned at their ends to ensure equal horizontal displacements but avoiding transfer of moments. Figure 93(b) shows a structure similar to Figure 93(a) but with coupling provided by slabs and beams, which are treated in the model as rigid at the intersections of the vertical and horizontal segments, and deformable in the horizontal part corresponding to the opening length. In the case of walls with several openings, as shown in Figure 93(c) and Figure 93(d), it is necessary to clearly identify the vertical and horizontal segments for which the critical forces will be determined (dark gray regions) and the intersections between them that form the rigid zones (light gray regions). Depending on the arrangement of openings, different possibilities must be considered so that the most unfavorable situation is identified and idealized in the frame model. Two possibilities are shown for the same wall in Figure 93(c); in the first, the inferior central pier is more vulnerable to flexure, while in the second, the most critical condition is shear.

Figure 93: Frame idealization for masonry shear walls.

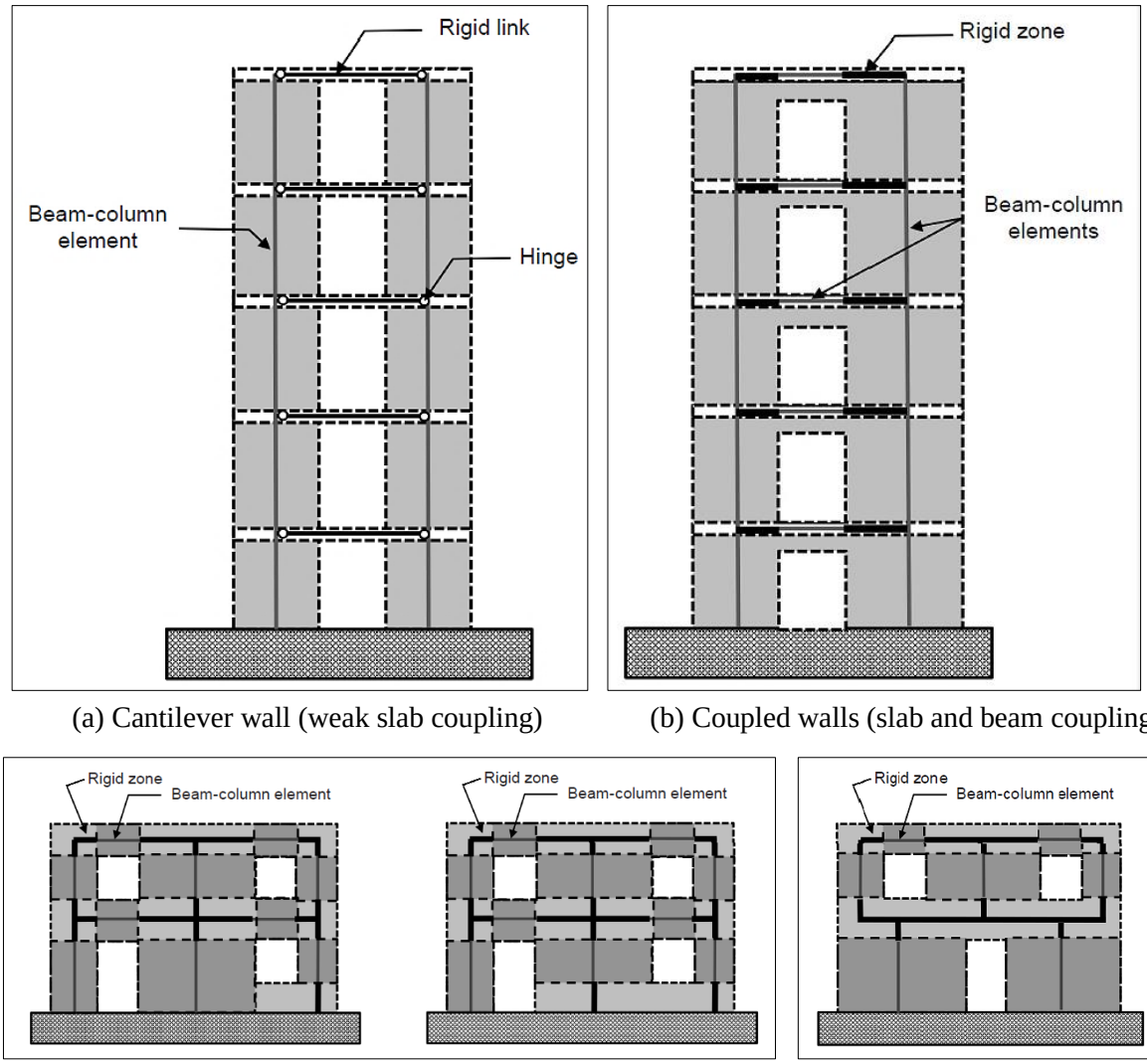

(a) Cantilever wall (weak slab coupling) (b) Coupled walls (slab and beam coupling)

(c) Regular arrangement of openings (d) Irregular arrangement of openings

Source: Adapted from Kingsley et al. (2014).

For the horizontal elements of the frame, Milani et al. (2009) confirm that it is appropriate to consider the rigid offsets at the ends of the bars so that the deformable segment has a length equal to the opening length. However, there are more possibilities regarding the effective height of the piers beside the direct form considering the height of the adjacent opening, Figure 94(a). Based on observations of unreinforced masonry buildings damaged by earthquakes, Dolce (1989) indicates an effective height calculated geometrically, assuming an angle of 30° for the cracks from the corners of the openings, as illustrated in Figure 94(b). In turn, Lagomarsino et al. (2013) admit that cracks can also occur with an inclination of 45° and that the actual cracking pattern must be observed when evaluating existing buildings. Another option, according to Lagomarsino et al. (2013), is to determine the effective height by the average of the heights of the adjacent openings or, for piers at the wall ends, between the heights of the opening and the floor, Figure 94(c).

Figure 94: Definition of the effective height of masonry piers.

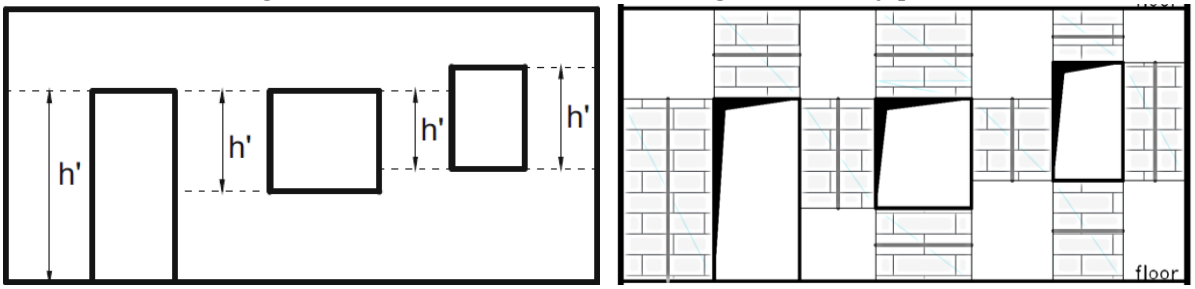

(a) Minimum clear height between adjacent openings

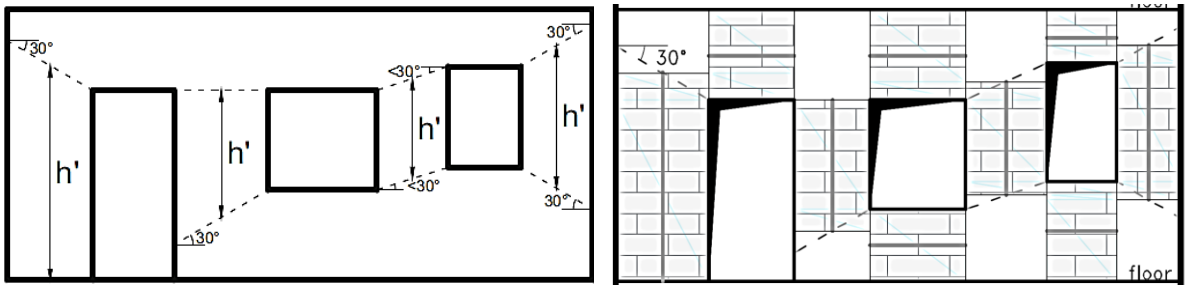

(b) Maximum inclination of the cracks at 30°

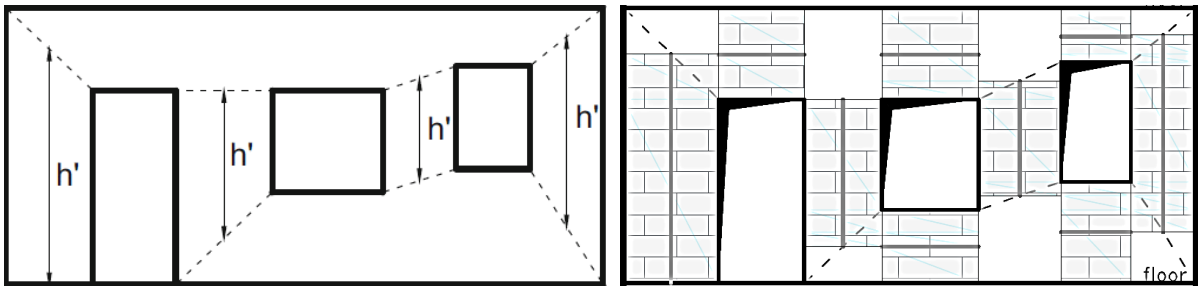

(c) Average height of adjacent openings

Source: Adapted from Dolce (1989), Bracchi et al., (2015), and Quagliarini et al. (2017).

Regardless of the configuration adopted, the overall initial stiffness of the structure is, in general, satisfactorily estimated. However, the adoption of the effective height of the piers equal to the height of the adjacent opening generates stiffer offsets than in situations with slopes according to the cracks, which implies, therefore, a slightly higher global stiffness and a lower displacement capacity (Quagliarini et al., 2017).

The failure modes can be considered in the equivalent frame model through simplified strength criteria associated with the maximum lateral load expressed by equations suggested in the literature and/or design codes and standards. These equations, as discussed in Chapter 3, involve several parameters and are based, in most cases, on experimental evidence. Therefore, simplified idealizations are necessary for the material constitutive law and a yield defined by the lower of the flexure or shear strengths (Lagomarsino et al., 2013; Quagliarini et al., 2017). A failure criterion based on the applied axial load and bilinear constitutive relationship for the material is illustrated in Figure 95 for unreinforced masonry.

Figure 95: Simplified failure criterion for unreinforced masonry.

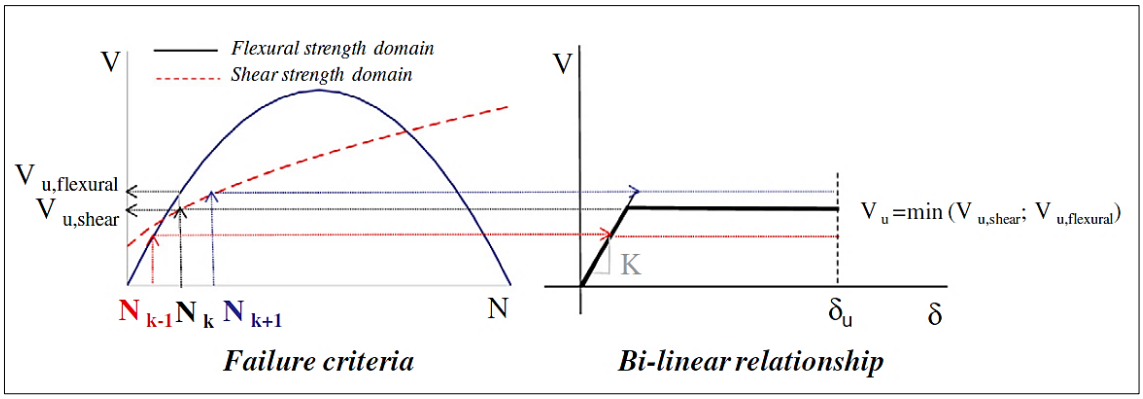

Source: Lagomarsino et al. (2013).

Another way to evaluate failure modes in frame models is by applying the plastic hinge concept. In this approach, it is necessary to previously define the probable positions and the type of plastic hinges that would form along the segments. As illustrated in Figure 96, flexural plastic hinges, governed by the moment-rotation curve (M-θ), are usually placed at the ends of the effective length of the elements, while plastic shear hinges, governed by the force-displacement curve (V-δ), are positioned in the middle of the elements. The elastic stiffness of the piers and beams commands the response of the structure until the non-linearity of the hinges is activated, which are defined with elastoplastic behavior (Salonikios et al., 2003; Knox and Ingham, 2012a, 2012b).

Figure 96: Modeling details for piers and beams with localized plastic hinges.

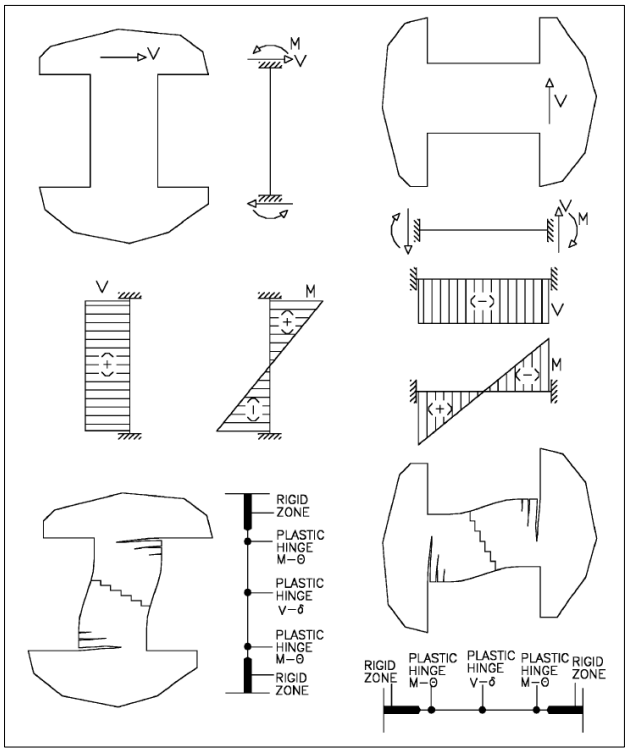

Source: Salonikios et al. (2003).

Peruch et al. (2019) comment that although these approaches were initially applied to unreinforced masonry, they can be expanded to other masonry structures. In their research, for example, the authors discuss the calibration of the inelastic behavior of a frame element for reinforced masonry made of hollow concrete blocks. Strength criteria based on the maximum lateral load corresponding to the flexural and shear modes were considered for the constitutive law of materials, which was assumed as a simplified envelope with three linear branches, Figure 97. For flexure, the maximum load was estimated by moment-curvature analysis, while the expressions by Matsumura (1988), Shing et al. (1990), and MSJC (2013) were tested for shear. Experimental results available in the literature of cantilever walls tested under cyclic lateral loads were used to calibrate the behavior parameters of the element.

Figure 97: Simplified envelope with three linear branches for reinforced masonry.

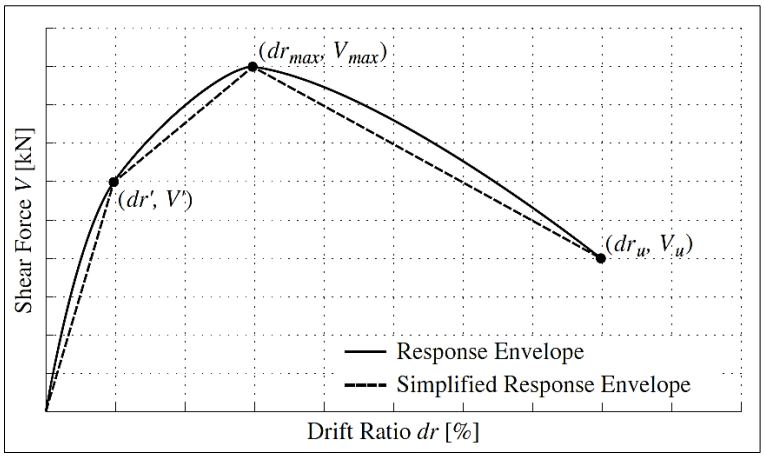

Source: Peruch et al. (2019).

In addition to the degree of coupling between the piers by the beams and the geometric and behavioral definitions of the elements, stiffness is also one of the intrinsic uncertainties in equivalent frame modeling (Bracchi et al., 2015). Lateral stiffness is one of the most important aspects in linear and non-linear design methods. For example, the process for obtaining seismic performance factors, which allows incorporation of the inelastic capacity of seismic force-resisting systems when dimensioned using linear analysis methods (NIST, 2010), is conditioned by the lateral stiffness, as discussed in Chapter 4. Besides the stiffness, the SPFs are also conditioned to the strength and deformation (drift) capacities of the structure that are synthesized in an idealized equivalent elastoplastic response.

Furthermore, valid estimation of the longitudinal and transverse elastic modulus of the elements is essential for evaluating wall lateral stiffness. It is shown in Table 33 how the longitudinal modulus of elasticity of masonry (E) is estimated by different standards when there is no possibility of experimental determination. Among the standards mentioned in

Table 33, TMS 402/602 (2016) and EN 1996-1-1 (2005) are the only ones that mention the shear (transverse) modulus, which should be estimated as $G = 0.4E$. Although not mentioned in these two standards, according to Croce et al. (2018), this relationship was obtained by applying Poisson's ratio (υ) equal to 0.25 in Equation 87, which correlates the elastic constants of an isotropic material.

$$G = \frac{E}{2(1+\upsilon)} \qquad \text{Eq. 87}$$

Table 33: Longitudinal modulus of elasticity of masonry in different standards.

Standard	Block type	
	Concrete	Clay
ABNT NBR 16868-1 (2020)	$800f'_m$ if $f_b \leq 20$ MPa $750f'_m$ if f_b = 22 e 24 MPa $700f'_m$ if $f_b \geq 26$ MPa	$600f'_m$
TMS 402/602 (2016)	$900f'_m$	$700f'_m$
CSA S304 (2014)	$850f'_m \leq 20$ GPa	$850f'_m \leq 20$ GPa
EN1996-1-1 (2005)	$1000f'_m$	$1000f'_m$
NZS 4230 (2004)	15 GPa	15 GPa

Source: Author.

5.1.2 Case studies

Some studies are discussed here in more detail to study the application and comparison of simplified models applied to masonry structures. The various possible arrangements and the particularities considered in the models are emphasized, mainly for the equivalent frame model.

Although the equivalent frame method is widespread, it is difficult to find research with an experimental basis for its application to analyze partially grouted and reinforced masonry shear walls with openings. Most of the research reported in the literature is on historic buildings or modeling improvements that often cause the main feature of the method to be lost, which is exactly the objectivity and ease of application.

a) Hendry (1981)

Hendry (1981) used experimental results of a three-dimensional structure tested at full scale, Figure 98, to assess five basic analysis methods to estimate displacements and stresses in coupled shear walls. As depicted in Figure 99, the models of the cantilever approach, equivalent frame, wide column frame, continuum, and finite elements were evaluated.

The authors commented that the cantilever wall method, Figure 99(b), is the most used for designing masonry structures due to its simplicity. Regarding the equivalent frame method,

Figure 99(c), it was recommended to include the axial and shear deformations in the analysis when using computational tools that help the calculations. The equivalent frame had its behavior changed when considering the horizontal links connecting the elements with infinite stiffness, Figure 99(d). In the continuum method, Figure 99(e), the connection between the walls was replaced by an equivalent shear medium continuous over the full height of the walls, not considering the axial deformation of the medium and the shear deformation of the walls. According to the authors, the finite element method, Figure 99(f), is a powerful analysis tool for complex structures but not very practical for the usual design situations at that time.

Figure 98: Experimental structure of reference for the study of Hendry (1981).

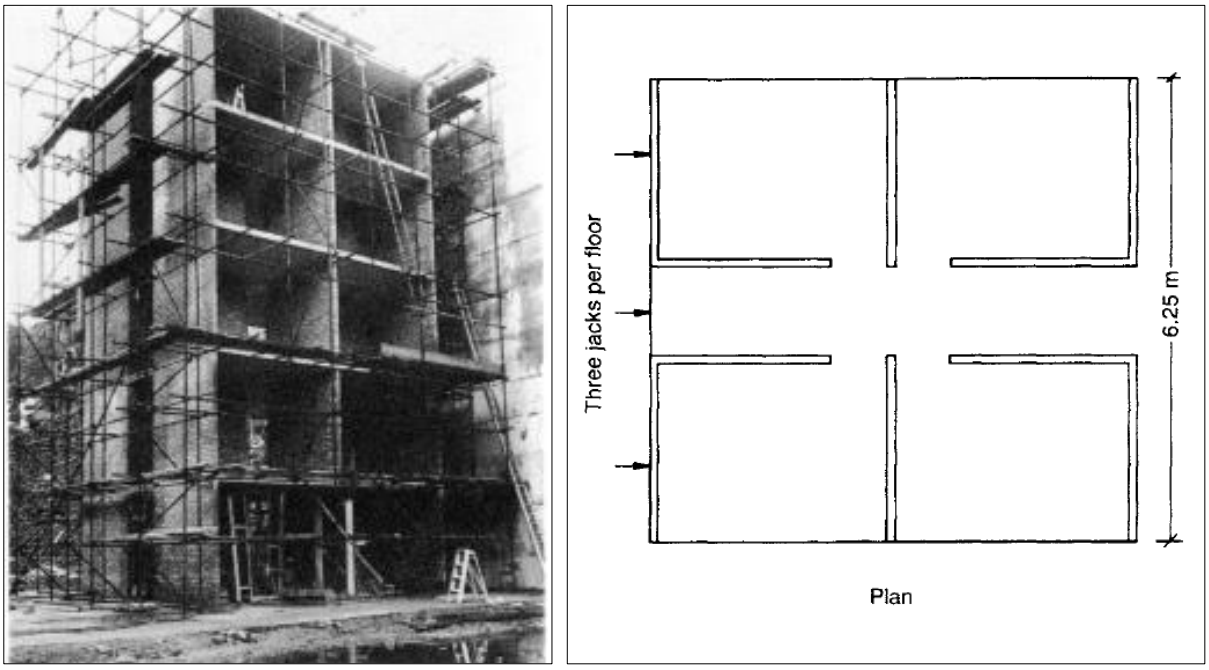

Source: Hendry (1981).

Figure 99: Theoretical idealization of walls with openings by Hendry (1981).

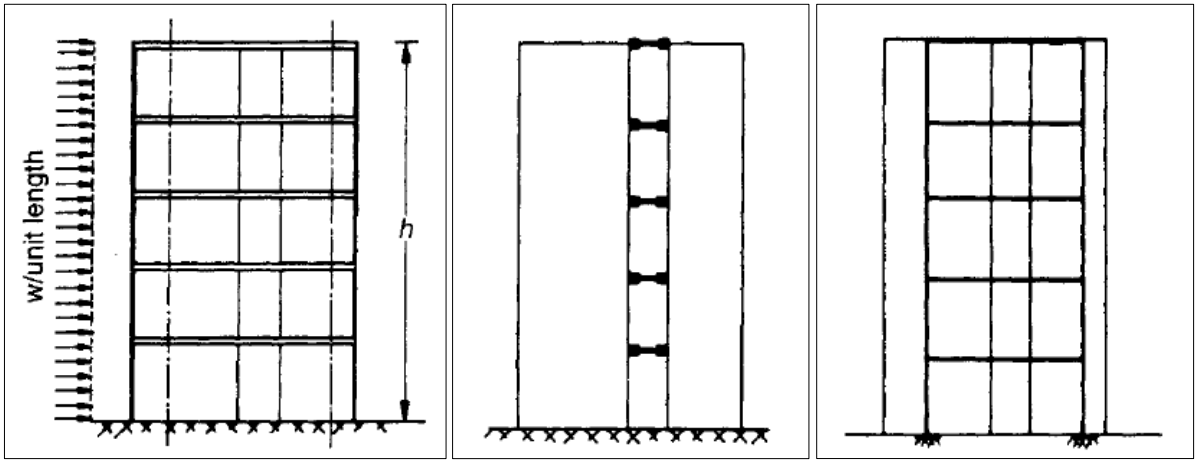

(a) Elevation (b) Individual cantilever (c) Equivalent frame

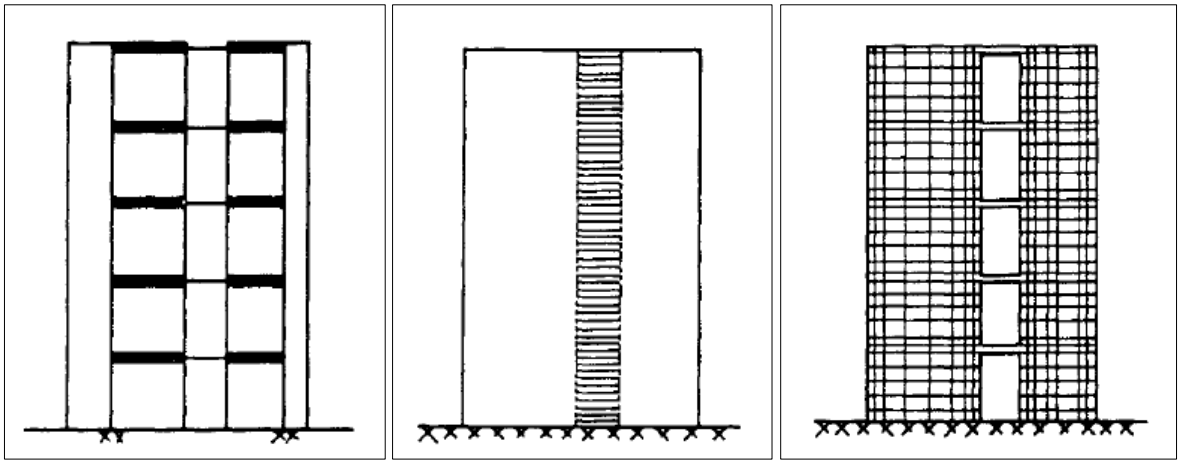

(d) Wide column frame (e) Continuum (f) Finite elements

Source: Hendry (1981).

Hendry (1981) performed the analyses by adapting the three-dimensional system to an equivalent two-dimensional one of walls and beams with the same areas and moments of inertia of the actual structure. The comparison between the lateral displacements is shown in Figure 100(a), while the stress distribution along the base of the walls at the first story for the experiment and models can be seen in Figure 100(b).

Figure 100: Comparison of the results of the models evaluated by Hendry (1981).

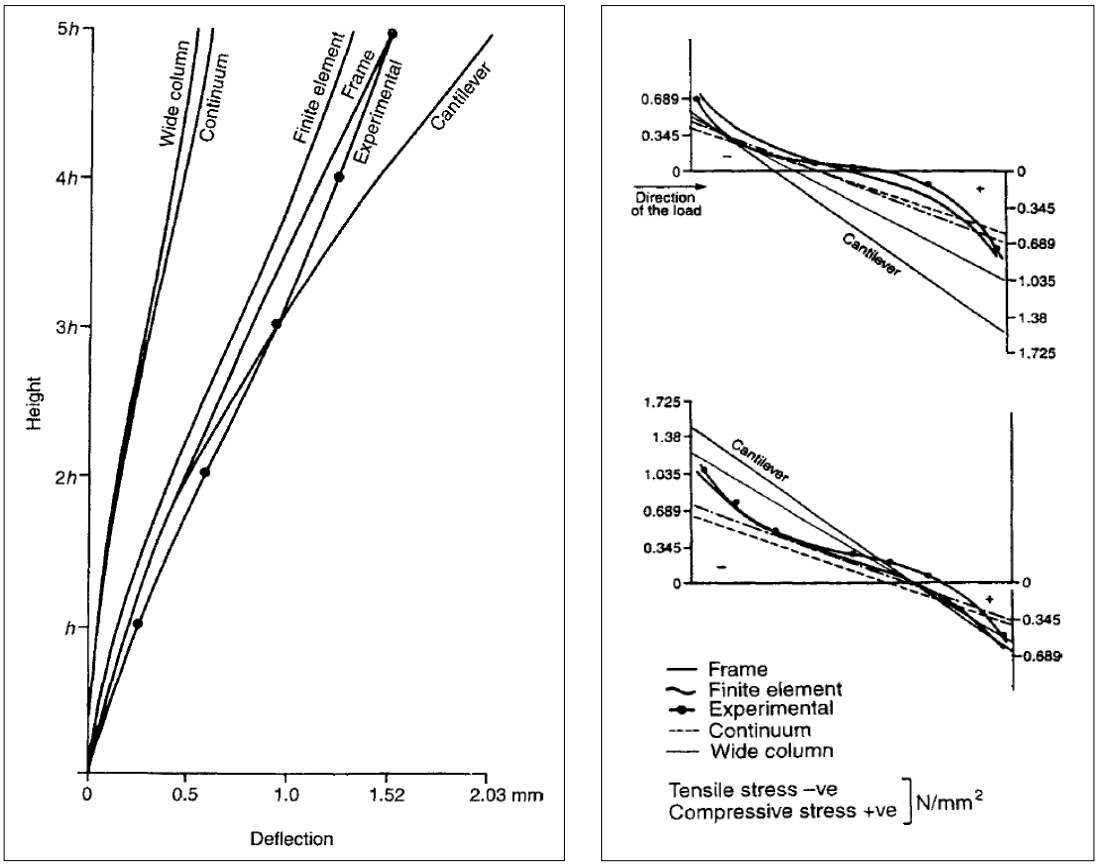

(a) Deflection (b) Stress at wall base

Source: Adapted from Hendry (1981).

The results showed that the models closest to the structure's actual behavior were the equivalent frame and the finite element, the latter being the only one capable of simulating the non-linear stress distribution. The wide column frame and continuum methods did not present satisfactory results; therefore, their use was not recommended by the authors. The cantilever method provided very conservative results and, according to the authors, should be used for preliminary estimations of bending moments and shear forces on the walls. It was also commented that the hypotheses assumed for the interaction between the elements in the models may have caused the differences between the experimental and theoretical results.

b) Kappos et al. (2002)

Kappos et al. (2002) evaluated the accuracy of models for practical use in engineering to analyze unreinforced masonry buildings subjected to lateral actions. The authors' main objective was to determine under which conditions the equivalent frame model can be used to design and verify masonry structures. The study was initially carried out in an elastic regime for a typical wall with openings and a real three-dimensional building with and without the rigid diaphragm effect provided by the slabs; then, analyzes were made for the inelastic behavior of the typical wall. The wall in question refers to previous studies of Seible and Kingsley (1991), while the three-dimensional structure was discussed by Karantoni and Fardis (1992).

The authors tested several variations of the equivalent frame (EF) and plane finite element (FE) models for the typical wall. Concerning the equivalent frame model, the options were: full rigid offsets horizontally (EF1), full rigid offsets horizontally and vertically (EF2), Figure 101(a), and full horizontal and half vertical rigid offsets (EF3). This last consideration was thought to clarify the doubt about the extension to be adopted for the rigid offsets since its excess can confer a much greater stiffness to the model than exists in the actual wall. Variations in the plane finite element model are related to mesh refinement; a model with a coarse mesh was generated using elements with dimensions delimited by the geometry of the walls (FE-C), Figure 101(b), and another model with a smaller mesh (FE-R), Figure 101(c). Versions with rigid diaphragm were designed for all models (EF1D, EF2D, EF3D, FE-CD, and FE-RD). Such modeling was extended to the three-dimensional analysis of the building.

Concerning the material properties, Kappos et al. (2002) considered the longitudinal modulus of elasticity of masonry according to the European standard recommendation, $E = 1000 f_m'$, maximum compressive strain $\varepsilon_u = 0.002$ and tensile strength $f_t = 0.1 f_m'$. For the nonlinear analyses, a constitutive model was adopted with a parabolic stress-strain relationship

and stiffness degradation due to cracking when the element presented a compression deformation higher than ε_u. After reaching the cracking condition, the residual shear stiffness was recalculated as 60% of the uncracked value. An additional analysis was performed with a reduced value for the modulus of elasticity, $E = 550 f'_m$, which showed an improvement in the behavior of the initial branch of the numerical curve compared to the experimental curve.

Figure 101: Wall geometry and models analyzed by Kappos et al. (2002).

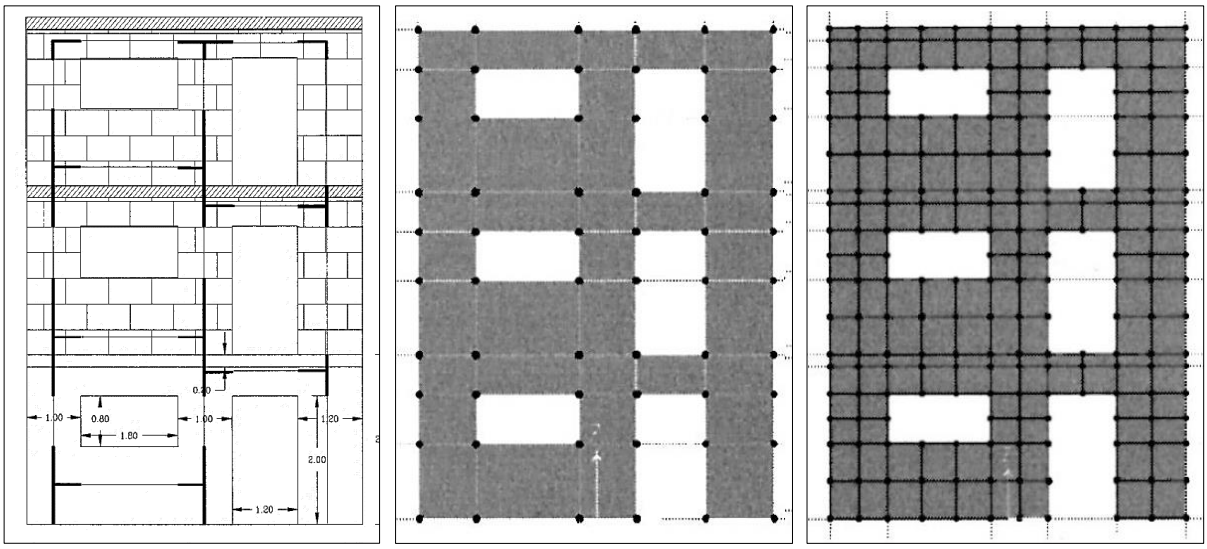

(a) EF with full rigid offsets (b) FE with coarse mesh (c) FE with smaller mesh

Source: Kappos et al. (2002).

The main discussion of results was about the displacements at the story levels, which are presented in the graphs of Figure 102. The authors concluded that the effect of the rigid diaphragm was negligible in the models of the 2D structure, Figure 102(a), but it was crucial for the general behavior of the 3D structure, Figure 102(b), distributing the displacements between the shear walls and not causing significant out-of-plane deformations. The mesh refinement did not make any difference concerning the displacements; however, it was essential in mapping the distribution and concentration of stresses. The equivalent frame model with full horizontal and vertical rigid offsets was the frame option that presented elastic displacements consistent with the refined mesh finite element model and stress results with differences within an acceptable range for design. Furthermore, the inelastic analyses showed that the response of these two models for the initial stiffness and the lateral load capacity of the wall were similar. It was impossible to establish an inelastic comparison of the ultimate displacements because the finite element model was induced by forces while the equivalent frame model was induced by displacements.

Figure 102: Comparison of displacements of the models tested by Kappos et al. (2002).

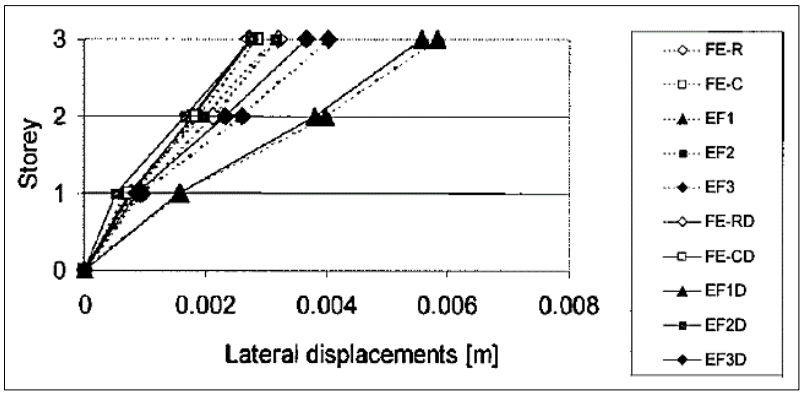

(a) Plane structure (typical wall)

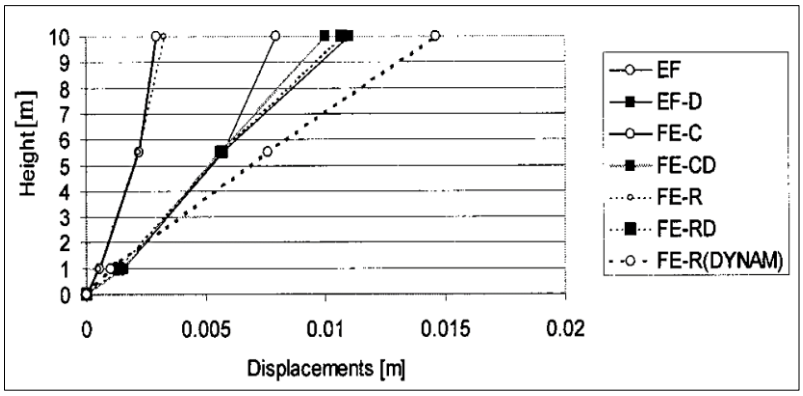

(b) Three-dimensional structure (building)
Source: Kappos et al. (2002).

c) Tena-Colunga and Rivera-Hernandez (2018), Tena-Colunga and Liga-Paredes (2020)

These authors proposed a geometric adaptation to the equivalent frame and continuum models in situations with several openings in the same story, especially when misaligned. The focus of the new approach was to obtain, specifically, in a simplified and approximated way, the lateral stiffness and the profile of elastic lateral displacements of shear walls with multiple openings since these parameters are essential in displacement-based design methods.

The proposed simplification consists of transforming a wall with multiple openings into an equivalent wall with a single opening. The fundamental premise defended by the authors is that if the area and the effective eccentricity of the openings are kept constant, the stiffness and lateral displacements of the equivalent wall will be similar to those of the actual wall. Some adjustments are indicated for the geometric properties of the cross-section, adopting, then, equivalent area and second moment of area.

Walls with different arrangements of openings and number of floors (3, 6, 12, and 18) were evaluated considering the proposed simplification attributed to equivalent frame models,

continuum, and plane finite elements with refined mesh, the latter adopted as the reference. Three variations were considered for the equivalent frame model: one version assuming perfect rigid offsets (infinite area and inertia) at the ends of the vertical and horizontal bars, Figure 103(a); another version considering perfect rigid offsets only at the end of the horizontal bars; and the last one with rigid offsets with the equivalent area and inertias calculated as a function of the wall geometry, Figure 103(b), as proposed by Schwaighofer and Microys (1969) and described in Equations 88 to 91.

Figure 103: Variations adopted by Tena-Colunga and Rivera-Hernández (2018) in the rigid offsets of the equivalent frame model.

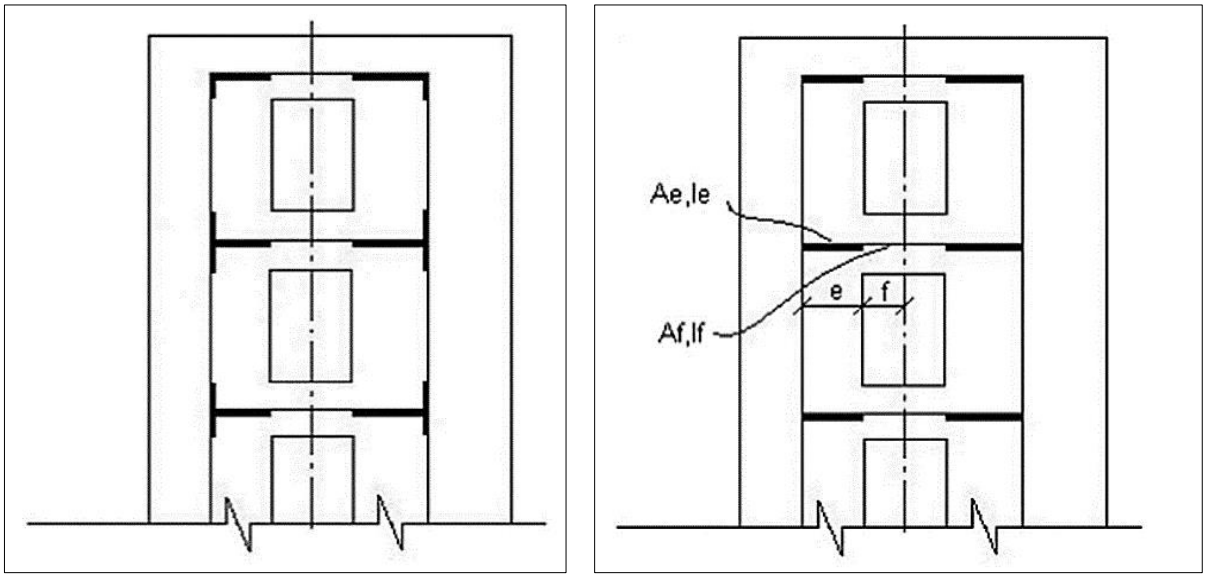

(a) Horizontal and vertical rigid offsets (b) Horizontal rigid offsets

Source: Tena-Colunga and Rivera-Hernandez (2018).

$$A_e = K_1 A_f \quad \text{Eq. 88}$$

$$I_e = K_2 I_f \quad \text{Eq. 89}$$

$$K_1 = 100\left(\frac{e}{f}\right) \quad \text{Eq. 90}$$

$$K_2 = 0.0593\left(\frac{e}{f}\right)^4 + 99.348\left(\frac{e}{f}\right)^3 + 302.43\left(\frac{e}{f}\right)^2 + 296\left(\frac{e}{f}\right) + 1.7778 \quad \text{Eq. 91}$$

where: e is the distance between the vertical bar and the opening side, and f is the distance between the opening side and its central axis, see Figure 103(b).

The authors commented that the gain in wall stiffness conferred by the slabs can be incorporated into the frame models through the inertia admitted for the coupling beam. Based on the section transformation principle, an equivalent thickness (b_{eq}) is calculated for the slab

as a function of the extension of its flanges using Equation 92. Thus, the coupling beam has its second moment of area calculated for the geometry highlighted in Figure 104.

$$b_{eq} = b_f \left(\frac{E_s}{E_w}\right) \quad \text{Eq. 92}$$

where: b_f is the extension of the flanges, generally defined as a function of the slab thickness; E_s and E_w are, respectively, the longitudinal modulus of elasticity of the slab and wall.

Figure 104: Equivalent geometry for the coupling beams considering the slabs.

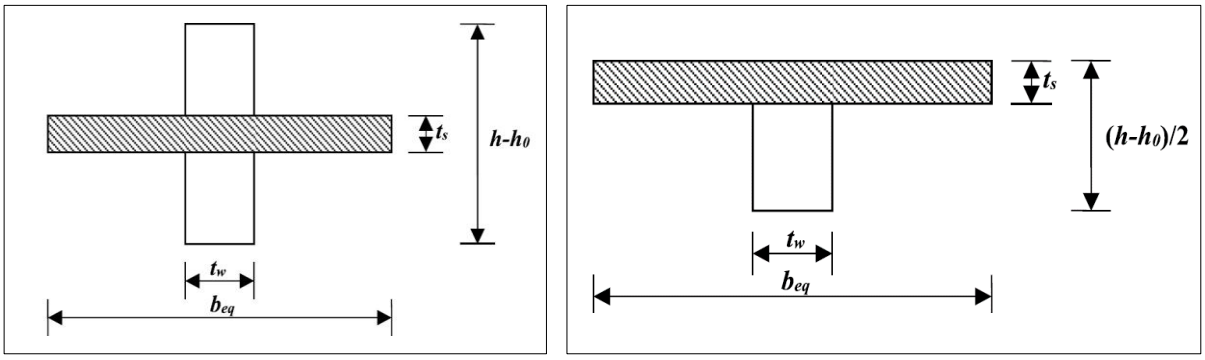

(a) Intermediate stories (b) Top story

Source: Tena-Colunga and Liga-Paredes (2020).

The results were plotted graphically in displacement profiles similar to those in Figure 102 for the different situations evaluated, including model variations and opening parameters for the proposed simplification. Regarding the frame models, the analysis allowed to conclude that, in general, the version with the rigid offsets suggested by Schwaighofer and Microys (1969) presented the best approximations. In addition, the contribution of the slab stiffness was more significant for walls with typical door openings and less impacting on walls with symmetrically arranged window openings since, in this situation, stiffer beams (greater height) were already formed.

d) Pirsaheb et al. (2021)

Pirsaheb et al. (2021) proposed a numerical procedure to assess the progressive failure of unreinforced perforated masonry shear walls. The method, called the Multi-Pier-Macro (MPM) method, consists of equivalent braced frames simulating the piers and spandrels, as illustrated in Figure 105. The diagonals (braces) were set as truss elements with elastic and plastic deformation, while the vertical and horizontal elements were set as beam elements with elastic flexural behavior and with inertia sufficiently small to maintain the behavior mostly axially. The inelastic behavior was computed using concentrated tensile and compressive

plastic hinges, which their color indicates the level of plasticization according to the stress-strain curve adopted as the material constitutive relationship.

The geometrical dimensions of the vertical and horizontal elements were calculated by equating the second moment of area of the equivalent system and the actual wall. In turn, the cross-section area of braces was calculated by equating the shear stiffness of the actual wall and the equivalent system. Diagonals axially rigid were used in the intersection regions between piers and spandrels to represent the rigid zones.

Figure 105: Equivalent geometry for the coupling beams considering the slabs.

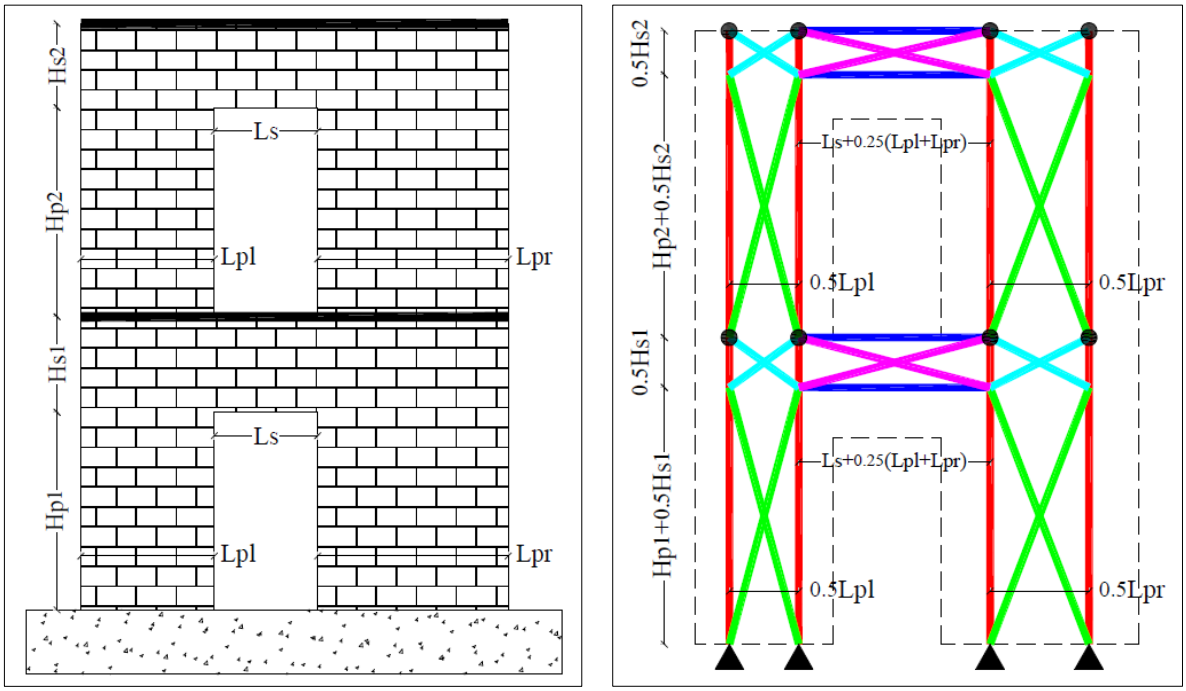

(a) Full-scale masonry wall (b) MPM equivalent system

Source: Pirsaheb et al. (2021).

The failure mechanism is deduced based on which plastic hinge is activated. Horizontal and vertical tensile cracks and crushing occur when the hinges in the vertical and horizontal elements on piers and spandrels yield. Shear failure and toe crushing are identified when the plastic hinges in the braces reach their limits.

The authors stated that the approach can be useful in typical design for its simplicity. Also, the authors highlighted the fast execution, the reliability in simulating the global behavior and damage progress, and the need for only generalist FE software with non-linear trusses.

5.2 LINEAR FRAME MODELS

5.2.1 Modeling development

The experimental masonry walls W1, W2, D1, and D2 were modeled using the Structural Analysis Program SAP2000 (Computer and Structures Inc. (CSI), 2019). The material properties of the masonry and concrete were accounted for by the average compressive strength, elastic modulus, Poisson's ratio, and shear modulus, summarized in Table 34. The reinforcement was not included in the modeling.

Table 34: Properties of materials used in linear modeling.

Material	Parameter	Value for the material type (a)	(b)	Reference of the used value
Concrete (a) Middle slabs (b) Top beam	Compressive strength (f_c')	36.1 MPa	31.5 MPa	Test results (Fortes and Parsekian, 2017)
	Elastic modulus (E_c)	33,647 MPa	31,430 MPa	$5600\sqrt{f_c'}$ (ABNT NBR 6118, 2014)
	Poisson's ratio (ν_c)	0.20	0.20	Specified (ABNT NBR 6118, 2014)
	Shear modulus (G_c)	14,020 MPa	13,096 MPa	$E_c/[2(1+\nu_c)]$ (SAP2000-CSI, 2019)
Masonry (a) Ungrouted (b) Grouted	Compressive strength (f_m')	11.8 MPa	12.2 MPa	Test results (Fortes and Parsekian, 2017)
	Elastic modulus (E_m)	10,620 MPa	10,980 MPa	$900f_m'$ (TMS 402/602, 2016)
	Poisson's ratio (ν_m)	0.25	0.25	Specified (TMS 402/602, 2016)
	Shear modulus (G_m)	4,248 MPa	4,392 MPa	$E_m/[2(1+\nu_m)]$ (SAP2000-CSI, 2019)

Source: Author.

The vertical load, including the self-weight, was applied as concentrated loads at the frame nodes. The horizontal displacement was applied monotonically and increasingly at the frame top nodes, which were constrained to simulate the diaphragm effect.

Two geometrical arrangements were tested: (1) portal frames and (2) braced frames, as described in the following subsections.

5.2.1.1 Portal frame

The portal frame (PF) models consisted of vertical and horizontal one-dimensional elements forming an equivalent frame, as illustrated in Figure 106. The vertical elements were placed at the centroid of the wall piers, while the position of the horizontal elements was defined to equalize the height of stories. This strategy implied that the elements of the intermediate slabs in the walls with door openings were inserted through the top center point instead of the centroid. The walls with window openings had an extra horizontal element to represent the masonry region below the opening in the first story. All vertical and horizontal elements were defined with the effective uncracked net cross-section of the corresponding wall portion.

Five model variations related to element connections and rigid offsets (zones) were made for each wall type:

- Model PF1(cantilever model) – Horizontal elements pinned to the vertical elements at the pier axes, and no rigid zones;
- Model PF2 – As model PF1 but with horizontal elements fixed to the vertical elements;
- Model PF3 – As model PF2 with horizontal rigid offsets delimited by the effective length of the beam, Figure 107(a) and Figure 107(b);
- Model PF4 – As model PF2 with horizontal rigid offsets delimited by the length of the opening, Figure 107(c) and Figure 107(d);
- Model PF5 – As model PF2 with horizontal and vertical rigid offsets delimited, respectively, by the length and height of the opening, Figure 107(e) and Figure 107(f).

For Model PF3, the effective length was taken as the distance between the faces of the supports plus the smallest value between half of the beam height and the distance from the support axis to the support face for each side.

Figure 106: Geometrical arrangements of portal frame models; dimensions in mm.

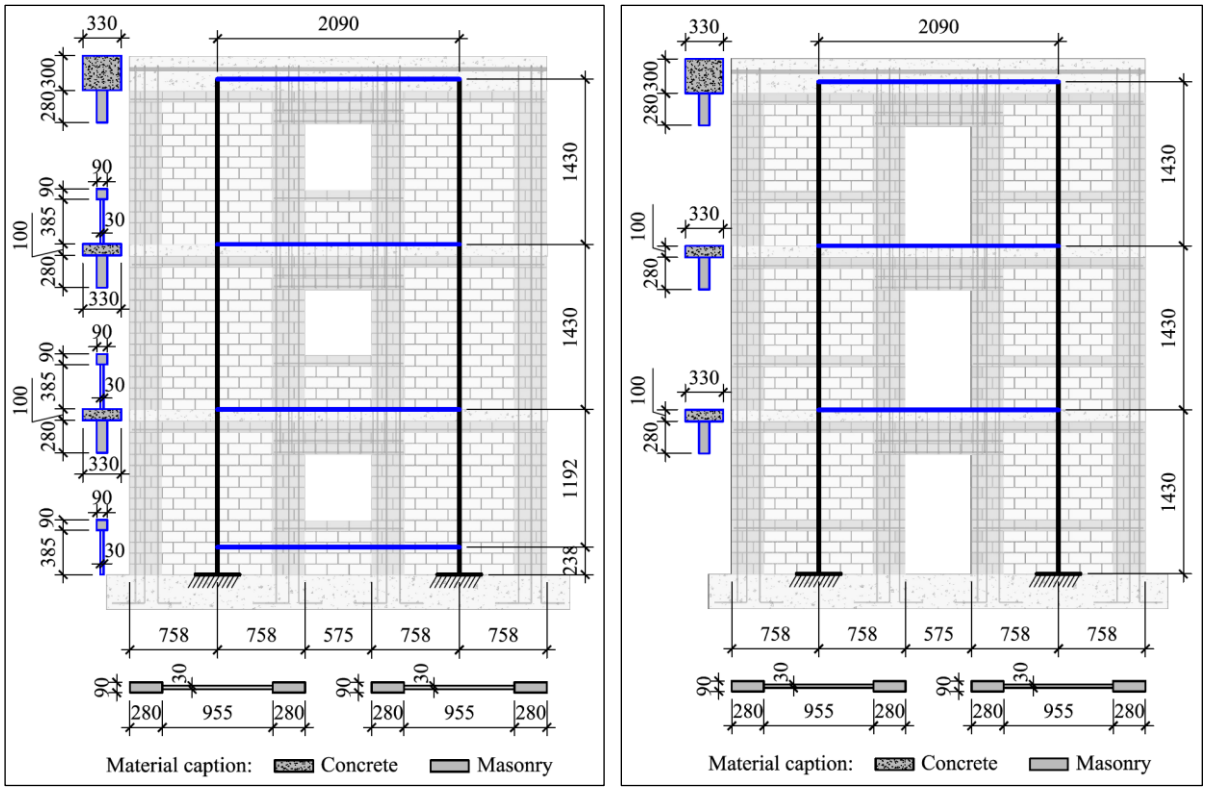

(a) Walls W1 and W2 (b) Walls D1 and D2

Source: Author.

Figure 107: Distinction between variations in the portal frame models, in which the thicker lines depict the rigid offsets; dimensions in mm.

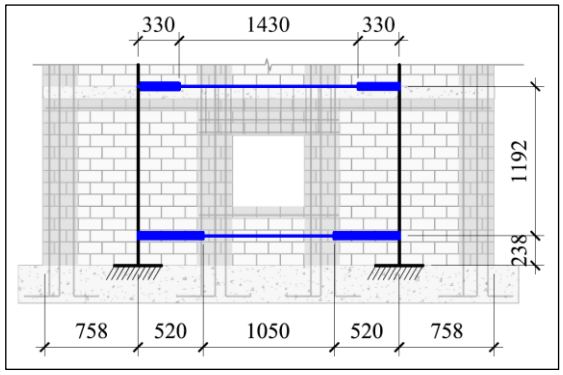

(a) Model PF3 – Walls W1 and W2

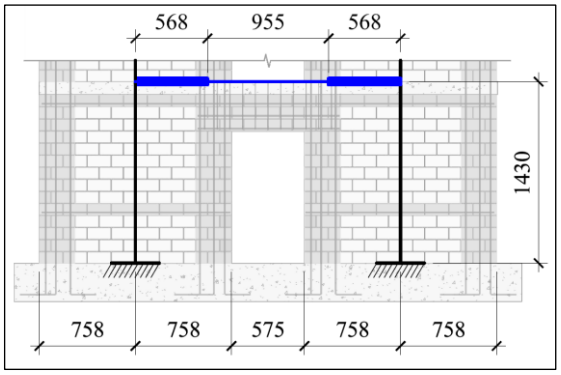

(b) Model PF3 – Walls D1 and D2

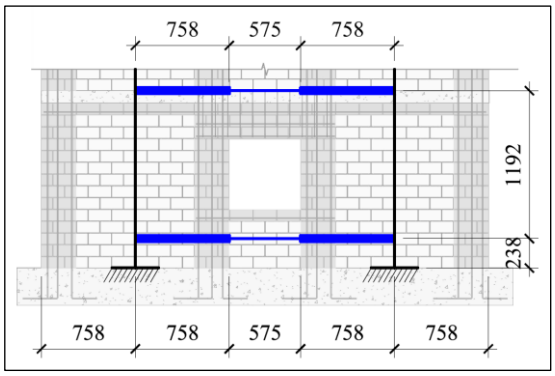

(c) Model PF4 – Walls W1 and W2

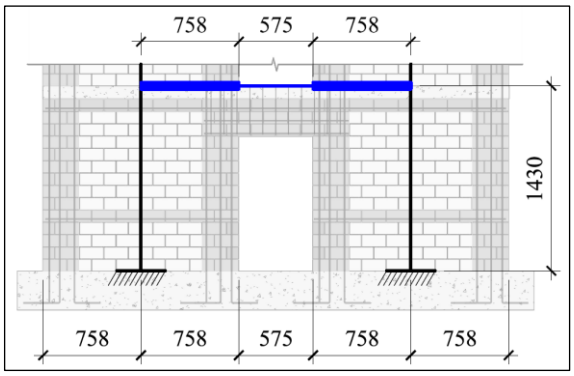

(d) Model PF4 – Walls D1 and D2

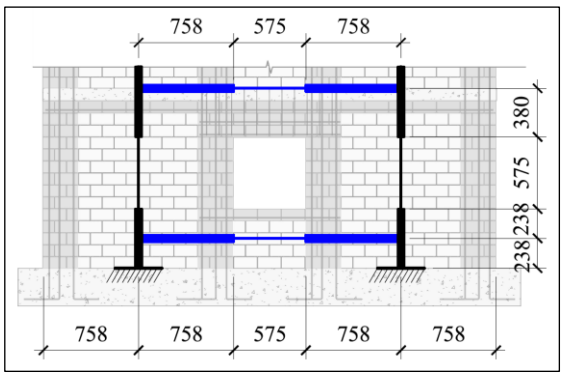

(e) Model PF5 – Walls W1 and W2

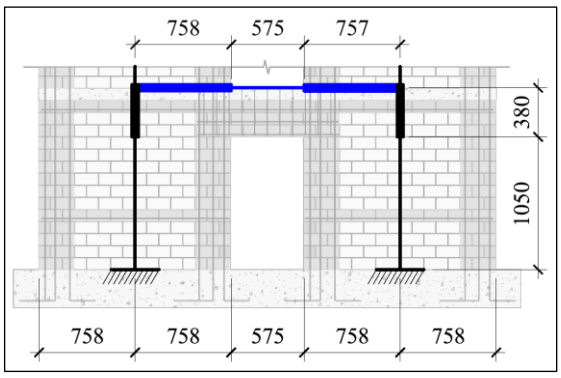

(f) Model PF5 – Walls D1 and D2

Source: Author.

5.2.1.2 Braced frame

The braced frame (BF) models incorporated some characteristics presented in the model of Pirsaheb et al. (2021) by using vertical, horizontal, and diagonal one-dimensional elements to form an equivalent braced frame for each wall pier, as shown in Figure 108. The vertical elements represented half of the wall piers, placed at their centroid. As with the portal frame models, the position of the horizontal elements was defined to equalize the height of stories. Consequently, the position of those elements determined the inclination of the braces. While

the vertical and horizontal elements were implemented as beam elements and with fixed connections, the diagonals were truss elements pinned to the frames.

All vertical and horizontal elements were assembled with the effective uncracked net cross-section of the corresponding wall portion. Differently, the cross-sectional area of the diagonals (Equation 93) was determined by equating their stiffness (Equation 94) with the shear stiffness of the ungrouted region into the related wall pier (Equation 95). Therefore, the width of diagonals could be calculated assuming the same equivalent net thickness of the ungrouted masonry.

$$A_d = \frac{G A_{p_{ug}} L_d}{2.4 E H_{p_{ug}} (\cos\theta_d)^2} \quad \text{Eq. 93}$$

$$K_d = \frac{2 E A_d}{L_d} (\cos\theta_d)^2 \quad \text{Eq. 94}$$

$$K_{p_{ug}} = \frac{G A_{p_{ug}}}{1.2 H_{p_{ug}}} \quad \text{Eq. 95}$$

where: G = shear modulus (MPa); E = elastic modulus (MPa); $A_{p_{ug}}$ = effective horizontal cross-section area of the ungrouted region into the pier (mm²); $H_{p_{ug}}$ = height of the ungrouted region into the pier (mm); L_d = diagonal length (mm); θ_d = diagonal angle related to horizontal direction (deg).

Figure 108: Geometrical arrangements of braced frame models; dimensions in mm.

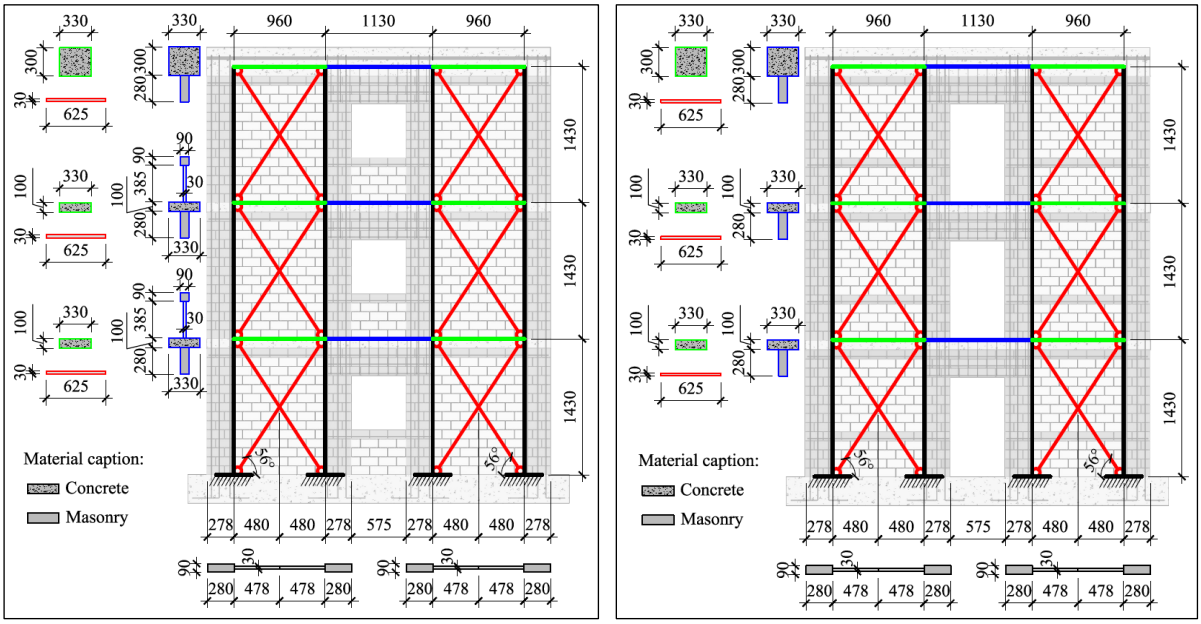

(a) Walls W1 and W2 (b) Walls D1 and D2

Source: Author.

5.2.2 Assessment of initial lateral stiffness, deflection, and load distribution

The response of the linear models is plotted together with the backbone curve of the experimental walls in Figure 109 to provide a graphical comparison. An overall view of the load-displacement curves is presented in Figure 109(a) and Figure 109(c), and a zoom of the initial stage is shown in Figure 109(b) and Figure 109(d), where it is possible to identify better the difference between the lateral stiffness of the curves. In these graphs, the lateral displacement is related to the wall top, and the lateral load is the total reaction load. Also, the elastic lateral deflected shapes of the experimental and numerical walls corresponding to the load point of approximately 15 kN are plotted in Figure 110. In addition to the curves, the results are presented in detail in Table 35, including the lateral displacement, and the inter-story and top drifts and stiffnesses of the experimental and numerical walls. The experimental results are an average envelope of the pull and push regimes, and the initial stiffness was defined as the tangent stiffness for a load of approximately 15 kN.

Figure 109: Top load-displacement curves of all linear models and experimental walls.

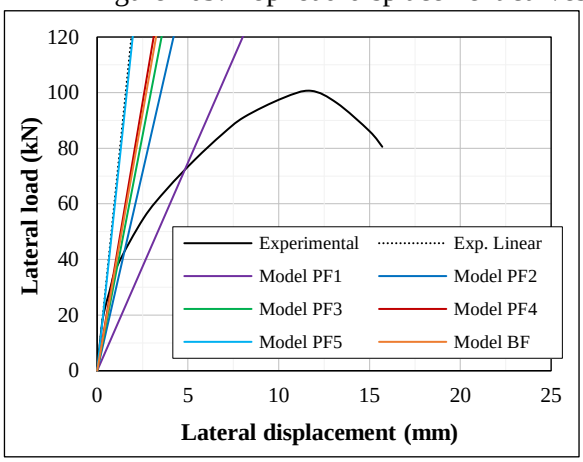

(a) Walls W1 and W2 – Overall view

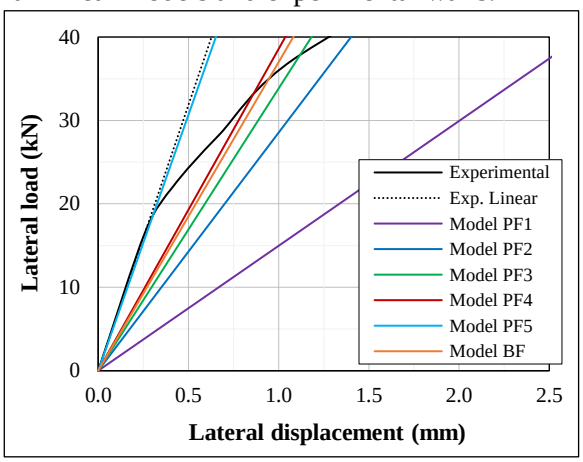

(b) Walls W1 and W2 – Zoom

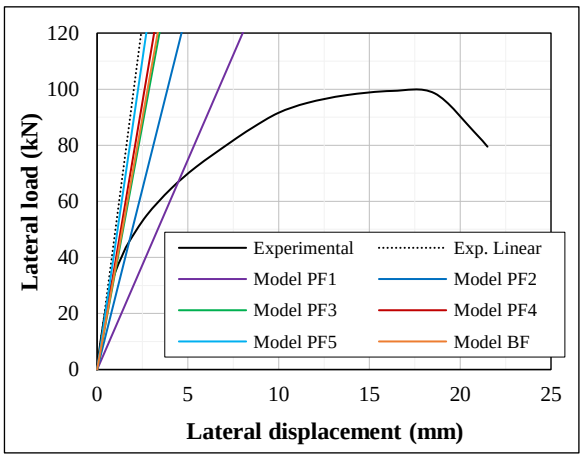

(c) Walls D1 and D2 – Overall view

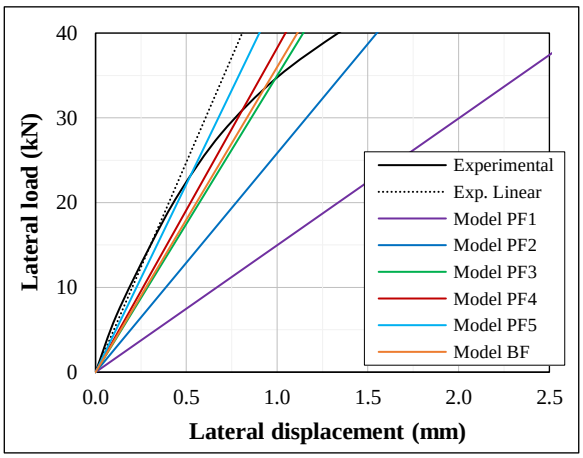

(d) Walls D1 and D2 – Zoom

Source: Author.

Figure 110: Experimental and numerical elastic deflected shapes of walls.

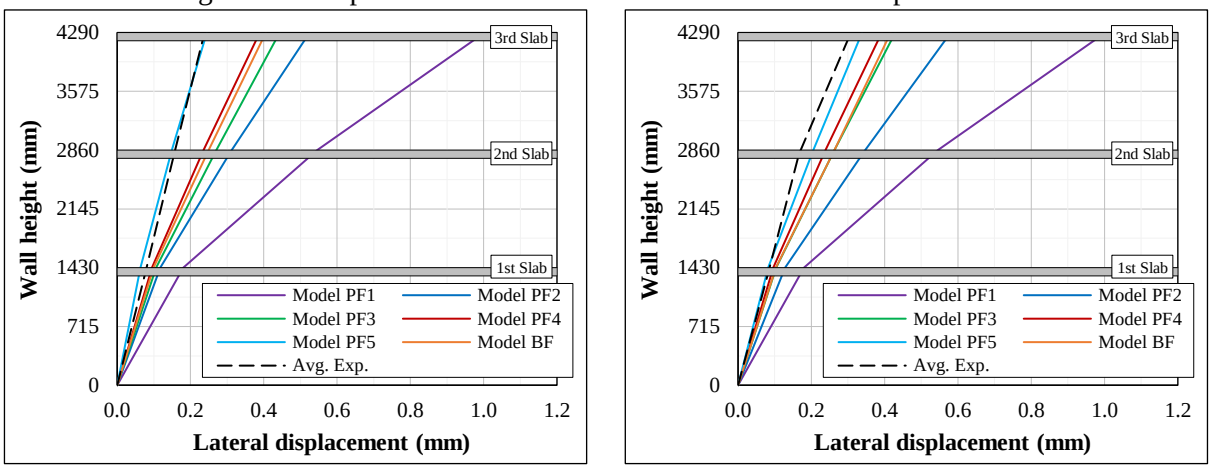

(a) Walls W1 and W2 (b) Walls D1 and D2

Source: Author.

Table 35: Experimental and numerical elastic results.

Wall	Story	Parameter	Avg. Test	Model PF1	Model PF2	Model PF3	Model PF4	Model PF5	Model BF
W1 & W2	1st	δ (mm)	0.08	0.18	0.12	0.11	0.09	0.06	0.10
		Drift (%)	0.005	0.013	0.008	0.007	0.007	0.004	0.007
		K_0 (kN/mm)	194.0	83.2	127.3	141.1	158.0	237.3	151.7
	2nd	δ (mm)	0.15	0.55	0.31	0.27	0.24	0.15	0.25
		Drift (%)	0.005	0.026	0.014	0.012	0.010	0.006	0.011
		K_0 (kN/mm)	193.4	41.1	77.3	91.2	106.6	175.2	99.4
	3rd	δ (mm)	0.24	1.00	0.53	0.44	0.39	0.24	0.41
		Drift (%)	0.006	0.032	0.015	0.012	0.011	0.007	0.011
		K_0 (kN/mm)	163.3	32.8	70.3	87.0	97.8	156.6	96.3
	Top	δ (mm)	0.24	1.00	0.53	0.44	0.39	0.24	0.41
		Drift (%)	0.006	0.023	0.012	0.010	0.009	0.006	0.009
		K_0 (kN/mm)	63.7	15.0	28.6	33.8	38.6	61.3	37.0
D1 & D2	1st	δ (mm)	0.08	0.18	0.13	0.10	0.10	0.08	0.10
		Drift (%)	0.006	0.013	0.009	0.007	0.007	0.006	0.007
		K_0 (kN/mm)	180.6	83.2	116.8	144.1	156.0	181.9	145.3
	2nd	δ (mm)	0.17	0.55	0.35	0.26	0.24	0.21	0.26
		Drift (%)	0.006	0.026	0.015	0.011	0.010	0.009	0.011
		K_0 (kN/mm)	180.8	41.1	68.8	94.5	105.6	122.4	93.9
	3rd	δ (mm)	0.30	1.00	0.58	0.43	0.39	0.34	0.42
		Drift (%)	0.010	0.032	0.016	0.012	0.011	0.009	0.011
		K_0 (kN/mm)	109.4	32.8	64.1	90.2	97.4	112.4	97.6
	Top	δ (mm)	0.30	1.00	0.58	0.43	0.39	0.34	0.42
		Drift (%)	0.007	0.023	0.014	0.010	0.009	0.008	0.010
		K_0 (kN/mm)	49.5	15.0	25.8	35.0	38.2	44.3	36.0

Source: Author.

Examination of Figure 109, Figure 110, and the results in Table 35 reveals that Model PF1 was the most flexible, being up to 82.4% and 76.5% less stiff than the experimental walls when compared the inter-story and top lateral stiffnesses, respectively. Regarding the inter-story and top lateral drifts, Model PF1 achieved, respectively, values up to six and four times higher than the experimental walls. This implies that using a cantilever model to simulate coupled perforated walls is highly conservative. Model PF2 was almost twice as stiff as Model PF1 but still notably different to the tested walls.

The stiffness became greater and, consequently, the deflections decreased as rigid offsets were applied in the portal frame modeling (Models PF3, PF4, and PF5). Including rigid offsets on the horizontal and vertical elements (Model PF5) resulted in lateral deflections and stiffnesses closer to those of the experimental walls. The differences were about ±4% and ±10% related to the top of walls W1-2 and D1-2, respectively, and ±20% and ±3% related to the inter-story values for walls W1-2 and D1-2, respectively. Exceptionally, the inter-story drift and stiffness of the second story in walls D1-2 deviated from this small range, being in Model PF5 up to 48% more conservative than the experimental tests. Comparing Model PF5 (horizontal and vertical rigid offsets) with Models PF3 and PF4 (only horizontal rigid offsets), it may be seen that vertical offsets were more crucial for the lateral deflection and stiffness in walls W1-2 (with window openings) than in walls D1-2 (with door openings). This distinction can be credited to the masonry regions below the openings in walls W1-2 that did not exist in walls D1-2. Kappos et al. (2002) also observed minimal differences using a similar approach with horizontal and vertical rigid offsets.

In general, the experimental walls had elastic inter-story drifts similar in the first and second stories, but higher in the third story, mainly for walls D1-2, while the frame models presented significant differences in the inter-story drifts from the first to the second story and minor changes from the second to the third story. The portal frame models had inter-story drifts and stiffnesses with more remarkable differences from the tests for the third story in walls W1-2 and for the second story in walls D1-2. The smallest differences were observed for the first story in both types of walls. In turn, the braced frame model had more notable variations from the tests for the second story in both types of wall, and the lowest deviations for the first story in walls W1-2 and for the third story in walls D1-2.

Model BF presented deflections and lateral stiffness between Models PF3 and PF4, with conservative differences up to 70% to 30% compared to the experimental walls W1-2 and D1-2, respectively, related to the wall top and up to 95% related to the inter-story values.

The distribution of loads throughout the wall elements in the first story (the critical story) is analyzed by comparing the distribution with the results from the FE model developed in the previous chapters. The internal loads were extracted from the FE model using the software tool that integrates the stress in the elements in the same alignment; e.g., all elements of the first course of the right wall pier, as shown in Figure 111. To compare the BF-results, in which each pier has two vertical elements, the reaction loads at the bottom of both vertical elements were transferred to the bottom center of their respective pier, as illustrated in Figure 112. The results are presented in Table 36, taking walls D1-2 as an example and considering a lateral load level of approximately 15 kN.

Figure 111: Internal loads extraction in the FE model.

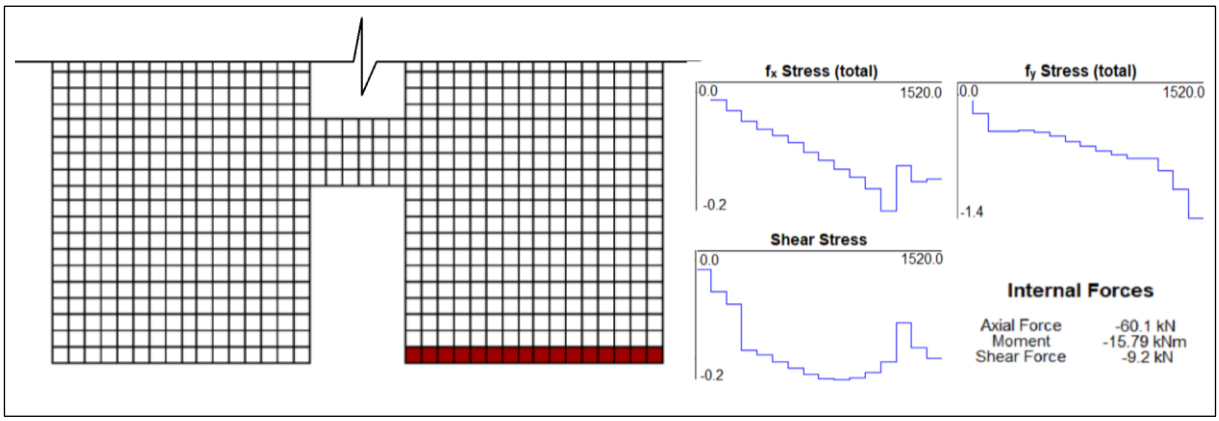

Source: Author.

Figure 112: Internal loads extraction in the model BF; dimensions in mm.

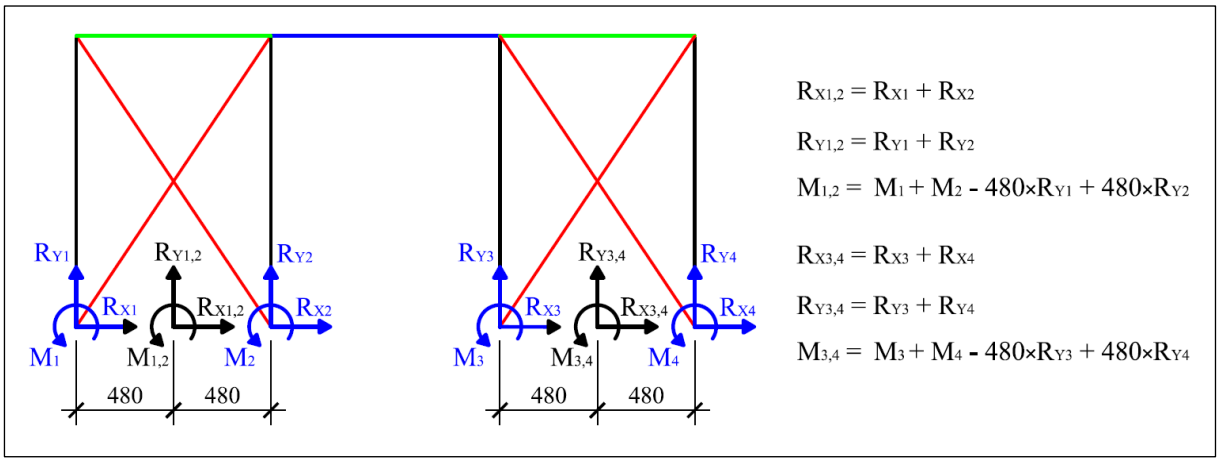

Source: Author.

The comparison of internal loads between the portal frame models and the FE model in the linear phase confirms the conservatism of models PF1 and PF2 and better approximations as vertical rather than only horizontal rigid offsets are implemented in the elements. As verified in Table 36, Models PF3-5 and BF could represent the load distribution with less discrepancy.

Table 36: Internal loads of elements in the first story of walls D1-2.

Model	Left Pier			Right Pier			Beam		
	N (kN)	V (kN)	M (kN·m)	N (kN)	V (kN)	M (kN·m)	N (kN)	V (kN)	M (kN·m)
FE Model	-20.9	7.3	14.0	-60.1	9.2	15.8	-0.3	5.1	1.2
Model PF1	-40.4	7.5	32.1	-40.4	7.5	32.1	0.0	0.0	0.0
Model PF2	-30.5	6.5	17.4	-50.3	6.5	17.4	0.0	1.6	1.6
Model PF3	-20.7	8.7	16.9	-60.1	8.7	16.9	0.0	5.7	2.7
Model PF4	-19.3	8.5	14.3	-61.5	8.5	14.3	0.0	7.3	2.1
Model PF5	-19.9	8.5	15.1	-60.8	8.5	15.1	0.0	6.5	1.8
Model BF	-22.4	8.0	16.2	-58.5	8.5	16.6	-0.3	4.8	2.7

Source: Author.

5.2.3 Defining the envelope lateral response using SPFs and ultimate drifts

The three approaches (BL1, BL2, and TL) discussed in Chapter 4 (section 4.4.1.1) to idealize the lateral response and calculate the SPFs of masonry walls were used in this study associated with the linear models and ultimate top drifts to predict the envelope load-displacement curves of the walls. The process was done in reverse starting from an adopted ultimate displacement and using the previously calculated SPFs and the initial (elastic) lateral stiffness of the linear models to generate the envelope curves.

The ultimate displacement (d_u) was fixed first equal to that obtained in the experimental tests, which corresponds to the displacement at a load $V_u = 0.8V_{max}$ in the post-peak stage, and second, by using an ultimate top drift of 0.4%. Morandi et al. (2022) used this value of ultimate drift for unreinforced masonry walls submitted to compressive stress less than 15% of the characteristic compressive strength of the masonry based on the gross section and with a diagonal shear failure mode. The experimental walls studied here failed in a diagonal shear mode, and were subjected to compressive stress (including the self-weight) of approximately 4% of the masonry compressive strength.

Although the walls explored in this study were grouted and reinforced, these materials were concentrated at the pier ends, resulting in large unreinforced masonry panels that were the weak region of the walls and governed the failure mode. Also, eight story-height perforated concrete masonry walls with reinforcement at the pier ends tested by Voon and Ingham (2008) were analyzed. No axial load was applied to any of those eight masonry walls and all failed in a diagonal tension mode. The results for the maximum and ultimate loads and their corresponding displacements and drifts, considering an average of the pull and push regimes, are presented in Table 37. Note that the drift ranged from 0.11 to 0.32%, with an average of

0.20%, at the peak stage, and from 0.27 to 0.50%, with an average of 0.40%, at the ultimate load ($0.8V_{max}$). These results corroborate that 0.40% may be a reasonable value for the ultimate drift of walls submitted to a low axial load.

Table 37: Results of the walls tested by Voon and Ingham (2008).

Wall	Peak stage			Post-peak stage		
	V_{max} (kN)	d_{Vmax} (mm)	Drift (%)	V_u (kN)	d_u (mm)	Drift (%)
1	49.6	4.1	0.17	39.7	9.2	0.38
2	40.0	2.8	0.11	32.0	8.2	0.34
3	33.9	4.4	0.18	27.1	10.2	0.43
4	48.3	3.3	0.14	38.6	8.6	0.36
5	51.4	2.9	0.12	41.1	6.5	0.27
6	94.5	6.2	0.26	75.6	11.4	0.48
7	82.7	7.8	0.32	66.1	12.0	0.50
8	88.0	7.6	0.31	70.4	11.8	0.49
Average			0.20			0.40
Range			0.11 - 0.32			0.27 - 0.50

Source: Author.

Since the level of vertical pre-compression impacts the wall behavior, the investigation was expanded to walls with a higher axial load. For that, results from the finite element models produced and validated in the previous chapters for the same experimental walls (W1-2; D1-2) with a compressive stress of approximately 20% of the masonry compressive strength were used. Hence, d_u of the idealized load-displacement curves in these cases was first fixed equal to that obtained in the models, and second, by imposing an ultimate top drift of 0.3%, as used by Morandi et al. (2022) for walls subjected to compressive stresses higher than 15% of the masonry compressive strength.

Given d_u, the elastic displacement (d_{el}) is obtained by dividing d_u by the displacement amplification factor (C_d). Then, the elastic load (V_{el}) is found by multiplying d_{el} by the lateral stiffness (K_0) of the specific linear model. For the BL1 approach, the lateral stiffness of models of the walls studied here was reduced by approximately 75% and 45% for the cases with low and high pre-compression, respectively, since this approach shifts the initial behavior of the walls as a consequence of maintaining the peak load and total energy in the idealization, as seen in Figure 80(a).

Regarding both the BL1 and BL2 approaches, the yielding load plateau (V_y) is obtained by multiplying V_{el} by the overstrength factor (Ω). Also, the yield displacement (d_y) can be found from the intersection of the two branches, or dividing V_y by K_0, or by dividing d_u by the structural ductility factor (μ_d). For the TL approach, d_y can be found from d_u / μ_d but $V_{el} \cdot \Omega$ results in V_{max} instead of V_y, which, in turn, can be calculated by $K_0 \cdot d_y$. Furthermore, for the

TL approach, it is necessary to use the auxiliary variable $\Delta_d = d_{Vmax}/d_y$ to obtain the displacement corresponding to V_{max}.

A numerical example using walls W1-2 is demonstrated by the flowchart in Figure 113 to elucidate the process using the three approaches. After calculating all the main points, the idealized load-displacement curves can be plotted. For this example, an ultimate top drift of 0.4% was assumed, with an initial lateral stiffness obtained from model PF5 and SPFs specific for these walls calculated in accordance with the discussion in Chapter 4. In practical design situations, the ultimate drift should be adopted according to the literature and/or obeying design codes aiming to limit damage through limiting drifts at given values depending on the structural features. Similarly, the SPFs can also be found in the literature and/or design codes according to the seismic force-resisting system.

Figure 113: Numerical example defining the main points of the predicted idealized responses.

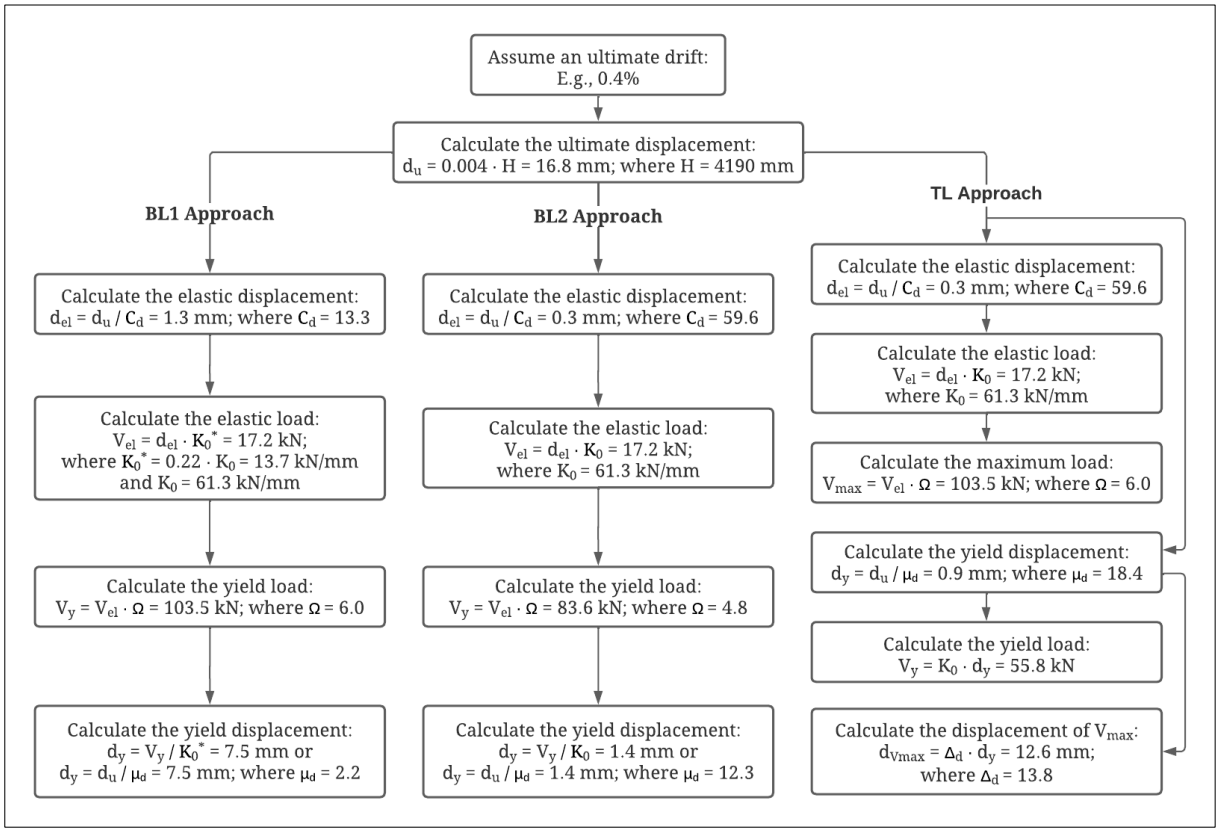

Source: Author.

The predicted idealized load-displacement curves of the experimental walls for the three approaches are shown in Figure 114 for d_u from the tests and in Figure 115 for d_u limited to a top drift of 0.4%. Also, the predicted idealized curves of the numerical walls (FE models) with the higher axial load are shown in Figure 116 for d_u from the models and in Figure 117 for d_u limited to a top drift of 0.3%; only the TL approach was used in these cases.

Figure 114: Predicted idealized curves of the experimental walls for d_u from the tests.

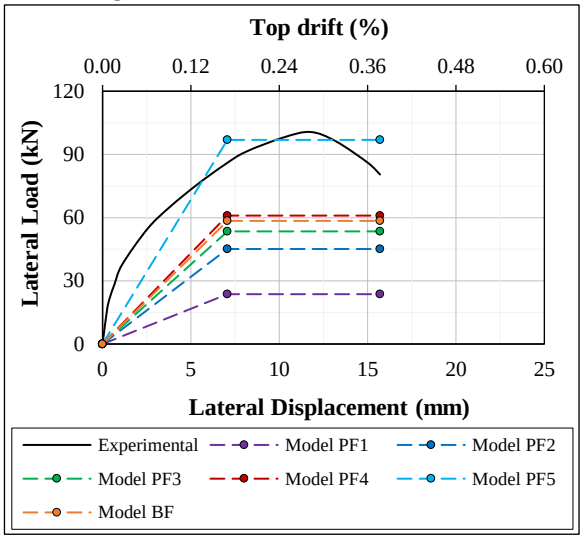

(a) Walls W1 and W2 – BL1

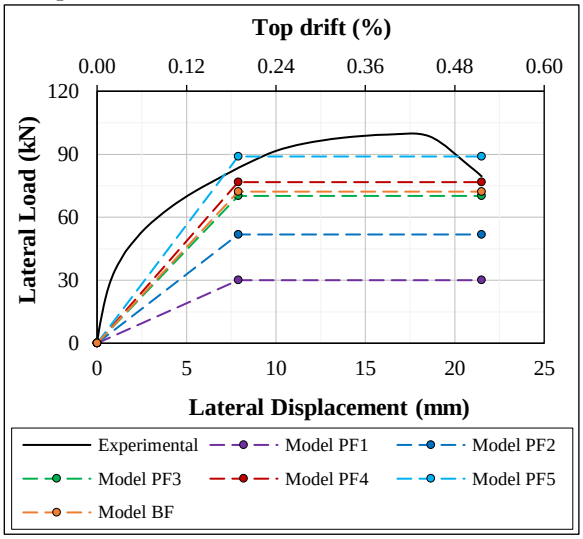

(b) Walls D1 and D2 – BL1

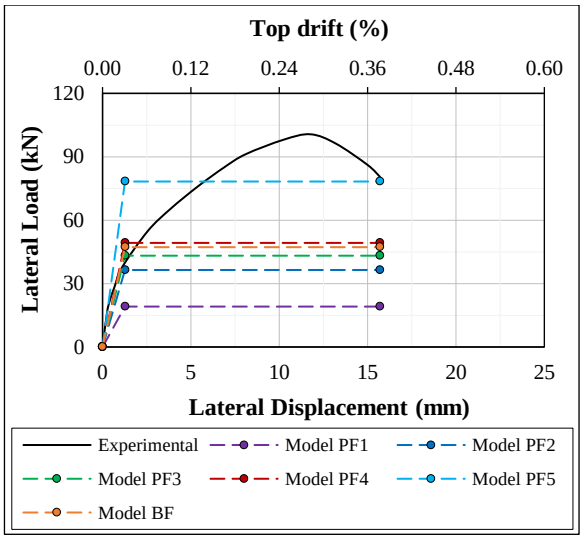

(c) Walls W1 and W2 – BL2

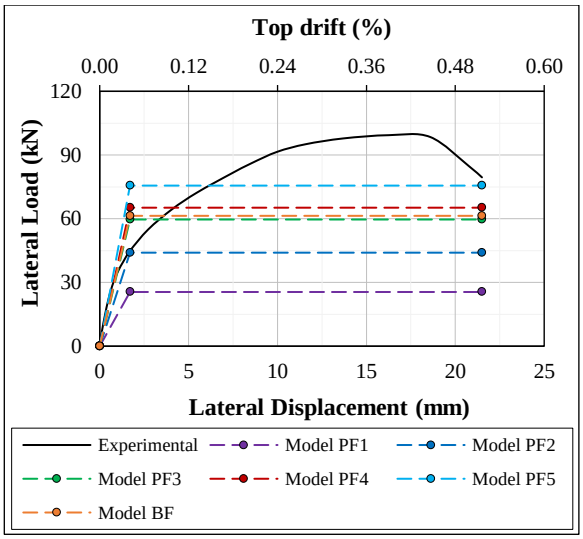

(d) Walls D1 and D2 – BL2

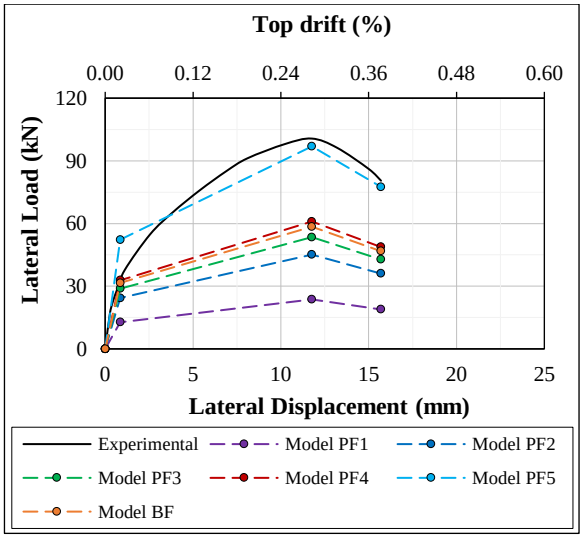

(e) Walls W1 and W2 – TL

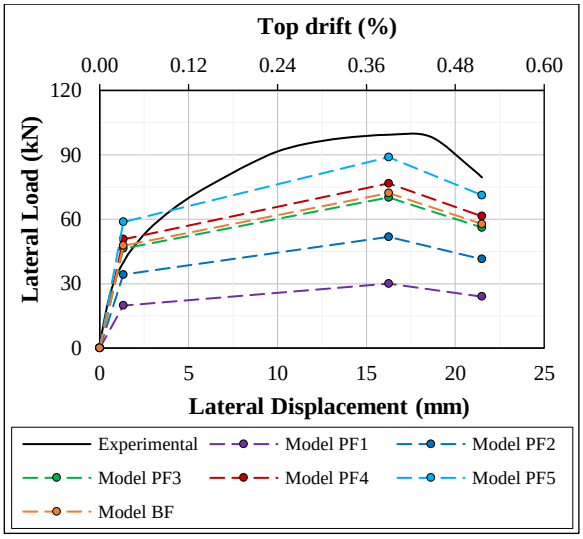

(f) Walls D1 and D2 – TL

Source: Author.

Figure 115: Predicted idealized curves of the experimental walls for d_u from the drift of 0.4%.

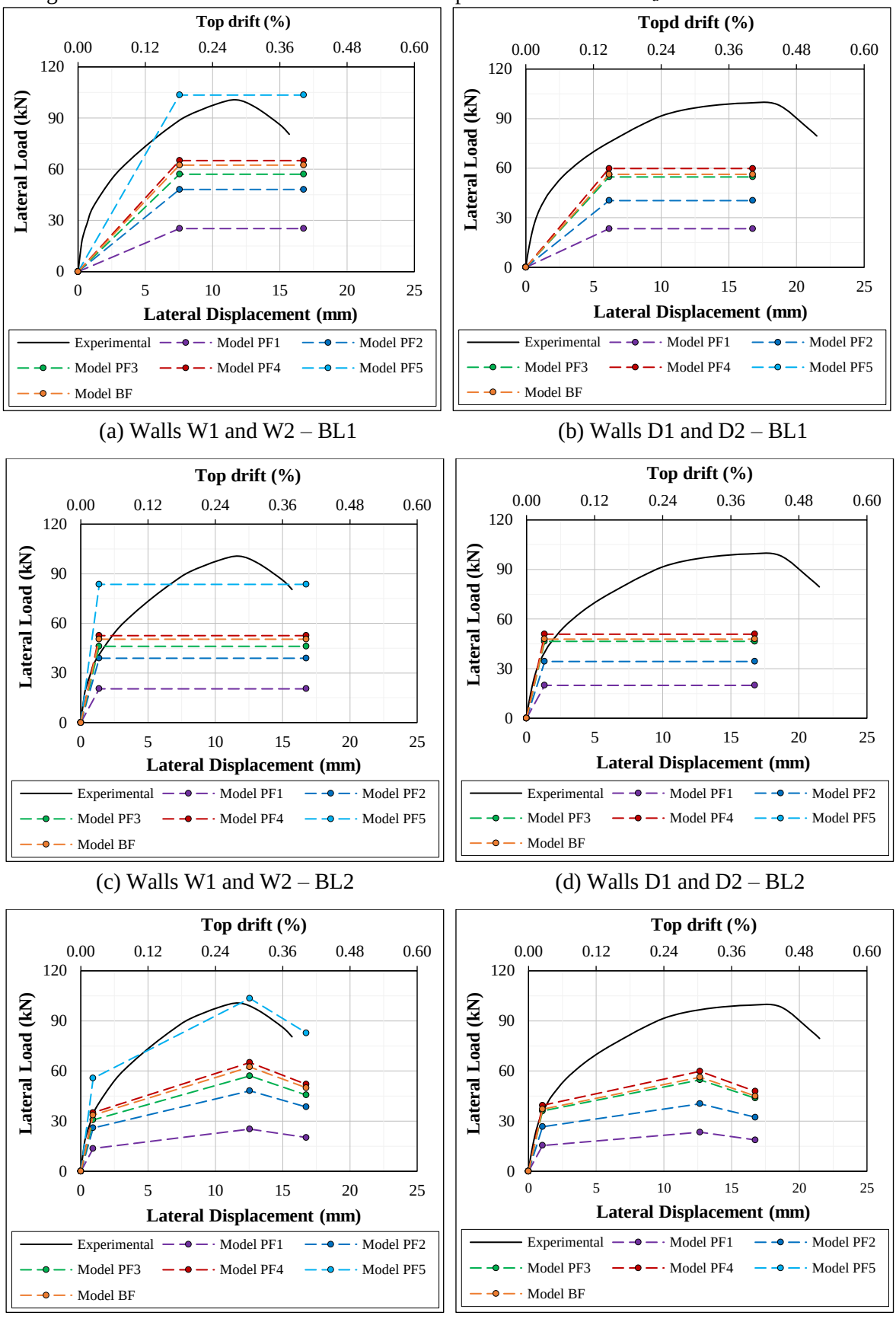

(a) Walls W1 and W2 – BL1

(b) Walls D1 and D2 – BL1

(c) Walls W1 and W2 – BL2

(d) Walls D1 and D2 – BL2

(e) Walls W1 and W2 – TL

(f) Walls D1 and D2 – TL

Source: Author.

Figure 116: Predicted idealized curves of the numerical walls for d_u from the models.

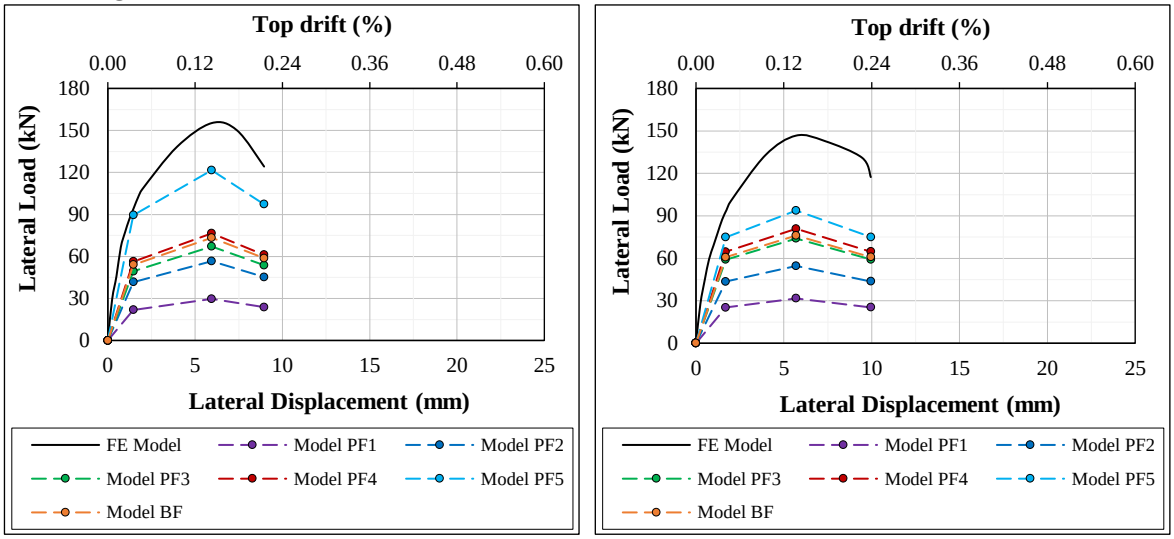

(a) Walls W1 and W2 – TL (b) Walls D1 and D2 – TL

Source: Author.

Figure 117: Predicted idealized curves of the numerical walls for d_u from the drift of 0.3%.

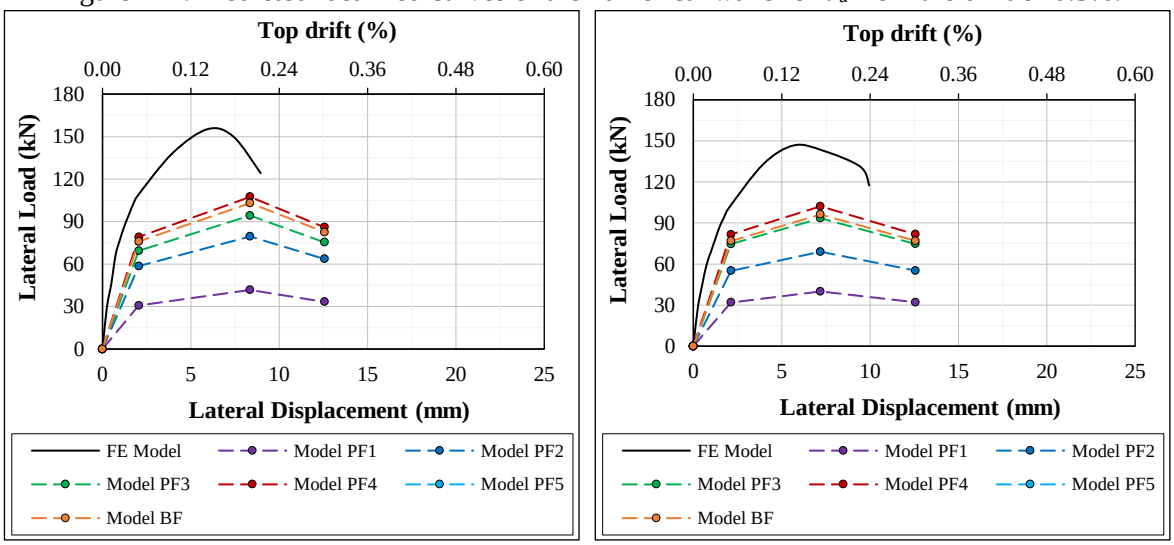

(a) Walls W1 and W2 – TL (b) Walls D1 and D2 – TL

Source: Author.

As can be observed in Figure 114 to Figure 117, the idealized load-displacement curves of models PF5 and PF1 were, respectively, the closest and farthest predictions of the actual wall responses in all cases. In other words, the idealized curves fitted better the actual response when the lateral stiffness of the linear models was closer to that of the reference walls.

The predicted lateral load capacity of walls was more conservative for the same displacement as long as linear models with lower lateral stiffness were used. The differences in the lateral load capacity were proportional to the differences in the lateral stiffness. For example, considering d_u from the tests and the TL approach, Model PF1 had K_0 = 15 kN/mm (-76%) and V_{max} = 23.7 kN (-76%) and Model PF5 had K_0 = 61.3 kN/mm (-4%) and V_{max} = 96.9

kN (-4%) compared to K_0 = 63.7 kN/mm and V_{max} = 100.7 kN from the experimental walls W1-2, Figure 114(e). Doing the same analyses for the experimental walls D1-2, Model PF1 had K_0 = 15 kN/mm (-70%) and V_{max} = 30 kN (-70%) and Model PF5 had K_0 = 44.3 kN/mm (-10%) and V_{max} = 89 kN (-10%) compared to K_0 = 49.5 kN/mm and V_{max} = 99.4 kN from the tests, Figure 114(f). Although there was no case in which a linear model has lateral stiffness higher than that of the reference walls, the analyses point out that in this scenario, the load capacity would be overestimated.

The numerical walls (FE models), which were submitted to the higher pre-compression ($0.2f'_m$), had a lateral stiffness 23% and 40% higher than that of the experimental walls with window (W1-2) and door openings (D1-2), respectively. These differences are even larger when comparing the FE models with the linear models since the lateral stiffness of the linear models is independent of the applied axial load. As a consequence, the predicted idealized load-displacement curves using the linear models were also more conservative. For instance, considering d_u from the models and the TL approach, Model PF1 had K_0 = 15 kN/mm (-81%) and V_{max} = 29.7 kN (-81%) and Model PF5 had K_0 = 61.3 kN/mm (-22%) and V_{max} = 121.6 kN (-22%) compared to K_0 = 78.3 kN/mm and V_{max} = 155.3 kN from walls W1-2, Figure 116(a). For walls D1-2, Model PF1 had K_0 = 15 kN/mm (-78%) and V_{max} = 31.7 kN (-78%) and Model PF5 had K_0 = 44.3 kN/mm (-36%) and V_{max} = 93.8 kN (-36%) compared to K_0 = 69.3 kN/mm and V_{max} = 146.7 kN from the FE model, Figure 116(b).

Imposing the ultimate top drift of 0.40% for the cases with the lower axial load implied an ultimate displacement that was 7% unconservative for walls W1-2 and 22% conservative for walls D1-2, as seen in Figure 115. Compared to the idealized curves with the ultimate displacement equal to the tests, those differences provoked a proportional increase of 7% for walls W1-2 and a decrease of 22% for walls D1-2 in the predicted lateral capacity for all models using all approaches. One may interpret this to mean that an imposed ultimate top drift higher than the actual top drift amplifies the estimation of the lateral capacity and vice-versa, using the proposed approaches.

For the cases with the higher axial load, imposing the ultimate top drift of 0.30% provided an unconservative ultimate displacement for both types of walls. The idealized curves had a d_u 40% and 26% higher for walls W1-2, and walls D1-2, respectively, than the FE models, as illustrated in Figure 117. As stated before, additions in the ultimate displacement caused a proportional increase in the predicted lateral capacity when compared to the idealized curves with the ultimate displacement equal to the FE models.

An ultimate top drift of 0.2% was also evaluated for the walls with high pre-compression since using a value of 0.3% implied remarkably unconservative ultimate displacements. The responses using the model PF5 and the TL approach are shown in Figure 118.

Figure 118: Predicted idealized curves of the numerical walls for d_u from the drifts of 0.3% and 0.2%.

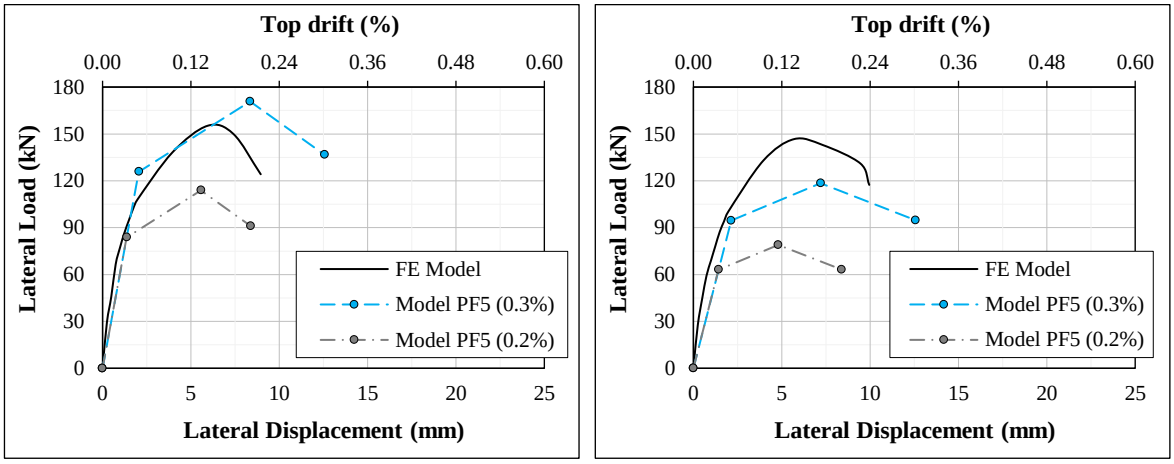

(a) Walls W1 and W2 – TL (b) Walls D1 and D2 – TL

Source: Author.

It may be seen in Figure 118 that the ultimate displacements derived from the imposed ultimate top drift of 0.2% for the numerical walls with high pre-compression were conservative in both cases assessed. For the experimental walls W1-2, and D1-2, the ultimate displacement of the idealized curves from the drift of 0.2% was, respectively, 6% and 16% smaller than that from the models, showing a better estimation than when a drift of 0.3% was used. For these cases, the notable differences in the lateral load capacity are mainly due to the differences in the lateral stiffness.

It is important to note that the analyses show the high sensitivity of the method to predict the envelope lateral response related to the ultimate drift and initial lateral stiffness. Also, the three approaches (BL1, BL2, and TL) to idealize the lateral response are feasible, each one with its particularities, as long as the corresponding SPFs are used. Consequently, the necessity is evident of using linear models with a lateral stiffness compatible with that adopted during the process of obtaining the SPFs.

5.3 NON-LINEAR BRACED FRAME MODEL

5.3.1 Modeling development

Some attempts were made to simulate the non-linear behavior of the experimental walls using the PF and BF models with the same geometries presented in section 5.2.1, still operating

with the software SAP2000. However, only the non-linear BF models are presented since the PF models did not demonstrate coherent results.

Concentrated plastic hinges assigned to the frame elements were used to simulate the post-yield behavior. The elastic material properties (Table 34) control the behavior of the members until the inelastic behavior of the hinges is activated. As illustrated in Figure 119, flexural hinges were allocated at the beginning and end of the pier and beam elements, while axial hinges were assigned to the diagonal (brace) elements.

Figure 119: Location of the plastic hinges.

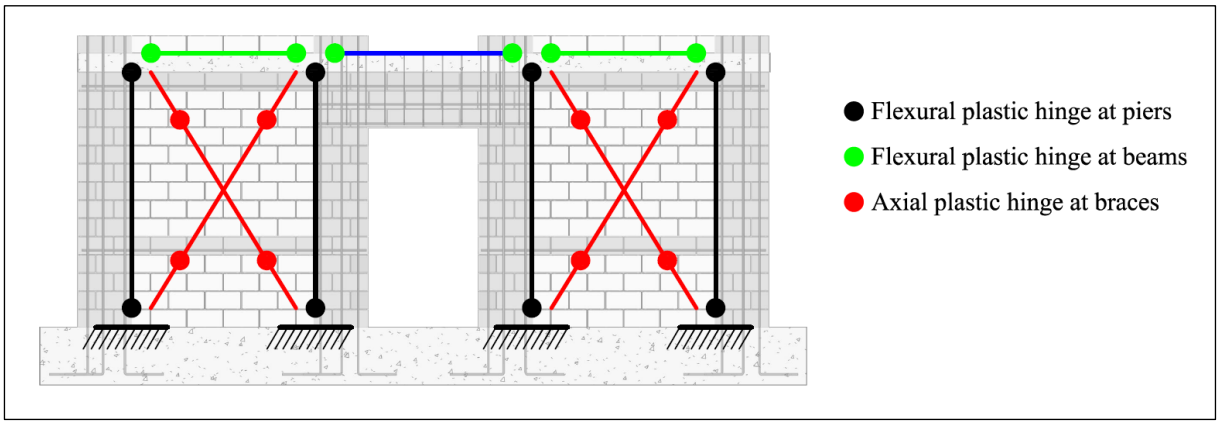

Source: Author.

The flexural hinge properties were computed automatically according to the ASCE 41-13 (2014) criteria for concrete columns and beams using the moment-rotation curve based on the element material and section properties. For that, the sections included the longitudinal reinforcement and had the average non-linear material data specified in Table 38. P-M interaction was not considered in the hinges.

The axial hinge behavior was defined by the stress-strain curve plotted in Figure 120, in which the critical tension and compressive capacities were calculated by using Equation 96 (Pirsaheb et al., 2021) and Equations 97-101, respectively. The pure shear strength of masonry (f_{v0}) was assumed equal to 0.2 MPa (EN 1996-1, 2005) in Equation 96. The critical compressive capacity considered only the contribution of the ungrouted region into the respective wall pier by adapting the equation proposed in Chapter 3 (section 3.3.2) to predict the maximum lateral load capacity of walls with a diagonal shear failure mode. Also, the approach indicated in section 3.4.1 for perforated walls is based on the strength of the wall piers with dimensions limited by diagonal shear cracks formed from the upper corner of the opening to the lower corner of the opening of the same story. The reduced-scale walls were converted to equivalent full-scale walls to proceed with the calculation as an equation requirement.

Table 38: Non-linear properties of materials used in the flexural hinges.

Material	Parameter	Value for the material type (a)	Value for the material type (b)	Reference of the used value
Concrete (a) Middle slabs (b) Top beam	Compressive strength (f_c')	36.1 MPa	31.5 MPa	Test results (Fortes and Parsekian, 2017)
	Peak comp. strain (ε_{cp})	$2.07 \cdot 10^{-3}$	$2.04 \cdot 10^{-3}$	$1.8 + 0.0075 f_c'$ (Wong et al., 2013)
	Ultimate comp. strain (ε_{cu})	$3.50 \cdot 10^{-3}$	$3.50 \cdot 10^{-3}$	Specified (ABNT NBR 6118, 2014)
Masonry (a) Ungrouted (b) Grouted	Critical comp. strength ($f_{m,cr}'$)	8.0 MPa	8.3 MPa	$0.8 \cdot 0.85 \cdot f_m'$ (Pirsaheb et al., 2021)
	Critical comp. strain ($\varepsilon_{m,cr}$)	$7.56 \cdot 10^{-4}$	$7.56 \cdot 10^{-4}$	$f_{m,cr}'/E_m$ (Pirsaheb et al., 2021)
	Ultimate comp. strain ($\varepsilon_{m,u}$)	$3.00 \cdot 10^{-3}$	$3.00 \cdot 10^{-3}$	Specified (ABNT NBR 16868-1, 2020)
Reinforcement Ø9.5 mm	Yield strength ($f_{s,y}$)	540 MPa		Test results (Fortes and Parsekian, 2017)
	Ultimate strength ($f_{s,u}$)	742 MPa		Test results (Fortes and Parsekian, 2017)
	Elastic modulus (E_s)	203,512 MPa		Test results (Fortes and Parsekian, 2017)
	Hardening strain ($\varepsilon_{s,cr}$)	$2.00 \cdot 10^{-3}$		Test results (Fortes and Parsekian, 2017)
	Ultimate strain ($\varepsilon_{s,u}$)	$82.0 \cdot 10^{-3}$		Test results (Fortes and Parsekian, 2017)

Source: Author.

Figure 120: Stress-strain curve of axial hinges applied to the diagonal elements.

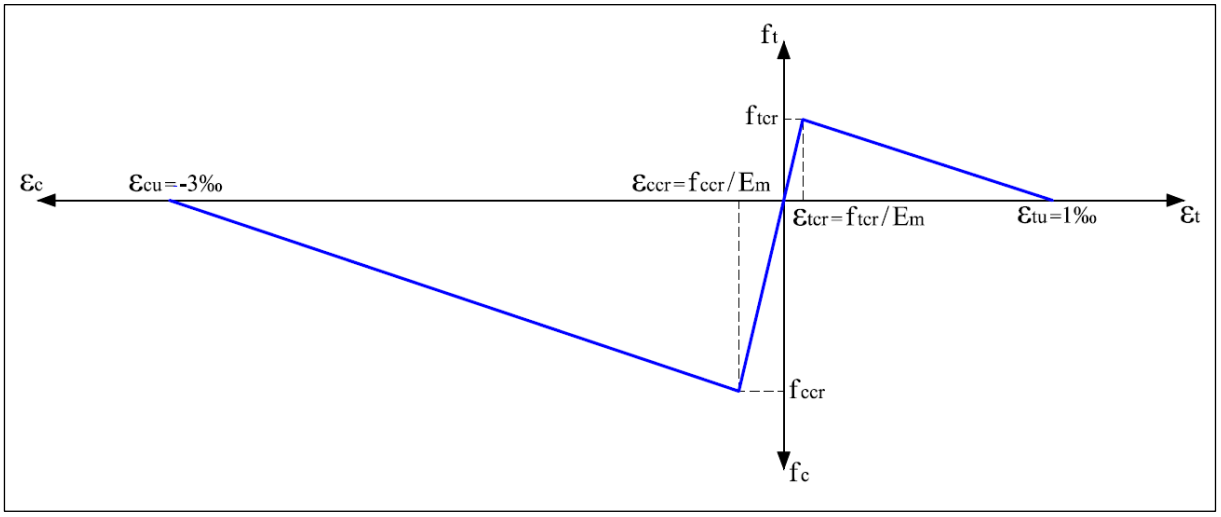

Source: Author.

$$f_{tcr} = (0.375 f_{v0} + 0.5\sigma)\sin(2\theta_d') \quad \text{Eq. 96}$$

$$f_{ccr} = \frac{k_{gv} k_{gh} \beta_r A_{ph_{ug}} \sqrt{k f_m'} + 0.144 P \left(L_{p_{ug}}/H_{op}\right) + 0.02 A_v f_y \sqrt{f_m'} + 0.02 \rho_h A_{pv_{ug}} f_y \sqrt{f_m'}}{A_{ph_{ug}} \sin\theta_d} \quad \text{Eq. 97}$$

$$k_{gh} = 1.633 - 0.079 \ln\left(H_{op}/n_{ugph}\right) \geq 1.0 \quad \text{Eq. 98}$$

$$k_{gv} = 5.539 - 0.583 \ln\left(L_{p_{ug}}/n_{ugpv}\right) \quad \text{Eq. 99}$$

$$\beta_r = \begin{cases} 0.183 - 0.14\left(H_{\text{op}}/L_{p_{ug}}\right) & if \quad 0.25 \le H_{\text{op}}/L_{p_{ug}} < 0.5 \\ 0.134 - 0.034\left(H_{\text{op}}/L_{p_{ug}}\right) & if \quad 0.5 \le H_{\text{op}}/L_{p_{ug}} < 1.0 \\ 0.19 - 0.091\left(H_{\text{op}}/L_{p_{ug}}\right) & if \quad 1.0 \le H_{\text{op}}/L_{p_{ug}} < 2.0 \end{cases} \qquad \text{Eq. 100}$$

$$k_c = 1 - 0.058(5 - r)^{1.07} \qquad \text{Eq. 101}$$

where: f_{v0} = shear strength of masonry (MPa); σ = pre-compression stress (MPa); f_y = yield strength of the specified reinforcement (MPa); P = axial compressive load on the considered section (N); $A_{ph_{ug}}$= effective horizontal cross-sectional area of the ungrouted region into the pier (mm²); $A_{pv_{ug}}$= effective vertical cross-sectional area of the ungrouted region into the pier (mm²); A_v = total cross-sectional area of vertical reinforcement in the considered section (mm²); ρ_h = net horizontal reinforcement ratio in the considered section; H_{op}= height of the opening adjacent to the pier (mm); $L_{p_{ug}}$= length of the ungrouted region into the pier (mm); θ_d = diagonal angle related to horizontal direction (deg); θ_d' = diagonal angle related to vertical direction (deg); n_{ugph} = number of the horizontal ungrouted panels formed along the height H_{op}; n_{ugpv} = number of the vertical ungrouted panels formed along the length $L_{p_{ug}}$; r = prism height-to-thickness ratio.

5.3.2 Assessment of model performance

The model performance was evaluated by comparing the initial lateral stiffness, lateral load capacity and corresponding lateral displacement at the top of the walls against the data of the experimental tests. The FE models developed in the previous chapters were also used in the comparisons, mainly as a reference for the situation with the higher pre-compression ($\sigma = 0.2f_m'$), as done in section 5.2.3. The envelope curves of walls with low and high axial loads are shown in Figure 121 and Figure 122, respectively, while a summary of results is presented in Table 39. Model BF-A represents the original response from the modeling, and model BF-B has the response of model BF-A with an imposed post-peak of $0.8V_{max}$ limited to the ultimate drifts of 0.4% and 0.2% for the cases with low and high pre-compression, respectively.

Furthermore, the lateral deflected shapes of the experimental and numerical walls with low and high axial pre-compression are plotted in Figure 123 and Figure 124 for some levels of the maximum lateral load: $0.2V_{max}$, $0.4V_{max}$, $0.6V_{max}$, $0.8V_{max}$, V_{max}, and $0.8V_{max}$*, this last one corresponding to the instant when the load had dropped 20% after the peak.

As for the linear frame models, the distribution of loads throughout the wall elements in the first story of the non-linear model BF is compared with results from the FE model. The results are presented in Table 40, taking walls D1-2 as an example and considering different lateral load levels.

Figure 121: Envelope load-displacement curves of the experimental tests and models with the lower pre-compression ($\sigma = 0.04 f'_m$).

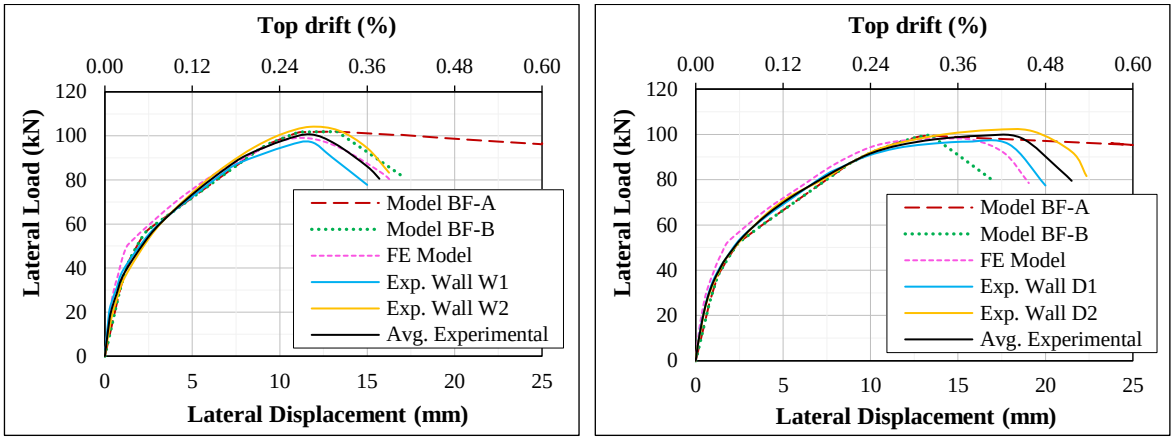

(a) Walls W1 and W2 (b) Walls D1 and D2

Source: Author.

Figure 122: Envelope load-displacement curves of the FE model and models BF with the higher pre-compression ($\sigma = 0.2 f'_m$).

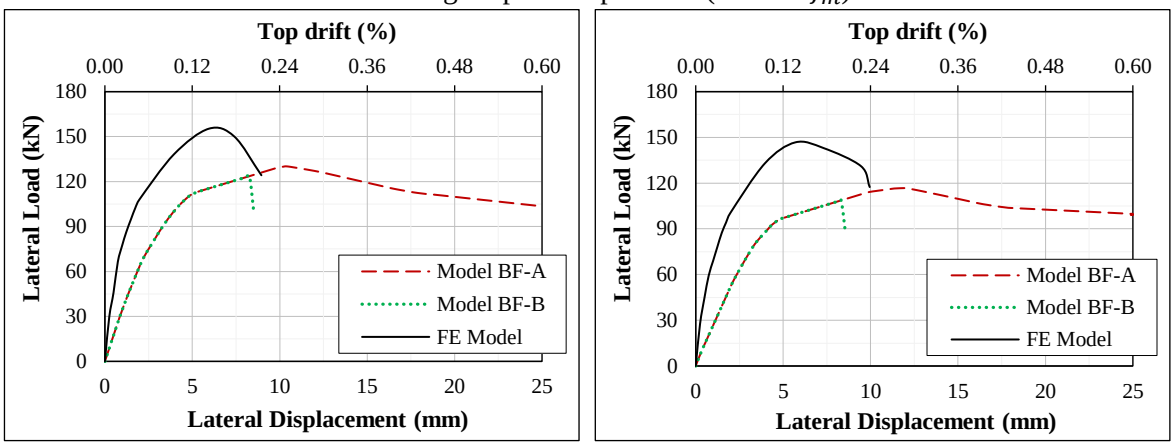

(a) Walls W1 and W2 (b) Walls D1 and D2

Source: Author.

Table 39: Results of the experimental tests and models with the low and high pre-compressions.

Wall (axial load case)	Response	Stiffness		Force		Top displacement			
		K_0 (kN/mm)	ΔK_0 (%)	V_{max} (kN)	ΔV_{max} (%)	d_{Vmax} (mm)	Δd_{Vmax} (%)	d_u (mm)	Δd_u (%)
W1 & W2 ($\sigma = 0.04 f'_m$)	Model BF	37.0	---	101.9	---	13.3	---	17.0*	---
	FE Model	72.9	-49.2	98.9	3.1	11.7	13.4	16.4	3.9
	Exp. Wall W1	82.8	-55.3	97.2	4.9	11.8	12.5	15.0	13.6
	Exp. Wall W2	48.0	-22.9	104.1	-2.1	11.7	13.4	16.3	4.5
	Avg. Experimental	63.7	-41.9	100.7	1.3	11.8	12.5	15.7	8.5

D1 & D2 ($\sigma = 0.04f'_m$)	Model BF	36.0	---	99.5	---	13.5	---	17.0*	---
	FE Model	61.9	-41.8	98.1	1.4	13.9	-3.2	19.0	-10.5
	Exp. Wall D1	52.6	-31.6	96.8	2.8	15.5	-13.2	20.0	-15.0
	Exp. Wall D2	46.7	-22.9	102.0	-2.5	17.0	-20.9	22.3	-23.7
	Avg. Experimental	49.5	-27.3	99.4	0.1	16.2	-17.0	21.5	-20.9
W1 & W2 ($\sigma = 0.2f'_m$)	Model BF	37.0	---	130.2	---	10.3	---	8.6*	---
	FE Model	78.3	-52.7	155.3	-16.2	6.0	72.2	9.0	-5.3
D1 & D2 ($\sigma = 0.2f'_m$)	Model BF	36.0	---	116.7	---	11.9	---	8.6*	---
	FE Model	69.3	-48.1	146.7	-20.5	5.7	108.4	10.0	-14.3

*Value corresponding to the imposed ultimate drifts in Model BF-B.

Source: Author.

Figure 123: Experimental and numerical deflected shapes of walls with the lower pre-compression ($\sigma = 0.04f'_m$) for different lateral load levels.

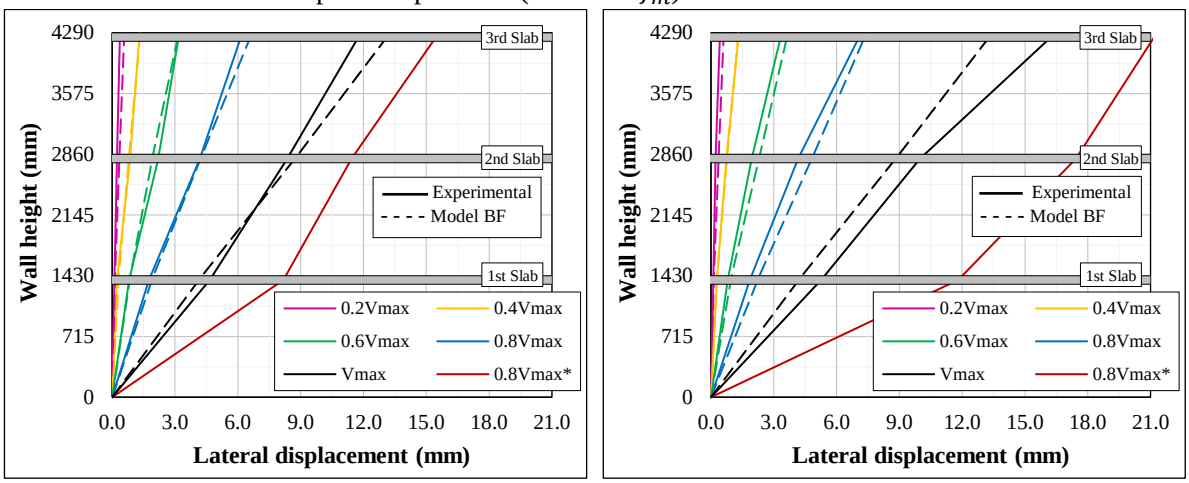

(a) Walls W1 and W2 (b) Walls D1 and D2

Source: Author.

Figure 124: Deflected shapes of the FE model and models BF with the higher pre-compression ($\sigma = 0.2f'_m$) for different lateral load levels.

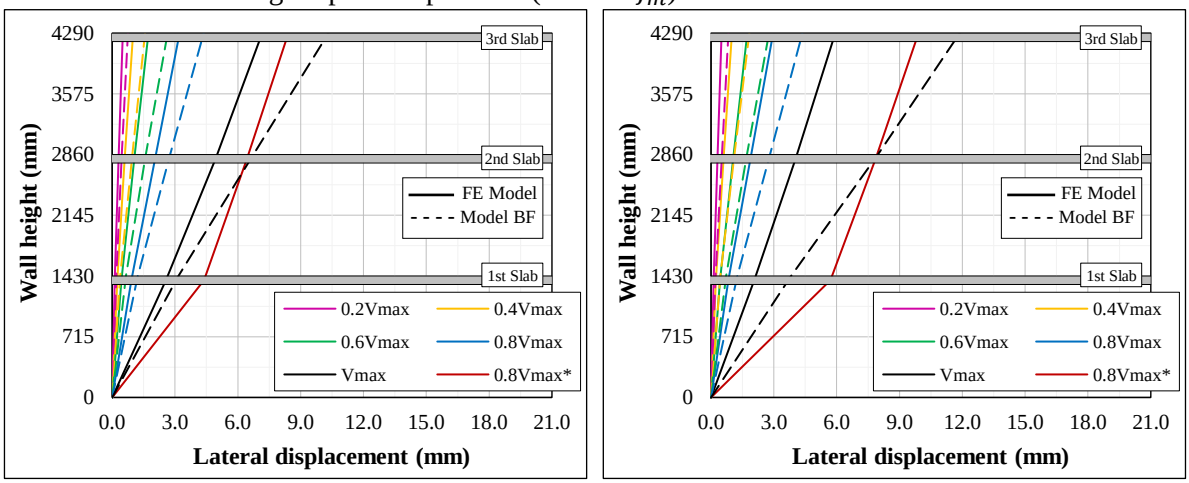

(a) Walls W1 and W2 (b) Walls D1 and D2

Source: Author.

Table 40: Element loads in the first story of walls D1-2 for the non-linear FE and BF models.

Lateral load level (kN)	Model	Left Pier			Right Pier			Beam		
		N (kN)	V (kN)	M (kN·m)	N (kN)	V (kN)	M (kN·m)	N (kN)	V (kN)	M (kN·m)
15	FE Model	-20.9	7.3	14.0	-60.1	9.2	15.8	-0.3	5.1	1.2
	Model BF	-22.4	8.0	16.2	-58.5	8.5	16.6	-0.3	4.8	2.7
50	FE Model	18.4	13.3	17.5	-99.5	36.6	72.9	-1.3	15.8	3.5
	Model BF	19.6	25.9	48.6	-100.5	24.5	48.9	-0.2	19.3	11.0
90	FE Model	64.7	28.0	37.7	-145.8	62.1	128.4	5.2	25.6	7.2
	Model BF	112.5	45.6	35.2	-193.2	45.2	35.5	-0.1	56.3	31.9
99	FE Model	75.7	29.5	41.4	-156.4	68.4	138.6	5.9	28.1	8.2
	Model BF	149.5	50.2	15.1	-230.4	49.3	15.3	-0.1	68.6	38.8

Source: Author.

As can be seen in Figure 121, there was good agreement between the envelope curves of the model BF and the experimental walls up to the peak load. Unlike the FE model, model BF-A was not able to simulate the post-peak behavior of the walls, not presenting the expected strength degradation. This problem was dealt with in model BF-B by imposing an ultimate load of $0.8V_{max}$ with a corresponding ultimate displacement limited to a drift of 0.4%.

The average experimental lateral stiffness, maximum lateral load, and corresponding lateral displacement at the top of walls W1-2 were 63.7 kN/mm, 100.7 kN, and 11.8 mm, respectively. The model BF for these walls resulted in a lateral stiffness of 37 kN/mm, a peak load of 101.9 kN, and a corresponding displacement of 13.3 mm, which were 41.9% lower, 1.3% higher, and 12.5% higher, respectively, than the experimental results. For walls D1-2, the average experimental results for the lateral stiffness, peak load, and the corresponding displacement were 49.5 kN/mm, 99.4 kN, and 16.2 mm, respectively, against 36 kN/mm (-27.3%), 99.5 kN (+0.1%) and 13.5 mm (-17%) obtained from the model BF. With the imposed ultimate drift of 0.4% to the model BF-B, the ultimate displacement was 8.5% higher for walls W1-2 and 20.9% lower for walls D1-2.

Regarding the walls with the higher pre-compression, substantial differences exist between the envelope curves of model BF and the FE model, even in the pre-peak stage, Figure 122. The maximum lateral load differences were reasonable, with the model BF being more conservative than the FE model by 16.2% for walls W1-2 and 20.5% for walls D1-2. However, model BF was up to 52.7% more flexible than the FE model, which directly influenced a displacement at the peak load up to 108.4% higher. A possible reason for this contrast may be the absence of the interaction between axial load and moment in the strength capacity of the flexural hinges; many attempts were made to include this interaction, but all stopped due to

numerical convergence problems. Dealing with this limitation, imposing the drift limit of 0.2%, as in model BF-B, resulted in acceptable conservatism.

The deflected shapes of the walls with the lower pre-compression obtained with model BF are compatible with the experimental walls up to the peak load, as observed in Figure 123. The major difference between inter-story drifts was found in the third story at the stage of maximum lateral load; the values for the Model BF were approximately 29% higher and lower than the experimental walls W1-2 and D1-2, respectively. Concerning the walls with the higher axial load, the comparison of the deflected shapes shown in Figure 124 corroborates that model BF is significantly more flexible than the FE Model for all lateral load levels.

The results in Table 40 show that the reaction loads calculated at the bottom center point of each pier from model BF match the reaction loads integrated at the bottom center point of each pier in the linear phase of the FE model. As the lateral load increases and the wall behavior becomes more non-linear, significant differences in the axial force and moment are noted. Unlike the FE model, Model BF presented similar values for the moment in both left and right wall piers, appearing to be incapable of representing this phenomenon correctly. Numerous variables were adjusted in an attempt to understand what causes this behavior, but nothing became apparent.

5.4 CONCLUDING REMARKS

Linear and non-linear frame models were assessed in simulating the behavior of in-plane loaded, multi-story, perforated, partially grouted masonry walls. Regarding the linear models, portal and braced frame models were tested to simulate the initial lateral stiffness of the walls. Furthermore, the linear models were used in a newly proposed method to define the envelope lateral response of walls based on SPFs and ultimate top drifts. The braced frame model was also used to simulate the entire non-linear behavior of the walls employing concentrated plastic hinges. According to the analysis, the following comments and conclusions can be made:

- The cantilever model was the most conservative to simulate the initial lateral stiffness and internal load distribution of the coupled perforated walls. The stiffness became greater as rigid offsets were implemented in the portal frame modeling. Including rigid offsets on the horizontal and vertical elements resulted in a portal frame model with a lateral stiffness and internal loads reasonably close to that of the experimental

walls. The braced frame model was also able to represent reasonably the initial lateral stiffness and internal load distribution in the walls;

- Given adequate SPFs and ultimate top drifts, it was possible to reproduce the envelope of the idealized lateral response of the walls using the initial lateral stiffness of the linear models. The idealized curves fitted the actual response better when the lateral stiffness of the linear models was closer to that of the reference walls, being the differences in the lateral load capacity proportional to the differences in the lateral stiffness;
- The three approaches (BL1, BL2, and TL) examined to idealize the lateral response are feasible, each one with its particularities, as long as the corresponding SPFs are used. Also, the analysis reveals the necessity of using linear models with a lateral stiffness compatible with that adopted during the process of obtaining the SPFs;
- The method to define the envelope of the wall lateral response is also sensitive to the imposed ultimate top drift. An ultimate top drift higher than the actual top drift amplified the estimation of the lateral load capacity and vice-versa, using all the proposed approaches. Values of 0.4% and 0.2% proved to be reasonable options for the cases in which the walls were subjected to a pre-compression of $0.04f'_m$ and $0.2f'_m$, respectively;
- The non-linear braced frame model could accurately simulate the envelope curves of the experimental walls up to the peak load but did not present the expected strength degradation in the post-peak stage. This issue could be overcome by imposing an ultimate load of $0.8V_{max}$ with a corresponding ultimate displacement limited to a drift of 0.4%. Regarding the walls with the higher pre-compression ($\sigma = 0.2f'_m$), the BF model was reasonably conservative in predicting the maximum lateral load, but it was considerably more flexible than the FE model: imposing the drift limit of 0.2% made the result acceptably conservative. Model BF could satisfactorily represent the distribution of loads between the elements in the linear phase, but was imprecise in the non-linear stage. Dealing with the model limitation, further improvements are needed to account for the interaction between axial load and moment in the strength capacity of the flexural plastic hinges on the vertical elements without affecting numerical convergence.

6. CONCLUSIONS

The research presented here was based on the use of experimental tests from the research group and also on those found in the literature, as well as adequately validated numerical models with the purpose of expanding the knowledge about the behavior of structural masonry shear walls, especially for partially grouted walls with grout and reinforcement at their ends. The specific conclusions from the analyses carried out throughout the different chapters of the thesis and suggestions for future work are presented below.

a) Chapter 2: Parametric study

The study presented in Chapter 2 aimed to investigate, using finite element modeling, the influence of various parameters on the behavior of partially grouted multi-story masonry shear walls with openings. The numerical model was used to analyze the different variations of the walls as a function of the load capacity, displacement preceding the maximum load, and initial lateral stiffness. The results allow concluding that:

- The wall load capacity was significantly impacted by changes in the strengths of the ungrouted and grouted masonry, in the mortar shear strength, in the vertical reinforcement ratio, and in the aspect ratio. Around 10% of the wall load capacity varied as a consequence of a variation of about 120% in the axial stress. Except for the aspect ratio, all of these parameters had a positive correlation with the wall load capacity. The wall capacity was not affected significantly by the opening size, reinforcement spacing, or horizontal reinforcement ratio;
- The deflection of the walls positively correlated with the strengths of the ungrouted and grouted masonry, the aspect ratio, and the opening width, and negatively with the vertical reinforcement ratio and the axial stress. Changes in the mortar shear strength, horizontal reinforcement ratio, and spacing between reinforcements did not significantly impact the displacements. The opening height and deflection of the walls did not exhibit a clear relationship;
- There is a limit where increasing the ungrouted and grouted masonry's strengths have no further impact on the walls' capacity and deflection, which in this case were around 65% and 40% of the strength of the base model, respectively;

- The initial stiffness of the walls was susceptible to changes in the strengths of the ungrouted and grouted masonry, in the joint mortar shear strength, and especially in the axial stress and aspect ratio. The modifications in the opening size and the spacing and size of the reinforcement had a smaller impact on the initial stiffness;
- The load capacity and initial stiffness were positively correlated to the axial stress while the displacement was negatively correlated with it; the aspect ratio had the inverse effect. The failure mode was altered by both factors: an increase in the axial load made the failure shear-dominated, while an increase in the aspect ratio made the failure flexural-dominated;
- As the alterations imposed on the opening dimensions in this analysis reflected a reduction of, at most, 12.5% in the effective cross-sectional area and with a failure mode dominated by shear, the results addressing the opening dimensions should not be taken as absolute. More investigations are required to confirm the effect of significant changes in the opening size.

b) Chapter 3: Shear load capacity prediction

The FEM developed previously in Chapter 2 was recalibrated and revalidated to be used in the study of Chapter 3. The accuracy of expressions to predict the SLC of unperforated PGMW was evaluated by comparing a new proposed shear equation with some relevant already existing ones. Additionally, different approaches were investigated to find the best reliable strategy for estimating the SLC of single and multi-story PGMW with openings. The following conclusions can be made in light of the findings:

- The simulated scenarios could demonstrate that certain accurate predictions made with the existing shear equations are actually false positives. The absence of a term for the contribution of the vertical reinforcement and/or the underestimation of the masonry contribution caused by restrictions on the aspect ratio frequently served to balance off the overestimation of the contribution of the horizontal reinforcement and vice versa;
- Among all the equations examined, the ones from TMS 402/602 (2016) and CSA S304 (2014) delivered the most inaccurate estimations of the shear load capacity of the unperforated PGMW for both the computational and experimental datasets. The SLC of walls with horizontal reinforcement tended to be overpredicted insecurely using the TMS 402/602 (2016) equation and with a high variability using the CSA

S304 (2014) equation. The code equations tended to overestimate and underestimate, respectively, the SLC of walls with large and small horizontal spacing between grouted cells, particularly because these equations were developed for FGMW and further adjusted for PGMW using a simple constant reduction factor;

- Among the evaluated existing shear equations, that one of Dillon and Fonseca (2015) performed the best predictions for the walls of the numerical dataset, whereas the equations of Izquierdo et al. (2021), and Seif ElDin et al. (2019a) were the most accurate for the walls of the experimental dataset;
- The new proposed equation included the effects of the aspect ratio, vertical and horizontal grouting and reinforcement, and axial loading to ensure a suitable level of accuracy in estimating the SLC of the walls. Thus, the proposed equation provided the best statistical indicators among all the shear equations studied for unperforated PGMW of both the numerical and experimental datasets;
- The reduction of the effective horizontal cross-sectional area can be associated with the significant decrease in SLC of the single-story walls caused by the presence of openings. Even in a smaller proportion, the SLC of the walls also decreased when the window openings were replaced with door openings. Since the lateral load was applied at the top of the highest story, the diagonal struts found more areas of masonry between the stories to pass through, reducing the impact of the openings on walls with more stories. More research is needed to assess the impact of openings in multi-story PGMW when lateral loads are applied at each story level;
- The approach of predicting the SLC of perforated PGMW by only reducing the effective horizontal cross-sectional area in the shear equation did not yield appropriate results since this approach ignores the opening height. The approach which considered the strength of the wall as the sum of the strengths of the wall piers with dimensions limited by the diagonal shear crack forming from the upper corner of the opening to the lower diagonally opposite corner of the opening of the same story produced the most accurate predictions. The applicability of this strategy employing the newly presented shear equation for walls with openings positioned asymmetrically requires further investigation.

Finally, besides proposing a new accurate and complete shear equation for PGMW, this study indicates the need of updating the shear expression of the TMS 402/602 (2016) and CSA

S304 (2014). It is suggested to reduce the influence of the horizontal reinforcement, include the effect of the vertical reinforcement, revise the limits for the aspect ratio, consider the interrelation between the applied axial loading and aspect ratio, and separate equations for FGMW and PGMW or, at least, account for the non-linear influence of the grout spacing instead of using a constant reduction factor.

c) Chapter 4: Seismic behavior and performance

In Chapter 4, the FEM was further validated and used to evaluate the in-plane behavior and seismic performance of multi-story perforated walls with grout and reinforcement concentrated at the wall piers ends. The following observations and conclusions can be drawn according to the analysis:

- The FEMs achieved an excellent fit in the lateral and diagonal displacements, and SG and SP readings, proving to be able also to simulate the more specific behavior of the experimental walls analyzed;
- Experimental and numerical results supported the idea that the reinforced masonry effectively coupled the wall piers imposing a frame-type action;
- In general, the lateral displacement profile along the wall height was linear up to close to the maximum lateral load, i.e., the wall behaved like a solid composite with shear deformations and a linear distribution of the lateral load along the height. It became non-linear after the peak load with predominantly horizontal displacement at the first story caused by the major cracks in the ungrouted masonry in this region;
- The lateral displacement profile along the wall height demonstrated that the wall behaved like a solid composite with shear deformations and a linear distribution of the lateral load along the height up to close to the maximum lateral load. The crack increasing in the ungrouted masonry, mainly at the first story, turned the behavior non-linear after the peak load with predominantly horizontal displacement;
- The structure appears to have performed as a continuous frame as a result of the concentration of grout and reinforcement at the ends of the wall piers, with the grouted portions behaving like columns and the ungrouted portions working as confined masonry;
- The trilinear approach fits the actual response of the walls better than the bilinear elastoplastic idealizations while maintaining the three key characteristics: initial

elastic stiffness, lateral load capacity, and decline in the post-peak phase. Adopting the bilinear methods and disregarding the post-peak stage led to SPFs that can be seen as favorably conservative but ignoring the wall's actual extra ductility;

- The findings demonstrated that while a high vertical pre-compression level might enhance the lateral load capacity, it could also cause brittle behavior with the loss of ductility evidenced by the reduction in the SPFs. It is suggested to employ more walls in a building to maintain a low level of pre-compression and ensure ductile behavior;
- When subjected to the higher axial load, walls with only one grouted/reinforced cell at the pier ends and walls without grout/reinforcement near the openings failed at the peak load without the capacity to continue carrying load and deforming further in a post-peak phase. Thus, it is suggested to avoid this detailing to resist seismic actions;
- The behavior and seismic performance of walls were affected by changes in the amount of vertical reinforcement at the wall pier ends, while maintaining the amount of grout, in the case of the lower axial load, but not significantly in the case of the larger pre-compression. Placing the reinforcement nearer to the ends was more efficient in the reduced axial stress scenario;
- The in-plane response of the walls worsened as a result of fewer grouted/reinforced cells present at the wall pier ends. While the ductility was reduced more in the higher axial load scenario, the decrease of the lateral load capacity was greater for the lower level of axial load;
- Concentrating the grouting and reinforcement at the ends of the wall piers instead of dispersing them uniformly throughout the piers resulted in a reduction in ductility and SPFs but an improvement in lateral load capacity. These options are equivalent in terms of detailing efficiency, measured by the product $V_{max} \cdot R_d$. This finding implies that the ASCE/SEI 7 (2016) and NBCC (2015) reinforcement spacing limits for shear walls can be relaxed at the center of the walls as long as the total amount of grout and reinforcement is maintained and concentrated at the wall ends, resulting in similar design efficiency. Experimental results would be pertinent to support these numerical findings;
- The stiffness degradation was more pronounced when the walls were subjected to the lower pre-compression level, rapidly reducing in the initial stages and progressively decreasing thereafter. The stiffness degradation curve for all walls with the same

axial load has a similar format, with the best fit produced using a power function for walls with the lower axial load and a logarithmic function for walls with the higher pre-compression.

d) Chapter 5: Simplified frame models

The behavior of in-plane loaded, multi-story, perforated, partially grouted masonry walls was evaluated using linear and non-linear frame models in Chapter 5. Portal and braced linear frame models were tested to predict the walls' initial lateral stiffness. The linear models were also employed with SPFs and ultimate top drifts in a newly suggested approach for defining the lateral envelope response of walls. Moreover, the braced frame model was used to simulate the entire non-linear behavior of the walls employing concentrated plastic hinges. After the analysis, the following comments and conclusions are:

- The cantilever model was the most conservative in predicting the initial lateral stiffness and internal load distribution of the coupled perforated walls. The stiffness increased as rigid offsets were included in the portal frame modeling. The portal frame model with rigid offsets on the horizontal and vertical elements had lateral stiffness and internal loads that was close to the experimental walls. The initial lateral stiffness and internal load distribution of the walls were also reasonably predicted by the braced frame model;
- The envelope of the idealized lateral response of the walls could be replicated using the initial lateral stiffness of the linear models with appropriate SPFs and ultimate top drifts. When the lateral stiffness of the linear models was closer to that of the reference walls, the idealized curves more closely fitted the actual response. The variations in lateral load capacity were proportional to changes in lateral stiffness;
- As long as the proper SPFs are used, all three approaches (BL1, BL2, and TL) intended to idealize the lateral response are feasible, each with its particularities. The research also demonstrates the need for adopting linear models with lateral stiffnesses consistent with those used to derive the SPFs;
- The method to define the envelope of the wall lateral response is also sensitive to the imposed ultimate top drift. Using all of the suggested approaches, an ultimate top drift higher than the actual top drift amplified the estimation of the lateral load capacity and vice-versa. Ultimate top drifts of 0.4% and 0.2% proved to be

reasonable options for the cases in which the walls were subjected to a pre-compression of $0.04f'_m$ and $0.2f'_m$, respectively;

- The non-linear braced frame model accurately simulated the envelope curves of the experimental walls up to the peak load but did not exhibit the expected strength degradation in the post-peak phase. This problem might be addressed by imposing an ultimate load of $0.8V_{max}$ and limiting the corresponding ultimate displacement to a drift of 0.4%. The BF model was reasonably conservative in predicting the maximum lateral load of the walls with the higher pre-compression ($\sigma = 0.2f'_m$). However, in these cases, the BF model was considerably more flexible than the FE model: imposing the drift limit of 0.2% made the result acceptably conservative. In the linear stage, Model BF could correctly depict how loads were distributed among the elements, but it was inaccurate in the non-linear stage. Further improvements are required to handle the model limitations by considering the interaction between axial load and moment in the strength capacity of the flexural plastic hinges on the vertical elements without affecting the numerical convergence.

e) Future research

The outcomes of this research are restricted to the parameters and conditions examined, and do not encompass other scenarios that require further exploration or improvement. Therefore, the following suggestions are proposed for future work:

- Due to the lack of experimental data, it is recommended to perform more reduced and full-scale tests on masonry shear walls with grout and reinforcement concentrated at their ends. It would be advantageous to do tests distributing the same amount of grouting and reinforcement along the wall piers to compare both cases;
- Additional verification of the finite element model efficiency using different wall arrangements from other experimental studies would enhance the model's applicability and confirm the conclusions outlined in this thesis;
- More investigations are suggested to verify the impact of greater variations in the opening dimensions and position (e.g., asymmetrically) on the wall behavior and the estimation of the SLC using the proposed equation and approaches. Also, it is recommended to evaluate the influence of the openings in multi-story PGMW when the lateral load is applied at the level of each story;

- The seismic performance factors obtained in Chapter 4 are specific to the isolated walls examined and may not correspond to the overall building system response. Further research is needed to suggest SPFs for buildings using the detailing type studied here;
- It is suggested to study the compatibility of seismic performance factors applied in linear design methods when models with different lateral stiffness are used;
- Considering the potential, and also the limitations, of the braced frame model presented in Chapter 5, more development and improvement of the model is required concerning the features of hinges or trying different software packages that enable the application of the constitutive relationships directly in the elements.

REFERENCES

Abdulla, K. F., L. S. Cunningham, and M. Gillie, 2017, Simulating masonry wall behaviour using a simplified micro-model approach: Engineering Structures, v. 151, p. 349–365, doi:10.1016/J.ENGSTRUCT.2017.08.021.

Aguilar, V., C. Sandoval, J. M. Adam, J. Garzón-Roca, and G. Valdebenito, 2016, Prediction of the shear strength of reinforced masonry walls using a large experimental database and artificial neural networks: Structure and Infrastructure Engineering, v. 12, no. 12, p. 1661–1674, doi:10.1080/15732479.2016.1157824.

Akkaya, Y., S. Guner, and F. J. Vecchio, 2019, Constitutive model for inelastic buckling behavior of reinforcing bars: ACI Structural Journal, v. 116, no. 2, doi:10.14359/51711143.

American Concrete Institute (ACI), 2005, ACI Committee 530-88: Building code requirements for masonry structures and specifications for masonry structures: Boulder, CO: Farmington Hills, MI, Masonry Standards Joint Committee.

American Society for Testing and Materials (ASTM), 2009, ASTM A615 / A615M - 09: Standard specification for deformed and plain carbon-steel bars for concrete reinforcement: West Conshohocken, PA.

American Society for Testing and Materials (ASTM), 2010, ASTM C39 / C39M - 10: Standard test method for compressive strength of cylindrical concrete specimens: West Conshohocken, PA.

American Society for Testing and Materials (ASTM), 2010, ASTM C140-10: Standard test methods for sampling and testing concrete masonry units and related units: West Conshohocken, PA.

American Society for Testing and Materials (ASTM), 2010, ASTM C476-10: Standard specification for grout for masonry: West Conshohocken, PA.

American Society for Testing and Materials (ASTM), 2009, ASTM C780-09: Standard test method for preconstruction and construction evaluation of mortars for plain and reinforced unit masonry: West Conshohocken, PA.

American Society for Testing and Materials (ASTM), 2010, ASTM C1314-10: Standard test method for compressive strength of masonry prisms: West Conshohocken, PA.

American Society of Civil Engineers, 2014, Seismic Evaluation and Retrofit of Existing Buildings ASCE/SEI 41-13: Reston, VA, doi:10.1061/9780784412855.

American Society of Civil Engineers (ASCE), 2016, ASCE/SEI 7-16: Minimum design loads and associated criteria for buildings and other structures: Reston, Virginia.

Anderson, D. L., and M. J. N. Priestley, 1992, In-plane shear strength of masonry walls, in 6th Canadian Masonry Symposium: p. 223–234.

Angelillo, M., P. B. Lourenço, and G. Milani, 2014, Masonry behaviour and modelling, in Angelillo M. (eds) Mechanics of Masonry Structures. CISM International Centre for Mechanical Sciences, vol 551: Vienna, Springer, p. 1–26, doi:10.1007/978-3-7091-1774-3_1.

Associação Brasileira de Normas Técnicas (ABNT), 2014, NBR 6118: Projeto de Estruturas de Concreto - Procedimento: Rio de Janeiro, Brasil.

Associação Brasileira de Normas Técnicas (ABNT), 2006, NBR 15421: Projeto de estruturas resistentes a sismos - Procedimento: Rio de Janeiro, Brasil.

Associação Brasileira de Normas Técnicas (ABNT), 2020, NBR 16868-1: Alvenaria estrutural - Parte 1: Projeto: Rio de Janeiro, Brasil.

Assumpção, M. et al., 2014, Intraplate seismicity in Brazil, in P. Talwani (ed.) Intraplate Earthquakes: Cambridge, Cambridge U.P, p. 50–71.

Assumpção, M. de S., M. Pirchiner, J. C. Dourado, and L. V. Barros, 2016, Terremotos no Brasil: preparando-se para eventos raros: Boletim SBGf, no. 96, p. 25–29.

Augenti, N., 2004, Il calcolo sismico degli edifici in muratura.

Australia Standards (AS), 2011, Code of practice for the use of masonry – Part 2: Structural use of reinforced and prestressed masonry (AS 3700): Sydney.

Banting, B. R., and W. W. El-Dakhakhni, 2014, Seismic performance quantification of reinforced masonry structural walls with boundary elements: Journal of Structural Engineering, v. 140, no. 5, p. 04014001, doi:10.1061/(ASCE)ST.1943-541X.0000895.

Baptista, L., 2015, Os 7 maiores terremotos que já ocorreram no Brasil: <https://exame.abril.com.br/brasil/os-7-maiores-terremotos-que-ja-ocorreram-no-brasil/> (accessed June 19, 2022).

BBCBrasil, 2014, Conheça os cinco terremotos mais fortes do mundo: <http://www.bbc.com/portuguese/noticias/2014/04/140402_cinco_%0Amaiores_terremotos_lgb%0A> (accessed May 10, 2019).

Benedetti, D., 2004, Costruzioni in muratura: duttilità, norme ed esperienze: Ingegneria sismica, v. 21, no. 3, p. 5–18.

Benedetti, D., P. Carydis, and P. Pezzoli, 1998, Shaking table tests on 24 simple masonry buildings: Earthquake Engineering and Structural Dynamics, v. 27, no. 1, p. 67–90, doi:10.1002/(SICI)1096-9845(199801)27:1<67::AID-EQE719>3.0.CO;2-K.

Bentz, E. C., 2000, Sectional analysis of reinforced concrete members, in PhD Thesis, Department of Civil Engineering, University of Toronto: p. 310.

Blondet, J. M., R. L. Mayes, T. Kelly, F. R. Villablanca, and R. E. Klingner, 1989, Performance of engineered masonry in the chilean earthquake of March 3, 1985, in Implications for U.S. design practice: University of Texas at Austin.

Bolhassani, M., A. A. Hamid, C. Johnson, and A. E. Schultz, 2016a, Shear strength expression for partially grouted masonry walls: Engineering Structures, v. 127, p. 475–494, doi:10.1016/j.engstruct.2016.09.001.

Bolhassani, M., A. A. Hamid, C. Johnson, F. L. Moon, and A. E. Schultz, 2016b, New design detail to enhance the seismic performance of ordinary reinforced partially grouted masonry structures: Journal of Structural Engineering, v. 142, no. 12, p. 04016142, doi:10.1061/(ASCE)ST.1943-541X.0001620.

Boult, B. F., 1979, Concrete masonry prism testing: American Concrete Institute Journal, Proceedings, v. 76, no. 4, p. 513–536.

Bracchi, S., M. Rota, A. Penna, and G. Magenes, 2015, Consideration of modelling uncertainties in the seismic assessment of masonry buildings by equivalent-frame approach: Bulletin of Earthquake Engineering, v. 13, no. 11, p. 3423–3448, doi:10.1007/s10518-015-9760-z.

British Standards Institution (BSI), 2000, Code of practice for the use of masonry – Part 2: Structural use of reinforced and prestressed masonry (BS 5628-2): London.

Calderón, S., C. Sandoval, G. Araya-Letelier, E. Inzunza, and O. Arnau, 2021a, Influence of different design parameters on the seismic performance of partially grouted masonry shear walls: Engineering Structures, v. 239, doi:10.1016/j.engstruct.2021.112058.

Calderón, S., C. Sandoval, G. Araya-Letelier, E. Inzunza, and G. Milani, 2021b, Quasi-static testing of concrete masonry shear walls with different horizontal reinforcement schemes: Journal of Building Engineering, v. 38, doi:10.1016/j.jobe.2021.102201.

Calderón, S., C. Sandoval, and O. Arnau, 2017, Shear response of partially-grouted reinforced masonry walls with a central opening: Testing and detailed micro-modelling: Materials and Design, v. 118, p. 122–137, doi:10.1016/j.matdes.2017.01.019.

Calderón, S., C. Sandoval, E. Inzunza, C. Cruz-Noguez, A. B. Rahim, and L. Vargas, 2019, Influence of a window-type opening on the shear response of partially-grouted masonry shear walls: Engineering Structures, v. 201, p. 109783, doi:10.1016/j.engstruct.2019.109783.

Calderón, S., C. Sandoval, G. Milani, and O. Arnau, 2021c, Detailed micro-modeling of partially grouted reinforced masonry shear walls: extended validation and parametric study: Archives of Civil and Mechanical Engineering, v. 21, no. 3, p. 94, doi:10.1007/s43452-021-00237-z.

Canadian Standards Association (CSA), 2004, Design of masonry structures (CSA S304.1-04): Mississauga, Ont., Canada.

Canadian Standards Association (CSA), 2014, Design of masonry structures (CSA S304-14): Mississauga, Canada.

Candeias, P. J. O. X., E. P. de M. F. Coelho, and P. J. B. B. Lourenço, 2008, Avaliação da vulnerabilidade sísmica de edifícios de alvenaria, in Tese (Doutorado) – Escola de Engenharia, Universidade do Minho: p. 338.

Carvalho, E. C., and C. S. Oliveira, 1997, Construção anti-sísmica: Edifícios de pequeno porte, in Laboratório Nacional de Engenharia Civil, 4a edição.

Chavez, K. H., and F. S. Fonseca, 2018, Parametric study on multi-story, partially grouted, perforated, masonry shear walls by finite element analysis, in Master thesis, Brigham Young University: p. 187.

Computer and Structures Inc. (CSI), 2019, SAP2000 V.21: Integrated solution for structural analysis and design.: Berkeley, CA, USA.

Croce, P., M. L. Beconcini, P. Formichi, P. Cioni, F. Landi, C. Mochi, F. de Lellis, E. Mariotti, and I. Serra, 2018, Shear modulus of masonry walls: a critical review: Procedia Structural Integrity, v. 11, p. 339–346, doi:10.1016/J.PROSTR.2018.11.044.

Dantas, R. O. O., 2013, Subsídios para o projeto de estruturas sismo resistentes, in Master Thesis (In Portuguese) – Programa de Pós-Graduação em Estruturas e Construção Civil, Universidade Federal do Rio Grande do Norte: p. 200.

Davis, C. L., and D. Mclean, 2008, Evaluation of design provisions for in-plane shear in masonry walls: Washington State University.

Dhanasekar, M., J. A. Thamboo, and S. Nazir, 2017, On the in-plane shear response of the high bond strength concrete masonry walls: Materials and Structures, v. 50, no. 5, p. 214, doi:10.1617/s11527-017-1078-7.

Dillon, P., and F. S. Fonseca, 2015, Shear strength prediction methods for grouted masonry shear walls, in PhD Dissertation. Brigham Young University: p. 661.

Dolce, M., 1989, Models for in-plane loading of masonry walls, in Corso sul consolidamento degli edifici in muratura in zona sismica. Ordine degli ingegneri.

Drysdale, R. G., and A. A. Hamid, 2005, Masonry structures: Behavior and design: Mississauga, Ontario, Canadian Masonry Design Centre.

Drysdale, R. G., A. Hamid, and L. R. Baker, 1999, Masonry structures: behaviour and design: 2d Ed., The Masonry Society, Boulder, CO.

Eixenberger, J. G., 2017, Seismic analysis of and provisions for dry-stack concrete masonry wall systems with surface bond in low-rise buildings: Provo, UT, Brigham Young University.

Eligehausen, R., E. Popov, and V. Bertero, 1983, Local bond stress-slip relationship of deformed bars under generalized excitations. Report No. UCB/EERC-83/23: Earthquake Engineering Center, University of California, Berkeley.

Elmapruk, J. H., and M. A. ElGawady, 2010, Shear strength of partially grouted squat masonry shear walls, in Master's thesis, Washington State University.

Elmapruk, J., M. A. ElGawady, and R. Hassanli, 2020, Experimental and Analytical Study on the Shear-Strength of Partially Grouted Masonry Walls: Journal of Structural Engineering, v. 146, no. 8, p. 04020147, doi:10.1061/(ASCE)ST.1943-541X.0002704.

Elmeligy, O., N. Aly, and K. Galal, 2021, Sensitivity analysis of the numerical simulations of partially grouted reinforced masonry shear walls: Engineering Structures, v. 245, p. 112876, doi:10.1016/j.engstruct.2021.112876.

Elshafie, H., A. Hamid, and E. Nasr, 2002, Strength and stiffness of masonry shear walls with openings: The Masonry Society Journal, v. 20, no. 1, p. 49–60.

EN 1996-1, 2005, Eurocode 6: Design of masonry structures - Part 1-1: General rules for reinforced and unreinforced masonry structures: CEN.

Ezzeldin, M., L. Wiebe, and W. El-Dakhakhni, 2016, Seismic collapse risk assessment of reinforced masonry walls with boundary elements using the FEMA P695 methodology: Journal of Structural Engineering, v. 142, no. 11, doi:10.1061/(ASCE)ST.1943-541X.0001579.

Facconi, L., G. Plizzari, and F. Vecchio, 2014, Disturbed stress field model for unreinforced masonry: Journal of Structural Engineering, v. 140, no. 4, p. 04013085, doi:10.1061/(ASCE)ST.1943-541X.0000906.

Fattal, S. G., 1993, Strength of partially-grouted masonry shear walls under lateral loads. (NISTIR 5147), in National Institute of Standards and Technology.

Federal Emergency Management Agency (FEMA), 2004, FEMA 450-1: NEHRP recommended provisions for seismic regulations for new buildings and other structures: Washington, D. C.

Federal Emergency Management Agency (FEMA), 2009, FEMA P695: Quantification of building seismic performance factors: Washington, D. C.

Fódi, A., and I. Bódi, 2010, Comparison of shear behavior of masonry walls with and without reinforcement: Pollack Periodica, v. 5, no. 3, p. 71–82, doi:10.1556/Pollack.5.2010.3.7.

Fortes, E. S., and G. A. Parsekian, 2017, Caracterização da alvenaria estrutural de alta resistência, in PhD Dissertation (In Portuguese). Universidade Federal de São Carlos: p. 350.

Francisco, W. C., 2020, O Terremoto no Haiti: <https://brasilescola.uol.com.br/geografia/o-terremoto-no-haiti.htm> (accessed July 27, 2020).

Frumento, S., G. Magenes, P. Morandi, and G. M. Calvi, 2009, Interpretation of experimental shear tests on clay brick masonry walls and evaluation of q-factors for seismic design: Iuss Press Pavia.

Ganz, H. R., 1985, Masonry walls subjected to normal and shear forces, in Ph.D. Thesis, ETH Zurich, Switzerland (in German).

Ghanem, G. M., A. S. Essawy, and A. A. Hamid, 1992, Effect of steel distribution on the behavior of partially reinforced masonry shear walls, in Proceedings of 6th Canadian Masonry Symposium.

Haach, V. G., G. Vasconcelos, and P. B. Lourenço, 2011, Parametrical study of masonry walls subjected to in-plane loading through numerical modeling: Engineering Structures, v. 33, no. 4, p. 1377–1389, doi:10.1016/j.engstruct.2011.01.015.

Hassanli, R., M. A. ElGawady, and J. E. Mills, 2015, Strength and Seismic Performance Factors of Posttensioned Masonry Walls: Journal of Structural Engineering, v. 141, no. 11, doi:10.1061/(asce)st.1943-541x.0001272.

Hatzinikolas, M., Y. Korany, and S. Brzev, 2015, Masonry design for engineers and architects: Edmonton, AB, Canadian Masonry Publications.

He, X. G., and A. K. H. Kwan, 2001, Modeling dowel action of reinforcement bars for finite element analysis of concrete structures: Computers & Structures, v. 79, no. 6, p. 595–604, doi:10.1016/S0045-7949(00)00158-9.

Hegemier, G. A., G. Krishnamoorthy, R. O. Nunn, and T. v. Moorthy, 1978, Prism tests for the compressive strength of concrete masonry, in Proceedings of the North American Masonry Conference: p. 18, 18–1–18–17.

Hendry, A. W., 1981, Structural Brickwork: London, Macmillan Education UK, doi:10.1007/978-1-349-81439-8.

Hognestad, E., 1951, A study of combined bending and axial load in reinforced concrete members: Bulletin Series No. 399, v. 49, no. Urbana: Engineering Experimental Station, The University of Illinois.

Hoque, N., and S. Lissel, 2013, In-plane cyclic testing of reinforced concrete masonry walls to assess the effect of varying reinforcement anchorage and boundary conditions, in Master's thesis, University of Calgary: doi:10.11575/PRISM/26545.

Hordjik, D. A., H. W. Reinhardt, and H. A. W. Cornelissen, 1987, Fracture mechanics parameters of concrete from uniaxial tests as influenced by specimen length, in Proc. SEM-RILEM Int. Conf. on Fracture of Concrete and Rock, 31(2): S. P. Shah, and S. E. Swartz, eds., p. 138–149.

Hoshikuma, J., K. Kawashima, K. Nagaya, and A. W. Taylor, 1997, Stress-strain model for confined reinforced concrete in bridge piers: Journal of Structural Engineering, v. 123, no. 5, p. 624–633, doi:10.1061/(ASCE)0733-9445(1997)123:5(624).

Hung, J., C. Cruz, C. Sandoval, and B. Banting, 2018, Analysis of partially grouted masonry shear walls using artificial neural networks, in Proceedings of 10th International Masonry Conference.

Ingham, J. M., B. J. Davidson, D. R. Brammer, and K. C. Voon, 2001, Testing and codification of partially grout-filled nominally-reinforced concrete masonry subjected to in-plane cyclic loads: Masonry Society Journal, v. 19, no. 1, p. 83–96.

Izquierdo, K. N., and C. Cruz-Noguez, 2021, Statistical prediction methods for the in-plane shear strength of partially grouted masonry walls, in Master's thesis, University of Alberta.

Izquierdo, K., C. Cruz-Noguez, and A. Mohsenijam, 2021, Stepwise regressions for predicting the in-plane shear strength of partially grouted masonry walls, in 14th Canadian Masonry Symposium.

Johnson, C. A., and A. E. Schultz, 2014, Simulated seismic testing of partially-grouted masonry subassemblages, in NCEE 2014 - 10th U.S. National Conference on Earthquake Engineering: Frontiers of Earthquake Engineering: doi:10.4231/D3HX15R69.

Kappos, A. J., G. G. Penelis, and C. G. Drakopoulos, 2002, Evaluation of simplified models for lateral load analysis of unreinforced masonry buildings: Journal of Structural Engineering, v. 128, no. 7, p. 890–897, doi:10.1061/(ASCE)0733-9445(2002)128:7(890).

Karantoni, F. v., and M. N. Fardis, 1992, Computed versus Observed Seismic Response and Damage of Masonry Buildings: Journal of Structural Engineering, v. 118, no. 7, doi:10.1061/(asce)0733-9445(1992)118:7(1804).

Kingsley, G. R., P. B. Shing, and T. Gangel, 2014, Seismic design of special reinforced masonry shear walls: a guide for practicing engineers, in NIST GCR 14-917-31. NEHRP Seismic Design Technical Brief: p. 42.

Klingner, R. E., and G. Leiva, 1992, Behavior and design of multi-story masonry walls under in-plane seismic loading, in Earthquake Engineering, Tenth World Conference.

Knox, C. L., and J. M. Ingham, 2012a, Assessment of perforated unreinforced masonry walls responding in-plane: PhD Thesis. Department of Civil and Environmental Engineering. University of Auckland, New Zealand.

Knox, C. L., and J. M. Ingham, 2012b, Non-linear equivalent frame modelling: Assessment of a two storey perforated unreinforced masonry wall: 2012 NZSEE Annual Technical Conference, no. 076.

Koutras, A., and P. B. Shing, 2018, Shake-table testing and performance assessment of a partially grouted reinforced masonry building, in Lecture Notes in Civil Engineering: doi:10.1007/978-3-319-67443-8_41.

Koutromanos, I., and P. S. Shing, 2010, Example application of the FEMA P695 (ATC-63) methodology for the collapse performance evaluation of reinforced masonry shear wall structures, in Proc., 9th US National and 10th Canadian Conf. on Earthquake Engineering.

Lagomarsino, S., A. Penna, A. Galasco, and S. Cattari, 2013, TREMURI program: An equivalent frame model for the nonlinear seismic analysis of masonry buildings: Engineering Structures, v. 56, p. 1787–1799, doi:10.1016/j.engstruct.2013.08.002.

Long, L. M., 2006, Behaviour of half-scale reinforced concrete masonry shear walls, in Master's thesis, McMaster University: p. 222.

Long, L., A. A. Hamid, and R. G. Drysdale, 2005, Small-scale modeling of concrete masonry using 1/2-scale units: a preliminary study, in Proceedings of the Tenth Canadian Masonry Symposium: p. 484–493.

Lotfi, H. R., and P. B. Shing, 1991, An appraisal of smeared crack models for masonry shear wall analysis: Computers & Structures, v. 41, no. 3, p. 413–425, doi:10.1016/0045-7949(91)90134-8.

Magenes, G., D. Bolognini, and C. Baggio, 2000, Metodi semplificati per l'analisi sismica non lineare di edifici in muratura. Rome, Italy: CNR-Gruppo Nazionale per la Difesa dai Terremoti: Preprint o Ernesto G FRPs. Co.

Marques, R. F. P., and P. J. B. B. Lourenço, 2012, Metodologias inovadoras no cálculo sísmico de estruturas em alvenaria simples e confinada. Phd Thesis (in portuguese) – Escola de Engenharia, Universidade do Minho: Guimarães, Portugal, 248 p.

Masonry Standards Joint Committee (MSJC), 2005, Building code requirements for masonry structures: ACI 530/ASCE 5/TMS 402, American Concrete Institute, Detroit, American Society of Civil Engineers, New York, and The Masonry Society, Boulder, Colo.

Masonry Standards Joint Committee (MSJC), 2013, Building code requirements for masonry structures, in TMS 402/ ACI 530/ ASCE 5, The Masonry Society, American Concrete Institute, and American Society of Civil Engineers.

Matsumura, A., 1986, Shear strength of reinforced hollow unit masonry walls, in 2nd Meeting of the Joint Technical Coordinating Committee on Masonry Research, U.S.-Japan Coordinated Program for Masonry Building Research.

Matsumura, A., 1988, Shear strength of reinforced masonry walls, in Ninth World Conference on Earthquake Engineering: p. 121–126.

Meli, R., A. Z. Wolff, and L. Esteve, 1968, Comportamiento de muros de mampostería hueca ante carga lateral alternada: Revista Ingeniera, v. 38, no. 3, p. 371–390.

Milani, G., K. Beyer, and A. Dazio, 2009, Upper bound limit analysis of meso-mechanical spandrel models for the pushover analysis of 2D masonry frames: Engineering Structures, v. 31, no. 11, p. 2696–2710, doi:10.1016/j.engstruct.2009.06.015.

Minaie, E., and F. Moon, 2009, Behaviour and vulnerability of reinforced masonry shear walls, in Ph.D. Thesis, Drexel University: p. 488.

Minaie, E., M. Mota, F. L. Moon, and A. A. Hamid, 2010, In-plane behavior of partially grouted reinforced concrete masonry shear walls: Journal of Structural Engineering, v. 136, no. 9, p. 1089–1097, doi:10.1061/(ASCE)ST.1943-541X.0000206.

Mohammadi, R. K., and M. H. Naggar, 2004, Modifications on equivalent lateral force method, in 13th World Conference on Earthquake Engineering.

Montardo, D. K., 2006, Afinal, acontecem terremotos no Brasil?, in Simpronoroeste. Artigo No164.

Morandi, P., 2006, New proposals for simplified seismic design of masonry buildings: University of Pavia, Italy, Pavia, Italy.

Morandi, P., C. Butenweg, K. Breis, K. Beyer, and G. Magenes, 2022, Latest findings on the behaviour factor q for the seismic design of URM buildings: Bulletin of Earthquake Engineering, v. 20, no. 11, p. 5797–5848, doi:10.1007/s10518-022-01419-7.

National Building Code of Canada (NBCC), 2015, Canadian Commission on Building and Fire Codes. National Research Council of Canada: Ottawa, Ontario, Canada.

National Earthquake Hazards Reduction Program (NEHRP), 1997, Recommended provisions for seismic regulations for new buildings and other structures. Part-1 Provisions. Building Seismic Safety Council: Washington, USA.

National Earthquake Hazards Reduction Program (NEHRP), 1988, Recommended provisions for the development of seismic regulations for new buildings. Building Seismic Safety Council: Washington, D.C.

National Institute of Standards and Technology (NIST), 2010, Evaluation of the FEMA P-695 methodology for quantification of building seismic performance factors (NIST GCR 10-917-8), prepared by the NEHRP Consultants Joint Venture for the National Institute of Standards and Technology: Gaithersburg, Maryland.

Newmark, N. M., and W. J. Hall, 1982, Earthquake spectra and design: El Cerrito, Calif: Earthquake Engrg. Res. Inst.

Nolph, S. M., and M. A. ElGawady, 2010, In-plane shear performance of partially grouted masonry shear walls, in Master Thesis. Washington State University: p. 150.

Nolph, S. M., and M. A. ElGawady, 2012, Static cyclic response of partially grouted masonry shear walls: Journal of Structural Engineering, v. 138, no. 7, p. 864–879, doi:10.1061/(asce)st.1943-541x.0000529.

Norma Chilena Oficial, 2012, NCh 433:2012 – Diseno sísmico de difícios – Earthquake resistant design of buildings: Santiago, Chile.

Oan, A. F., and N. G. Shrive, 2014, A simple design model for the diagonal shear of partially grouted concrete masonry panels, in 9th International Masonry Conference: p. 1–11.

Oan, A. F., and N. G. Shrive, 2010, Effect of steel reinforcement on shear strength of concrete masonry walls, in 8th International Masonry Conference: p. 1413–1422.

Oan, A. F., and N. G. Shrive, 2009, Shear of concrete masonry walls, in 11th Canadian Masonry Symposium: p. 29–38.

Palermo, D., and F. J. Vecchio, 2001, Behaviour cyclically loaded shear walls: ASCE Special publication, no. Modeling of Inelastic Behaviour of RC Structures under Seismic Loads, Shing and Tanabe Eds, p. 562–579.

Parsekian, G. A., A. A. Hamid, and R. G. Drysdale, 2012, Comportamento e dimensionamento de alvenaria estrutural: São Carlos, São Paulo, EdUFSCar, 625 p.

Pasquantonio, R. D., G. A. Parsekian, F. S. Fonseca, and N. G. Shrive, 2020, Experimental and numerical characterization of the interface between concrete masonry block and mortar: IBRACON Strucutures and Materials Journal, v. 13, no. 3, p. 578–592, doi:10.1590/s1983-41952020000300008.

Paulay, T., and M. J. N. Priestly, 1992, Seismic design of reinforced concrete and masonry buildings: Hoboken, NJ, USA, John Wiley & Sons, Inc., doi:10.1002/9780470172841.

Peruch, M., E. Spacone, and P. B. Shing, 2019, Cyclic analyses of reinforced concrete masonry panels using a force-based frame element: Journal of Structural Engineering, v. 145, no. 7, doi:10.1061/(ASCE)ST.1943-541X.0002335.

Pirsaheb, H., P. Wang, M. Javad Moradi, and G. Milani, 2021, A Multi-Pier-Macro MPM method for the progressive failure analysis of perforated masonry walls in-plane loaded: Engineering Failure Analysis, v. 127, p. 105528, doi:10.1016/j.engfailanal.2021.105528.

Priestley, M. J. N., 1986, Flexural strength of rectangular unconfined masonry shear walls with distributed reinforcement: Journal of Masonry Society, v. 5.

Priestley, M. J. N., and D. M. Elder, 1982, Cyclic loading tests of slender concrete masonry shear walls: Bulletin of the New Zealand Society for Earthquake Engineering, v. 15, no. 1, p. 3–21, doi:10.5459/bnzsee.15.1.3-21.

Priestley, M. J. N., and D. M. Elder, 1983, Stress-strain curves for unconfined and confined concrete masonry: ACI Journal Proceedings, v. 80, no. 3, p. 192–201.

Psilla, N., and T. P. Tassios, 2009, Design models of reinforced masonry walls under monotonic and cyclic loading: Engineering Structures, v. 31, no. 4, doi:10.1016/j.engstruct.2008.12.003.

Quagliarini, E., G. Maracchini, and F. Clementi, 2017, Uses and limits of the Equivalent Frame Model on existing unreinforced masonry buildings for assessing their seismic risk: A review: Journal of Building Engineering, v. 10, p. 166–182, doi:10.1016/j.jobe.2017.03.004.

Ramírez, P., C. Sandoval, and J. L. Almazán, 2016, Experimental study on in-plane cyclic response of partially grouted reinforced concrete masonry shear walls: Engineering Structures, v. 126, p. 598–617, doi:10.1016/j.engstruct.2016.08.010.

Rizaee, S., and S. Lissel, 2015, Assessing bond beam horizontal reinforcement efficacy with different end anchorage conditions in concrete block masonry shear walls, in Master's thesis, University of Calgary: doi:http://dx.doi.org/10.11575/PRISM/25017.

Salonikios, T., C. Karakostas, V. Lekidis, and A. Anthoine, 2003, Comparative inelastic pushover analysis of masonry frames: Engineering Structures, v. 25, no. 12, p. 1515–1523, doi:10.1016/S0141-0296(03)00118-4.

Sandoval, C., S. Calderón, and J. L. Almazán, 2018, Experimental cyclic response assessment of partially grouted reinforced clay brick masonry walls: Bulletin of Earthquake Engineering, v. 16, no. 7, p. 3127–3152, doi:10.1007/s10518-018-0308-x.

Sangirardi, M., D. Liberatore, and D. Addessi, 2019, Equivalent frame modelling of masonry walls based on plasticity and damage: International Journal of Architectural Heritage, v. 13, no. 7, p. 1098–1109, doi:10.1080/15583058.2019.1645240.

Schultz, A. E., 1994, Research program on the seismic resistance of partially–grouted masonry shear walls: Gaithersburg, Maryland, Report No. NISTIR 5481, Building and Fire Research Laboratory, National Institute of Standards and Technology.

Schultz, A. E., 1996, Seismic resistance of partially–grouted masonry shear walls: Worldwide Advances in Structural Concrete and Masonry. American Society of Civil Engineers (ASCE), p. 211–222.

Schultz, A. E., R. S. Hutchinson, and G. S. Cheok, 1998, Seismic performance of masonry walls with bed joint reinforcement, in Structural Engineers World Congress.

Schwaighofer, J., and H. F. Microys, 1969, Analysis of shear walls using standard computer programs: Am Concrete Inst-J, v. 66, no. 12, doi:10.14359/7450.

Seckin, M., 1981, Hysteretic behaviour of cast-in-place exterior beam-column-slab subassemblies, in Ph.D. Thesis, Department of Civil Engineering, University of Toronto: p. 266.

Seible, F., and G. R. Kingsley, 1991, Experimental and Numerical Methods in Earthquake Engineering: Modeling of Concrete and Masonry Structures Subjected to Seismic Loading: Kluwer, Dordrecht.

Seif ElDin, H. M., N. Aly, and K. Galal, 2019a, In-plane shear strength equation for fully grouted reinforced masonry shear walls: Engineering Structures, v. 190, p. 319–332, doi:10.1016/j.engstruct.2019.03.079.

Seif ElDin, H. M., A. Ashour, and K. Galal, 2019b, Seismic performance parameters of fully grouted reinforced masonry squat shear walls: Engineering Structures, v. 187, p. 518–527, doi:10.1016/j.engstruct.2019.02.069.

Seif ElDin, H. M., and K. Galal, 2016, In-plane shear behaviour of fully grouted reinforced masonry shear walls. Ph.D. Thesis, Concordia University: Montreal, Canada.

Shahzada, K., A. N. Khan, A. S. Elnashai, M. Ashraf, M. Javed, A. Naseer, and B. Alam, 2012, Experimental seismic performance evaluation of unreinforced brick masonry buildings: Earthquake Spectra, v. 28, no. 3, doi:10.1193/1.4000073.

Shedid, M. T., R. G. Drysdale, and W. W. El-Dakhakhni, 2008, Behavior of fully grouted reinforced concrete masonry shear walls failing in flexure: Experimental results: Journal of Structural Engineering, v. 134, no. 11, p. 1754–1767, doi:10.1061/(asce)0733-9445(2008)134:11(1754).

Shedid, M. T., W. W. El-Dakhakhni, and R. G. Drysdale, 2010, Alternative strategies to enhance the seismic performance of reinforced concrete-block shear wall systems: Journal of Structural Engineering, v. 136, no. 6, p. 676–689, doi:10.1061/(ASCE)ST.1943-541X.0000164.

Shedid, M. T., W. W. El-Dakhakhni, and R. G. Drysdale, 2011, Seismic response modification factors for reinforced masonry structural walls: Journal of Performance of Constructed Facilities, v. 25, no. 2, p. 74–86, doi:10.1061/(ASCE)CF.1943-5509.0000144.

Shing, P., and L. Cao, 1997, Analysis of partially grouted masonry shear walls: Grant/Contract Reports (NISTGCR), National Institute of Standards and Technology, Gaithersburg, MD.

Shing, P. B., E. Klamerus, H. Spaeh, and J. L. Noland, 1988, Seismic performance of reinforced masonry shear walls, in 9th World Conference on Earthquake Engineering: p. 103–108.

Shing, P. B., J. L. Noland, E. Klamerus, and H. Spaeh, 1989, Inelastic behavior of boncrete masonry shear walls: Journal of Structural Engineering, v. 115, no. 9, p. 2204–2225, doi:10.1061/(ASCE)0733-9445(1989)115:9(2204).

Shing, P. B., M. Schuller, and V. S. Hoskere, 1990, In-plane resistance of reinforced masonry shear walls: Journal of Structural Engineering, v. 116, no. 3, p. 619–640, doi:10.1061/(ASCE)0733-9445(1990)116:3(619).

Standard Association of New Zealand (NZS), 2004, Code of practice for the design of masonry structures (NZS 4230): Wellington, New Zealand.

Standard Association of New Zealand (NZS), 1999, Concrete masonry buildings not requiring specific engineering design (NZS 4229): Wellington, New Zealand.

Sveinsson, B. I., H. D. McNiven, and H. Sucuoglu, 1985, Cyclic loading tests of masonry single piers — Volume 4: Additional tests with height to width ratio of 1: Earthquake Engineering Research Center, Univ. of California, Berkeley, CA.

Tena-Colunga, A., and A. E. Liga-Paredes, 2020, Approximation of lateral stiffness for walls with two bands of openings considering slab stiffness effects: Journal of Building Engineering, v. 30, p. 101310, doi:10.1016/j.jobe.2020.101310.

Tena-Colunga, A., and G. Rivera-Hernández, 2018, Approximations of elastic lateral displacement profiles for walls with openings: Structures, v. 13, p. 153–165, doi:10.1016/j.istruc.2017.12.007.

The Masonry Society (TMS), 2016, Building code requirements for masonry structures (TMS 402-16): Longmont, Colorado, USA.

Tomaževič, M., 2007, Damage as a measure for earthquake-resistant design of masonry structures: Slovenian experience: Canadian Journal of Civil Engineering, v. 34, no. 11, doi:10.1139/L07-128.

Tomažević, M., 1999, Earthquake-resistant design of masonry buildings: London, Imperial College Press.

Tomaževič, M., V. Bosiljkov, and P. Weiss, 2004, Structural Behavior Factor for Masonry Structures: 13th World Conference on Earthquake Engineering, no. 2642.

Tomaževič, M., and T. Velechovsky, 1992, Some aspects of testing small-scale masonry building models on simple earthquake simulators: Earthquake Engineering & Structural Dynamics, v. 21, no. 11, p. 945–963, doi:10.1002/eqe.4290211102.

Tomaževič, M., and P. Weiss, 1994, Seismic behavior of plain- and reinforced-masonry buildings: Journal of Structural Engineering, v. 120, no. 2, p. 323–338, doi:10.1061/(ASCE)0733-9445(1994)120:2(323).

Uang, C., 1991, Establishing R (or Rw) and Cd factors for building seismic provisions: Journal of Structural Engineering, v. 117, no. 1, p. 19–28, doi:10.1061/(ASCE)0733-9445(1991)117:1(19).

Uang, C., and A. Maarouf, 1994, Deflection amplification factor for seismic design provisions: Journal of Structural Engineering, v. 120, no. 8, p. 2423–2436, doi:10.1061/(ASCE)0733-9445(1994)120:8(2423).

Uniform Building Code (UBC), 1988, in International Conference of Building Officials.

Vargas, L., C. Sandoval, P. Ramírez, G. Araya-Letelier, and S. Calderón, 2020, Shear strength prediction of partially-grouted concrete masonry walls with openings, in Kubica, Kwiecien, and Bednarz, eds., Brick and block masonry - From historical to sustainable masonry: CRC Press, p. 1008–1015.

Vecchio, F. J., 2000, Disturbed stress field model for reinforced concrete: formulation: Journal of Structural Engineering, v. 126, no. 9, doi:10.1061/(asce)0733-9445(2000)126:9(1070).

Vecchio, F. J., 1992, Finite element modeling of concrete expansion and confinement: Journal of Structural Engineering, v. 118, no. 9, p. 2390–2406, doi:10.1061/(ASCE)0733-9445(1992)118:9(2390).

Vecchio, F. J., 1999, Towards cyclic load modeling of reinforced concrete: ACI Structural Journal, v. 96, no. 2, p. 193202.

Vecchio, F. J., and M. P. Collins, 1986, The modified compression-field theory for reinforced concrete elements subject to shear: ACI Structural Journal, v. 83, no. 2, p. 219–231.

Vecchio, F. J., and D. Lai, 2004, Crack shear-slip in reinforced concrete elements: Journal of Advanced Concrete Technology, v. 2, no. 3, doi:10.3151/jact.2.289.

VecTor2, V4.4, 2019, Version 4.4, in University of Toronto.

Voon, K. C., and J. M. Ingham, 2007, Design expression for the in-plane shear strength of reinforced concrete masonry: Journal of Structural Engineering, v. 133, no. 5, p. 706–713, doi:10.1061/(ASCE)0733-9445(2007)133:5(706).

Voon, K. C., and J. M. Ingham, 2006, Experimental in-plane shear strength investigation of reinforced concrete masonry walls: Journal of Structural Engineering, v. 132, no. 3, p. 400–408, doi:10.1061/(ASCE)0733-9445(2006)132:3(400).

Voon, K. C., and J. M. Ingham, 2008, Experimental in-plane strength investigation of reinforced concrete masonry walls with openings: Journal of Structural Engineering, v. 134, no. 5, p. 758–768, doi:10.1061/(ASCE)0733-9445(2008)134:5(758).

Voon, K. C., and J. M. Ingham, 2002, Shear strength of masonry walls, in Department of Civil and Environmental Engineering, University of Auckland: p. 294.

Walraven, J. C., 1981, Fundamental analysis of aggregate interlock: Journal of the Structural Division, v. 107, no. 11, p. 2245–2270, doi:10.1061/JSDEAG.0005820.

Walraven, J. C., and H. W. Reinhardt, 1981, Theory and experiments on the mechanical behaviour of cracks in plain and reinforced concrete subjected to shear loading: Concrete Mechanics – Part A, Heron, v. 26, no. 1 A.

Wong, P. S., F. J. Vecchio, and H. Trommels, 2013, VecTor2 & FormWorks User's Manual. 2nd ed, in University of Toronto.

Yanez, F., A. Maximiliano, A. Homberg, and O. Ogaz, 2004, Behavior of confined masonry shear walls with large openings, in 13th World Conference on Earthquake Engineering.

Zhang, Z., J. Murcia-Delso, C. Sandoval, G. Araya-Letelier, and F. Wang, 2021, In-plane shear strength and damage fragility functions for partially-grouted reinforced masonry walls with bond-beam reinforcement: Engineering Structures, v. 242, p. 112569, doi:10.1016/j.engstruct.2021.112569.

Zhang, Y., and Z. Wang, 2000, Seismic behavior of reinforced concrete shear walls subjected to high axial loading: ACI Structural Journal, v. 97, no. 5, doi:10.14359/8809.

APPENDIX A – Details on the constitutive laws used in the modeling

Some details on the constitutive and behavioral relationships adopted in the numerical models are described in the following sections. More specific information can be found in the software manual (Wong et al., 2013).

1. MASONRY BEHAVIOR

1.1. Compression pre-peak response

1.1.1. Hognestad (1951)

The Hognestad model is a parabola, Figure 125, described by Equation 102 with a symmetric relationship at peak stress corresponding to ε_p strain, decreasing to zero stress at zero and $2\varepsilon_p$ strain points. The initial tangent stiffness is predefined as shown in Equation 103.

Figure 125: Hognestad (1951) parabolic compression response.

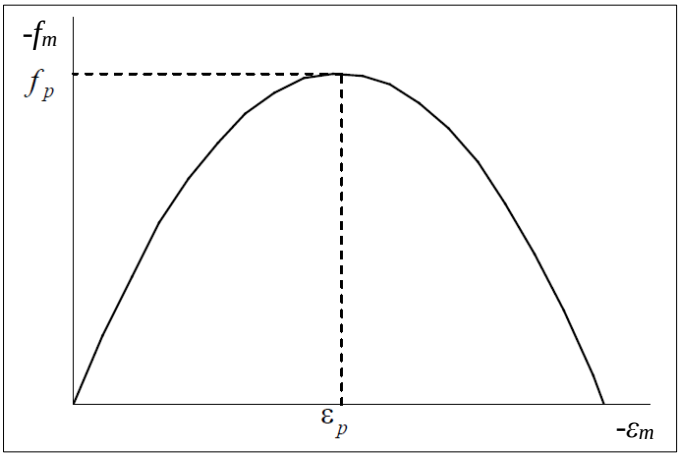

Source: Adapted from Wong et al. (2013).

$$f_m = -f_p \left[2\left(\frac{\varepsilon_m}{\varepsilon_p}\right) - \left(\frac{\varepsilon_m}{\varepsilon_p}\right)^2 \right] < 0 \quad for \quad \varepsilon_m < 0 \qquad \text{Eq. 102}$$

$$E_m = {2f_p}\Big/{|\varepsilon_p|} \qquad \text{Eq. 103}$$

where: f_m = principal compressive stress; f_p = peak compressive stress; ε_m = principal compressive strain; ε_p = peak compressive strain; E_m = initial tangent stiffness.

1.1.2. Hoshikuma et al. (1997)

The ascending branch of the compression stress-strain curve of Hoshikuma et al. (1997), Figure 126, is denoted by the relationship shown in Equation 104, where the deviation from the

linear-elastic response is characterized by the term in brackets. The parameter *n* is defined in function of the initial tangent stiffness and secant stiffness, as shown in Equations 105 and 106.

Figure 126: Hoshikuma et al. (1997) compressive pre-peak response.

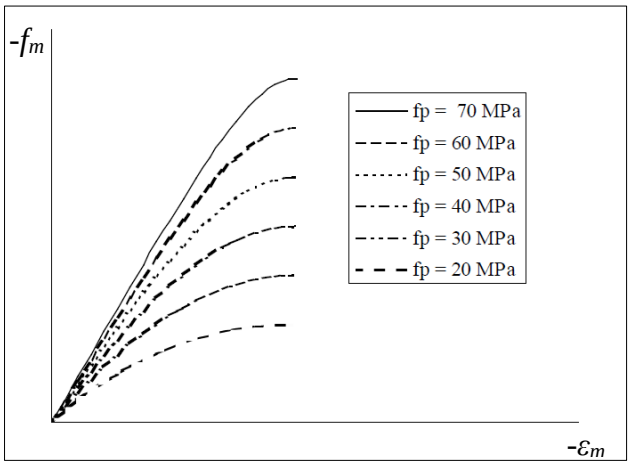

Source: Wong et al. (2013).

$$f_m = E_m\,\varepsilon_m\left[1 - \frac{1}{n}\left(\frac{\varepsilon_m}{\varepsilon_p}\right)^{n-1}\right] \quad for \quad \varepsilon_p < \varepsilon_m < 0 \qquad \text{Eq. 104}$$

$$n = \frac{E_m}{E_m - E_{sec}} \qquad \text{Eq. 105}$$

$$E_{sec} = {f_p}\Big/{|\varepsilon_p|} \qquad \text{Eq. 106}$$

where: f_m = principal compressive stress; f_p = peak compressive stress; ε_m = principal compressive strain; ε_p = peak compressive strain; E_m = initial tangent stiffness; E_{sec} = secant stiffness.

1.2. Compression post-peak response

1.2.1. Masonry (Park-Kent)

The post-peak response in the stress-strain curve of the modified Park-Kent model for masonry (Priestley and Elder, 1983) comprises, as illustrated in Figure 140, a linear descending branch and a final horizontal plateau at 20% of the masonry compressive strength. The model is expressed mathematically in Equations 107 and 108.

$$f_m = -f_p\left[1 + Z_m\left(\varepsilon_m - \varepsilon_p\right)\right] < 0 \;\; or \;\; f_m = -0.2f_p \;\; for \;\; \varepsilon_m < \varepsilon_p < 0 \qquad \text{Eq. 107}$$

$$Z_m = \left(\frac{3 + 0.29f_j}{145f_j - 1000} - 0.002\right)^{-1} \leq 1 \qquad \text{Eq. 108}$$

where: f_m = principal compressive stress; f_p = peak compressive stress; f_j = mortar compressive strength; ε_m = principal compressive strain; ε_p = peak compressive strain.

Figure 127: Masonry Park-Kent post-peak compression response.

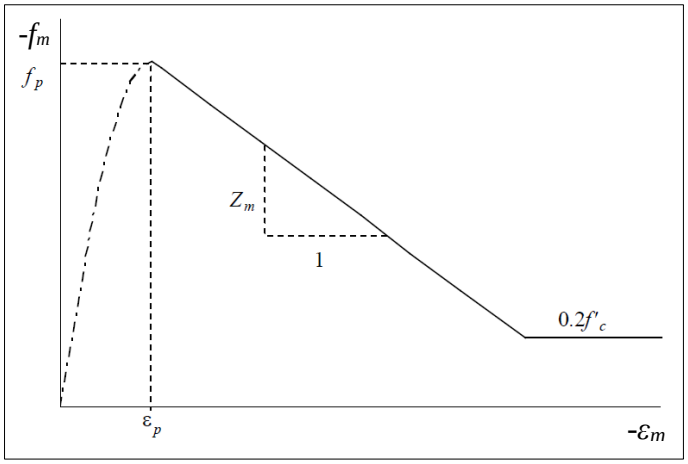

Source: Adapted from Wong et al. (2013).

1.3. Compression softening

The compression softening behavior for masonry in the VecTor2 software is controlled by a strength-and-strain softened model, as shown in Figure 128, to reduce both the uniaxial compressive strength (f'_m) and corresponding strain (ε_o) to determine the peak compressive strength (f_p) and corresponding strain (ε_p) used in the compression response model. In addition to the compression softening parameter (β_d), which is adopted according to the Vecchio 1992-A model, the parameters β_1 (Kupfer/Richart Model) and β_m are applied to account for the confinement and orthotropic effects. Equations 109 to 118 calculate the adjusted peak compressive strength and corresponding strain.

Figure 128: Strength and strain-softened compression response.

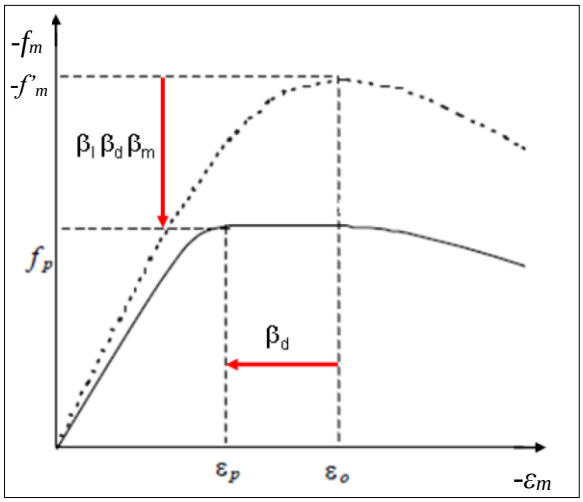

Source: Adapted from Wong et al. (2013).

$$f_p = \beta_d \beta_1 \beta_m f'_m \quad \text{Eq. 109}$$

$$\varepsilon_p = \beta_d \varepsilon_o \quad \text{Eq. 110}$$

$$\beta_d = (1 + C_s C_d)^{-1} \leq 1 \quad \text{Eq. 111}$$

$$C_d = \begin{cases} 0 & if \;\; r < 0.28 \\ 0.35(r - 0.28)^{0.80} & if \;\; r \geq 0.28 \end{cases} \quad \text{Eq. 112}$$

$$r = {}^{-\varepsilon_{m1}}/_{\varepsilon_{m2}} \leq 400 \quad \text{Eq. 113}$$

$$C_s = \begin{cases} 0 & if\ shear\ slip\ is\ not\ considered \\ 0.55 & if\ shear\ slip\ is\ considered \end{cases} \quad \text{Eq. 114}$$

$$\beta_1 = \left[1 + 0.92\left(\frac{f_{mn}}{f'_m}\right) - 0.76\left(\frac{f_{mn}}{f'_m}\right)^2\right] + 4.1\left(\frac{f_{ml}}{f'_m}\right) \quad for \quad f_{m2} < f_{m1} < 0 \quad \text{Eq. 115}$$

$$f_{mn} = -(f_{m2} - f_{m1}) > 0 \quad \text{Eq. 116}$$

$$f_{ml} = -f_{m1} > 0 \quad \text{Eq. 117}$$

$$\beta_m = {}^{\sigma_{2,max}}/_{f'_m} \quad \text{Eq. 118}$$

where: f'_m = maximum compressive strength off masonry; f_p = actual compressive strength of masonry; f_{m1} and f_{m2} = normal lateral stresses acting on the masonry; $\sigma_{2,max}$ = principal compressive strength defined according to the Ganz failure criteria; ε_{m1} = principal tensile strain; ε_{m2} = principal compressive strain; ε_p = peak compressive strain.

1.4. Tension pre-peak response

In tension, prior to cracking, the stress-strain relationship is linear-elastic (Equations 119 and 120) until the principal tensile stress (f_{m1}) reaches the maximum tensile strength (f'_t), as illustrated in Figure 129.

$$f_{m1} = E_m \varepsilon_{m1} \quad for \quad 0 < \varepsilon_{m1} < \varepsilon_{cr} \quad \text{Eq. 119}$$

$$\varepsilon_{cr} = {}^{f_{cr}}/_{E_m} \quad for \;\; f_{cr} = f'_t \quad \text{Eq. 120}$$

where: f_{m1} = principal tensile stress; f_{cr} = cracking stress determined by the cracking criterion model; E_m = initial tangent stiffness; ε_{m1} = principal tensile strain; ε_{cr} = cracking strain.

Figure 129: Tension pre-peak response.

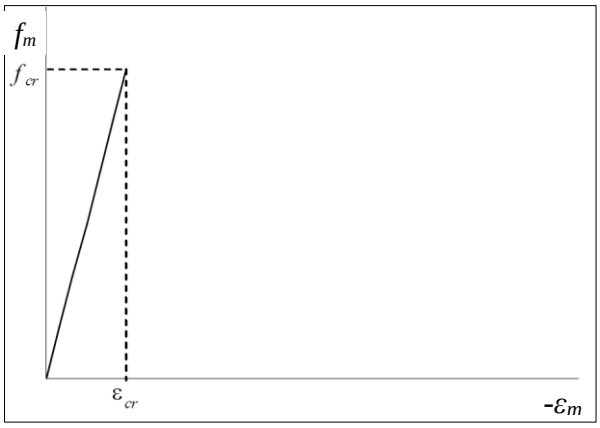

Source: Adapted from Wong et al. (2013).

1.5. Tension stiffening

1.5.1. Modified Bentz (2003)

The Modified Bentz (2003) is the default model in VecTor2 for tension stiffening. As described in Equations 121 and 122, the formulation includes the proportion of reinforcement and bond properties.

$$f_{m1} = \frac{f_t'}{1+\sqrt{c_t \varepsilon_{m1}}} \quad for \quad \varepsilon_{m1} > \varepsilon_t' \qquad \text{Eq. 121}$$

$$c_t = \frac{2.16}{\sum_{i=1}^{n} 4(\rho_i/d_{bi})|\cos(\theta-\alpha_i)|} \qquad \text{Eq. 122}$$

where: f_{m1} = principal tensile stress; f_t' = maximum tensile strength; E_m = initial tangent stiffness; ε_{m1} = principal tensile strain; ρ_i = reinforcement ratio; d_{bi} = rebar diameter; θ = inclination of the principal direction; α_i = inclination of reinforcement.

1.6. Tension softening

1.6.1. Nonlinear (Hordijk)

The nonlinear crack softening behavior suggested by Hordijk et al. (1987) for the post-peak tensile stress-strain curve is an exponential function, Equation 123, to indicate the relationship between the tensile stress and the crack opening. The pre- and post-peak tensile stress-strain constitutive relationship is illustrated in Figure 143.

$$f_{m1} = f_t' \left\{ \left[1 + \left(3\frac{\varepsilon_{m1}}{\varepsilon_{tu}} \right)^3 \right] e^{-6.93\frac{\varepsilon_{m1}}{\varepsilon_{tu}}} - 0.027\frac{\varepsilon_{m1}}{\varepsilon_{tu}} \right\} \quad for \quad \varepsilon_{m1} > \varepsilon_{cr} \qquad \text{Eq. 123}$$

$$\varepsilon_{tu} = 5.136\left(G_f/f_t' L_r\right) \qquad \text{Eq. 124}$$

where: f_{m1} = principal tensile stress; f_t' = maximum tensile strength; ε_{m1} = principal tensile strain; ε_{tu} = ultimate tensile strain; ε_{cr} = cracking strain; G_f = fracture energy; L_r = representative length.

Figure 130: Tensile stress-strain constitutive relation.

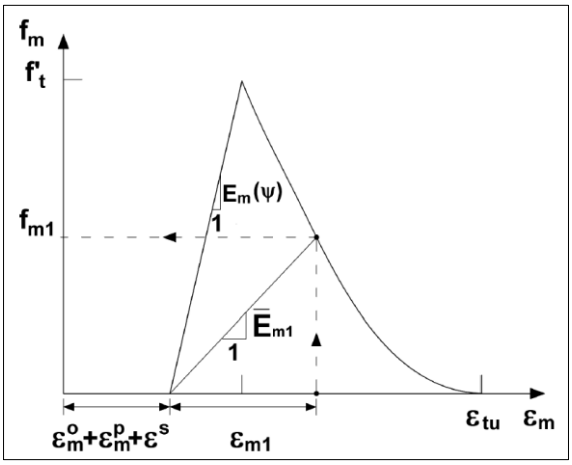

Source: Facconi et al. (2014).

1.7. Cracking criterion

1.7.1. Mohr-Coulomb (Stress)

Shear failure is defined as a combination of shear stress (τ) and normal stresses (f_{m1} and f_{m3}) with a failure envelope tangent to the Mohr's circles, as depicted in Figure 131. A stress-independent component and a stress-dependent component constitute the shear strength. The first type is the cohesion (*c*), Equation 125, which is calculated by taking into account that, at failure in uniaxial compression, the maximum compressive stress (f_{m3}) is equal to the masonry compressive strength (f'_m), and that f_{m1} is null. The second type is the internal friction angle (ϕ), assumed equal to 37° in VecTor2.

When f_{m3} is null, f_{m1} is equal to f_{cru}, Equation 126, being f_{m3} calculated using Equation 127 given a set of principal concrete stresses ($\varepsilon_{m3} < \varepsilon_{m2} < \varepsilon_{m1}$). Once the principal compressive stress has been established, the principal tensile stress (f_{m1}) of the Mohr's circle tangent to the failure envelope determines the cracking strength, as shown in Equation 128.

$$c = f_m' \left(\frac{1-\sin\phi}{2\cos\phi}\right) \quad \text{Eq. 125}$$

$$f_{cru} = f_m' \left(\frac{2c\cdot\cos\phi}{2\cos\phi}\right) \quad \text{Eq. 126}$$

$$f_{m3} = \begin{cases} -f'_m \left[2\left(\frac{\varepsilon_{m3}}{\varepsilon_o}\right) - \left(\frac{\varepsilon_{m3}}{\varepsilon_o}\right)^2\right] & for \quad \varepsilon_{m3} < \varepsilon_o < 0 \\ -f'_m & for \quad \varepsilon_o < \varepsilon_{m3} < 0 \\ 0 & for \quad 0 < \varepsilon_{m3} \end{cases} \quad \text{Eq. 127}$$

$$f_{cr} = f_{cru}\left(1 + \frac{f_{m3}}{f'_m}\right) \quad for \quad 0.2f'_t \leq f_{cr} < f'_t \quad \text{Eq. 128}$$

where: c = cohesion; f'_m= masonry compressive strength; ϕ = internal friction angle; f_{m1} = principal tensile stress; f_{m3} = maximum compressive stress; f'_t = maximum tensile strength.

Figure 131: Mohr-Coulomb (Stress) cracking criterion.

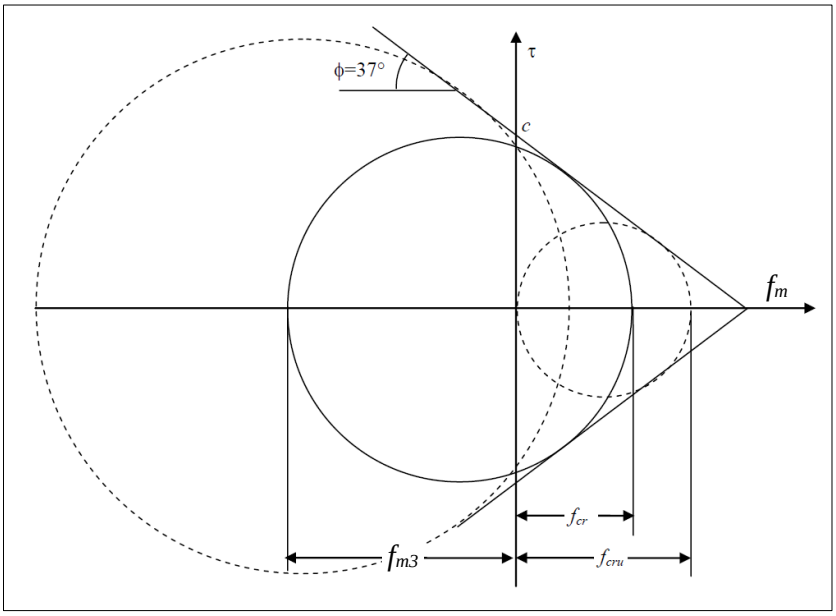

Source: Adapted from Wong et al. (2013).

1.8. Joint shear slip

In VecTor2, masonry is defined as a continuum that, even when uncracked, may slip along the head and bed joints, as illustrated in Figure 132. The shear stress and shear strain parallel to the joint can be calculated from the total stress vector. Therefore, based on the estimated shear strain along the joints, the shear slip (δ_s) and the average shear slip strain (γ_s) can be determined using Equations 129 and 130, respectively. The adopted elastic-plastic shear stress–strain relationship is shown in Figure 133.

$$\delta_s = \gamma \cdot th_i \quad \text{Eq. 129}$$

$$\gamma_s = {}^{\delta_s}/_{sp_i} \quad \text{Eq. 130}$$

where: δ_s = shear slip; γ_s = average shear slip strain; th_i = joint thickness; sp_i = joint spacing.

Figure 132: Masonry joint slip.

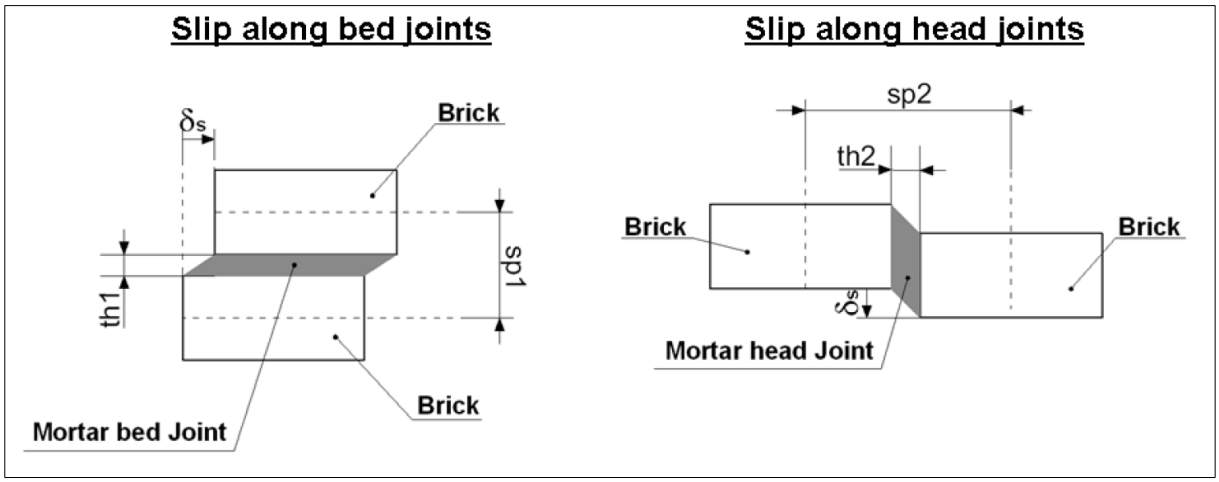

Source: Wong et al. (2013).

Figure 133: Shear stress–strain relationship for bed and head joints.

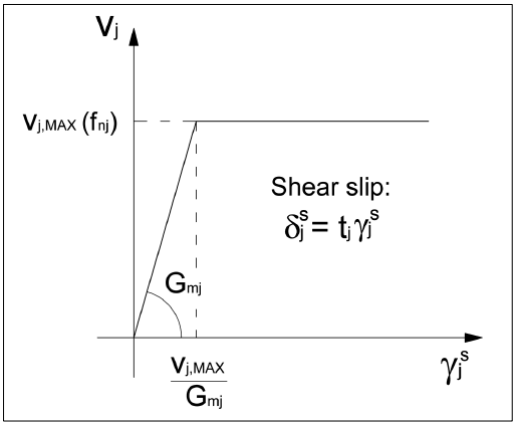

Source: Facconi et al. (2014).

1.9. CRACK SLIP

1.9.1. Walraven stress model

Based on an investigation of the crack structure and contact area of the crack faces, the Walraven stress model is a modified version of the formulations presented by Walraven and Reinhardt (1981). In this model, the slip along the crack is calculated using Equations 131-134.

$$\delta_s = \frac{V_{ci} + V_{co}}{1.8w^{-0.8} + (0.234w^{-0.707} - 0.2)\cdot f'_m} \quad \text{Eq. 131}$$

$$V_{ci} = 0.18V_{ci,max} + 1.64f_{ci} - 0.82\frac{{f_{ci}}^2}{V_{ci,max}} \quad \text{Eq. 132}$$

$$V_{ci,max} = \frac{0.18\sqrt{f'_m}}{0.31 + \frac{24w}{a_g + 16}} \quad \text{Eq. 133}$$

$$V_{co} = \frac{f'_m}{30} \quad (in\ MPa) \qquad \text{Eq. 134}$$

where: δ_s = slip along the crack; V_{ci} = local shear stresses on the crack; $V_{ci,max}$ = maximum shear stresses on the crack; V_{co} = initial offset in the crack shear-slip relationship; w = crack width; f_{ci} = small local compressive stresses across the crack; f'_m= masonry compressive strength; a_g = maximum aggregate size.

2. REINFORCEMENT BEHAVIOR

2.1. Strain hardening

As illustrated in Figure 134, reinforcement is modeled as ductile steel with a trilinear stress-strain response comprising an initial linear-elastic response, a yield plateau, and a linear strain-hardening phase until rupture. The reinforcement stress (f_s) in tension and compression is determined according Equation 135.

Figure 134: Stress-strain behavior of reinforcement.

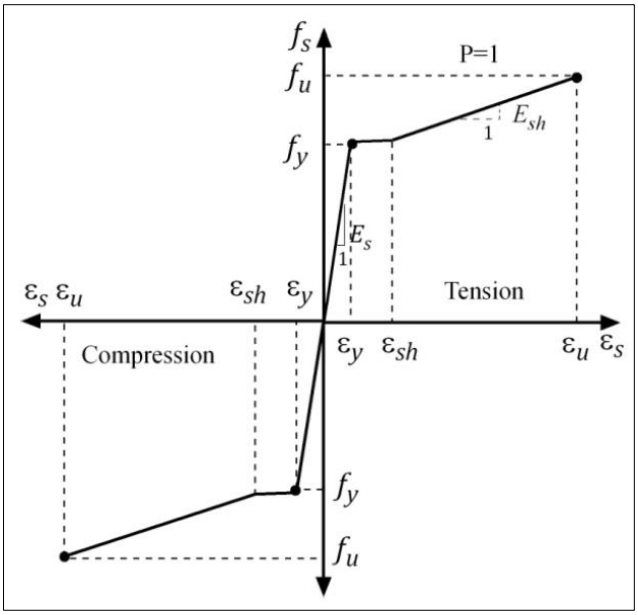

Source: Wong et al. (2013).

$$f_s = \begin{cases} E_s\varepsilon_s & for \quad \varepsilon_s \le \varepsilon_y \\ f_y & for \quad \varepsilon_y < \varepsilon_s \le \varepsilon_{sh} \\ f_u + (f_y - f_u)\left(\frac{\varepsilon_u - \varepsilon_s}{\varepsilon_u - \varepsilon_{sh}}\right)^P & for \quad \varepsilon_{sh} < \varepsilon_s \le \varepsilon_u \\ 0 & for \quad \varepsilon_u < \varepsilon_s \end{cases} \qquad \text{Eq. 135}$$

$$E_{sh} = \frac{f_u - f_y}{\varepsilon_u - \varepsilon_{sh}} \qquad \text{Eq. 136}$$

where: ε_s = reinforcement strain ($\varepsilon_s = |\varepsilon_s|$); ε_y = yield strain; ε_{sh} = strain at the onset of the strain hardening; ε_u = ultimate strain; E_s = elastic modulus; f_y = yield strength; f_u = ultimate strength; P = strain-hardening parameter.

2.2. Hysteretic response

2.2.1. Seckin model with Bauschinger effect

Proposed by Seckin (1981), as revealed in Figure 135, this model incorporates the Bauschinger effect, in which the reinforcement displays premature yielding upon load reversal following plastic prestraining due to microscopic stress changes. When reloading to a strain of ε_j in a positive cycle, the reinforcing stress (f_s) expresses the Bauschinger effect by employing a Ramberg-Osgood formulation, as demonstrated in Equations 137-139. Unloading is linear according to Equation 140.

Figure 135: Reinforcement hysteretic response of Seckin model.

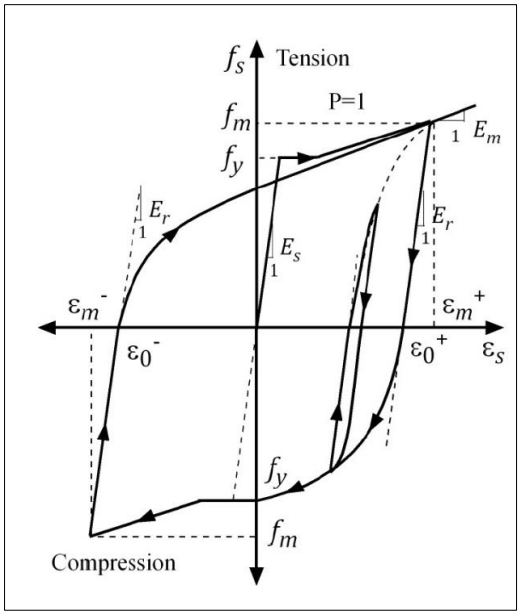

Source: Wong et al. (2013).

$$f_s = E_r(\varepsilon_j - \varepsilon_o) + \frac{E_m - E_r}{N(\varepsilon_m - \varepsilon_o)^{N-1}}(\varepsilon_m - \varepsilon_o)^N \quad \text{Eq. 137}$$

$$N = \frac{(E_m - E_r)(\varepsilon_m - \varepsilon_o)}{f_m - E_r(\varepsilon_m - \varepsilon_o)} \quad \text{Eq. 138}$$

$$E_r = \begin{cases} E_s & for \quad (\varepsilon_m - \varepsilon_o) \le \varepsilon_y \\ E_s\left[1.05 - 0.05\frac{(\varepsilon_m - \varepsilon_o)}{\varepsilon_y}\right] & for \quad \varepsilon_y < (\varepsilon_m - \varepsilon_o) < 4\varepsilon_y \\ E_s & for \quad 4\varepsilon_y \le (\varepsilon_m - \varepsilon_o) \end{cases} \quad \text{Eq. 139}$$

$$f_s = f_{sj-1} + E_r(\varepsilon_j - \varepsilon_{j-1}) \quad \text{Eq. 140}$$

where: ε_o = plastic offset strain in the current cycle; ε_y = yield strain; ε_m = maximum positive strain attained in previous cycles; E_m = tangent stiffness at ε_m; E_r = unloading modulus; E_s = elastic modulus of the monotonic stress-strain response; f_m = stress corresponding to ε_m.

2.3. Dowel action

2.3.1. Tassios model (crack slip)

An elastic-plastic relationship is used to represent the dowel force-displacement, in which the dowel force (V_d) resulting from the relative displacement of cracks (δ_s) is calculated using Equations 141-145. Thus, the shear resistance due to dowel action is determined as a smeared contribution using Equation 146.

$$V_d = E_s I_z \lambda^3 \delta_s \leq V_{du} \quad \text{Eq. 141}$$

$$I_z = {\pi d_b^4}/{64} \quad \text{Eq. 142}$$

$$\lambda = \sqrt[4]{\frac{k_c d_b}{4 E_s I_z}} \quad \text{Eq. 143}$$

$$k_c = \frac{101.6\sqrt{f'_m}}{d_b^{2/3}} \quad \text{Eq. 144}$$

$$V_{du} = 1.27 d_b^2 \sqrt{f'_m f_y} \quad \text{Eq. 145}$$

$$v_d = {\rho_s V_d}/{A_s} \quad \text{Eq. 146}$$

where: δ_s = shear slip along the crack; d_b = diameter of the reinforcement; E_s = elastic modulus of the reinforcement; f_y = yield strength of the reinforcement, f'_m = masonry compressive strength; I_z = area moment of inertia of the reinforcement; λ = relative stiffness of the masonry to that to the reinforcing bar; k_c = stiffness of notional foundation; V_{du} = ultimate dowel force, corresponding to plastic hinging of the reinforcement and crushing of the surrounding concrete in multiaxial compression; ρ_s = reinforcement ratio; A_s = area of the reinforcement.

2.4. Buckling

2.4.1. Refined Dhakal-Maekawa (RDM) Model

This model considers that buckling starts when the compressive reinforcement strain exceeds its yield strain and the unsupported length to diameter ratio ($b/t = L/D$) for the reinforcing bars exceeds 5.0. The typical response obtained using this model is shown in Figure 136. Since the list of equations to describe this model is extensive, it is advised to consult the software manual or the original literature to see the formulation deduction sequence.

Figure 136: Typical average compressive response obtained from RDM model.

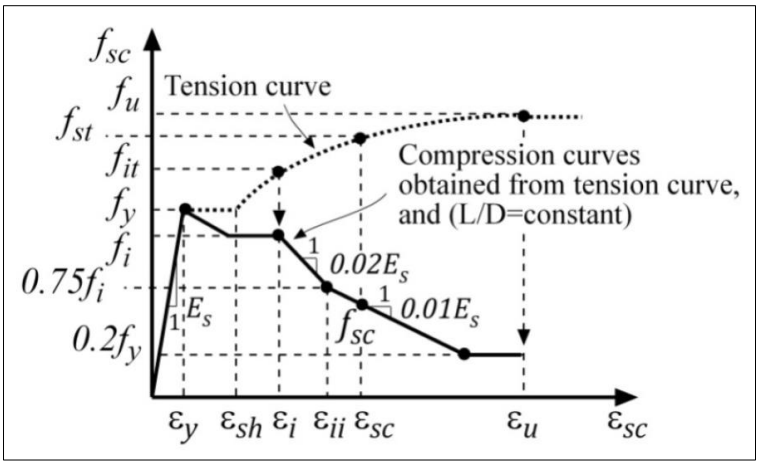

Source: Wong et al. (2013).

2.5. Bond

2.5.1. Eligehausen Model

As illustrated in Figure 137, the confined and unconfined bond stress-slip relationships proposed by Eligehausen et al. (1983) comprise an ascending non-linear branch, a constant bond stress plateau, a linearly dropping branch, and a sustaining residual stress branch. As for the buckling model, it is advised to consult the software manual or the original literature to see the vast list of equations that describe this model.

Figure 137: Eligehausen bond stress-slip response.

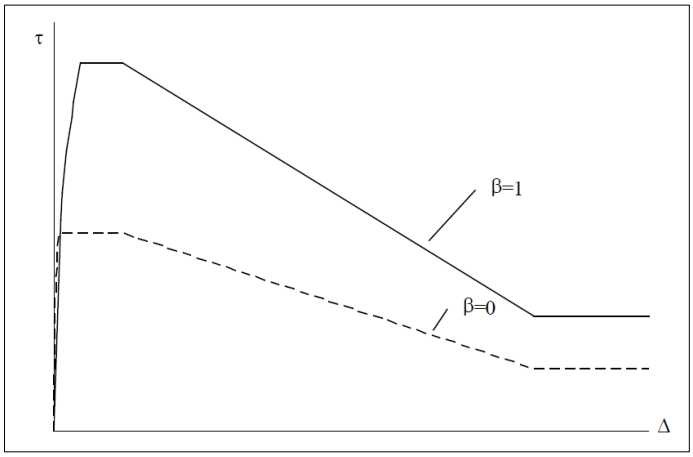

Source: Wong et al. (2013).

APPENDIX B – Hysteresis of the numerical models of Chapter 2

Figure 138: Hysteresis curves of models varying the compressive strength of ungrouted masonry.

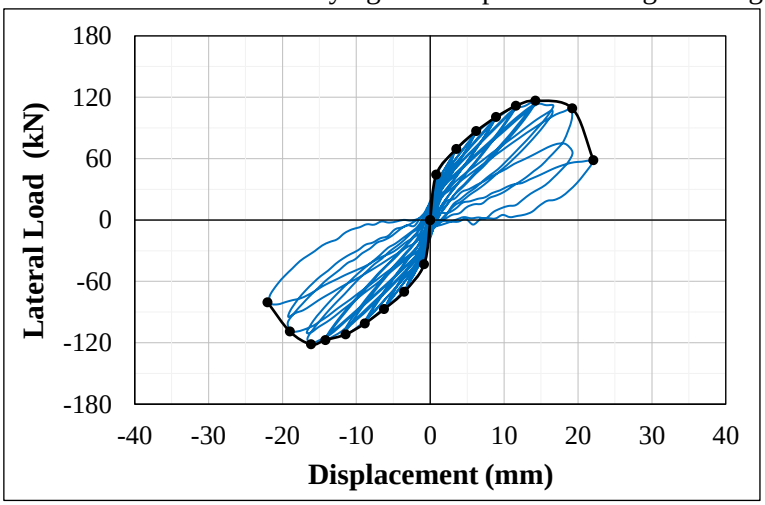

(a) Model 1 (17.2 MPa)

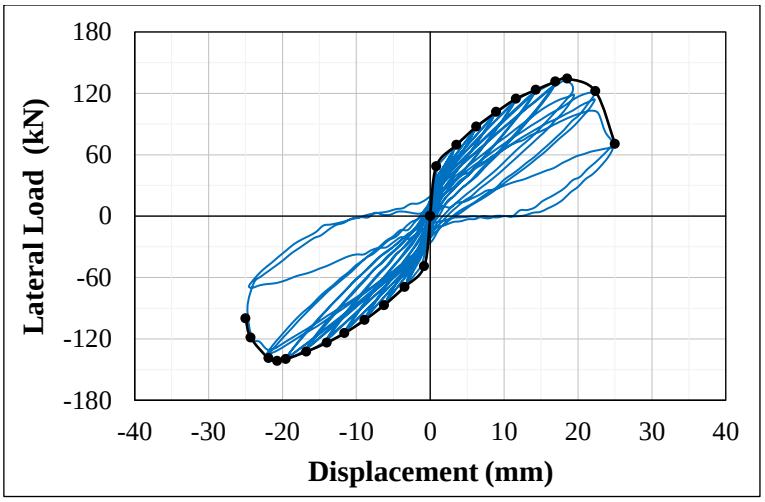

(b) Model 2 (20.7 MPa)

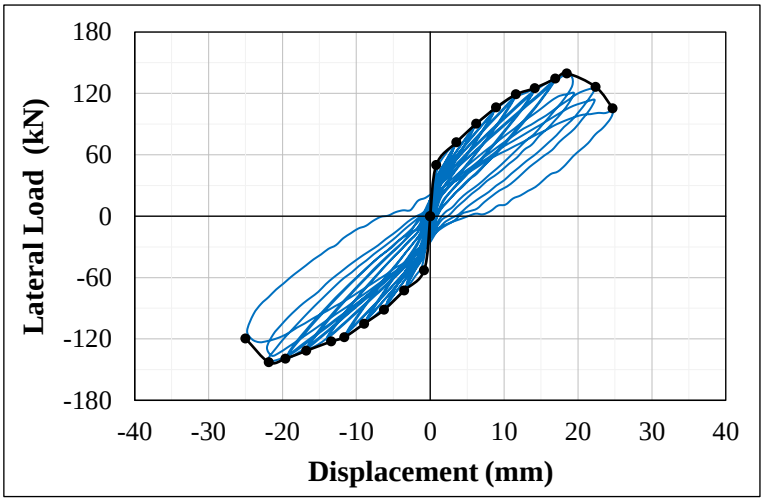

(c) Model 3 (24.1 MPa)

Figure 139: Hysteresis curves of models varying the compressive strength of grouted masonry.

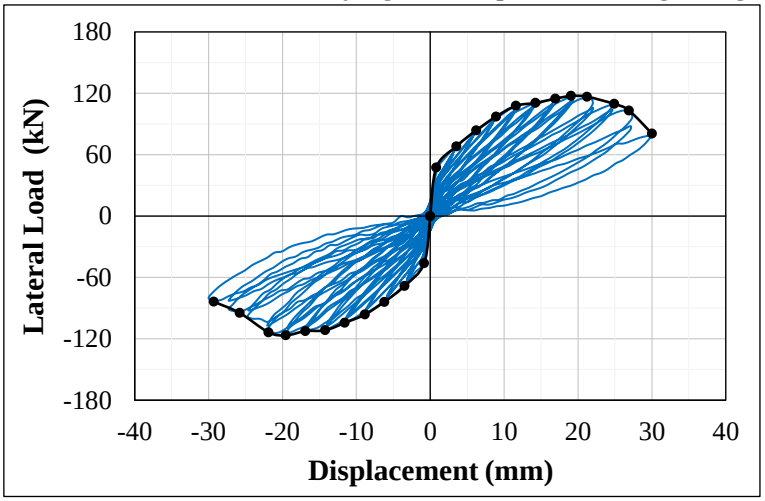

(a) Model 1 (17.2 MPa)

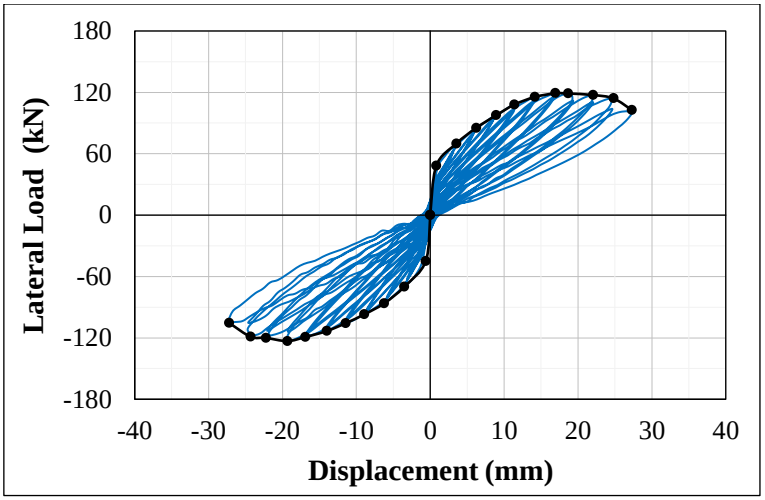

(b) Model 2 (20.7 MPa)

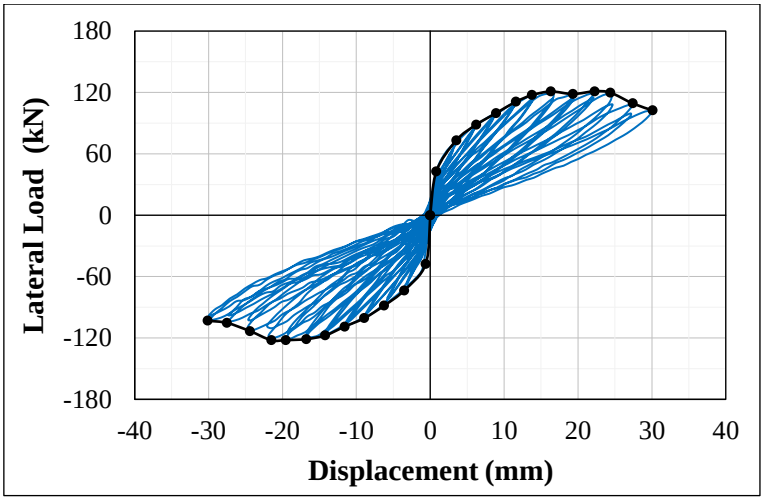

(c) Model 3 (24.1 MPa)

Figure 140: Hysteresis curves of models varying the mortar shear strength.

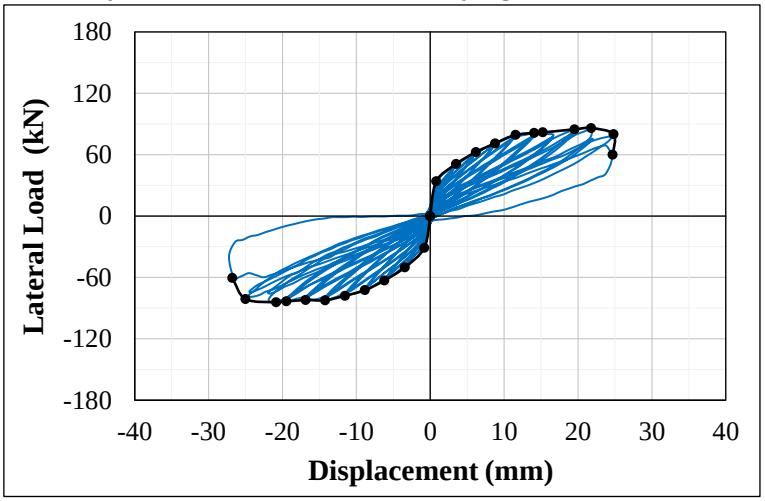

(a) Model 1 (140.2 kPa)

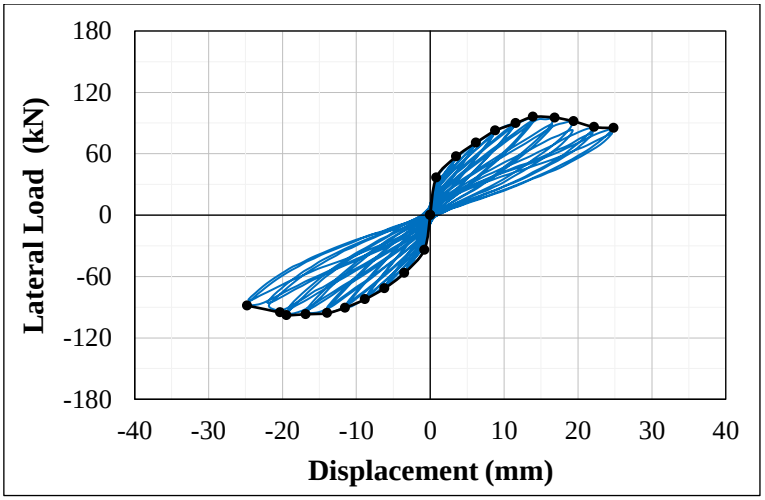

(b) Model 2 (210.3 kPa)

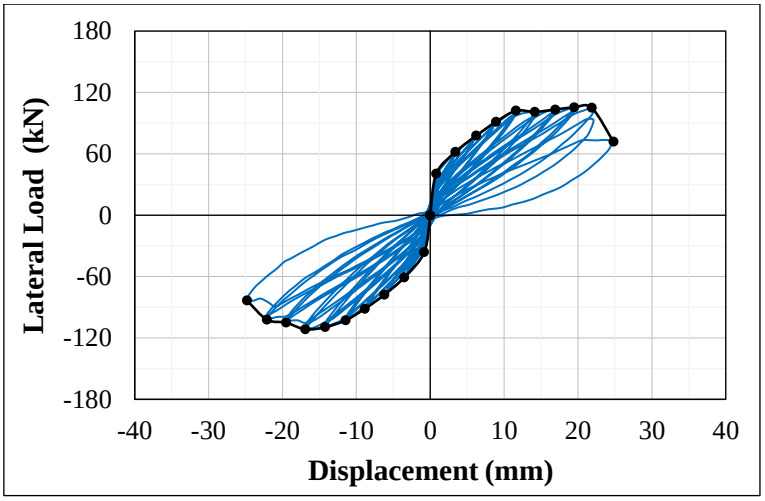

(c) Model 3 (280.4 kPa)

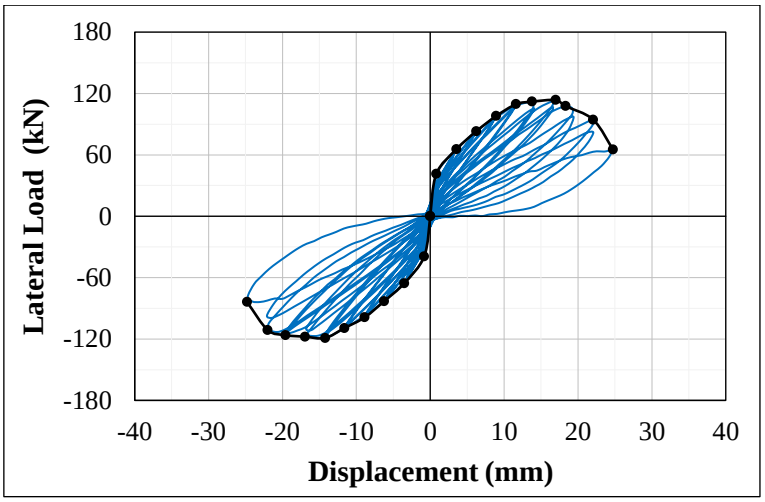

(d) Model 4 (350.5 kPa)

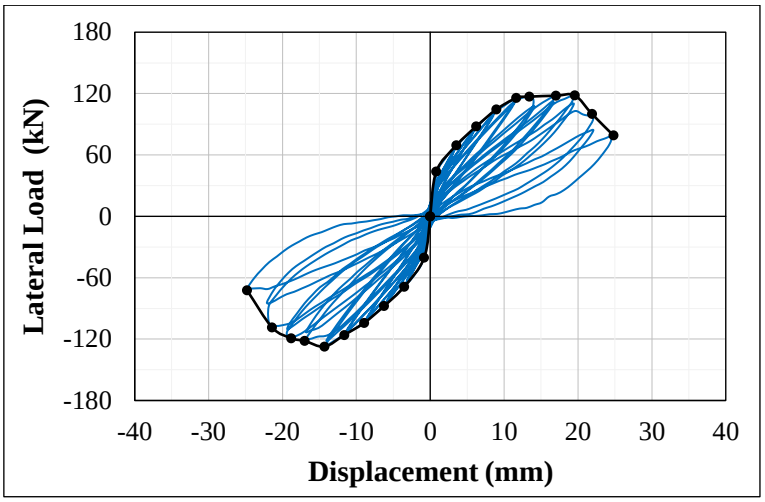

(e) Model 5 (420.6 kPa)

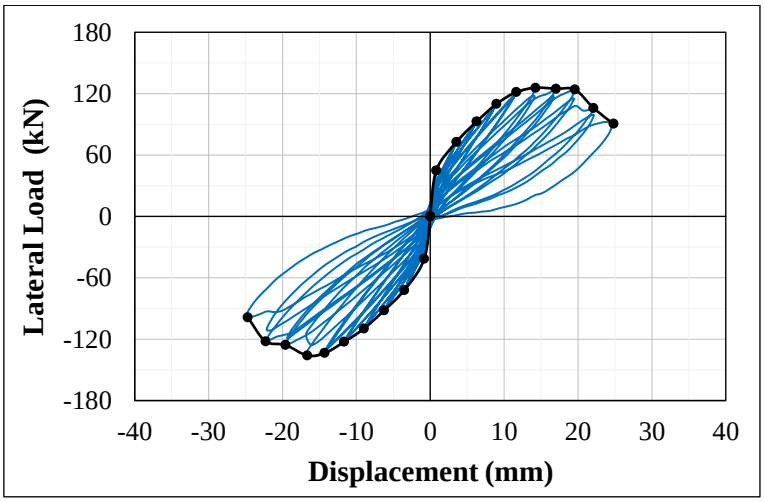

(f) Model 6 (490.7 kPa)

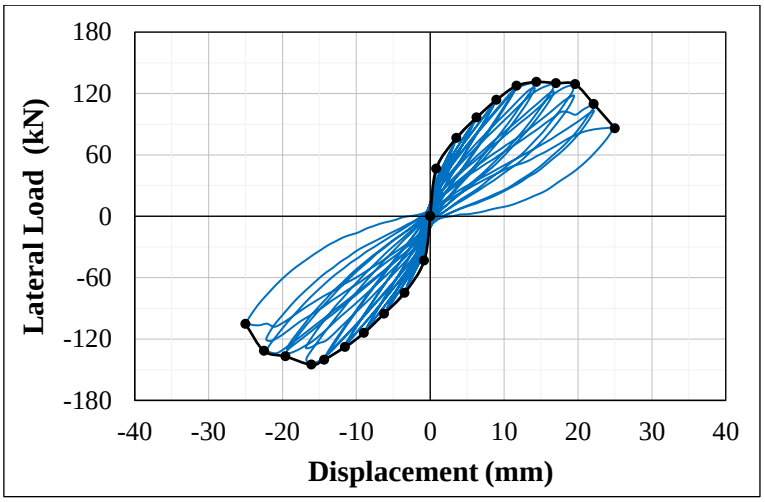

(g) Model 7 (560.8 kPa)

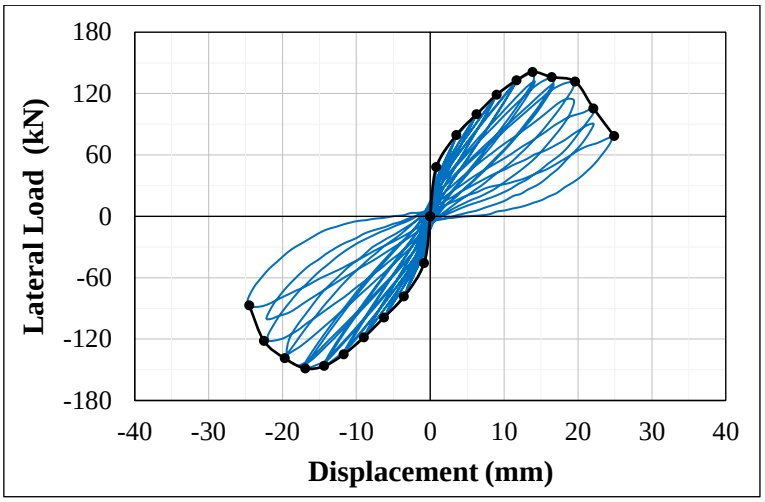

(h) Model 8 (630.9 kPa)

Figure 141: Hysteresis curves of models varying the reinforcement size (reinforcement ratio).

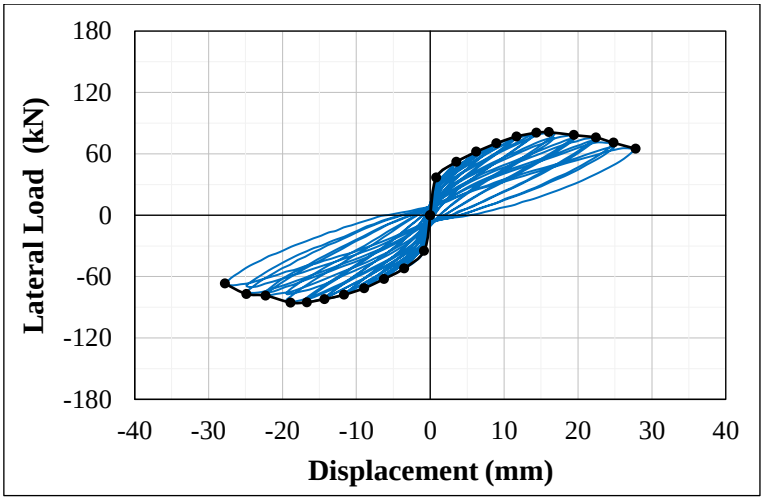

(a) Model 1 (Ø6.3V - Ø9.5H; 0.0011V – 0.00105H)

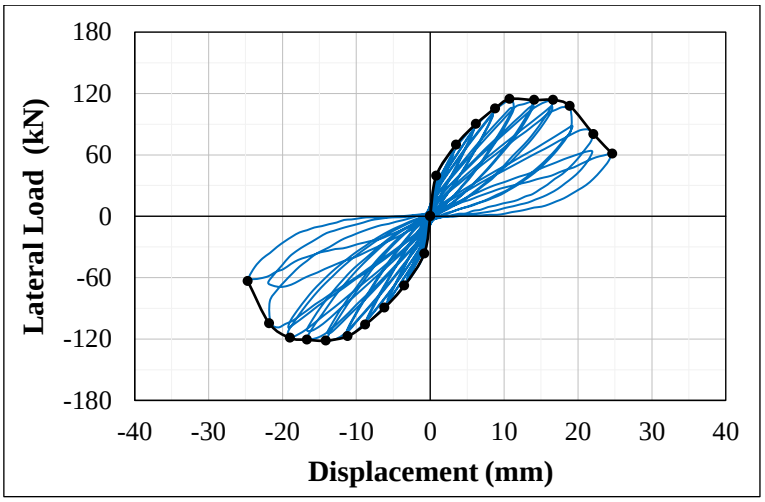

(b) Model 2 (Ø12.7V - Ø9.5H; 0.0045V – 0.00105H)

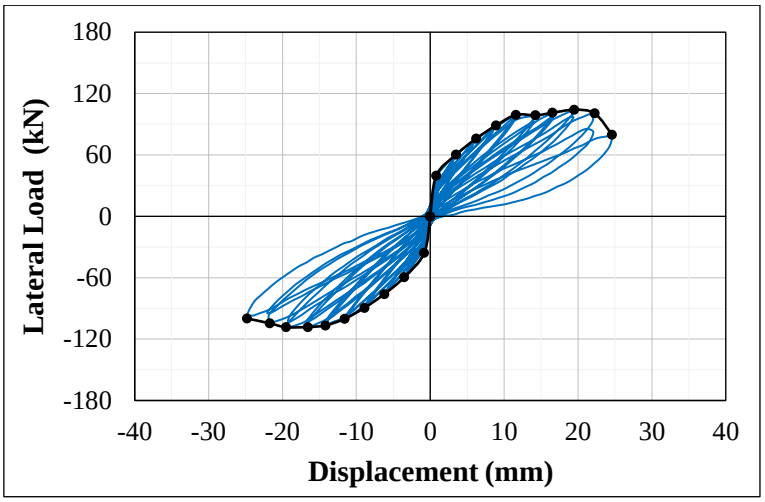

(c) Model 3 (Ø9.5V - Ø6.3H; 0.0025V – 0.00048H)

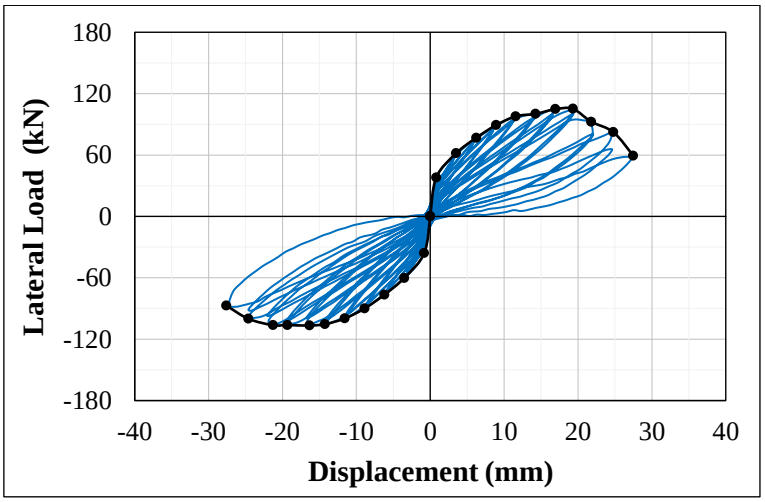

(d) Model 4 (Ø9.5V - Ø12.7H; 0.0025V – 0.00191H)

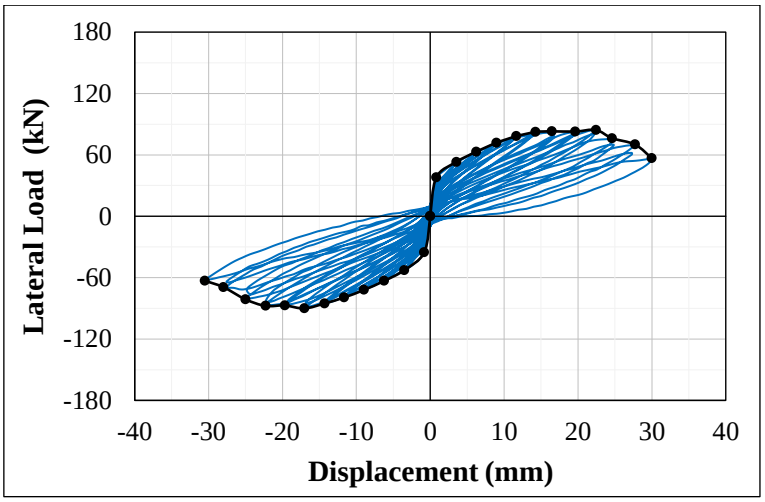

(e) Model 5 (Ø6.3V - Ø6.3H; 0.0011V – 0.00048H)

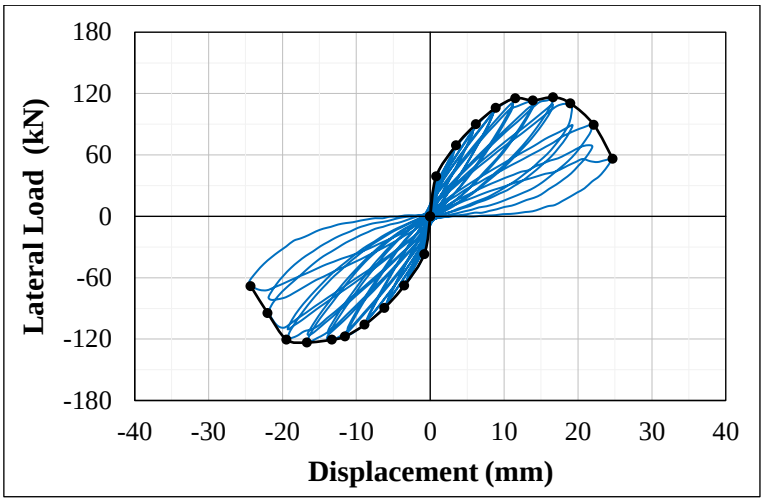

(f) Model 6 (Ø12.7V - Ø12.7H; 0.0045V – 0.00191H)

Figure 142: Hysteresis curves of models varying the vertical reinforcement spacing.

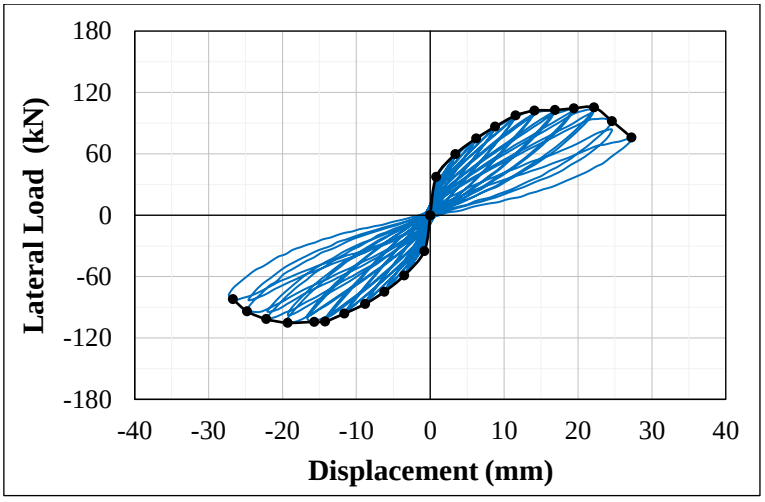

(a) Model 1 (406 mm)

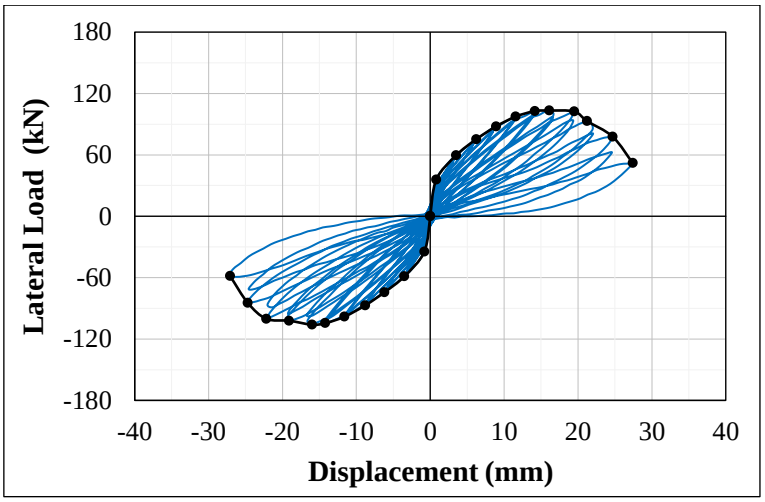

(b) Model 2 (610 mm)

Figure 143: Hysteresis curves of models varying the horizontal reinforcement spacing.

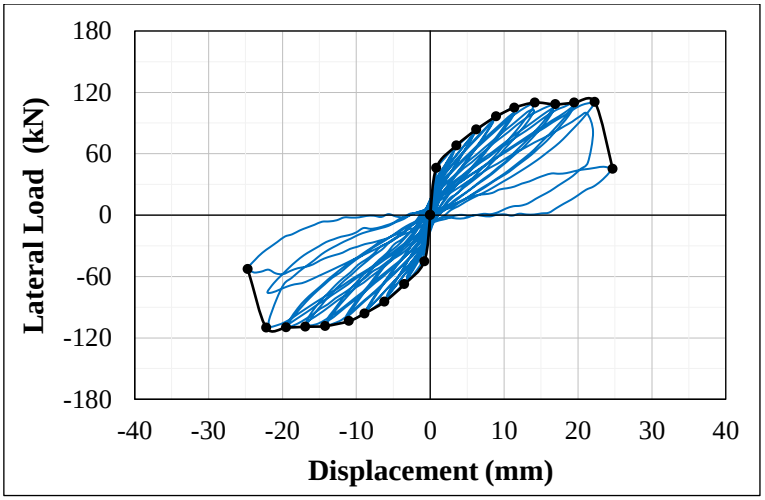

(a) Model 1 (508 mm)

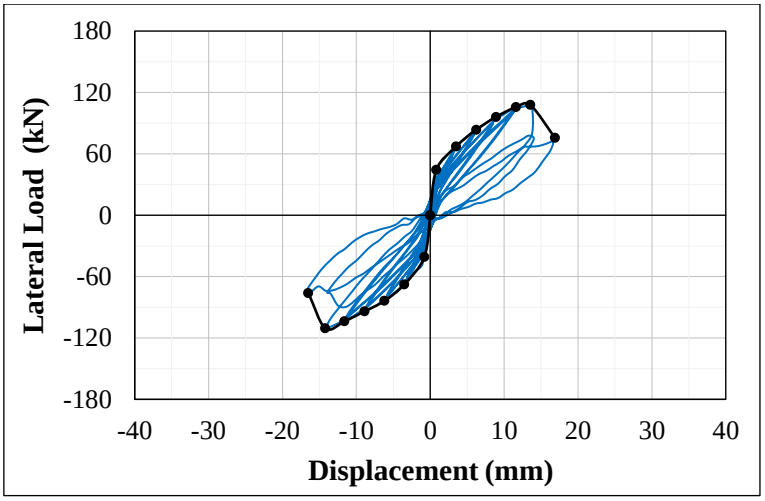

(b) Model 2 (610 mm)

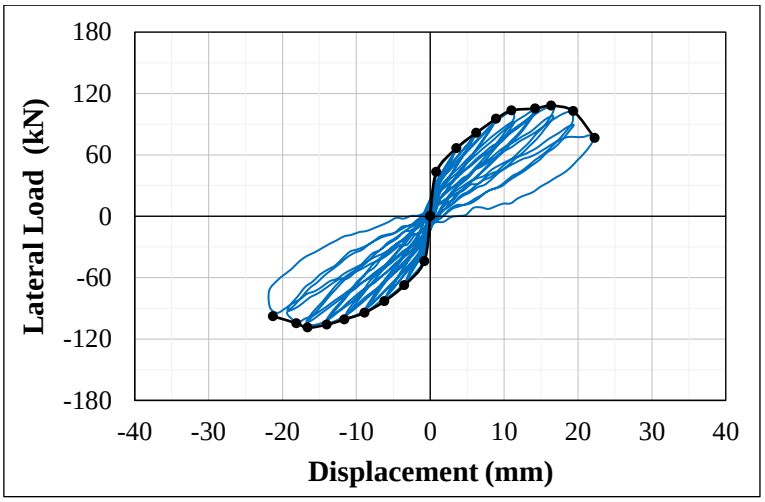

(c) Model 3 (1118 mm)

Figure 144: Hysteresis curves of models varying the axial stress.

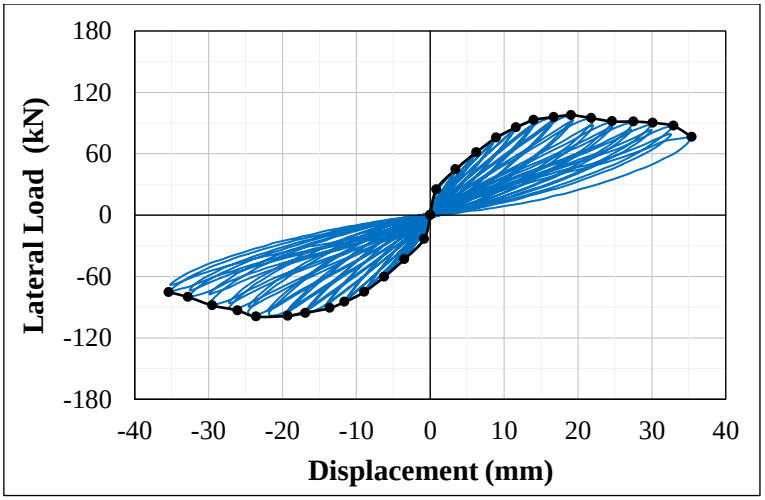

(a) Model 1 (0 kPa)

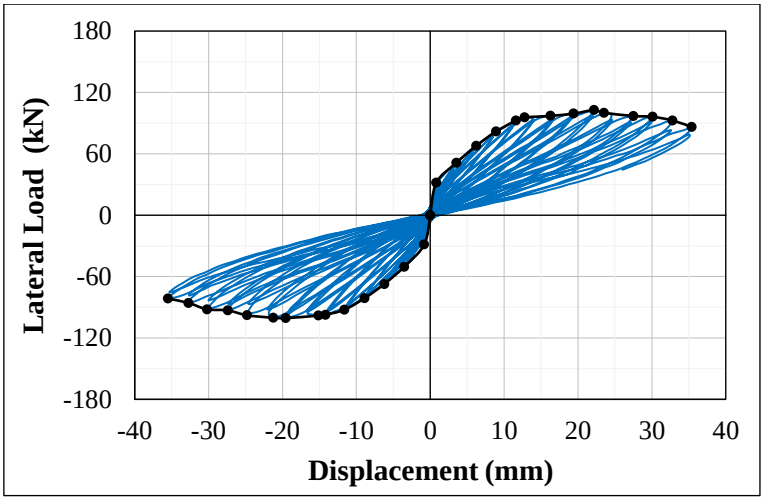

(b) Model 2 (65 kPa)

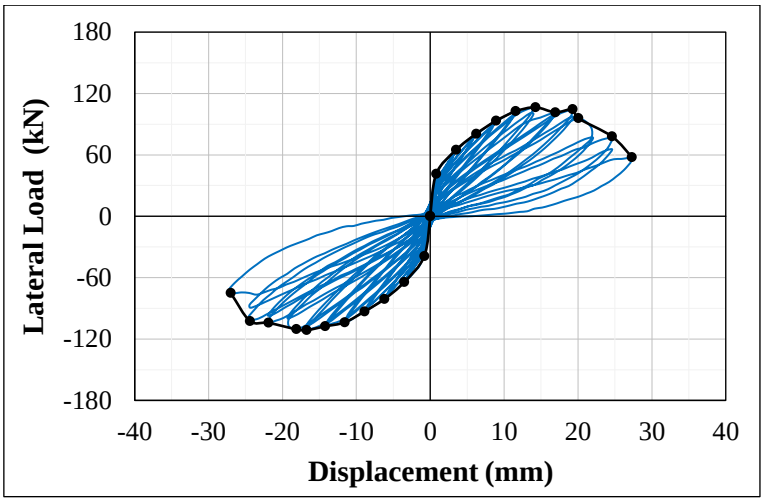

(c) Model 3 (194 kPa)

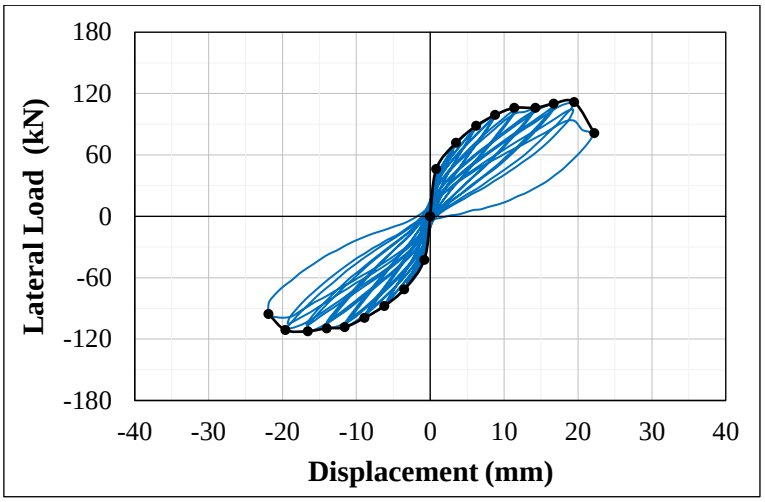

(d) Model 4 (259 kPa)

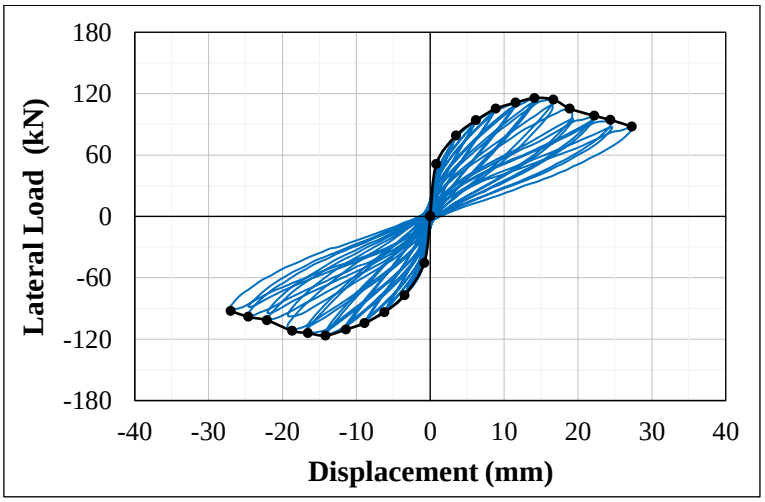

(e) Model 5 (324 kPa)

Figure 145: Hysteresis curves of models varying the aspect ratio.

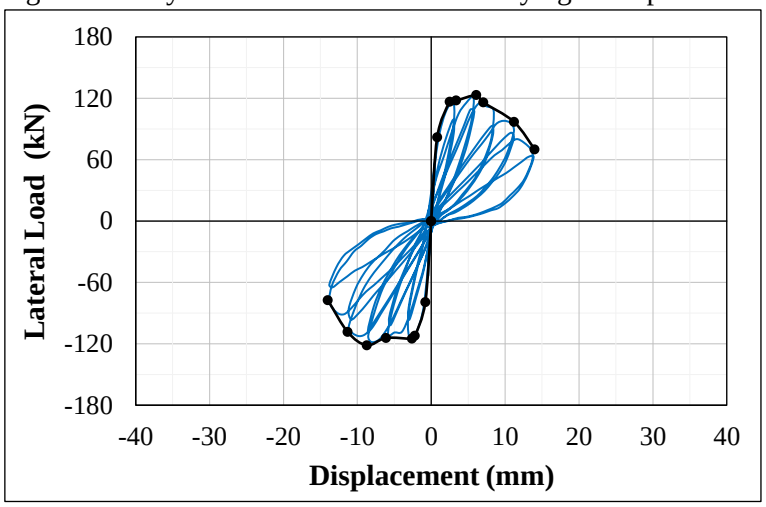

(a) Model 1 (0.45 - 1 Story)

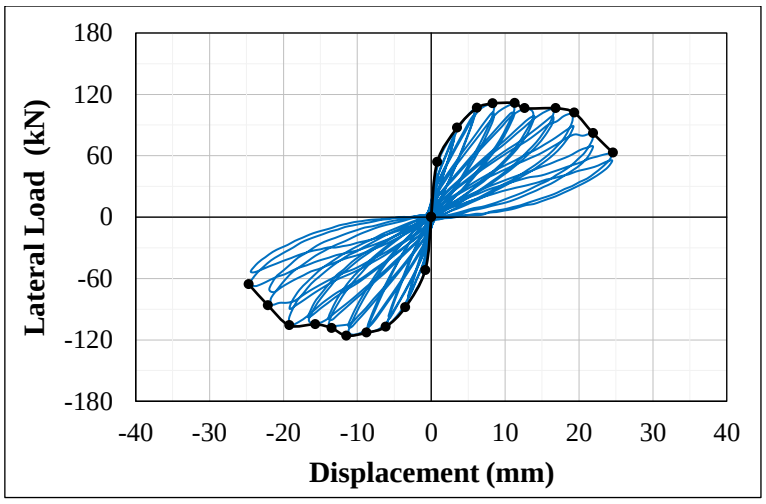

(b) Model 2 (0.84 - 2 Stories)

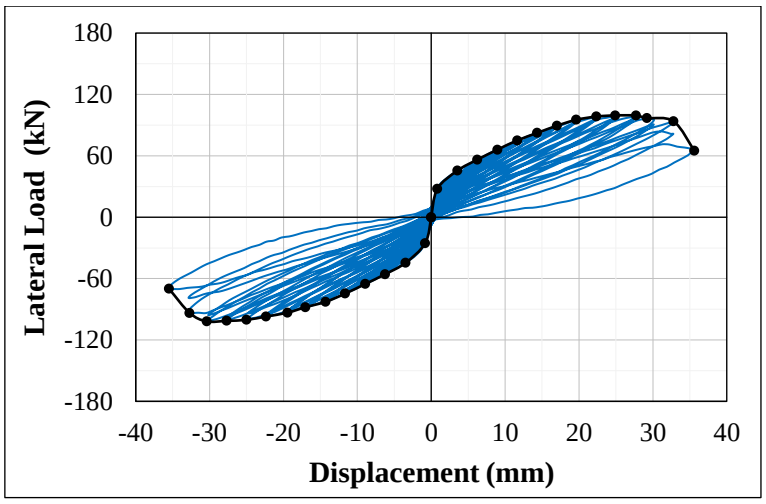

(c) Model 3 (1.63 - 4 Stories)

Figure 146: Hysteresis curves of models varying the opening size (height × length).

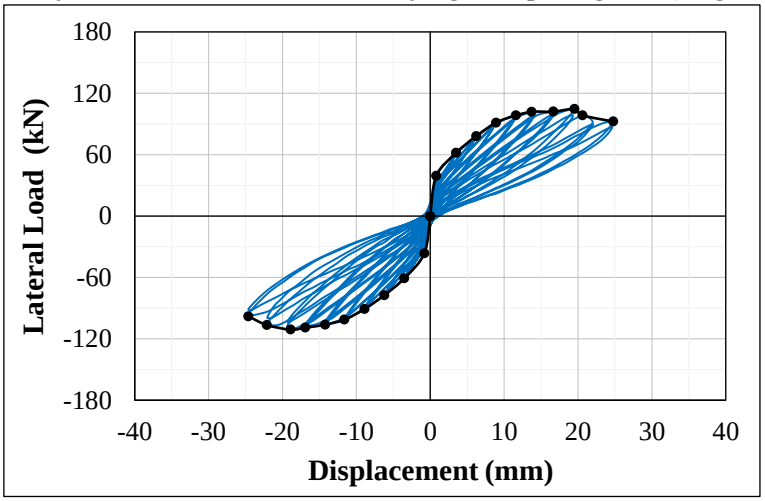

(a) Model 1 (475 mm × 570 mm)

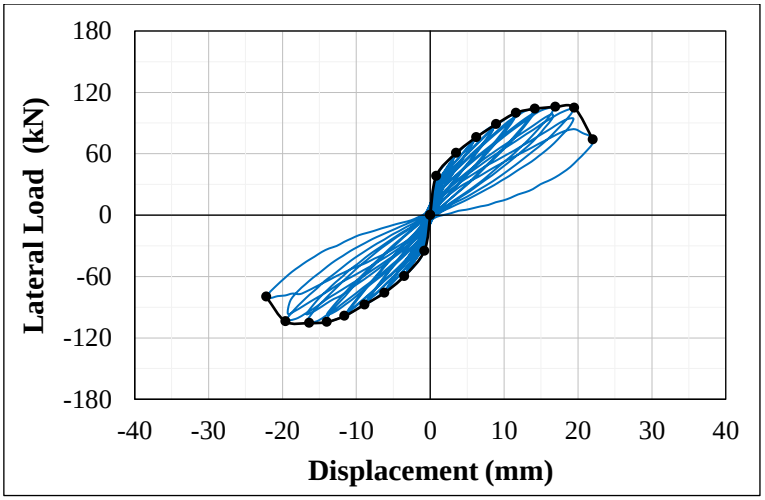

(b) Model 2 (665 mm × 570 mm)

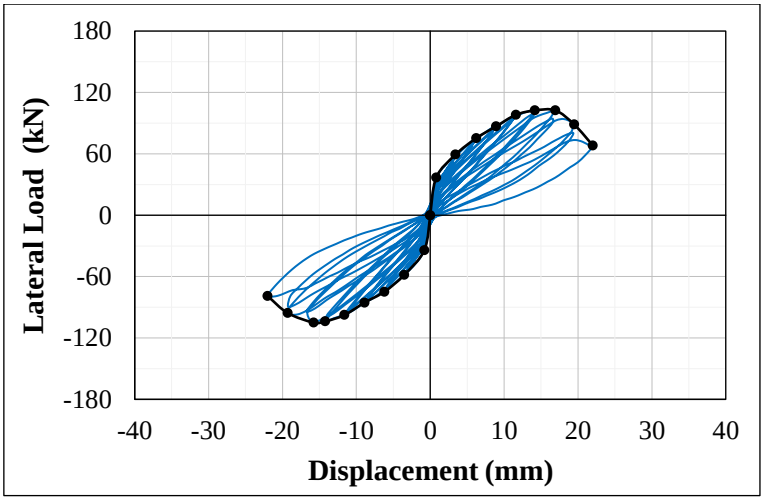

(c) Model 3 (755 mm × 570 mm)

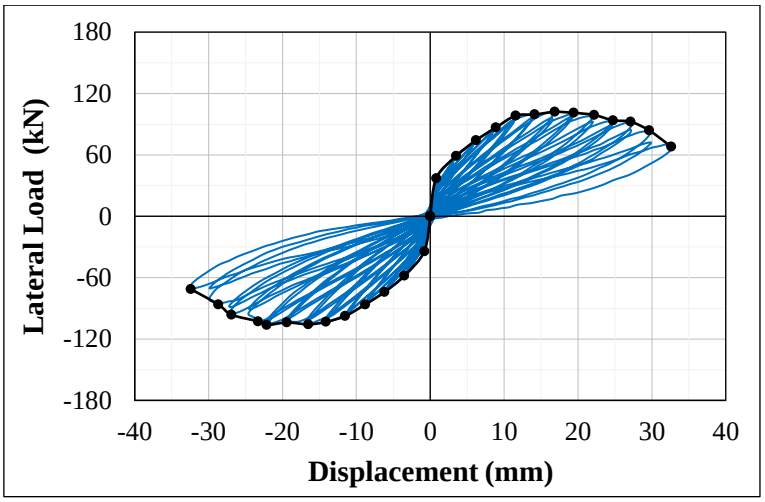

(d) Model 4 (570 mm × 760 mm)

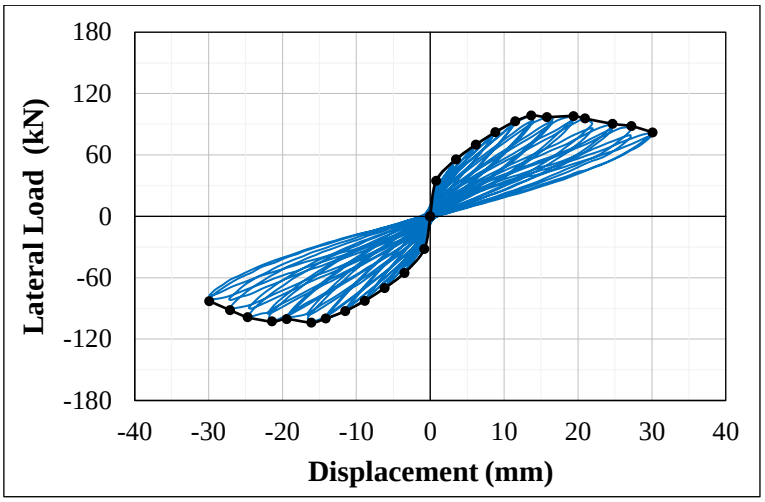

(e) Model 5 (570 mm × 950 mm)

APPENDIX C – Tables and details about the database used in Chapter 3

The main aspects of the walls studied using finite element modeling are presented in Table 41. It should be noted that:

- The bold texts indicate the parameter that differs from the reference wall 1;
- The height of the top RC beam (300 mm) is not included in the height of the walls as listed in column #3;
- The weight of the top RC beam (8.4 kN) is added to the external applied load shown in column #11;
- In column #4 the number of openings in the vertical and horizontal directions and their dimensions are given; for example, for wall 88, 3×2×(665×570) means 3 sets of openings vertically, being 2 at each horizontal level with each opening 665 mm long and 570 mm high;
- The reinforcement detail is presented in columns #12 and #13; using wall 86 as an example, the A_{sv} of 4×3Ø9.5 @1140 means that the reinforcement is distributed in 4 parts with 3 vertical cells of blocks, each containing a bar of 9.5 mm diameter, and these parts have an average spacing of 1140 mm between their centers;
- The grouting detail (columns #14 and #15) is presented with the same interpretation as the reinforcement detail;
- Almost all walls had a grouted/reinforced course immediately below the top RC beam. Walls 30 to 32 and 38 to 42 are the exceptions and so they are marked with * in column #15;
- The yield, ultimate strength and Elastic Modulus of the reinforcement are equal to 540 MPa, 742 MPa and 203.5 GPa, respectively;
- The equivalent thickness of the grouted and ungrouted masonry elements are equal to 90 and 30 mm, respectively;
- The mass densities of the concrete and masonry elements are equal to 2,400 and 2,250 kg/m^3, respectively;
- The walls without openings (1 to 58) were not modeled with intermediate RC slabs whereas the walls with opening (59 to 96) had the stories separated by intermediate RC slabs with 2 horizontal rebars of 9.5 diameter.

The main characteristics of the experimental walls studied from the literature are presented in Table 42. It should be noted that:

- The effective height presented in column #6 was used to account for different boundary conditions – single or double curvature;
- The masonry strength shown in column #10 is a weighted average value based on the net area of grouted and ungrouted blocks in the wall (CSA S304, 2014). This value was corrected using Equation 41 (Dillon and Fonseca, 2015), which normalizes the height-to-thickness ratio of prisms to 5 (BS 5628-2, 2000; AS 3700, 2011; CSA S304, 2014);
- The horizontal bars in the bond beams in the top and bottom courses were not included in the area of horizontal reinforcement listed in column #17 since their anchorage length is insufficient (Blondet et al., 1989; Shing et al., 1990);
- The average spacing of reinforcement (columns #15 and #18) and grout (columns #20 and #21) was calculated by taking the dimensions of the wall divided by the number of bars and grouts, respectively.

To be consistent, the same corrections and adjustments in the masonry strength, horizontal bars in the top and bottom bond beams, and spacing of reinforcements and grouts, were applied in both the numerical and experimental walls before analyzing the shear strength prediction equations.

Table 41: Characteristics of the walls studied using finite element modeling in Chapter 3.

#1	#2	#3	#4	#5	#6	#7	#8	#9	#10	#11	#12	#13	#14	#15	#16	#17	#18
Wall nº	l_w (mm)	h_w (mm)	Opening (mm × mm)	A_{ev} (mm²)	$A_{eh,ug}$ (mm²)	$A_{eh,g}$ (mm²)	$f'_{m,ug}$ (MPa)	$f'_{m,g}$ (MPa)	f_j (kPa)	P (kN)	A_v (Ømm @mm)	A_h (Ømm @mm)	G_v (Qty @mm)	G_h (Qty @mm)	V_{max}^- (kN)	V_{max}^+ (kN)	$V_{max,avg}$ (kN)
1	3,610	1,330	---	51,300	74,100	102,600	11.8	12.2	370	59.1	4×3Ø9.5 @1140	2×1Ø9.5 @665	4×3 @1203	2×1 @665	-124.0	134.1	129.1
2	**4,275**	1,330	---	51,300	**94,050**	102,600	11.8	12.2	370	59.1	**4×3Ø9.5 @1362**	2×1Ø9.5 @665	**4×3 @1425**	2×1 @665	-134.1	148.6	141.4
3	**3,040**	1,330	---	51,300	**57,000**	102,600	11.8	12.2	370	59.1	**4×3Ø9.5 @950**	2×1Ø9.5 @665	**4×3 @1013**	2×1 @665	-114.0	121.2	117.6
4	3,610	**1,615**	---	51,300	74,100	102,600	11.8	12.2	370	59.1	4×3Ø9.5 @1140	2×1Ø9.5 @665	4×3 @1203	2×1 @665	-119.4	120.5	120.0
5	3,610	1,330	---	51,300	74,100	102,600	**15.5**	**13.9**	**406**	59.1	4×3Ø9.5 @1140	2×1Ø9.5 @665	4×3 @1203	2×1 @665	-133.7	138.0	135.9
6	3,610	1,330	---	51,300	74,100	102,600	**19.3**	**16.5**	**453**	59.1	4×3Ø9.5 @1140	2×1Ø9.5 @665	4×3 @1203	2×1 @665	-150.0	155.0	152.5
7	3,610	1,330	---	51,300	74,100	102,600	11.8	12.2	370	**28.7**	4×3Ø9.5 @1140	2×1Ø9.5 @665	4×3 @1203	2×1 @665	-114.1	122.4	118.3
8	3,610	1,330	---	51,300	74,100	102,600	11.8	12.2	370	**89.5**	4×3Ø9.5 @1140	2×1Ø9.5 @665	4×3 @1203	2×1 @665	-134.6	144.0	139.3
9	3,610	**950**	---	**39,900**	74,100	102,600	11.8	12.2	370	**8.4**	4×3Ø9.5 @1140	---	4×3 @1203	---	-119.1	122.5	120.8
10	3,610	1,330	---	**39,900**	74,100	102,600	11.8	12.2	370	**8.4**	4×3Ø9.5 @1140	---	4×3 @1203	---	-105.5	110.0	107.8
11	3,610	1,330	---	**39,900**	**79,800**	**85,500**	11.8	12.2	370	**8.4**	**5×1Ø10 @855**	---	**5×2 @902**	---	-82.4	89.6	86.0
12	3,610	**1,805**	---	**39,900**	74,100	102,600	11.8	12.2	370	**8.4**	4×3Ø9.5 @1140	---	4×3 @1203	---	-104.7	97.3	101.0
13	3,610	**2,185**	---	**39,900**	74,100	102,600	11.8	12.2	370	**8.4**	4×3Ø9.5 @1140	---	4×3 @1203	---	-93.2	98.3	95.8
14	3,610	**2,565**	---	**39,900**	74,100	102,600	11.8	12.2	370	**8.4**	4×3Ø9.5 @1140	---	4×3 @1203	---	-96.7	97.2	97.0
15	3,610	**2,850**	---	**39,900**	74,100	102,600	11.8	12.2	370	**8.4**	4×3Ø9.5 @1140	---	4×3 @1203	---	-96.1	94.3	95.2
16	3,610	**3,230**	---	**39,900**	74,100	102,600	11.8	12.2	370	**8.4**	4×3Ø9.5 @1140	---	4×3 @1203	---	-87.6	94.3	91.0
17	3,610	**3,610**	---	**39,900**	74,100	102,600	11.8	12.2	370	**8.4**	4×3Ø9.5 @1140	---	4×3 @1203	---	-83.6	91.7	87.7
18	3,610	**3,990**	---	**39,900**	74,100	102,600	11.8	12.2	370	**8.4**	4×3Ø9.5 @1140	---	4×3 @1203	---	-85.3	81.4	83.4
19	3,610	**4,750**	---	**39,900**	74,100	102,600	11.8	12.2	370	**8.4**	4×3Ø9.5 @1140	---	4×3 @1203	---	-73.4	72.1	72.8
20	3,610	**5,510**	---	**39,900**	74,100	102,600	11.8	12.2	370	**8.4**	4×3Ø9.5 @1140	---	4×3 @1203	---	-61.3	60.1	60.7
21	3,610	**6,270**	---	**39,900**	74,100	102,600	11.8	12.2	370	**8.4**	4×3Ø9.5 @1140	---	4×3 @1203	---	-48.0	50.2	49.1
22	3,610	1,330	---	51,300	74,100	102,600	11.8	12.2	370	59.1	**4×3Ø12.7 @1140**	2×1Ø9.5 @665	4×3 @1203	2×1 @665	-134.9	146.7	140.8
23	3,610	1,330	---	51,300	**85,500**	**68,400**	11.8	12.2	370	59.1	**4×2Ø9.5 @1140**	2×1Ø9.5 @665	**4×2 @1203**	2×1 @665	-109.4	118.5	114.0
24	3,610	1,330	---	51,300	74,100	102,600	11.8	12.2	370	59.1	4×3Ø9.5 @1140	**2×1Ø12.7 @665**	4×3 @1203	2×1 @665	-124.2	134.2	129.2
25	3,610	1,330	---	**57,000**	74,100	102,600	11.8	12.2	370	59.1	4×3Ø9.5 @1140	**3×1Ø8.0 @443**	4×3 @1203	**3×1 @443**	-131.4	138.7	135.1
26	3,610	1,330	---	**57,000**	74,100	102,600	11.8	12.2	370	59.1	4×3Ø9.5 @1140	**3×1Ø9.5 @443**	4×3 @1203	**3×1 @443**	-131.1	139.1	135.1
27	3,610	1,330	---	51,300	74,100	102,600	11.8	12.2	370	59.1	4×3Ø9.5 @1140	**1×1Ø9.5 @1330**	4×3 @1203	2×1 @665	-123.9	134.0	129.0
28	3,610	1,330	---	51,300	74,100	102,600	11.8	12.2	370	59.1	4×3Ø9.5 @1140	---	4×3 @1203	2×1 @665	-120.1	133.0	126.6
29	3,610	1,330	---	**57,000**	74,100	102,600	11.8	12.2	370	59.1	4×3Ø9.5 @1140	---	4×3 @1203	**3×1 @443**	-121.8	136.8	129.3
30	3,610	1,330	---	**45,600**	74,100	102,600	11.8	12.2	370	**8.4**	4×3Ø9.5 @1140	---	4×3 @1203	**1×1 @665***	-110.3	111.7	111.0
31	3,610	1,330	---	51,300	74,100	102,600	11.8	12.2	370	**8.4**	4×3Ø9.5 @1140	---	4×3 @1203	**2×1 @443***	-115.6	114.1	114.9
32	3,610	1,330	---	**62,700**	74,100	102,600	11.8	12.2	370	**8.4**	4×3Ø9.5 @1140	---	4×3 @1203	**4×1 @266***	-112.8	121.3	117.1
33	3,610	1,330	---	**39,900**	74,100	102,600	11.8	12.2	370	59.1	4×3Ø9.5 @1140	---	4×3 @1203	---	-120.8	130.7	125.8
34	3,610	1,330	---	**39,900**	74,100	102,600	11.8	12.2	370	59.1	**4×3Ø12.7 @1140**	---	4×3 @1203	---	-131.6	142.6	137.1

#1	#2	#3	#4	#5	#6	#7	#8	#9	#10	#11	#12	#13	#14	#15	#16	#17	#18
Wall n°	l_w **(mm)**	h_w **(mm)**	**Opening (mm × mm)**	A_{ev} **(mm²)**	$A_{eh,uq}$ **(mm²)**	$A_{eh,q}$ **(mm²)**	$f'_{m,uq}$ **(MPa)**	$f'_{m,q}$ **(MPa)**	f_j **(kPa)**	P **(kN)**	A_v **(Ømm @mm)**	A_h **(Ømm @mm)**	G_v **(Qty @mm)**	G_h **(Qty @mm)**	V_{max}^- **(kN)**	V_{max}^+ **(kN)**	$V_{max,avg}$ **(kN)**
35	3,610	1,330	---	**39,900**	**79,800**	**85,500**	11.8	12.2	370	59.1	**2×1Ø16 @3420**	---	**5×2 @902**	---	-94.5	110.3	102.4
36	3,610	1,330	---	**39,900**	**79,800**	**85,500**	11.8	12.2	370	59.1	**5×1Ø10 @855**	---	**5×2 @902**	---	-102.1	111.5	106.8
37	3,610	**2,470**	---	**74,100**	74,100	102,600	11.8	12.2	370	**8.4**	4×3Ø9.5 @1140	---	4×3 @1203	---	-93.9	93.1	93.5
38	3,610	**2,470**	---	**78,900**	74,100	102,600	11.8	12.2	370	**8.4**	4×3Ø9.5 @1140	---	4×3 @1203	**1×1 @1235***	-100.8	96.3	98.6
39	3,610	**2,470**	---	**85,500**	74,100	102,600	11.8	12.2	370	**8.4**	4×3Ø9.5 @1140	---	4×3 @1203	**2×1 @823***	-101.2	100.7	101.0
40	3,610	**2,470**	---	**96,900**	74,100	102,600	11.8	12.2	370	**8.4**	4×3Ø9.5 @1140	---	4×3 @1203	**4×1 @494***	-106.3	96.5	101.4
41	3,610	**2,470**	---	**108,300**	74,100	102,600	11.8	12.2	370	**8.4**	4×3Ø9.5 @1140	---	4×3 @1203	**6×1 @353***	-105.6	103.5	104.6
42	3,610	**2,470**	---	**119,700**	74,100	102,600	11.8	12.2	370	**8.4**	4×3Ø9.5 @1140	---	4×3 @1203	**8×1 @274***	-107.9	102.5	105.2
43	3,610	**2,760**	---	**105,600**	74,100	102,600	11.8	12.2	370	59.1	4×3Ø9.5 @1140	**4×1Ø9.5 @690**	4×3 @1203	**4×1 @690**	-120.7	114.1	117.4
44	3,610	**2,760**	---	**105,600**	74,100	102,600	**15.5**	**13.9**	**406**	59.1	4×3Ø9.5 @1140	**4×1Ø9.5 @690**	4×3 @1203	**4×1 @690**	-140.2	130.7	135.5
45	3,610	**2,760**	---	**105,600**	74,100	102,600	11.8	12.2	370	**28.7**	4×3Ø9.5 @1140	**4×1Ø9.5 @690**	4×3 @1203	**4×1 @690**	-110.7	101.4	106.1
46	3,610	**2,760**	---	**82,800**	74,100	102,600	11.8	12.2	370	**8.4**	4×3Ø9.5 @1140	---	4×3 @1203	---	-93.8	97.8	95.8
47	3,610	**2,760**	---	**105,600**	74,100	102,600	11.8	12.2	370	59.1	**4×3Ø12.7 @1140**	**4×1Ø9.5 @690**	4×3 @1203	**4×1 @690**	-137.4	130.2	133.8
48	3,610	**2,760**	---	**105,600**	74,100	102,600	11.8	12.2	370	59.1	4×3Ø9.5 @1140	**4×1Ø12.7 @690**	4×3 @1203	**4×1 @690**	-123.0	112.7	117.9
49	3,610	**2,760**	---	**82,800**	74,100	102,600	11.8	12.2	370	59.1	4×3Ø9.5 @1140	---	4×3 @1203	---	-111.4	106.1	108.8
50	3,610	**2,760**	---	**82,800**	74,100	102,600	11.8	12.2	370	59.1	**4×3Ø12.7 @1140**	---	4×3 @1203	---	-120.1	117.6	118.9
51	3,610	**4,190**	---	**159,900**	74,100	102,600	11.8	12.2	370	59.1	4×3Ø9.5 @1140	**6×1Ø9.5 @698**	4×3 @1203	**6×1 @698**	-103.2	108.1	105.7
52	3,610	**4,190**	---	**159,900**	74,100	102,600	**19.3**	**16.5**	**453**	59.1	4×3Ø9.5 @1140	**6×1Ø9.5 @698**	4×3 @1203	**6×1 @698**	-141.5	134.2	137.9
53	3,610	**4,190**	---	**159,900**	74,100	102,600	11.8	12.2	370	**89.5**	4×3Ø9.5 @1140	**6×1Ø9.5 @698**	4×3 @1203	**6×1 @698**	-113.3	108.6	111.0
54	3,610	**4,190**	---	**125,700**	74,100	102,600	11.8	12.2	370	**8.4**	4×3Ø9.5 @1140	---	4×3 @1203	---	-91.3	85.5	88.4
55	3,610	**4,190**	---	**159,900**	74,100	102,600	11.8	12.2	370	59.1	**4×2Ø9.5 @1140**	**6×1Ø9.5 @698**	**4×2 @1203**	**6×1 @698**	-89.6	88.6	89.1
56	3,610	**4,190**	---	**177,000**	74,100	102,600	11.8	12.2	370	59.1	4×3Ø9.5 @1140	**9×1Ø9.5 @465**	4×3 @1203	**9×1 @465**	-108.0	104.4	106.2
57	3,610	**4,190**	---	**125,700**	74,100	102,600	11.8	12.2	370	59.1	4×3Ø9.5 @1140	---	4×3 @1203	---	-91.2	82.9	87.1
58	3,610	**4,190**	---	**125,700**	74,100	102,600	11.8	12.2	370	59.1	**4×3Ø12.7 @1140**	---	4×3 @1203	---	-100.8	95.1	98.0
59	3,610	1,330	**1×1×(570×570)**	51,300	**57,000**	102,600	11.8	12.2	370	59.1	4×3Ø9.5 @1140	2×1Ø9.5 @665	4×3 @1203	2×1 @665	-114.7	120.9	117.8
60	3,610	1,330	**1×1×(1,140×570)**	51,300	**39,900**	102,600	11.8	12.2	370	59.1	4×3Ø9.5 @1140	2×1Ø9.5 @665	4×3 @1203	2×1 @665	-106.0	111.1	108.6
61	3,610	1,330	**1×2×(665×570)**	51,300	**34,200**	102,600	11.8	12.2	370	59.1	**6×2Ø9.5 @684**	2×1Ø9.5 @665	**6×2 @722**	2×1 @665	-98.7	105.0	101.9
62	**4,275**	1,330	**1×1×(1,045×570)**	51,300	**62,700**	102,600	11.8	12.2	370	59.1	**4×3Ø9.5 @1362**	2×1Ø9.5 @665	**4×3 @1425**	2×1 @665	-114.3	125.6	120.0
63	**3,040**	1,330	**1×1×(570×570)**	51,300	**39,900**	102,600	11.8	12.2	370	59.1	**4×3Ø9.5 @950**	2×1Ø9.5 @665	**4×3 @1013**	2×1 @665	-106.9	107.5	107.2
64	3,610	1,330	**1×1×(570×1,045)**	51,300	**57,000**	102,600	11.8	12.2	370	59.1	4×3Ø9.5 @1140	2×1Ø9.5 @665	4×3 @1203	2×1 @665	-108.4	113.4	110.9
65	3,610	1,330	**1×1×(1,140×1,045)**	51,300	**39,900**	102,600	11.8	12.2	370	59.1	4×3Ø9.5 @1140	2×1Ø9.5 @665	4×3 @1203	2×1 @665	-94.6	102.0	98.3
66	3,610	1,330	**1×2×(665×1,045)**	51,300	**34,200**	102,600	11.8	12.2	370	59.1	**6×2Ø9.5 @684**	2×1Ø9.5 @665	**6×2 @722**	2×1 @665	-92.1	96.6	94.4
67	3,610	1,330	**1×1×(665×1,045) 1×1×(665×570)**	**39,900**	**34,200**	102,600	11.8	12.2	370	59.1	**6×2Ø9.5 @684**	2×1Ø9.5 @665	**6×2 @722**	2×1 @665	-92.0	101.6	96.8
68	**4,275**	1,330	**1×1×(1,045×1,045)**	**39,900**	**62,700**	102,600	11.8	12.2	370	59.1	4×3Ø9.5 @1140	2×1Ø9.5 @665	4×3 @1203	2×1 @665	-112.6	116.9	114.8

#1	#2	#3	#4	#5	#6	#7	#8	#9	#10	#11	#12	#13	#14	#15	#16	#17	#18
Wall n°	l_w **(mm)**	h_w **(mm)**	**Opening (mm × mm)**	A_{ev} **(mm²)**	$A_{eh,uq}$ **(mm²)**	$A_{eh,q}$ **(mm²)**	$f'_{m,uq}$ **(MPa)**	$f'_{m,q}$ **(MPa)**	f_j **(kPa)**	P **(kN)**	A_v **(Ømm @mm)**	A_h **(Ømm @mm)**	G_v **(Qty @mm)**	G_h **(Qty @mm)**	V_{max}^- **(kN)**	V_{max}^+ **(kN)**	$V_{max,avg}$ **(kN)**
69	**3,040**	1,330	**1×1×(570×1,045)**	**39,900**	**39,900**	102,600	11.8	12.2	370	59.1	4×3Ø9.5 @1140	2×1Ø9.5 @665	4×3 @1203	2×1 @665	-92.9	101.1	97.0
70	3,610	1,330	**1×1×(570×570)**	**39,900**	**57,000**	102,600	**19.3**	**16.5**	**453**	59.1	4×3Ø9.5 @1140	2×1Ø9.5 @665	4×3 @1203	2×1 @665	-133.4	138.9	136.2
71	3,610	1,330	**1×1×(570×570)**	**39,900**	**57,000**	102,600	11.8	12.2	370	**89.5**	4×3Ø9.5 @1140	2×1Ø9.5 @665	4×3 @1203	2×1 @665	-116.4	127.2	121.8
72	3,610	1,330	**1×1×(760×570)**	**39,900**	**62,700**	**68,400**	11.8	12.2	370	59.1	**4×2Ø9.5 @1140**	2×1Ø9.5 @665	**4×2 @1203**	2×1 @665	-93.2	100.3	96.8
73	3,610	1,330	**1×1×(570×570)**	**39,900**	**57,000**	102,600	11.8	12.2	370	59.1	4×3Ø9.5 @1140	**3×1Ø9.5 @443**	4×3 @1203	**3×1 @443**	-116.3	126.9	121.6
74	3,610	1,330	**1×1×(570×570)**	**39,900**	**57,000**	102,600	11.8	12.2	370	59.1	4×3Ø9.5 @1140	---	4×3 @1203	---	-110.8	116.4	113.6
75	3,610	**2,760**	**2×1×(570×570)**	**39,900**	**57,000**	102,600	11.8	12.2	370	59.1	4×3Ø9.5 @1140	**4×1Ø9.5 @690**	4×3 @1203	**4×1 @690**	-105.4	112.2	108.8
76	3,610	**2,760**	**2×1×(1,140×570)**	**39,900**	**39,900**	102,600	11.8	12.2	370	59.1	4×3Ø9.5 @1140	**4×1Ø9.5 @690**	4×3 @1203	**4×1 @690**	-104.5	106.0	105.3
77	3,610	**2,760**	**2×2×(665×570)**	**39,900**	**34,200**	102,600	11.8	12.2	370	59.1	**6×2Ø9.5 @684**	**4×1Ø9.5 @690**	**6×2 @722**	**4×1 @690**	-99.4	99.7	99.6
78	3,610	**2,760**	**2×1×(570×1,045)**	**39,900**	**57,000**	102,600	11.8	12.2	370	59.1	4×3Ø9.5 @1140	**4×1Ø9.5 @690**	4×3 @1203	**4×1 @690**	-97.8	105.2	101.5
79	3,610	**2,760**	**2×1×(1,140×1,045)**	**39,900**	**39,900**	102,600	11.8	12.2	370	59.1	4×3Ø9.5 @1140	**4×1Ø9.5 @690**	4×3 @1203	**4×1 @690**	-93.3	93.9	93.6
80	3,610	**2,760**	**2×2×(665×1,045)**	51,300	**34,200**	102,600	11.8	12.2	370	59.1	**6×2Ø9.5 @684**	**4×1Ø9.5 @690**	**6×2 @722**	**4×1 @690**	-84.4	85.1	84.8
81	3,610	**2,760**	**2×1×(665×1,045) 2×1×(665×570)**	51,300	**34,200**	102,600	11.8	12.2	370	59.1	**6×2Ø9.5 @684**	**4×1Ø9.5 @690**	**6×2 @722**	**4×1 @690**	-92.1	93.2	92.7
82	3,610	**2,760**	**2×1×(570×570)**	51,300	**57,000**	102,600	**19.3**	**16.5**	**453**	59.1	4×3Ø9.5 @1140	**4×1Ø9.5 @690**	4×3 @1203	**4×1 @690**	-135.6	138.3	137.0
83	3,610	**2,760**	**2×1×(570×570)**	57,000	**57,000**	102,600	11.8	12.2	370	**89.5**	4×3Ø9.5 @1140	**4×1Ø9.5 @690**	4×3 @1203	**4×1 @690**	-111.8	118.2	115.0
84	3,610	**2,760**	**2×1×(760×570)**	51,300	**62,700**	**68,400**	11.8	12.2	370	59.1	**4×2Ø9.5 @1140**	**4×1Ø9.5 @690**	**4×2 @1203**	**4×1 @690**	-86.1	90.5	88.3
85	3,610	**2,760**	**2×1×(570×570)**	51,300	**57,000**	102,600	11.8	12.2	370	59.1	4×3Ø9.5 @1141	**4×1Ø12.7 @690**	4×3 @1203	**4×1 @690**	-110.2	112.9	111.6
86	3,610	**4,190**	**3×1×(570×570)**	**57,000**	**57,000**	102,600	11.8	12.2	370	59.1	4×3Ø9.5 @1140	**6×1Ø9.5 @698**	4×3 @1203	**6×1 @698**	-102.6	104.2	103.4
87	3,610	**4,190**	**3×1×(1,140×570)**	**45,600**	**39,900**	102,600	11.8	12.2	370	59.1	4×3Ø9.5 @1140	**6×1Ø9.5 @698**	4×3 @1203	**6×1 @698**	-97.7	96.8	97.3
88	3,610	**4,190**	**3×2×(665×570)**	**51,300**	**34,200**	102,600	11.8	12.2	370	59.1	**6×2Ø9.5 @684**	**6×1Ø9.5 @698**	**6×2 @722**	**6×1 @698**	-95.5	98.9	97.2
89	3,610	**4,190**	**3×1×(570×1,045)**	**62,700**	**57,000**	102,600	11.8	12.2	370	59.1	4×3Ø9.5 @1140	**6×1Ø9.5 @698**	4×3 @1203	**6×1 @698**	-99.1	98.5	98.8
90	3,610	**4,190**	**3×1×(1,140×1,045)**	**39,900**	**39,900**	102,600	11.8	12.2	370	59.1	4×3Ø9.5 @1140	**6×1Ø9.5 @698**	4×3 @1203	**6×1 @698**	-92.2	93.1	92.7
91	3,610	**4,190**	**3×2×(665×1,045)**	**39,900**	**34,200**	102,600	11.8	12.2	370	59.1	**6×2Ø9.5 @684**	**6×1Ø9.5 @698**	**6×2 @722**	**6×1 @698**	-85.6	80.2	82.9
92	3,610	**4,190**	**3×1×(665×1,045) 3×1×(665×570)**	**39,900**	**34,200**	102,600	11.8	12.2	370	59.1	**6×2Ø9.5 @684**	**6×1Ø9.5 @698**	**6×2 @722**	**6×1 @698**	-87.9	86.8	87.4
93	3,610	**4,190**	**3×1×(570×570)**	**39,900**	**57,000**	102,600	**19.3**	**16.5**	**453**	59.1	4×3Ø9.5 @1140	**6×1Ø9.5 @698**	4×3 @1203	**6×1 @698**	-128.5	129.9	129.2
94	3,610	**4,190**	**3×1×(570×570)**	**74,100**	**57,000**	102,600	11.8	12.2	370	**109.8**	4×3Ø9.5 @1140	**6×1Ø9.5 @698**	4×3 @1203	**6×1 @698**	-110.4	114.3	112.4
95	3,610	**4,190**	**3×1×(760×570)**	**78,900**	**62,700**	**68,400**	11.8	12.2	370	59.1	**4×2Ø9.5 @1140**	**6×1Ø9.5 @698**	**4×2 @1203**	**6×1 @698**	-83.7	81.9	82.8
96	3,610	**4,190**	**3×1×(570×570)**	**85,500**	**57,000**	102,600	11.8	12.2	370	59.1	4×3Ø9.5 @1141	**9×1Ø9.5 @465**	4×3 @1203	**9×1 @465**	-108.8	106.5	107.7

Source: Author.

Table 42: Characteristics of the experimental walls studied from the literature in Chapter 3.

#1	#2	#3	#4	#5	#6	#7	#8	#9	#10	#11	#12	#13	#14	#15	#16	#17	#18	#19	#20	#21	#22
Research	**Wall ID**	**Wall n°**	l_w (mm)	h_w (mm)	h_e (mm)	b_w (mm)	A_{ev} (mm²)	A_{eh} (mm²)	f'_m (MPa)	f_{mt} (kPa)	P (kN)	A_{vi} (mm²)	A_{vf} (mm²)	$s_{v,avg}$ (mm)	f_{yv} (MPa)	A_h (mm²)	$s_{h,avg}$ (mm)	f_{yh} (MPa)	$s_{gv,avg}$ (mm)	$s_{gh,avg}$ (mm)	$V_{max,avg}$ (kN)
Meli et al. (1968)	309	1	3,200	2,650	2,650	150	134,620	297,968	10.6	25.8	0.0	213	1016	650	245	58.9	410	245	800	---	189.0
	310	2	3,200	2,650	2,650	150	134,620	297,968	**10.3**	**23.8**	**196.0**	213	1016	650	245	58.9	410	245	800	---	241.0
	312	3	3,200	2,650	2,650	150	134,620	**259,280**	**9.2**	**15.7**	0.0	**71**	**508**	1,300	245	58.9	410	245	**1,600**	---	102.0
	313	4	3,200	2,650	2,650	150	134,620	**259,280**	**10.3**	**22.8**	0.0	**71**	**508**	1,300	245	58.9	410	245	**1,600**	---	118.0
	314	5	3,200	2,650	2,650	150	134,620	297,968	**10.1**	**21.4**	**98.1**	213	1016	**650**	245	---	---	---	800	---	250.0
	315	6	3,200	2,650	2,650	150	134,620	**259,280**	**10.2**	**22.0**	0.0	**71**	**508**	**1,300**	245	---	---	---	**1,600**	---	92.0
	316	7	3,200	2,650	2,650	150	134,620	297,968	**9.3**	**16.1**	**196.0**	213	1016	650	245	58.9	410	245	800	---	262.0
	317	8	3,200	2,650	2,650	150	134,620	297,968	**10.0**	**21.5**	0.0	213	1016	650	245	58.9	410	245	800	---	241.0
	318	9	3,200	2,650	2,650	150	134,620	297,968	**10.4**	**21.7**	0.0	213	1016	650	245	58.9	410	245	800	---	204.0
Schultz (1996)	1	10	2,845	1,422	711	195	120,597	242,283	13.9	21.7	267.0	0	1136	2,462	414	142.0	1,422	414	2,845	---	245.0
	3	11	**2,032**	1,422	711	195	120,597	**187,486**	**14.0**	21.7	**191.0**	0	1136	**1,829**	414	142.0	1,422	414	**2,032**	---	187.0
	5	12	**1,422**	1,422	711	195	120,597	**146,372**	**14.0**	21.7	**133.0**	0	1136	**1,219**	414	142.0	1,422	414	**1,422**	---	133.0
	7	13	2,845	1,422	711	195	120,597	242,283	13.9	21.7	266.0	0	1136	2,642	414	**329.0**	1,422	414	2,845	---	240.0
	9	14	**2,032**	1,422	711	195	120,597	**187,486**	**14.0**	21.7	**177.0**	0	1136	**1,829**	414	**329.0**	1,422	414	**2,032**	---	192.0
	11	15	**1,422**	1,422	711	195	120,597	**146,372**	**14.0**	21.7	**132.0**	0	1136	**1,219**	414	**329.0**	1,422	414	**1,422**	---	154.0
Minaie et al. (2010)	PCL1	16	3,861	2,640	2,640	195	218,499	348,487	9.4	25.8	243.9	568	568	1,219	439	284.0	2,642	414	1,287	1,321	315.0
	MC1	17	3,861	2,640	2,640	195	218,499	348,487	**7.2**	**12.6**	243.9	568	568	1,219	439	284.0	2,642	414	1,287	1,321	183.6
	PCL2	18	3,861	2,640	**1,320**	195	218,499	348,487	9.4	25.8	**0.0**	568	568	1,219	439	284.0	2,642	414	1,287	1,321	240.7
	MC2	19	3,861	2,640	**1,320**	195	218,499	348,487	**7.2**	**12.6**	**0.0**	568	568	1,219	439	284.0	2,642	414	1,287	1,321	227.3
Elmapruk and Elgawady (2010)	PG127-48	20	2,631	1,524	1,524	195	147,522	244,563	15.5	14.9	48.9	568	1136	1,219	427	200.0	1,524	452	1,316	762	238.0
	PG127-48I	21	2,631	1,524	1,524	195	147,522	244,563	15.5	14.9	48.9	568	1136	1,219	427	200.0	1,524	452	1,316	762	252.0
	PG180-48	22	2,631	1,524	1,524	195	147,522	244,563	15.5	14.9	48.9	568	1136	1,219	427	**284.0**	1,524	**427**	1,316	762	246.0
	PG254-48	23	2,631	1,524	1,524	195	147,522	244,563	15.5	14.9	48.9	568	1136	1,219	427	**400.0**	1,524	452	1,316	762	286.0
	PG127-32	24	2,631	1,524	1,524	195	147,522	**270,395**	**15.9**	14.9	48.9	568	1136	**813**	427	200.0	1,524	452	**658**	762	344.0
	PG127-24	25	2,631	1,524	1,524	195	147,522	**296,227**	**16.3**	14.9	48.9	**600**	1136	**610**	427	200.0	1,524	452	**658**	762	400.0
Nolph and Elgawady (2012)	PG085-48	26	2,631	2,337	2,337	195	199,228	244,563	11.6	15.0	49.3	774	1548	1,219	439	200.0	2,337	439	1,316	1,169	221.8
	PG120-48	27	2,631	2,337	2,337	195	199,228	244,563	11.6	15.0	49.3	774	1548	1,219	439	**284.0**	2,337	439	1,316	1,169	227.7
	PG169-48	28	2,631	2,337	2,337	195	199,228	244,563	11.6	15.0	49.3	774	1548	1,219	439	**400.0**	2,337	439	1,316	1,169	202.9
	PG085-32	29	2,631	2,337	2,337	195	199,228	**270,395**	**12.2**	15.0	49.3	**1136**	**1136**	**813**	439	200.0	2,337	439	**877**	1,169	260.0
	PG085-24	30	2,631	2,337	2,337	195	199,228	**296,227**	**12.8**	15.0	49.3	**1200**	**1136**	**610**	439	200.0	2,337	439	**658**	1,169	295.0
Hoque and Lissel (2013)	1A	31	1,800	1,800	900	190	175,008	202,883	16.6	5.7	410.1	200	400	800	450	200.0	1,800	450	900	900	209.3
	1B	32	1,800	1,800	900	190	175,008	202,883	16.6	5.7	**409.0**	200	400	800	450	200.0	1,800	450	900	900	226.4
	2A	33	1,800	1,800	900	190	175,008	202,883	16.6	5.7	**431.7**	200	400	800	450	200.0	1,800	450	900	900	252.4
	2B	34	1,800	1,800	900	190	175,008	202,883	16.6	5.7	**411.3**	200	400	800	450	200.0	1,800	450	900	900	228.6

#1	#2	#3	#4	#5	#6	#7	#8	#9	#10	#11	#12	#13	#14	#15	#16	#17	#18	#19	#20	#21	#22
Research	**Wall ID**	**Wall n°**	l_w (mm)	h_w (mm)	h_e (mm)	b_w (mm)	A_{ev} (mm²)	A_{eh} (mm²)	f'_m (MPa)	f_{mt} (kPa)	P (kN)	A_{vi} (mm²)	A_{vf} (mm²)	$s_{v,avg}$ (mm)	f_{yv} (MPa)	A_h (mm²)	$s_{h,avg}$ (mm)	f_{yh} (MPa)	$s_{qv,avg}$ (mm)	$s_{qh,\ avg}$ (mm)	$V_{max,avg}$ (kN)
	3A	35	1,800	1,800	900	190	175,008	202,883	16.6	5.7	**422.7**	200	400	800	450	200.0	1,800	450	900	900	242.5
	3B	36	1,800	1,800	900	190	175,008	202,883	16.6	5.7	**417.6**	200	400	800	450	200.0	1,800	450	900	900	236.0
	4A	37	1,800	1,800	900	190	175,008	202,883	16.6	5.7	**413.3**	200	400	800	450	**400.0**	**900**	450	900	**600**	215.9
	4B	38	1,800	1,800	900	190	175,008	202,883	16.6	5.7	**421.1**	200	400	800	450	**400.0**	**900**	450	900	**600**	240.7
	4C	39	1,800	1,800	900	190	175,008	202,883	16.6	5.7	**409.0**	200	400	800	450	**400.0**	**900**	450	900	**600**	190.7
	5A	40	1,800	1,800	900	190	**130,320**	202,883	16.6	5.7	**409.0**	200	400	800	450	**86.0**	**450**	**521**	900	---	206.5
	5B	41	1,800	1,800	900	190	**130,320**	202,883	16.6	5.7	**409.0**	200	400	800	450	**86.0**	**450**	**521**	900	---	213.3
	6A	42	1,800	1,800	900	190	**130,320**	202,883	16.6	5.7	**409.0**	200	400	800	450	**86.0**	**450**	**521**	900	---	203.5
	6B	43	1,800	1,800	900	190	**130,320**	202,883	16.6	5.7	**409.0**	200	400	800	450	**86.0**	**450**	**521**	900	---	211.4
	7A	44	1,800	1,800	900	190	**130,320**	202,883	16.6	5.7	**409.0**	200	400	800	450	**86.0**	**450**	**521**	900	---	176.7
	7B	45	1,800	1,800	900	190	**130,320**	202,883	16.6	5.7	**409.0**	200	400	800	450	**86.0**	**450**	**521**	900	---	185.4
Rizaee and Lissel (2015)	1A	46	1,800	1,800	900	190	179,552	202,883	14.5	22.1	432.0	200	400	800	448	200.0	1,800	448	900	900	252.5
	2A	47	1,800	1,800	900	190	179,552	202,883	14.5	22.1	**476.0**	200	400	800	448	200.0	1,800	448	900	900	301.5
	3B	48	1,800	1,800	900	190	179,552	202,883	14.5	22.1	**484.0**	200	400	800	448	200.0	1,800	448	900	900	311.0
	4B	49	1,800	1,800	900	190	179,552	202,883	14.5	22.1	**482.0**	200	400	800	448	200.0	1,800	448	900	900	308.0
	5C	50	1,800	1,800	900	190	179,552	202,883	**17.4**	**9.5**	**409.0**	200	400	800	448	**100.0**	1,800	**456**	900	900	224.0
	6C	51	1,800	1,800	900	190	179,552	202,883	**17.4**	**9.5**	**409.0**	200	400	800	448	**100.0**	1,800	**456**	900	900	203.0
	7D	52	1,800	1,800	900	190	179,552	202,883	**17.4**	**11.5**	**409.0**	200	400	800	448	**100.0**	1,800	**456**	900	900	226.0
	8D	53	1,800	1,800	900	190	179,552	202,883	**17.4**	**11.5**	**409.0**	200	400	800	448	**100.0**	1,800	**456**	900	900	220.0
	9E	54	1,800	1,800	900	190	179,552	202,883	**17.4**	**11.0**	**409.0**	200	400	800	448	**100.0**	1,800	**456**	900	900	220.0
	10E	55	1,800	1,800	900	190	179,552	202,883	**17.4**	**11.0**	**409.0**	200	400	800	448	**100.0**	1,800	**456**	900	900	199.0
	11F	56	1,800	1,800	900	190	179,552	202,883	**11.6**	**9.3**	**409.0**	200	400	800	448	200.0	**900**	448	900	600	196.0
	12F	57	1,800	1,800	900	190	179,552	202,883	**11.6**	**9.3**	**409.0**	200	400	800	448	200.0	**900**	448	900	600	208.0
	13G	58	1,800	1,800	900	190	179,552	202,883	**11.6**	**11.6**	**409.0**	200	400	800	448	**100.0**	1,800	**456**	900	900	195.0
	14G	59	1,800	1,800	900	190	179,552	202,883	**11.6**	**11.6**	**409.0**	200	400	800	448	**100.0**	1,800	**456**	900	900	218.0

Source: Author.

APPENDIX D – Factored contribution of the proposed shear equation

Table 43: Factored contribution of the proposed shear equation for the numerical dataset.

Wall nº	$k_{gv}k_{gh}V_m$		V_p		V_{rv}		V_{rh}		V_n (kN)
	(kN)	(%V_n)	(kN)	(%V_n)	(kN)	(%V_n)	(kN)	(%V_n)	
1	345.6	58.4	101.9	17.2	132.9	22.5	11.1	1.9	591.5
2	366.3	57.7	124.7	19.6	132.8	20.9	11.1	1.7	634.8
3	319.4	58.3	84.7	15.5	133.0	24.3	11.1	2.0	548.2
4	311.9	57.8	83.9	15.5	132.9	24.6	11.1	2.1	539.8
5	380.3	59.0	105.4	16.4	146.2	22.7	12.2	1.9	644.1
6	418.8	59.6	109.7	15.6	161.1	22.9	13.4	1.9	703.0
7	345.6	64.0	50.2	9.3	132.9	24.6	11.1	2.1	539.8
8	345.6	54.0	150.3	23.5	132.9	20.8	11.1	1.7	639.8
9	362.3	70.2	21.0	4.1	132.9	25.7	0.0	0.0	516.2
10	325.8	68.8	15.0	3.2	132.9	28.1	0.0	0.0	473.7
11	304.5	79.6	16.5	4.3	61.3	16.0	0.0	0.0	382.3
12	290.1	66.8	11.0	2.5	132.9	30.6	0.0	0.0	434.0
13	281.2	66.4	9.1	2.2	132.9	31.4	0.0	0.0	423.2
14	272.3	65.9	7.8	1.9	132.9	32.2	0.0	0.0	413.0
15	265.7	65.5	7.0	1.7	132.9	32.8	0.0	0.0	405.5
16	256.8	64.9	6.1	1.6	132.9	33.6	0.0	0.0	395.8
17	247.9	64.2	5.5	1.4	132.9	34.4	0.0	0.0	386.3
18	221.7	61.7	5.0	1.4	132.9	37.0	0.0	0.0	359.5
19	174.2	56.0	4.2	1.3	132.9	42.7	0.0	0.0	311.3
20	126.7	48.1	3.6	1.4	132.9	50.5	0.0	0.0	263.2
21	79.2	36.8	3.1	1.5	132.9	61.7	0.0	0.0	215.2
22	345.6	50.5	90.4	13.2	237.5	34.7	11.1	1.6	684.6
23	300.3	59.5	105.2	20.8	88.4	17.5	11.0	2.2	504.9
24	345.6	57.9	101.9	17.1	132.9	22.3	16.0	2.7	596.4
25	356.0	58.7	101.9	16.8	132.9	21.9	15.7	2.6	606.5
26	356.0	58.5	101.9	16.7	132.9	21.8	17.8	2.9	608.6
27	345.6	59.5	101.9	17.6	132.9	22.9	0.0	0.0	580.4
28	345.6	59.5	101.9	17.6	132.9	22.9	0.0	0.0	580.4
29	356.0	60.3	101.9	17.3	132.9	22.5	0.0	0.0	590.8
30	345.6	70.0	14.9	3.0	132.9	26.9	0.0	0.0	493.4
31	356.0	70.7	14.9	3.0	132.9	26.4	0.0	0.0	503.8
32	369.2	71.4	14.9	2.9	132.9	25.7	0.0	0.0	516.9
33	325.8	58.1	102.0	18.2	132.9	23.7	0.0	0.0	560.7
34	325.8	49.8	90.5	13.8	237.5	36.3	0.0	0.0	653.8
35	304.5	62.4	120.4	24.7	62.8	12.9	0.0	0.0	487.7
36	304.5	64.0	110.1	23.1	61.3	12.9	0.0	0.0	475.9
37	274.5	66.1	8.0	1.9	132.9	32.0	0.0	0.0	415.4
38	277.8	66.3	8.0	1.9	132.9	31.7	0.0	0.0	418.7
39	286.6	67.0	8.0	1.9	132.9	31.1	0.0	0.0	427.4
40	297.6	67.9	8.0	1.8	132.9	30.3	0.0	0.0	438.5
41	304.9	68.4	8.0	1.8	132.9	29.8	0.0	0.0	445.8
42	310.4	68.8	8.0	1.8	132.9	29.4	0.0	0.0	451.3
43	283.2	56.9	48.9	9.8	132.9	26.7	33.0	6.6	498.0
44	311.7	57.2	50.2	9.2	146.2	26.9	36.3	6.7	544.5
45	283.2	59.9	24.1	5.1	132.9	28.1	33.0	7.0	473.2
46	267.8	65.7	7.2	1.8	132.9	32.6	0.0	0.0	407.8
47	283.2	47.4	43.4	7.3	237.5	39.8	33.0	5.5	597.1
48	283.2	56.9	48.9	9.8	132.9	26.7	33.0	6.6	498.0

Wall nº	$k_{gv}k_{gh}V_m$		V_p		V_{rv}		V_{rh}		V_n
	(kN)	(%V_n)	(kN)	(%V_n)	(kN)	(%V_n)	(kN)	(%V_n)	(kN)
49	267.8	59.6	48.9	10.9	132.9	29.6	0.0	0.0	449.6
50	267.8	48.8	43.4	7.9	237.5	43.3	0.0	0.0	548.7
51	221.1	50.7	32.1	7.4	132.9	30.5	50.0	11.5	436.0
52	267.9	51.1	34.6	6.6	161.1	30.7	60.6	11.6	524.1
53	221.1	49.0	47.2	10.5	132.9	29.5	50.0	11.1	451.2
54	209.2	60.3	4.7	1.4	132.9	38.3	0.0	0.0	346.8
55	221.1	56.3	32.9	8.4	88.6	22.6	50.0	12.7	392.5
56	227.8	50.9	31.7	7.1	132.9	29.7	55.3	12.4	447.7
57	209.2	56.0	31.8	8.5	132.9	35.5	0.0	0.0	373.8
58	209.2	44.0	28.5	6.0	237.5	50.0	0.0	0.0	475.1

Source: Author.

Table 44: Factored contribution of the proposed shear equation for the experimental dataset.

Research	Wall nº	$k_{gv}k_{gh}V_m$		V_p		V_{rv}		V_{rh}		V_n
		(kN)	(%V_n)	(kN)	(%V_n)	(kN)	(%V_n)	(kN)	(%V_n)	(kN)
Meli et al. (1968)	1	168.6	89.1	0.0	0.0	19.6	10.4	0.9	0.5	189.1
	2	166.2	75.4	34.1	15.5	19.3	8.8	0.9	0.4	220.5
	3	103.0	91.6	0.0	0.0	8.6	7.6	0.9	0.8	112.5
	4	109.0	91.6	0.0	0.0	9.1	7.6	0.9	0.8	119.0
	5	164.6	82.0	17.1	8.5	19.1	9.5	0.0	0.0	200.8
	6	108.5	92.3	0.0	0.0	9.1	7.7	0.0	0.0	117.5
	7	157.9	74.8	34.1	16.1	18.4	8.7	0.9	0.4	211.2
	8	163.7	89.1	0.0	0.0	19.0	10.4	0.9	0.5	183.7
	9	167.0	89.1	0.0	0.0	19.4	10.4	0.9	0.5	187.3
Schultz (1996)	10	134.4	53.6	76.9	30.7	35.1	14.0	4.4	1.7	250.8
	11	115.1	59.3	39.3	20.3	35.2	18.1	4.4	2.3	194.0
	12	93.3	61.4	19.2	12.6	35.2	23.1	4.4	2.9	152.0
	13	134.4	53.0	76.6	30.2	35.1	13.8	7.4	2.9	253.6
	14	115.1	59.3	36.4	18.8	35.2	18.1	7.5	3.8	194.1
	15	93.3	60.2	19.0	12.3	35.2	22.7	7.5	4.8	155.0
Minaie et al. (2010)	16	172.0	65.9	51.4	19.7	30.6	11.7	7.2	2.8	261.2
	17	150.6	64.1	51.4	21.9	26.8	11.4	6.3	2.7	235.0
	18	209.9	84.7	0.0	0.0	30.6	12.3	7.2	2.9	247.7
	19	183.7	84.7	0.0	0.0	26.8	12.3	6.3	2.9	216.8
Elmapruk and Elgawady (2010)	20	165.0	70.1	6.1	2.6	57.3	24.3	7.1	3.0	235.5
	21	165.0	70.1	6.1	2.6	57.3	24.3	7.1	3.0	235.5
	22	165.0	69.3	6.1	2.6	57.3	24.1	9.5	4.0	237.9
	23	165.0	69.1	6.1	2.5	57.3	24.0	10.5	4.4	238.8
	24	240.0	77.1	6.1	2.0	58.0	18.6	7.2	2.3	311.3
	25	266.2	78.4	6.1	1.8	59.9	17.6	7.3	2.2	339.4
Nolph and Elgawady (2012)	26	125.7	60.1	8.0	3.8	69.4	33.2	6.0	2.9	209.1
	27	125.7	59.4	8.0	3.8	69.4	32.8	8.5	4.0	211.6
	28	125.7	58.4	8.0	3.7	69.4	32.3	11.9	5.5	215.0
	29	167.4	66.6	8.0	3.2	69.7	27.7	6.1	2.4	251.2
	30	207.7	70.3	8.0	2.7	73.4	24.8	6.3	2.1	295.3
Hoque and Lissel (2013)	31	166.7	65.3	59.1	23.2	22.0	8.6	7.3	2.9	255.1
	32	166.7	65.4	58.9	23.1	22.0	8.6	7.3	2.9	254.9
	33	166.7	64.6	62.2	24.1	22.0	8.5	7.3	2.8	258.2
	34	166.7	65.3	59.2	23.2	22.0	8.6	7.3	2.9	255.3
	35	166.7	64.9	60.9	23.7	22.0	8.6	7.3	2.9	256.9
	36	166.7	65.1	60.1	23.5	22.0	8.6	7.3	2.9	256.2

Research	Wall nº	$k_{gv}k_{gh}V_m$		V_p		V_{rv}		V_{rh}		V_n
		(kN)	($\%V_n$)	(kN)	($\%V_n$)	(kN)	($\%V_n$)	(kN)	($\%V_n$)	(kN)
Rizaee and Lissel (2015)	37	171.6	64.5	59.5	22.4	22.0	8.3	12.8	4.8	265.9
	38	171.6	64.2	60.6	22.7	22.0	8.2	12.8	4.8	267.0
	39	171.6	64.7	58.9	22.2	22.0	8.3	12.8	4.8	265.3
	40	152.1	64.3	58.9	24.9	22.0	9.3	3.6	1.5	236.7
	41	152.1	64.3	58.9	24.9	22.0	9.3	3.6	1.5	236.7
	42	152.1	64.3	58.9	24.9	22.0	9.3	3.6	1.5	236.7
	43	152.1	64.3	58.9	24.9	22.0	9.3	3.6	1.5	236.7
	44	152.1	64.3	58.9	24.9	22.0	9.3	3.6	1.5	236.7
	45	152.1	64.3	58.9	24.9	22.0	9.3	3.6	1.5	236.7
	46	155.8	63.5	62.2	25.4	20.5	8.3	6.8	2.8	245.3
	47	155.8	61.9	68.5	27.2	20.5	8.1	6.8	2.7	251.6
	48	155.8	61.6	69.7	27.6	20.5	8.1	6.8	2.7	252.8
	49	155.8	61.7	69.4	27.5	20.5	8.1	6.8	2.7	252.5
	50	170.7	66.7	58.9	23.0	22.4	8.8	3.8	1.5	255.8
	51	170.7	66.7	58.9	23.0	22.4	8.8	3.8	1.5	255.8
	52	170.7	66.7	58.9	23.0	22.4	8.8	3.8	1.5	255.8
	53	170.7	66.7	58.9	23.0	22.4	8.8	3.8	1.5	255.8
	54	170.7	66.7	58.9	23.0	22.4	8.8	3.8	1.5	255.8
	55	170.7	66.7	58.9	23.0	22.4	8.8	3.8	1.5	255.8
	56	143.4	63.3	58.9	26.0	18.3	8.1	6.1	2.7	226.7
	57	143.4	63.3	58.9	26.0	18.3	8.1	6.1	2.7	226.7
	58	139.3	63.4	58.9	26.8	18.3	8.3	3.1	1.4	219.7
	59	139.3	63.4	58.9	26.8	18.3	8.3	3.1	1.4	219.7

Source: Author.